DISCOVERING A PREDICTIVE METABOLIC SIGNATURE OF DRUG-INDUCED STRUCTURAL CARDIOTOXICITY

by

TARA JANE BOWEN

A thesis submitted to the University of Birmingham for the degree of

DOCTOR OF PHILOSOPHY

School of Biosciences

College of Life and Environmental Sciences

University of Birmingham

June 2023

UNIVERSITY OF
BIRMINGHAM

University of Birmingham Research Archive

e-theses repository

This unpublished thesis/dissertation is copyright of the author and/or third parties. The intellectual property rights of the author or third parties in respect of this work are as defined by The Copyright Designs and Patents Act 1988 or as modified by any successor legislation.

Any use made of information contained in this thesis/dissertation must be in accordance with that legislation and must be properly acknowledged. Further distribution or reproduction in any format is prohibited without the permission of the copyright holder.

ABSTRACT

Drug-induced structural cardiotoxicity is a leading cause of attrition and project failure in drug discovery and development, limiting the delivery by the pharmaceutical industry of safe and efficacious medicines. Overcoming this costly challenge requires comprehensive mapping of toxicological mechanisms and discovery of predictive, translational biomarkers, such that cardiac safety assessment of lead compounds and preclinical to clinical translation may be improved. Untargeted metabolomics is an established approach in toxicology for characterising endogenous metabolic responses to xenobiotic exposure, facilitating toxicological mode of action and metabolic biomarker discovery. With efforts to overcome challenges faced in the analysis of more advanced *in vitro* models, e.g., cardiac microtissues, and in the biological interpretation of data due to often low coverage and low confidence in metabolite annotation, untargeted metabolomics may help to deliver the unmet need. The approach is also capable of providing deep insights into xenobiotic fate, although this capability is yet to be fully demonstrated.

The overarching aim of this thesis was to develop and apply untargeted metabolomics workflows to characterise the fate and effects of xenobiotics in model systems, ultimately, to discover a molecular signature predictive of drug-induced structural cardiotoxicity. First, a workflow to discover and analyse xenobiotic-related measurements from routine ultra-high performance liquid chromatography-mass spectrometry (UHPLC-MS) untargeted metabolomics datasets was assembled. Implementation of this workflow clearly demonstrated how untargeted metabolomics can discover extensive xenobiotic biotransformation maps, temporally changing relative systemic exposure, and direct associations of endogenous biochemical responses to the internal dose.

Next, the need for a workflow enabling untargeted metabolomics analysis of cardiac microtissues was addressed. A filtration-based approach for harvesting microtissues was evaluated and the sensitivity and reproducibility of nano-electrospray direct infusion mass spectrometry (nESI-DIMS) measurements of intracellular extracts were assessed, revealing samples consisting of 28-pooled microtissues, harvested by filtration, are suitable for profiling the intracellular metabolome and lipidome. Subsequently, an extensive workflow combining nESI-DIMS untargeted metabolomics and lipidomics of intracellular extracts with complementary UHPLC-MS analysis of spent culture medium was implemented. The acquired data enabled investigation of time-resolved metabolic and lipid perturbations in cardiac microtissues induced by a structural cardiotoxin, demonstrating the workflow can facilitate toxicological mode of action and biomarker discovery.

To address the annotation challenge of untargeted metabolomics data and support biological inference, a library of 315 polar metabolites and 2350 lipids present in cardiac microtissue intracellular extracts and detectable by UHPLC-MS was curated. When used in place of larger, non-specific public metabolite databases, e.g., the Human Metabolome Database, the curated library should enable higher confidence annotation of untargeted metabolomics data.

Finally, implementation of the developed workflows in an extensive untargeted metabolomics study applying intracellular nESI-DIMS and extracellular UHPLC-MS-based analyses to measure the fate and effects of twelve xenobiotics, eight structurally cardiotoxic and four non-structurally cardiotoxic, each at two concentrations, after 6-, 48- and 72-hour exposures, in cardiac microtissues, enabled discovery of metabolic signatures predictive of drug-induced structural cardiotoxicity. This included the responses of creatine, ceramides, and several purine metabolism

intermediates. Future efforts to validate and mechanistically anchor the proposed structural cardiotoxicity metabolic biomarker panel and subsequently deploy as a high-throughput targeted assay are needed to translate the findings of this thesis into an improved cardiac safety screening capability for drug development.

ACKNOWLEDGEMENTS

I would like to extend my upmost gratitude to my supervisor, Professor Mark Viant. Thank you for providing me with the opportunity and for your enduring guidance and encouragement throughout the PhD. Your supervision has been invaluable to my development as a scientist. I would also like to thank Dr. Ralf Weber for his most useful input throughout the project.

I would like to extend great gratitude to Dr. Amy Pointon for her supervision, guidance, and inspiration. Thank you for your active involvement throughout this PhD, the direct relevance to an industrial challenge has been one of the most stimulating elements of my research. I would also like to thank to Dr. Amanda Wilson, your expert advice has been of great value. Dr. Andrew Hall, I cannot thank you enough for the huge amount of energy and time you have dedicated to this PhD project, you have been instrumental to its success. I am also grateful to you for ensuring my Cambridge site visits were a most enjoyable experience.

To all members of the fourth-floor metabolomics team, past and present, thank you for your patience and willingness to help. In particular, thank you Dr. Gavin Lloyd, for your endless support with statistics, Dr. Martin Jones and Dr. Lukas Najdekr, for offering many technical insights, and Dr. Matthew Smith, for your extensive help when facing a data processing challenge. Thank you also to the team for providing a welcoming and social environment in which to spend the past four and a half years, even during the most isolating of times (Covid-19 lockdowns). Dr. Annie Woolven, Dr. Judith Ngere, Dr. Rosemary Barnett, and Dr. Hanna Gruszczynska, thank you for your lasting support and friendship.

Thank you to the Biotechnology and Biological Sciences Research Council (BBSRC) and AstraZeneca for funding this PhD. Thanks also to Thermo Scientific for the provision of technical advice as part of the Thermo Alliance Partnership with the University of Birmingham, and to Beckman Coulter for the technology collaboration with the University of Birmingham.

To Nathanial (Nat), thank you for being by my side over the past four and a half years. Time spent with you has been a welcome distraction from the many challenges of my PhD journey and your patience, kindness and encouragement has been most appreciated.

To my family, thank you for all the love and support you have given me throughout my education – you'll be glad I am now finally ready to "leave school"! I will be forever grateful for the countless opportunities you have provided me. I would not have achieved all that I have without your selfless backing.

PUBLISHED MATERIAL

The content of Chapter 2 has been published in Nature Communications:

Simultaneously discovering the fate and biochemical effects of pharmaceuticals through untargeted metabolomics

Tara J. Bowen[1], Andrew D. Southam[1,2], Andrew R. Hall[3], Ralf J.M. Weber[1,2], Gavin R. Lloyd[2], Ruth Macdonald[4], Amanda Wilson[5], Amy Pointon[3], Mark R. Viant[1,2]

[1] School of Biosciences, University of Birmingham, Edgbaston, Birmingham B15 2TT, UK

[2] Phenome Centre Birmingham, University of Birmingham, Edgbaston, Birmingham B15 2TT, UK

[3] Safety Innovations, Clinical Pharmacology and Safety Sciences, BioPharmaceuticals R&D, AstraZeneca, Cambridge, UK

[4] Animal Sciences and Technology, Clinical Pharmacology and Safety Sciences, BioPharmaceuticals R&D, AstraZeneca, Cambridge, UK

[5] Integrated Bioanalysis, Clinical Pharmacology and Safety Sciences, BioPharmaceuticals R&D, AstraZeneca, Cambridge, UK

Nat Commun **14**, 4653 (2023). https://doi.org/10.1038/s41467-023-40333-7

Author contributions: T.J.B. developed the workflow, analysed the data, and prepared the manuscript. A.D.S. performed the laboratory experiments and provided conceptual advice. A.R.H. performed the laboratory experiments. R.J.M.W. provided technical support and conceptual advice. G.R.L. provided technical support and statistical advice. A.W. co-designed the experiments and gave conceptual advice. A.P. co-designed the experiments, gave conceptual advice, and co-supervised the project. M.R.V. developed the concept, co-designed the experiments, and supervised the project. All authors edited and approved the manuscript.

Raw data supporting the results presented in Chapter 2 have been made available to the public via MetaboLights (https://www.ebi.ac.uk/metabolights/MTBLS2746) and MassBank (https://massbank.eu/MassBank/; accession codes: MSBNK-UoB-XB000xxx, where xxx is 101–112, 200–215, 300–306, 400–406, 500–504, 600, 700–701, 800 or 900–902).

The content of Chapter 3 has been published in Metabolites:

> An Extensive Metabolomics Workflow to Discover Cardiotoxin-Induced Molecular Perturbations in Microtissues
>
> Tara J. Bowen[1], Andrew R. Hall[2], Gavin R. Lloyd[3], Ralf J.M. Weber[1,3], Amanda Wilson[4], Amy Pointon[2], Ralf J.M. Weber[1,3], Mark R. Viant[1,3]
>
> [1] School of Biosciences, University of Birmingham, Edgbaston, Birmingham B15 2TT, UK
>
> [2] Safety Innovations, Clinical Pharmacology and Safety Sciences, BioPharmaceuticals R&D, AstraZeneca, Cambridge, UK
>
> [3] Phenome Centre Birmingham, University of Birmingham, Edgbaston, Birmingham B15 2TT, UK
>
> [4] Integrated Bioanalysis, Clinical Pharmacology and Safety Sciences, BioPharmaceuticals R&D, AstraZeneca, Cambridge, UK
>
> Metabolites 2021, 11(9), 644; https://doi.org/10.3390/metabo11090644

Author contributions: Conceptualisation, T.J.B., A.R.H., A.W., A.P. and M.R.V.; methodology, T.J.B., A.R.H., G.R.L., R.J.M.W., A.W., A.P. and M.R.V.; formal analysis, T.J.B.; investigation, T.J.B. and A.R.H.; writing—original draft preparation, T.J.B.; writing—review and editing, T.J.B. and M.R.V.; visualisation, T.J.B.; funding acquisition, A.P. and M.R.V. All authors have read and agreed to the published version of the manuscript.

TABLE OF CONTENTS

Abstract ..... **ii**

Acknowledgements ..... **v**

Published material ..... **vii**

Table of Contents ..... **ix**

Table of Figures ..... **xii**

Table of Tables ..... **xv**

List of Abbreviations ..... **xvii**

CHAPTER 1: Introduction **1**

1.1 Safety in drug discovery and development 1

1.1.1 Discovery and development of a new medicine: the process 1

1.1.2 Targeting safety-related attrition 3

1.2 Structural cardiotoxicity: model systems and existing biomarkers 6

1.2.1 Physiologically relevant test systems 8

1.2.2 Predicting structural cardiotoxicity in vitro 11

1.3 Omics strategies in investigative toxicology 13

1.4 Toxico-metabolomics for biomarker discovery 15

1.4.1 Design of an untargeted toxico-metabolomics experiment: some considerations 17

1.4.2 Sample preparation for metabolomics analysis 20

1.4.3 Acquiring metabolomics data by mass spectrometry 23

1.4.4 Interrogating metabolomics data by statistical analysis 37

1.4.5 Challenges of metabolite annotation and identification 43

1.5 Importance and measurement of xenobiotic toxicokinetics 48

1.6 Research objectives 50

CHAPTER 2: Simultaneously discovering the fate and biochemical effects of pharmaceuticals through untargeted metabolomics **53**

2.1 Introduction 53

2.2 Materials and Methods 56

2.2.1 Chemicals 56

2.2.2 In vivo rat studies: animals, treatment and sampling 56

2.2.3 Cardiomyocyte study 57

2.2.4 Human plasma samples 58

2.2.5 Extraction of polar metabolites and lipids from cardiac tissue 59

2.2.6 Extraction of polar metabolites and lipids from cardiomyocytes 60

2.2.7 Extraction of polar metabolites and lipids from biofluids 61

2.2.8 Untargeted ultra-performance liquid chromatography-mass spectrometry 61

2.2.9 Untargeted metabolomics raw data processing 63

2.2.10 Xenobiotic-based data analysis and annotation 64

2.2.11 Endogenous metabolite and lipid-based data analysis 66

2.3 Results and Discussion 68

2.3.1 Development of untargeted workflow to discover xenobiotics 68

2.3.2 Untargeted workflow discovers fate of sunitinib in rat 75

2.3.3 Untargeted workflow discovers fate of KU60648 in rat 81

2.3.4 Temporally tracking pharmaceuticals and biotransformation products 86

2.3.5 Lipid responses associate with internal dose 92

2.3.6 Contrasting metabolic competencies of experimental models 104

2.3.7 Untargeted workflow discovers fate of pharmaceuticals in humans 107

2.4 Conclusions 110

CHAPTER 3: An extensive metabolomics workflow to discover cardiotoxin-induced molecular perturbations in microtissues 114

3.1 Introduction 114
3.2 Materials and Methods 118
3.2.1 Cell culturing and sunitinib exposure 118
3.2.2 High content biology assay 119
3.2.3 Microtissue sample collection 120
3.2.4 Intracellular nESI-DIMS Untargeted Metabolomics and Lipidomics 121
3.2.5 UHPLC-MS(/MS) untargeted metabolomics and quantitation of sunitinib 126
3.2.6 Statistical Analysis 130
3.3 Results and Discussion 132
3.3.1 Comparison of approaches for the sampling of cardiac microtissues for untargeted metabolomics 132
3.3.2 Sensitivity and reproducibility of nESI-DIMS untargeted metabolomics measurements using very low biomass samples 136
3.3.3 Probing molecular responses of cardiac microtissues to sunitinib exposure 139
3.4 Conclusion 151

CHAPTER 4: Characterising the cardiac microtissue metabolome and lipidome ... 153

4.1 Introduction 153
4.2 Materials and Methods 156
4.2.1 Materials 156
4.2.2 Cell culturing and sample collection 156
4.2.3 Extraction of intracellular polar compounds and lipids 157
4.2.4 Resuspension of dried extracts 158
4.2.5 Data acquisition by UHPLC-MS^n 158
4.2.6 Data processing and compound annotation 162
4.2.7 Pathway mapping 165
4.3 Results and Discussion 166
4.3.1 Analytical sensitivity and MS^n coverage 166
4.3.2 Annotating compounds detected within polar intracellular extracts of cardiac microtissues by HILIC UHPLC-MS^N 169
4.3.3 Annotating compounds detected within lipid intracellular extracts of cardiac microtissues by RP-C_{30} UHPLC-MS^N 173
4.4 Conclusions 177

CHAPTER 5: Discovering a predictive metabolic signature of drug-induced structural cardiotoxicity in cardiac microtissues 180

5.1 Introduction 180
5.2 Materials and Methods 184
5.2.1 Cell culturing 184
5.2.2 Exposures 184
5.2.3 Sample collection 186
5.2.4 Extraction of intracellular polar compounds and lipids 187
5.2.5 Resuspension of dried intracellular extracts 187
5.2.6 Data acquisition by nESI-DIMS 188
5.2.7 Processing and annotation of nESI-DIMS data 192
5.2.8 Sample preparation for UHPLC-MS 195
5.2.9 Data acquisition by UHPLC-MS 196
5.2.10 Quantitation of extracellular parent xenobiotic concentrations 197
5.2.11 Processing and annotation of UHPLC-MS untargeted data 197
5.3 Results and Discussion 201

5.3.1 Discovering the fate of xenobiotics in a cardiac microtissue test system 201
5.3.2 Exploring the metabolic responses of cardiac microtissues to xenobiotic exposure 212
5.3.3 Measuring the intracellular and extracellular effects of xenobiotic exposure: analytical sensitivity, reproducibility and mass accuracy 221
5.3.4 Discovering a predictive signature of drug-induced structural cardiotoxicity 225
5.4 Conclusions 238
CHAPTER 6: Conclusions and future work 240
6.1 Simultaneously discovering the fate and biochemical effects of xenobiotics through untargeted metabolomics 241
6.2 An extensive metabolomics workflow to discover cardiotoxin-induced molecular perturbations in microtissues 244
6.3 Characterising the cardiac microtissue metabolome and lipidome 246
6.4 Discovering a predictive metabolic signature of drug-induced structural cardiotoxicity in cardiac microtissues 248
6.5 Future directions 250
APPENDIX A 254
APPENDIX B 271
APPENDIX C 274
APPENDIX D 275
References i

TABLE OF FIGURES

Figure 1.1 Overview of the drug discovery and development process. 2
Figure 1.2 The omics cascade. 15
Figure 1.3 Schematics of the three mass spectrometers used for metabolomics data acquisition in this thesis. 25
Figure 1.4 Diagram describing the process of producing gas-phase ions by electrospray ionisation. 26
Figure 1.5 Graphical representation of a C-trap coupled to an Orbitrap mass analyser 29
Figure 1.6 Schematic of a typical ultra-high performance liquid chromatography instrument coupled to a mass spectrometer. 33
Figure 1.7 Image of a TriVersa Nanomate system and a conductive silicone nano-electrospray ionisation chip containing small nozzles which facilitate sample spray. 36
Figure 1.8 Schematic of a typical workflow for processing and analysing mass spectrometry-based untargeted metabolomics data. 38
Figure 1.9 Graphical representation of unsupervised multivariate analysis outputs. 41
Figure 1.10 Levels of confidence in small molecule identification using high resolution mass spectrometry data. 44
Figure 2.1 Schematic of the untargeted ADME/TK workflow. 69
Figure 2.2 Distribution of peak intensity fold changes observed in untargeted metabolomics toxicity datasets. 72
Figure 2.3 Application of the untargeted ADME/TK workflow to plasma of rats exposed to sunitinib. 77
Figure 2.4 Application of the untargeted ADME/TK workflow to plasma of rats exposed to KU60648. 83
Figure 2.5 Reliability of untargeted metabolomics relative peak intensity measurements of pharmaceuticals in rat plasma. 87
Figure 2.6 Temporal distribution of pharmaceuticals in plasma of exposed rats. 88
Figure 2.7 Temporal distribution of sunitinib and its biotransformation products in plasma of exposed rats 90
Figure 2.8 Temporal distributions of KU60648 and its biotransformation products in plasma of exposed rats. 91
Figure 2.9 Sunitinib-induced perturbation of the plasma metabolome of rats. 93
Figure 2.10 Sunitinib-induced perturbation of the cardiac tissue metabolome of rats. 95
Figure 2.11 Association of internal relative dose of sunitinib with the cardiac tissue lipidome of exposed rats. 96
Figure 2.12 Four sphingomyelins associated with sunitinib levels at the site of toxicity have significantly increased levels in plasma of exposed rats. 98
Figure 2.13 KU60648-induced perturbation of the plasma metabolome of rats. 99
Figure 2.14 KU60648-induced perturbation of the cardiac tissue metabolome of rats. 100
Figure 2.15 Association of internal relative dose of KU60648 with the cardiac tissue lipidome of exposed rats. 101
Figure 2.16 Four acylcarnitines associated with KU60648 levels at the site of toxicity have significantly increased levels in plasma of exposed rats. 103

Figure 2.17 Comparison of the metabolic competencies of cardiomyocyte (hiPSC-CM) *in vitro* cultures and rat by applying the untargeted ADME/TK workflow to four UHPLC-MS metabolomics datasets. 105
Figure 2.18 Temporal distribution of sunitinib in the intracellular extracts (coral) and culture medium (light blue) of hiPSC-CM cultures exposed to sunitinib. 106
Figure 2.19 Discovery of pharmaceuticals and their biotransformation products in a human plasma untargeted metabolomics dataset. 108
Figure 3.1 Peak intensity of internal standard. 125
Figure 3.2 Graphical summary of two approaches for sampling cardiac microtissues, incorporating isolation from culture medium, washing, and quenching of metabolism. 133
Figure 3.3 PCA score plots visualising the metabolic differences between samples harvested by centrifugation or filtration. 134
Figure 3.4 Evaluation of washing procedures for filtration-based sampling of microtissues. 136
Figure 3.5 Phenotypic perturbations induced by 72-hour exposure to a low and high dose of sunitinib in cardiac microtissues. 140
Figure 3.6 Quantitation of sunitinib concentrations in spent culture media of cardiac microtissues. 141
Figure 3.7 Assessment of total metabolic variability. 143
Figure 3.8 Univariate data analysis reveals significant perturbation of intracellular and extracellular features. 144
Figure 3.9 *k*-means cluster analysis reveals similarities in the temporal responses of intracellular lipid features. 145
Figure 3.10 PLS-DA scores plots discriminating between sunitinib exposed and control samples. 147
Figure 3.11 Consistency in features important to PLS-DA models. 148
Figure 3.12 Responses of extracellular metabolites following sunitinib exposure. 150
Figure 4.1 Flow chart describing MS^n data acquisition method when coupled to HILIC chromatography. 160
Figure 4.2 Flow chart describing MS^n data acquisition when coupled to RP-C_{30} chromatography. 161
Figure 4.3 Contribution of different approaches to polar compound annotations. 169
Figure 4.4 Proportion of toxicologically relevant metabolites. 173
Figure 4.5 Sources of lipid annotations. 174
Figure 4.6 LipidSearch annotation grades. 176
Figure 4.7 Abundance of lipids according to class. 177
Figure 5.1 SIM-based nESI-$DIMS^n$ data acquisition method. 191
Figure 5.2 Smooth spline functions for retention time alignment of HILIC positive data. 198
Figure 5.3 External calibration curves for quantitation of twelve parent xenobiotics. 203
Figure 5.4 Quantitation of eleven parent xenobiotics in spent culture medium of cardiac microtissues. 205
Figure 5.5 Parent xenobiotics and products of their biotransformation discovered in intracellular extracts and spent culture medium of exposed cardiac microtissues. 209
Figure 5.6 Magnitude of perturbation in cardiac microtissues induced by 72 exposure conditions. 214
Figure 5.7 Structural cardiotoxin-specific significant intracellular metabolic perturbations in cardiac microtissues. 217

Figure 5.8 Unsupervised clustering of metabolic responses induced by each exposure condition. 219
Figure 5.9 Inter-batch variation in processed metabolomics data. 222
Figure 5.10 Mass error of internal standard measurements across analytical sequences. 225
Figure 5.11 OPLS-DA model predictive of structural cardiotoxicity. 226
Figure 5.12 Conservation of predictive features over time. 229
Figure 5.13 The responses of intracellular ceramides in cardiac microtissues are predictive of the structural cardiotoxicity potential of exposure xenobiotics. 231
Figure 5.14 Intracellular levels of purine metabolism intermediates in cardiac microtissues are predictive of the structural cardiotoxicity potential of exposure xenobiotics. 233
Figure 5.15 Intracellular levels of pantothenic acid in cardiac microtissues are predictive of the structural cardiotoxicity potential of exposure xenobiotics. 234
Figure A.1 Chromatographic peaks of sunitinib and related compounds measured in rat plasma. 256
Figure A.2 Mass spectra of sunitinib biotransformation products measured in rat plasma. 257
Figure A.3 Chromatographic peaks of KU6068 and related compounds measured in rat plasma. 259
Figure A.4 Mass spectra of KU60648 biotransformation products measured in rat plasma. 260
Figure A.5 Confident annotation of pharmaceuticals detected in human plasma. 262
Figure A.6 Chromatographic peaks of pharmaceuticals and their biotransformation products measured in human plasma. 267
Figure A.7 Mass spectra of pharmaceuticals and their biotransformation products detected in human plasma. 269
Figure A.8 Confident annotation of four biotransformation products detected in human plasma. 270
Figure B.1 Comparison of measured MS/MS fragmentation spectra for each annotated feature (top) and reference spectra for the corresponding metabolite from the mzCloud library (www.mzcloud.org; bottom). 271
Figure B.2 Extracted ion chromatograms (EICs) showing matching retention times (±30-second tolerance) between each annotated feature, as measured in an intra-study QC sample (top EIC, labelled “intra-study QC”), and the corresponding reference standard (bottom EIC, labelled “standard”). 272
Figure B.3 Comparison of measured MS/MS fragmentation spectra for each annotated feature (top) and reference spectra for the corresponding metabolite from analysis of a reference standard. 273
Figure D.1 (Dis)similarity of the cardiac microtissue response to xenobiotics. 275
Figure D.2 Retention time shifts observed in HILIC positive dataset. 278
Figure D.3 Extracted ion chromatograms of parent xenobiotic peaks. 279
Figure D.4 MS/MS spectra of parent xenobiotics. 280
Figure D.5 Quantitation of eleven parent xenobiotics in stability control samples. 281
Figure D.6 OPLS-DA models predictive of structural cardiotoxicity. 282

TABLE OF TABLES

Table 1.1 Summary of Orbitrap characteristics for the three Thermo Scientific mass spectrometers used in this thesis. 30
Table 1.2 The levels of metabolite identification confidence, as defined by the Metabolomics Standards Initiative. 44
Table 2.1 Number of features in rat plasma and cardiac tissue untargeted metabolomics datasets before and after application of the three untargeted ADME/TK workflow filters. 76
Table 2.2 Number of significantly changing features in plasma and cardiac tissue of rats exposed to sunitinib compared to biological controls. 94
Table 2.3 Over-representation analysis of lipids significantly correlated to sunitinib levels in the cardiac tissue of exposed rats. 97
Table 2.4 Number of significantly changing features in plasma and cardiac tissue of rats exposed to KU60648 compared to biological controls. 100
Table 2.5 Over-representation analysis of lipids significantly correlated to KU60648 levels in the cardiac tissue of exposed rats. 103
Table 2.6 Number of features in the untargeted metabolomics datasets of hiPSC-CM cultures before and after application of the three untargeted ADME/TK workflow filters. 105
Table 2.7 Implementing the untargeted ADME/TK workflow on human plasma UHPLC-MS untargeted metabolomics data. 110
Table 3.1 Ion source parameters for data acquisition by two UHPLC-MS(/MS) assays 128
Table 3.2 Coverage, technical and total reproducibility of metabolomics datasets from microtissues harvested by either centrifugation or filtration. 134
Table 3.3 Sensitivity, technical and total reproducibility of metabolomics datasets from microtissue samples of varying biomass. 137
Table 3.4 Performance metrics for PLS-DA models. 147
Table 3.5 Results of over-representation pathway analysis of metabolites significantly perturbed by sunitinib exposure in cardiac microtissues. 149
Table 4.1 Ion source and ion optics settings for data acquisition by UHPLC-MS^n 159
Table 4.2 XCMS parameters used for full scan (MS^1) peak picking and grouping. 162
Table 4.3 Assessment of the analytical sensitivity and MS^n coverage of UHPLC-MS^n analyses of intracellular extracts from cardiac microtissues. 166
Table 4.4 Representation of metabolic pathways. 172
Table 5.1 Nominal concentrations of xenobiotic exposures. 186
Table 5.2 Spectral stitching nESI-DIMS method parameters. 189
Table 5.3 Concentrations of calibration standards and QC preparations for quantitation of parent xenobiotics. 196
Table 5.4 External calibration metrics. 204
Table 5.5 Difference between nominal and measured concentrations of eleven quantifiable xenobiotics. 207
Table 5.6 Biotransformation products of test xenobiotics discovered in the spent culture media of exposed cardiac microtissues. 211
Table 5.7 Quality assessment of batch- and assay-specific metabolomics data. 223
Table 5.8 Performance of OPLS-DA models. 227
Table 5.9 Proposed structural cardiotoxicity metabolic biomarker panel. 237
Table A.1 A summary of the datasets analysed 254
Table A.2 Summary of the two pharmaceuticals investigated in rats. 254

Table A.3 UK National Health Service Top20 most prescribed drugs between 2014 and 2020 and their detection. 261
Table C.1 Number of features reported by XCMS processing of UHPLC-MS datasets acquired by analysis of cardiomyocytes and rat cardiac tissue, before and after peak matrix filtering.....274
Table D.1 SIM window definitions for nESI-DIMS-based untargeted metabolomics. 276

LIST OF ABBREVIATIONS

2D	Two dimensional
3D	Three dimensional
3Rs	Replacement, Reduction and Refinement of the use of animals in science
ADME	Absorption, distribution, metabolism (biotransformation) and excretion
ADP	Adenosine diphosphate
ADR	Adverse drug reaction
AGC	Automatic gain control
AMP	Adenosine monophosphate
ANOVA	Analysis of variance
AO	Adverse outcome
AOP	Adverse outcome pathway
ATP	Adenosine triphosphate
au	Approximately unbiased
AUC	Area under the curve
BCAA	Branched chain amino acids
BEAMSpy	Birmingham mEtabolite Annotation for Mass Spectrometry
BER	Balanced error rate
CDI	Cellular Dynamics International, Fujifilm, US
CE	Collision energy
CID	Collision-induced dissociation
CII	Confidence-in-identification
CiPA	Comprehensive *in vitro* Proarrhythmia Assay
C_{max}	Maximum (clinical) blood concentration
CoA	Coenzyme A
cTn	Cardiac troponin
CV	Coefficient of variation
DC	Direct current
DDA	Data dependent acquisition
DIA	Data independent acquisition
DIMS	Direct infusion mass spectrometry
DMA	Deep metabolome annotation
DMSO	Dimethyl sulfoxide

DMTA	Design-Make-Test-Analyse
DNA	Deoxyribose nucleic acid
ECM	Extracellular matrix
EIC	Extracted ion chromatogram
Elite	Thermo Scientific Orbitrap Elite mass spectrometer
ER	Endoplasmic reticulum
ESI	Electrospray ionisation
FDA	United States Food and Drug Administration
FDR	False discovery rate
FT	Fourier transform
FT-ICR	Fourier transform ion cyclotron resonance
FWHM	Full width half maximum
GC-MS	Gas chromatography-mass spectrometry
glog	Generalised log
GMP	Guanosine monophosphate
HBRC	University of Birmingham's Human Biomaterials Resource Centre
HCA	Hierarchical clustering analysis
HCB	High content biology
HCD	Higher-energy collisional dissociation
hCFs	Human cardiac fibroblasts
hCMECs	Human cardiac microvascular endothelial cells
hERG	*human Ether-à-go-go-related gene*
hESC-CMs	Human embryonic stem cell-derived cardiomyocytes
HILIC	Hydrophilic interaction
hiPSC-CMs	Human-induced pluripotent stem cell-derived cardiomyocytes
HMDB	Human Metabolome Database
HRMS	High resolution mass spectrometry
HSD	Honestly significant difference test
i7	Biomek i7 Hybrid Workstation (Beckman Coulter)
IC_{30}	30% maximal inhibitory concentration
ICH	International Council for Harmonisation of Technical Requirements for Pharmaceuticals for Human Use
ID-X	Thermo Scientific ID-X Tribrid Orbitrap mass spectrometer
IR	Intensity ratio
IVIVE	*In vitro* to *in vivo* extrapolation

KE	Key event
KEGG	The Kyoto Encyclopaedia of Genes and Genomes
KNN	*k*-nearest neighbour
LC	Liquid chromatography
LIT	Linear ion trap
LLOQ	Lower limit of quantitation
LMSD	LIPID MAPS Structural Database
LVEF	Left ventricular ejection fraction
*m/*z	Mass-to-charge ratio
MAD	Median absolute deviation
MIE	Molecular initiating event
MoA	Mode of action
MoNA	MassBank of North America
MPS	Micro-physiological systems
mRSD	Median relative standard deviation
MS	Mass spectrometry
MSI	Metabolomics Standards Initiative
MVI	Missing value imputation
NaCl	Sodium chloride
NCE	New chemical entity
nESI	Nano-electrospray ionisation
NHS	National Health Service
NMR	Nuclear magnetic resonance
OPLS-DA	Orthogonal partial least squares discriminatory analysis
OSC	Orthogonal signal correction
PCA	Principal components analysis
PCB	Phenome Centre Birmingham
PFP	Pentafluorophenyl
PLS-DA	Partial least-squares discriminatory analysis
ppm	Parts-per-million
PQN	Probabilistic quotient normalisation
QC	Quality control sample
QE-Focus	Thermo Scientific Q-Exactive Focus Orbitrap mass spectrometer
QSAR	Quantitate structure-activity relationship
Quant-blanks	Quantitation (calibration) blank samples

Quant-QCs	Quantitation (calibration) quality control samples
R&D	Research and Development
RF	Radio frequency
RNA	Ribose nucleic acid
ROC	Receiver operator curve
ROS	Reactive oxygen species
RP	Reversed phase
rpm	Revolutions per minute
RSC	Robust spline correction
RSD	Relative standard deviation
RT	Retention time
SAR	Structure-activity relationship
SBC	Signal drift and batch correction
SD	Standard deviation
SIM	Selected ion monitoring
SNR	Signal-to-noise ratio
SWATH	Sequential Windowed Acquisition of All Theoretical Fragment Ions
TdP	Torsades de Pointes
TK	Toxicokinetics
TKi	Tyrosine kinase inhibitor
UHPLC	Ultra-high-performance liquid chromatography
ULOQ	Upper limit of quantitation
VIP	Variable importance in project
VPR	Valid peak ratio
Δψm	Mitochondrial membrane permeability

CHAPTER 1: INTRODUCTION

1.1 SAFETY IN DRUG DISCOVERY AND DEVELOPMENT

1.1.1 DISCOVERY AND DEVELOPMENT OF A NEW MEDICINE: THE PROCESS

The treatment of disease using safe and efficacious medicines is fundamental to the quality of modern life, yet the discovery and development of new medication (drugs) is no trivial task. It is estimated that the development of a single new prescription medicine takes 10 to 15 years and costs $2.6 billion (1). Meanwhile, only 5% of the ca. 8000 rare diseases that exist have an available treatment (1).

The process of drug discovery and development, spanning initial disease and target selection through to marketing and clinical use, is complex and exhaustive (Figure 1.1). Typically, small molecule drug discovery and development begins with a discovery phase during which appropriate targets for a chosen disease are selected and high-throughput screening is performed to identify ‘hits’ which modulate the activity of the target protein upon interaction, from a library containing millions of small molecules. Hit chemical series advance to lead generation and optimisation, transitioning through the ‘Design-Make-Test-Analyse (DMTA) cycle’. Here, the physicochemical properties are characterised, and pharmacokinetic, safety and efficacy estimated, then related to chemical structure, building structure-activity relationships (SAR) to recognise molecular features to be ‘designed out’, with the aim of optimising drug-like properties. This phase is responsible for rapid filtering out of molecules with suboptimal characteristics, condensing 10,000 to 100,000 compounds to a few (<10) lead and back-up series with the most promising characteristics. These lead and back-up series undergo non-clinical testing and development, i.e., the pre-clinical phase, where more in-depth characterisation of

pharmacokinetic, safety and efficacy of compounds ensues (1). For candidates with acceptable safety and efficacy, these data are compiled to build a profile which must be approved by regulators before proceeding to 'first-in-human' clinical trials (Phase I). Phase I trials typically focus on evaluating the safety of candidates and establish a maximally tolerated dose in normal healthy volunteers. Phase II, or proof-of-concept, clinical trials seek to demonstrate that the candidate compound treats the intended indication and to discover an optimal dose. Phase III trials are much larger in size and endeavour to confirm the efficacy and safety (2, 3). The success rate of clinical trials (Phases I-III combined) is <12%, but if clinical trials are successful, approval by regulatory agencies is sought, for eventual launch to market (1).

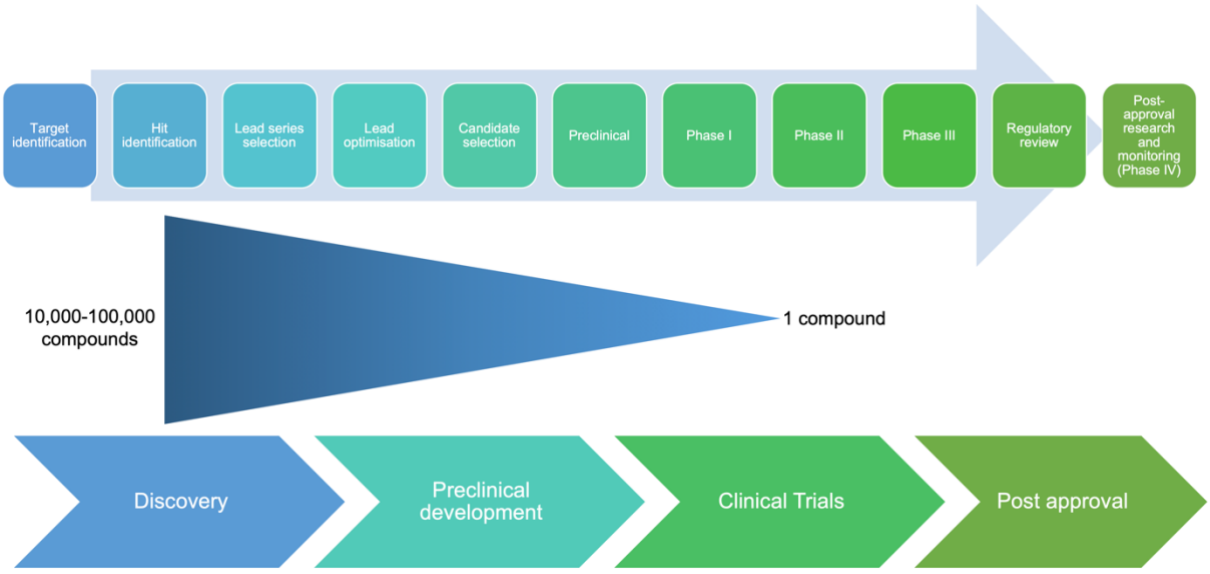


Figure 1.1 Overview of the drug discovery and development process.
Top, key steps in the process; middle, the filtering of 10,000-100,000 starting compounds to 1 compound by Phase II; bottom, the main phases of drug development. Adapted from (1, 3-5).

Over 97% of projects that begin at discovery phase fail to launch a safe and efficacious medicine to market (1). Thus, it becomes clear when considering this long, complex, and rigorous process, and its relatively low success rates, why such large sums of investment are required to get a drug to market.

Over the past decade, the productivity of research and development (R&D) within the pharmaceutical industry has declined, owing to increasingly rigorous requirements from regulatory bodies and growing difficulty to discover and develop truly innovative first-in-class new chemical entities (NCEs) (6). This has raised concern within the industry, with pharmaceutical companies now actively seeking to address the challenge. Proposed strategies include improving the efficiency of drug testing and decision making to enable more rapid delivery of safer, more effective medicines to patients in need. In part, this can be achieved by reducing the number of project closures and through shifting attrition to earlier phases of development, e.g., prior to candidate selection, thus limiting cost and time associated with failure (2, 4, 6).

1.1.2 Targeting safety-related attrition

A review of AstraZeneca's portfolio, published in 2014, revealed that unacceptable safety was the leading cause of attrition, accounting for >50% of project closures, with the majority occurring at the pre-clinical phase, but also dominating Phase I clinical trials. Furthermore, a lack of safety was also considered the root cause of further project failures by limiting the safety margin (the difference between the effective and maximum tolerated doses) (2). High attrition due to safety-related issues is not unique to AstraZeneca. Safety was the top cause of attrition at preclinical and Phase I stages, and the secondary cause of attrition at Phase II, amongst 812 oral compounds nominated between 2000 and 2010 at the top four pharmaceutical companies (GlaxoSmithKline, AstraZeneca, Eli Lilly and Company, and Pfizer) (7). Beyond attrition and project failure during drug discovery and development, the incidence of adverse drug reactions (ADRs), often the result of unexpected idiosyncratic toxicity, continues to be a concern (7). Tackling attrition due

to safety concerns and limiting the occurrence of ADRs is, consequentially, a key directive within the pharmaceutical industry (2, 7).

As per regulatory requirements, safety of NCEs is typically assessed through *in vivo* studies in toxicological species, e.g., rat and dog, whereby measurements of clinical chemistry, organ functionality and histological changes following repeat-dosing regimens are used to calculate safety margins and reveal adverse events (8). These approaches were found to be unsuccessful in detecting a safety signal for 40% of projects which went on to fail for safety-related concerns at a later stage (2), highlighting the limitations of existing preclinical safety screening. Reasons for this include poor cross-species translation of toxicological mechanism and/or pharmacokinetics (9), and late onset of toxicity or reliance on late-stage biomarkers, i.e., toxicological effects that do not reveal themselves until beyond the testing period, which can be relatively short in many *in vivo* studies. Furthermore, *in vivo* studies are associated with high costs and low throughput (10), and there are ethical concerns with relying on *in vivo* studies, particularly considering the growing commitment to the Replacement, Reduction and Refinement of the use of animals in science (3Rs) in drug development (11). Considering the shortfalls of these approaches to drug safety evaluation, alternative strategies are imperative to reducing attrition and ADRs.

Alternative strategies being introduced include *in silico* predictions or *in vitro* assays which directly measure a molecular event (e.g., modulation of protein activity) causally linked to toxicity, with the aim of understanding the potential impacts on key organs (5). These alternatives to animal-based safety studies can be cheaper, higher throughput and are accordant with commitment to the 3Rs (4, 5). Additionally, their

integration at an early stage of drug development can enable the results to impact chemistry through the DMTA cycle (5). Developments in this field have reduced safety-related attrition at preclinical and clinical phases, as revealed in a subsequent review of AstraZeneca's portfolio, published in 2018 (12). These improvements likely originate from improved screening, limiting the number of compounds proceeding to *in vivo* preclinical testing that ultimately going on to fail, thus also contribute toward the reduction and refinement in the use of animals (5). For example, the introduction of quantitative structure-activity relationship (QSAR) models to predict *human Ether-à-go-go-related gene* (hERG) potency resulted in a reduced fraction of compounds synthesised and/or undergoing high-throughput screening with 'high' hERG activity from 25% to 5-10% between 2003 and 2011 (4, 13-15). Notably, the growing evidence in the translational accuracy of *in vitro* approaches is beginning to influence regulatory requirements, with increasing acceptance of *in vitro* alternatives to traditional *in vivo* approaches, e.g., International Council for Harmonisation of Technical Requirements for Pharmaceuticals for Human Use (ICH)-S7B regulatory guidelines for screening ion channel inhibition, which has resulted in an absence of drugs withdrawn due to unacceptable risk of Torsades de Pointes (TdP, a clinical manifestation of functional cardiotoxicity) since its introduction (4, 13, 16). More recently, a substantial step toward complete replacement of animal-based safety studies was achieved with recent signed legislation enabling the U.S. Food and Drug Administration (FDA) to no longer require animal testing for approval of Phase I clinical trials (17).

Despite this encouraging progress, the development and implementation of new *in vitro* and *in silico* approaches for safety testing that possess high translational

relevance remains challenging. Mainly, developing *in vitro* assays to screen for safety signals typically relies on an understanding of the underlying mechanisms of toxicity and/or the availability of translational predictive biomarkers. Meanwhile, *in silico* prediction-based methods require both mechanistic understanding, and sufficient training and test datasets to build reliable models (5, 10). Yet for many safety signals such mechanistic understanding and availability of predictive biomarkers is limited, owing to the expansive and complex nature of xenobiotic interactions with biological systems, challenges in examining those interactions and discovering reproducible effects, and a lack of consolidation of vast data into organised knowledge. Where gaps in mechanistic understanding exist, and where there is a lack of predictive biomarkers, early-stage detection of associated safety issues remains elusive, and instances of idiosyncratic or unexplained toxicity at clinical phases continue (12). Ultimately, to reduce late-stage attrition and project failure, and consequentially improve R&D productivity, understanding of toxicological mechanisms must be furthered in unison with efforts to discover predictive safety biomarkers that can be implemented in early-stage NCE screening (4).

1.2 Structural cardiotoxicity: model systems and existing biomarkers

Drug-induced cardiotoxicity is a safety concern which remains poorly predicted during drug development (2, 18). Specifically, cardiotoxicity was the most common cause of preclinical safety-related project failure, and responsible for 24% of project closures due to poor safety at clinical phase, at AstraZeneca between 2005-2010 (2). It is also one of the top three reasons for post-approval market withdrawal (19).

Drug-induced cardiotoxicity can be classified as either functional or structural. Functional cardiotoxicity, defined as the acute alteration of myocardial electro-mechanical function, clinically manifests as arrhythmia and alteration of contractile function (18). The prediction of functional cardiotoxicity during drug discovery is well established through *in vitro* and *in silico* approaches assessing effect of NCEs on ion channel function, e.g., hERG assay, Comprehensive *in vitro* Proarrhythmia Assay (CiPA) initiative (13, 18). Other approaches based on drug effects on cardiac contractility have also been developed (20-23). Meanwhile, structural cardiotoxicity, defined as the morphological damage, change to intracellular organelles, and/or loss of viability of cardiomyocytes, is often not exposed until later stage *in vivo* repeat dose studies via histopathological endpoints (13, 16, 18, 24, 25). Beyond challenges in determining the structurally cardiotoxic potential of NCEs, heart failure, a clinical manifestation of structural cardiotoxicity and side effect of several marketed oncology drug classes, can only be diagnosed by retrospective approaches such as cardiac imaging and measuring troponin levels. As such, research to drive improvements in the ability to accurately predict structural cardiotoxicity is required to tackle the problem of late-stage attrition and project closure due to cardiac safety concerns, limit the continuation of damaging compounds into patients, and avoid termination of potentially efficacious medicines. This will require the development and use of highly physiologically relevant *in vitro* models, and discovery of translational predictive biomarkers such that findings from *in vitro* screens and preclinical species are reflective of clinical side effects.

1.2.1 PHYSIOLOGICALLY RELEVANT TEST SYSTEMS

Selection of the test system can be pivotal in terms of the translatability and predictive accuracy of *in vitro* experiment results. Traditionally, *in vitro* models employed in investigative toxicology and safety screening have consisted of two dimensional (2D) monolayers or suspensions of primary cells or cell lines. These models are limited by their lack of complexity and low physiological relevance (26). Recent developments in culturing methodologies has given rise to much improved options, from multi-cell type combinations and three dimensional (3D) cultures, which introduce physiologically-relevant cell-cell and cell-extracellular matrix (ECM) interactions (26-28), to more complex micro-physiological systems (MPS) and 'organ-on-a-chip' models that further mimic the microenvironment of organs and tissues through application of mechanical stimuli and perfusion of culture media generating oxygen and nutrient gradients (29).

In the field of cardiotoxicity, many studies have exploited human-induced pluripotent stem cell-derived cardiomyocytes (hiPSC-CMs) to investigate the functional and morphological effects of xenobiotic stimulus (20, 30-33). The popularity of these cells can be accounted for by their ability to spontaneously contract, unlike alternative cardiomyocyte cell lines, allowing measurements of contractility, a fundamental phenotypic factor in cardiology (34). Additionally, hiPSC-CMs overcome the ethical concerns associated with human embryonic stem cell-derived cardiomyocytes (hESC-CMs) and avoids the use of cells from preclinical species, helping to reduce the use of animals during drug discovery (21). However, the translatability and predictive capacity of hiPSC-CM monolayers is limited by their lack of cell-cell and cell-ECM interactions, lack of cell type diversity (non-cardiomyocytes are not

considered yet are proportional to >70% of the cell mass in the human myocardium, play key roles in cardiac biology and are expected to influence cardiac response to xenobiotic stimulus), and immature metabolic, electrophysiological and morphological phenotype compared to adult ventricular myocytes (14, 25, 27, 35).

Three-dimensional culturing of hiPSC-CMs with cardiac endothelial cells and cardiac fibroblasts, as scaffold-free, uniform sized, cardiac microtissues offers an enhancement in physiological relevance of *in vitro* cardiac model systems (21, 27, 36). Mainly, 3D culturing encourages the formation of cell-cell and cell-ECM interactions, supporting signalling between cells, while the presence of non-cardiomyocytes modulates the function of the cardiomyocytes and advances their maturity, as evidenced at the molecular, structural and functional level (21, 27, 37). Furthermore, the culturing conditions of cardiac microtissues in ultra-low adhesion 384-well microplates makes them amenable to high-throughput, unlike more complex “heart on a chip” technologies (38), enabling readouts of microtissue-based screening assays to influence lead optimisation.

The pertinence of cardiac microtissues for investigating and predicting drug-induced cardiotoxicity has been demonstrated. Through measuring the contractility of cardiac microtissues, the ionotropic effects of a panel of drugs at therapeutically relevant concentrations could be accurately assessed, including the direction of inotropy, which was not possible using hiPSC-CM monolayers (21). Additionally, imaging-based high-content biology measurements of cardiac microtissues, assessing mitochondrial membrane permeability ($\Delta\psi m$) and endoplasmic reticulum (ER) stress, coupled with cellular viability assays, were used to build phenotypic mechanistic fingerprints of structural cardiotoxicity for a panel of drugs. Measurements in cardiac

microtissues offered comparable sensitivity and improved specificity compared to hESC-CM monolayers (36). These examples provide evidence for the improved translational relevance of cardiac microtissues compared to monolayer single-cell cultures and highlight the value of employing more physiologically relevant *in vitro* models to investigate drug-induced structural cardiotoxicity.

Despite extensive efforts toward enhancing the translational relevance of *in vitro* models for toxicity (and efficacy) testing, there remain some limitations, e.g., the lack of interaction with other organ systems. Of particular relevance is the lack of interaction with the hepatic system, which is responsible for the majority of xenobiotic metabolism and clearance *in vivo*. While cardiac cells possess some xenobiotic metabolic competency, both *in vitro* and *in vivo* (39, 40), it is considered negligible compared to that of hepatocytes. Consequently, it's likely that the environment to which a cardiac *in vitro* model is exposed, i.e., only parent xenobiotic, in excess, does not reflect the *in vivo* exposure environment, where cardiac cells will be exposed to both parent xenobiotic and biotransformation products from the liver via the blood, and the abundances of these will vary temporally. This divergence from the *in vivo* exposure scenario can limit the translational accuracy of *in vitro* test results, e.g., if, *in vivo,* the hepatic system forms more toxic biotransformation products that are distributed to the heart. The development of interconnected liver-heart (41, 42) or human-on-a-chip (43) test systems offers a promising solution to this challenge but technology is not yet ready for large-scale and/or high-throughput implementation.

1.2.2 Predicting structural cardiotoxicity in vitro

Clinically, the gold standard for diagnosis of myocardial injury, which may be induced by xenobiotics or diseases, e.g., myocardial infarction, is through detection of increased cardiac troponin (cTn) release into the bloodstream. Compared to other established biomarkers of myocardial injury, e.g., lactate dehydrogenase and creatine kinase isoenzymes, cTn provides superior sensitivity and specificity. Meanwhile, cTn is a prominent example of reverse translation of biomarkers for drug development: it is employed during *in vivo* preclinical testing, complementing histopathology readouts for cardiac safety assessment (44, 45). The use of cTn as a biomarker of cardiac injury has also been extended to *in vitro* test systems, e.g., hiPSC-CMs, with demonstrated application in predicting the structurally cardiotoxic potential of xenobiotics (30, 46). However, while troponin is a highly sensitive, specific, and translational biomarker, it is released only after damage to the myocardium has occurred. *In vitro*, this means extracellular levels of cTn-1 tightly associate with cell viability measurements, indicating that cTn-1 offers little added value to an *in vitro*-based screening assay (30). Meanwhile, *in vivo,* structural cardiotoxicity is only discovered using cTn measurements if cardiac injury is induced within the timeframe of the experiment, yet structural cardiotoxicity may take much longer to establish and reach the measurable adverse outcome (AO). Consequently, the safety margin of candidate drugs is unreliably predicted and may lead to idiosyncratic toxicity during clinical trials or post-marketing. As such, there is a substantial need to discover alternative translational biomarkers which are prognostic of myocardial damage, and which can replace or complement cTn for cardiac safety assessment during drug development.

In recent years, *in vitro* assays based on multiparametric assessment of proposed key events of structural cardiotoxicity have been developed and tested. Doherty *et al*. employed a multi-parameter panel, composed of cell viability, caspase activation (biomarker of apoptosis), reactive oxygen species (ROS) generation (biomarker of mitochondrial damage), lipid formation, troponin secretion (biomarker of myocardial injury), and beat activity measurements, to assess drug-induced cardiotoxicity in hiPSC-CMs (30, 31). While the most sensitive parameter was beat activity, an indicator of functional cardiotoxicity, potency at therapeutically relevant concentrations against other parameters was used to evidence drug-specific structural cardiotoxic effects. Alternatively, Pointon *et al.* measured the effects of a panel of drugs on Δψm, ER integrity, calcium mobility, membrane permeability and cell viability of hESC-CMs and H9C2 cells (32). Similarly, the combined effects on the Δψm, ER integrity and cellular viability of cardiac microtissues has been investigated as an approach to predict structural cardiotoxicity of drugs (36).

These approaches indicate that structural cardiotoxicity is most likely the product of several intracellular toxicity pathways, i.e., mitochondrial stress, ER stress, perturbation to calcium signalling and lipid accumulation pathways, which converge at the physiological endpoint of morphological damage (47). Furthermore, evidence provided by Doherty *et al.*, Pointon *et al*., and Archer *et al.,* suggests that the primary mechanism driving the development of structural cardiotoxicity is compound specific, with further, more conserved perturbations triggered consequentially (30-32, 36). It is anticipated that the established assays discussed above do not probe the complete spectrum of effects induced by structural cardiotoxins, with further mechanisms which give rise to structural cardiotoxicity possible but yet to be discovered due to the

targeted nature of approaches taken. A more global, untargeted approach to discover the complete array of endogenous effects of structural cardiotoxins would allow more comprehensive mapping of contributing mechanisms and enable more informed selection of predictive biomarkers. Moreover, placing focus on determining molecular level events associated with structural cardiotoxicity could enable discovery of molecular biomarkers, e.g., metabolites, which are more readily translated and measurable across diverse test systems (i.e., *in vitro* and *in vivo)* and clinically.

1.3 OMICS STRATEGIES IN INVESTIGATIVE TOXICOLOGY

Investigative research to derive signatures of drug-induced toxicity and translate those signatures into organised knowledgebases of toxicological mechanisms or modes-of-action (MoA) is a promising strategy toward earlier prediction of ADRs (10). Adverse Outcome Pathways (AOPs), which describe the response of a biological system to xenobiotic exposure, are one such approach toward organised toxicological mechanistic knowledge (48). More specifically, AOPs define a sequential causal chain of key events (KE; a measurable toxicological endpoint, e.g., activation of a gene, cell proliferation) across successive levels of biological organisation, starting with a molecular initiating event (MIE; the initial point of chemical-biological interaction), and ending with an AO (a measurable change in morphology or physiology of an organism or system that results in impairment of the functional capacity or the capacity to compensate for stress), within a modular framework (10, 48-51). The organisation of mechanistic understanding as AOPs provides scientific rationale for monitoring early molecular and organelle level events, which are more sensitive and occur sooner after the MIE, in place of late-stage apical

endpoints, as typical of *in vivo* studies, for the prediction of toxicity (10, 48, 50, 52, 53).

Comprehensively mapping changes throughout networks of molecular interactions, e.g., transcriptional changes or modulation of cellular signalling, has been proposed to drive the discovery of MIEs and early KEs within AOPs. To this end, multiparametric, high-content approaches including omics technologies, which systematically map xenobiotic-induced perturbations at the molecular level, are powerful tools for investigative toxicology and AOP development (54-58). The impact of multiparametric approaches extends to the prediction of AOs, whereby one derived from the combined response of multiple parameters linked to KEs will likely lead to greater accuracy and enhanced sensitivity compared to a mono-parametric approach (58, 59).

Omics approaches encompass the comprehensive characterisation of biological molecules, including genes (genomics) and heritable modifications of deoxyribose nucleic acid (DNA) (epigenomics), transcripts (transcriptomics), proteins (proteomics), metabolites (metabolomics) and lipids (lipidomics) (Figure 1.2) (55, 57). Several studies have demonstrated the value of these data-rich approaches for developing mechanistic understanding and discovering predictive biomarkers of cardiotoxicity. As part of the EU/FP7 HeCaToS project to develop an *in silico* prediction system for drug safety assessment, Selevsek *et al*. integrated proteomic and transcriptomic measurements of cardiac microtissue responses to four anthracyclines to generate an interaction network and discover a common molecular signature of anthracycline-induced cardiotoxicity (60). Palmer *et al.* first identified metabolic-based biomarkers of both functional and structural cardiotoxicity before

developing a targeted metabolomics-based assay which measured the response of four metabolites representing different metabolic pathways to predict cardiotoxicity potential (61). Meanwhile, van Hasselt *et al*. implemented a transcriptomics approach, profiling transcriptional responses to 26 FDA-approved kinase inhibitors, to identify a gene signature predictive of cardiotoxicity risk of protein kinase inhibitors (62). Verheijen *et al*. also employed transcriptomics approach in the cardiotoxicity space, demonstrating pathway overrepresentation analysis of gene changes induced in cardiac microtissues could detect three known mechanisms of doxorubicin-induced cardiotoxicity (63).

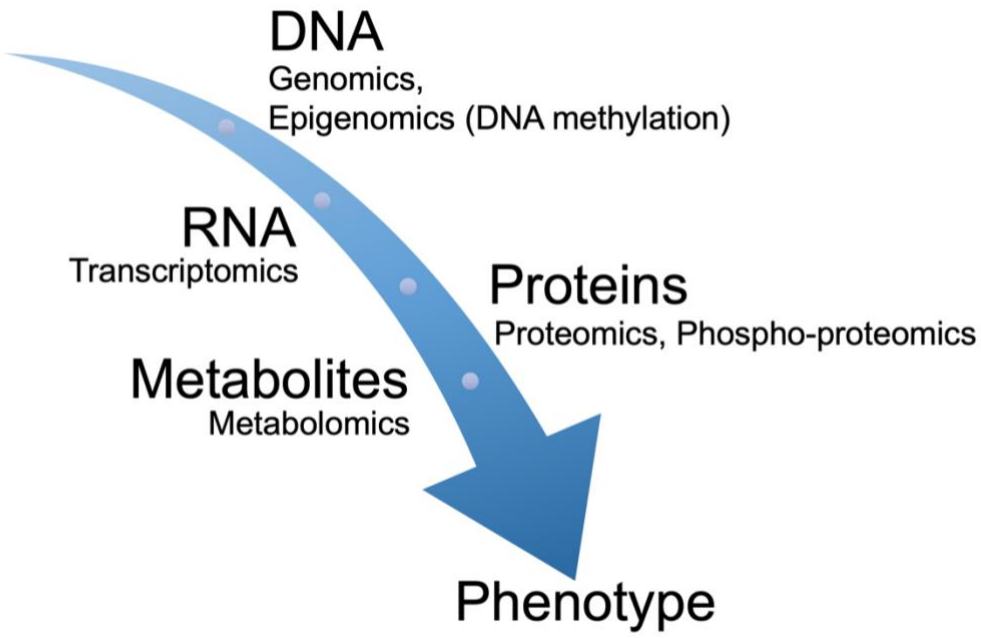


Figure 1.2 The omics cascade.
The organisation of biological molecules into levels, spanning DNA, i.e., the genome, through to phenotype, and the omics approaches for interrogating them. Adapted from (64-66).

1.4 TOXICO-METABOLOMICS FOR BIOMARKER DISCOVERY

The metabolome, defined as the ensemble of small molecules, i.e., molecular weight typically <1.5 kDa, which comprise the substrates, intermediary and end products of metabolism of a biological system, is a dynamic and time-sensitive snapshot of molecular phenotype, regulated by the complex interplay of genomic factors and

environmental stimuli. Major classes of endogenous metabolites include sugars, amino acids, nucleotides, fatty acids, and lipids. Within the cell, metabolites may serve as building blocks for larger molecules, including DNA, ribose nucleic acid (RNA) and proteins, or as energy stores. They also play a role in cell signalling and communication, thus regulating cellular processes (66-68). Taken together, and particularly considering the metabolome is the most downstream level of biological organisation, lying closest to phenotype, and thus most consistent with traditional toxicological end points compared with other '-omes' (Figure 1.2), metabolomics, i.e., the multi-disciplinary scientific study of metabolomes, has emerged as a formidable tool in investigative toxicology. The comprehensive measurement of metabolic responses to xenobiotic exposure can advance mechanistic understanding of toxicity through elucidation of toxicity pathways and networks and discover predictive or prognostic biomarkers of AOs (53, 64, 66, 69-71). Such application of metabolomics for toxicology purposes may be termed 'toxico-metabolomics' (52, 64).

Metabolomics studies may be broadly categorised into three strategies that differ in the number of compounds detected and the level of quantification which can be achieved. The three approaches are termed (1) untargeted metabolomics, (2) targeted metabolomics and, more recently established, (3) semi-targeted or hybrid metabolomics. Untargeted metabolomics is best suited to discovery-based studies. It is considered a hypothesis generating approach which aims for unbiased measurement of as many, typically several hundred, metabolites and lipids as possible. The metabolomes of different sample classes, e.g., xenobiotic exposed and biological control, are statistically compared, enabling discovery of molecular perturbations, at a feature, compound, or pathway level, depending on level of

annotation (52, 64, 68, 69). Meanwhile, targeted metabolomics, which involves the absolute quantification of a predefined set of metabolites using calibration curves of chemical standards, is applied in hypothesis testing studies, with experimental factors optimised to achieve highly precise and accurate measurements (52, 64, 68, 69). Like untargeted metabolomics, the hybrid approach aims to measure as many metabolites as possible, but with the addition of a predefined panel of approximately tens to hundreds of known metabolites which can be more confidently annotated or identified (64, 69).

To maximise the quality of results and the opportunity to elucidate toxicological mechanisms and discover predictive biomarkers, an untargeted toxico-metabolomics study requires careful experiment design, unbiased and reproducible sample collection and preparation, sensitive and reproducible data acquisition, robust data processing and statistical analysis, and confident metabolite annotation. These factors are considered in the sections that follow.

1.4.1 Design of an untargeted toxico-metabolomics experiment: some considerations

The design of a metabolomics experiment is highly dependent on the study's objectives and is integral to its success. First, the test system, which serves as a model for predicting the effects of xenobiotic exposure in human, must be selected. Traditionally, model species including rat have been the gold standard in toxicology. Measurements made from model species are the result of the complex interplay between a multitude of cell, tissue and organ types which are near impossible to fully replicate *in vitro* or incorporate into *in silico* models (72). As such, *in vivo* models offer some advantages in terms of translational predictivity, for example, they replicate,

although not precisely due to species-related differences, the dynamics of xenobiotic exposure within a human. Analysis of blood fractions (plasma, serum) is common for *in vivo*-based metabolomics. It provides a measure of the combined metabolic activity of all organs and tissues. Whilst it is challenging to directly associate changes in the blood metabolome to any one site of metabolism, less invasive sampling makes perturbations within the blood metabolome induced by xenobiotic exposure suitable for use as biomarkers (64, 67). Meanwhile, the analysis of tissue samples enables investigation of metabolic effects of external stimuli at their origin, thus is better suited to studies aiming to derive mechanistic hypotheses (64). Despite the benefits offered by investigating toxicology in whole organisms, *in vivo*-based approaches are expensive, of ethical concern, and their translational relevance is limited by species-related differences (11, 73).

Recent advances in *in vitro* models make them a worthy alternative. Regarding *in vitro* systems, the measurement of intracellular metabolites, or fingerprinting, provides a comprehensive snapshot of the status of metabolic processes within the cell at the time of sampling. Meanwhile, metabolic footprinting, i.e., measuring the excretion and consumption of metabolites by the cells, indicates the cumulative effect of metabolism over time (52, 64). Measuring the metabolic footprint may be deemed simpler given the relative ease and non-invasiveness of sampling spent culture media, however, it is less comprehensive than fingerprinting since only a fraction of intracellular metabolites are consumed or excreted (74, 75). *In vitro* systems are more economical, in keeping with the 3Rs and benefit from greater ability to limit confounding factors compared with *in vivo* models, favouring their usage (64).

The exposure conditions, including amount and length of exposure must also be considered. Biological responses to xenobiotic exposure are typically dose- or concentration-dependent, both in magnitude, but also mechanistically. For example, microtissues exposed to two concentrations of doxorubicin, reflective of a ‘therapeutic’ dose predicted to induce chronic cardiotoxicity, and a ‘toxic’ dose predicted to induce acute cardiotoxicity, respond differently, as indicated by transcriptomics (63). A good predictive biomarker would indicate that both concentrations were cardiotoxic, despite the differences in mechanism. As such, studies which aim to discover molecular signatures predictive of toxicity which are applicable across broad spectrum of specific mechanisms should include measuring responses to a range of (toxic) concentrations to maximise discovery potential. Similarly, in studies aiming to investigate mechanisms of toxicity, or to discover biomarkers specific to a mechanism, care should be taken to ensure the concentrations selected induces the desired effects without gross cytotoxicity, which would otherwise mask mechanism-specific perturbations (69, 75).

Regarding the length of exposure, it is known that toxicity develops over time, hence the inclusion of temporal resolution within a study design adds to the opportunity for discovering toxicological mechanisms. Considering an AOP, responses at the earliest time points, i.e., minutes of exposure in an *in vitro* model, will indicate MIEs, while responses measured at later time points, but before toxicity is observed, e.g., at a functional or structural level, will indicate molecular-level KEs (69, 75). Furthermore, considering discovery of predictive biomarkers, one which responds relatively early after exposure might be more amenable to integration into high-throughput screens, i.e., shorter exposure time giving rise to higher throughput, and

would maximise the advantages of molecular biomarkers compared to functional- or structural-based assays.

1.4.2 SAMPLE PREPARATION FOR METABOLOMICS ANALYSIS

The most optimal sample generation for untargeted metabolomics is efficient, reproducible and maximises metabolite yields. Ultimately, the aim is to harvest the sample from the biological system or *in vitro* platform and quench metabolism as soon as possible while avoiding the introduction of artefacts, e.g., by cell lysis or addition of substances that may interfere with analysis (76-79). The approach taken to achieve this goal is dependent on the sample type. For example, whole blood is collected from test subjects by venepuncture into sample tubes. Plasma or serum are then prepared from the blood, by addition of anticoagulant and centrifugation, or through natural clotting, respectively, removing cells, e.g., immune cells, whose own metabolomes would otherwise contaminate the samples, before rapid freezing and storage at -80℃ (67). Meanwhile, tissues are typically harvested by surgery or biopsy, where consideration must be taken to select and reproducibly sample the preferred section of a tissue for analysis, thus accounting for tissue heterogeneity, and choose whether to wash the harvested tissue with saline prior to quenching metabolism by rapid freezing to remove any contaminating blood (64).

Approaches taken to harvest cells are dependent on culture conditions, though the principles are shared; to efficiently and reproducibly isolate cells from their culture medium and rapidly quench metabolism (80, 81). The importance of isolating cells from the media for intracellular metabolomics may be explained by considering its composition: (1) metabolites which, if not removed, would be indistinguishable from the intracellular metabolome, contaminating measurements, (2) salts, e.g., Cl^-, SO_4^-,

PO_4^-, buffers, organic acids, and complex biological mixtures, e.g., fetal bovine serum, which can give rise to substantial analytical matrix effects (78, 79, 82). For adherent cells, isolation is typically achieved by aspiration of culture media while cells remain fixed to the culture vessel, followed by addition and aspiration of saline, to dilute and remove any residual media. This is a process, although dependent on the number of washing steps, which can be completed rapidly, i.e., within seconds, thus limiting additional metabolic turnover prior to quenching. The isolation of cells cultured in suspension is considered more challenging. Many reported approaches implement centrifugation as a strategy to 'pull down' the suspended cells, allowing aspiration of the media as applied to adherent cells (81, 83). However, the addition of the centrifugation step in practice adds several minutes to the protocol, permitting undesirable further metabolic turnover. This is exacerbated when one or more washing steps are required to efficiently remove residual media, since this would involve additional centrifugations (79). Others have tested alternative approaches; Bordag *et al*., Volmer *et al.*, and Hernandez Bort *et al.,* each developed and applied 'fast filtration' approaches to isolate bacterial and/or mammalian suspended cell cultures, substantially reducing time before quenching, reducing degradation of metabolites with very fast turnover rates, e.g., nucleotide triphosphates and glycolysis intermediates (79, 84, 85). Such a filtration-based approach was explored further in this thesis. Following isolation and washing, metabolic activity of harvested cells is quenched either through addition of organic extraction solvent, e.g., 60% (v/v) methanol supplemented with 0.85% (wt/v) ammonium bicarbonate (81), methanol/methyl tertiary-butyl ether/chloroform (40:30:30 v/v/v) (83), or rapid freezing in liquid nitrogen or ethanol-dry ice bath (79, 84, 85). Some report quenching by

addition of solvent prior to isolation (80, 81). This benefits from more immediate quenching, thus limiting metabolic turnover, but can result in leaching and loss of intracellular metabolites or less thorough isolation of cells, and their metabolites, from the extracellular medium (79, 81).

Prior to analysis, molecules of interest, i.e., metabolites and lipids, must be extracted from the biological samples and isolated from other components, e.g., proteins, contaminants, that would otherwise limit sensitivity of analytical measurements through matrix effects. Typically, crude extraction is performed by addition of organic solvents to precipitate proteins, producing a solution containing a relatively diverse set of metabolites (67, 77). Unfortunately, despite efforts to maximise metabolome coverage, e.g., the biphasic Bligh and Dyer method uses a final solvent mix of 2:2:1.8 (v/v/v) methanol/chloroform/water which gives rise to a polar and non-polar phase such that both polar metabolites and lipids are simultaneously extracted from the sample, no approach is capable of complete unbiased extraction of all metabolites (75-77, 86). An alternative strategy to biphasic extraction, is monophasic extraction performed on either separate aliquots of the same samples, or separate samples where this isn't feasible. Each monophasic extraction method can be optimised to extract a more specific set of metabolite classes, e.g., mix of aqueous and organic solvents such as acetonitrile and/or methanol with water for polar metabolites, and less polar mix of organic solvents such as isopropanol and acetonitrile or chloroform and methanol for lipids. Monophasic extraction has been demonstrated to yield greater number of metabolites with better reproducibility compared with biphasic approaches when applied to mammalian plasma, urine, and tissue samples (76, 77). Monophasic approaches have also been demonstrated for automated, high-

throughput extraction of metabolites and lipids from *in vitro* samples with low biomass, with 4:1 methanol/water (v/v) and 2:1 methanol/chloroform (v/v) solvent systems shown to yield the highest feature counts and best reproducibility for polar metabolomics and lipidomics, respectively (87).

1.4.3 Acquiring metabolomics data by mass spectrometry

Two analytical techniques dominate the field of metabolomics: nuclear magnetic resonance (NMR) spectroscopy and mass spectrometry (MS). Through measurement of the chemical shift between excited and relaxed spin states of isotopes, including the biologically relevant nuclei of ^{1}H, ^{13}C, ^{15}N, and ^{31}P, NMR produces spectra conveying structural information on compounds present in a given sample. The advantages of this analytical approach lie in its high technical reproducibility, unbiased measurement (both ^{1}H and ^{13}C are present in most biologically relevant small molecules), and capability of complete structural elucidation and metabolite identification. Despite this, MS is nowadays by far the more prevalent technique applied in metabolomics, largely due to its superior sensitivity and resolution, giving rise to greater metabolome coverage (66, 68, 88).

Mass spectrometers measure the mass-to-charge ratio (*m/z*) and relative abundance of ionised analytes in their gaseous phase. Two main parts: (1) an ion source, which forms gaseous-phase ions from the sample, (2) a mass analyser, which measures the *m/z* of analytes and separates them based on this property, are largely responsible for the selectivity and sensitivity of measurements. Various ion sources, which differ in their analyte ionisation mechanisms, and mass spectrometers, which may contain either a single or combinations of mass analyser(s) (i.e., tandem/hybrid mass spectrometers) that differ in their *m/z* measurement method, exist and are

commercially available (68). Research presented in this thesis employed three commercially available mass spectrometers: Thermo Scientific Q-Exactive Focus Orbitrap (QE-Focus), Thermo Scientific Orbitrap Elite (Elite) and Thermo Scientific Orbitrap ID-X Tribrid (ID-X) (Figure 1.3), coupled to either an electrospray ionisation (ESI), or nano electrospray ionisation (nESI) source.

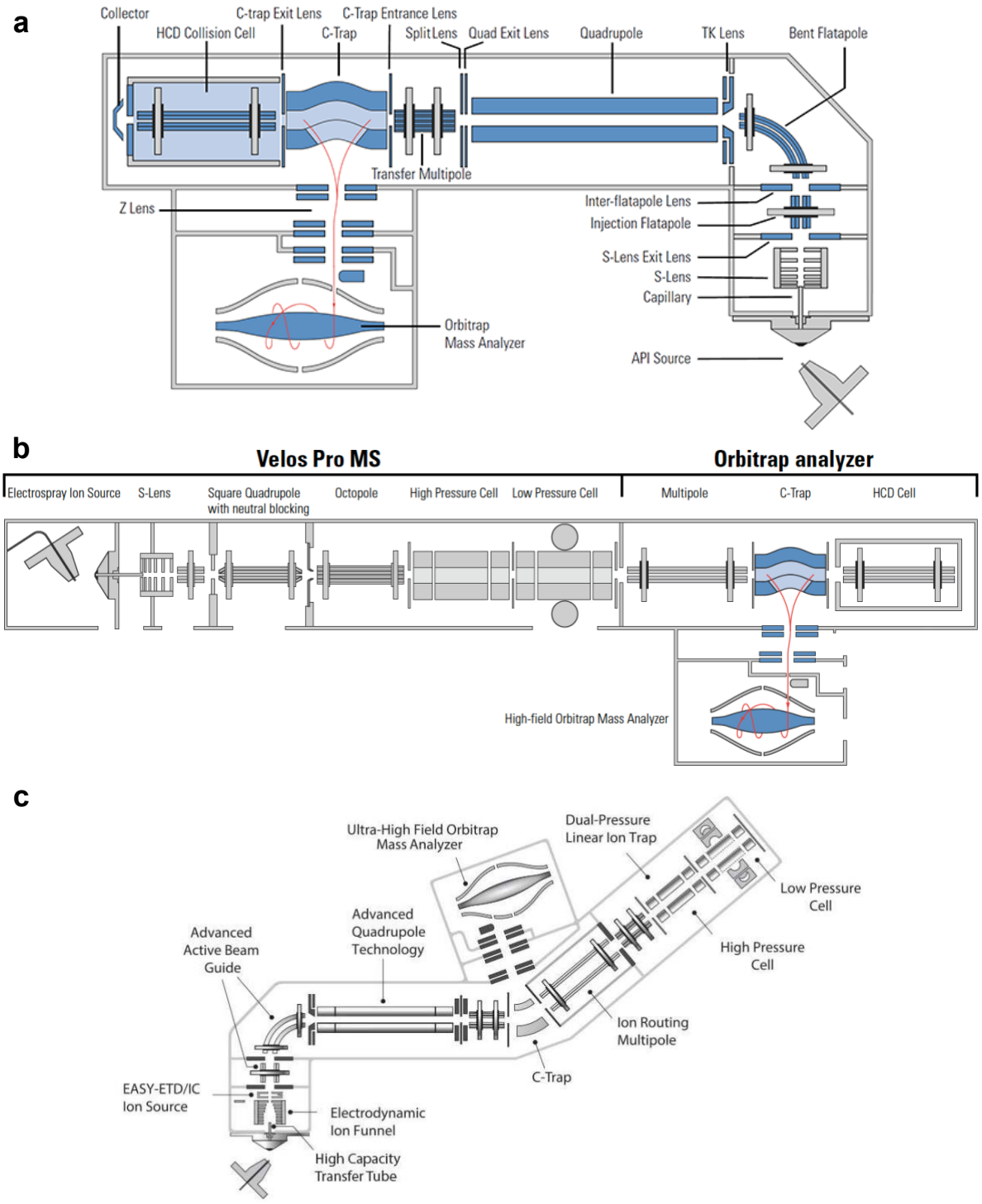


Figure 1.3 Schematics of the three mass spectrometers used for metabolomics data acquisition in this thesis.
a Thermo Scientific Q-Exactive Focus Orbitrap mass spectrometer, **b** Thermo Scientific Orbitrap Elite mass spectrometer, and **c** Thermo Scientific Orbitrap ID-X Tribrid mass spectrometer. Taken from www.thermofisher.com.

1.4.3.1 Electrospray ionisation

Ionisation sources coupled to mass spectrometers address the need for analytes, the majority of which are not naturally charged, to become charged for their detection. Although many approaches for analyte ionisation have been developed and implemented in mass spectrometry, ESI is the leading technique in MS-based metabolomics, owing largely to it being a soft ionisation technique, limiting the fragmentation of the small molecules, and its suitability for analysing liquid samples (89, 90).

The production of gas-phase ions by ESI occurs at atmospheric pressure. The process is initiated through the application of high voltages to the capillary through which the analyte solution enters, generating an electric field that encourages formation of a Taylor cone, from which the electrospray, a fine mist of charged droplets, is emitted. The application of heat assists solvent evaporation from the charged droplets and subsequent fission, giving rise to increasingly smaller and highly charged offspring droplets until a final release of gaseous analyte ions (Figure 1.4) (91, 92).

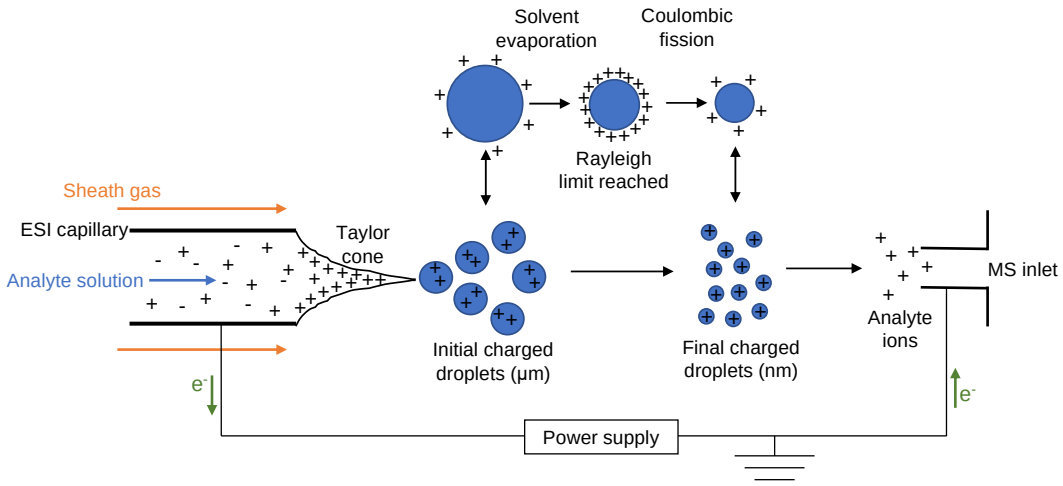


Figure 1.4 Diagram describing the process of producing gas-phase ions by electrospray ionisation.

An analyte solution enters through a capillary tube exposed to high voltages. The electrical field encourages distortion of the analyte solution into a Taylor cone, a conical meniscus with extremely intense electric field at its tip, through the accumulation of charges. The tip of the Taylor cone elongates towards the counter electrode until the attraction of charge overcomes the surface tension and liquid disperses into an aerosol of charged droplets, the electrospray. Progressive evaporation of solvent, aided by heat, gives rise to smaller droplets with increased charge density until their surface tension reaches the Rayleigh limit. At this point, the droplets dissociate by Coulombic fission, producing droplets with higher charge and smaller volume. This cycle of solvent evaporation and Coulombic fissions repeats until a final desorption producing gas-phase ions, the exact mechanism of which is disputed. The gas-phase ions continue toward the counter electrode and onwards into the vacuum of the mass spectrometer. Sheath gas (e.g., dry nitrogen) encourages nebulisation and helps direct the charged droplets toward the mass spectrometer (91, 92).

Nano-electrospray ionisation (nESI) is a form of ESI distinguishable from the conventional form primarily by the inlet flow rate, which is on the scale of a few nanolitres-per-minute. A consequence of the nano flow rates and smaller nozzle (capillary) diameter is smaller first-generation droplet sizes arising from the Taylor cone, thus the requirement for less evaporation/fission cycles to release gaseous phase ions. Consequently, nESI offers enhanced ionisation efficiency, reduced ion suppression, and lower sample consumption (91-94). This is particularly useful when sample biomass is limited, and maximal sensitivity is sought.

The list of potential ions formed by ESI is extensive. Ions are typically formed from addition or abstraction of a proton, producing the hydrogen cation ($[M+H]^+$) or anion ($[M-H]^-$), respectively, or through formation of adducts, e.g., $[M+Na]^+$, $[M+NH_4]^+$, $[M+Na-2H]^-$, $[M+COO]^-$. Additionally, some ions are formed through fragmentation within the source, e.g., $[M+H-H_2O]^+$, $[M+H-NH_3]^+$. Multiply charged ions are often also observed, e.g., 2+ or 3+ charge state. As such, multiple signals, or ‘features’, can be detected for a given compound, introducing complexity into ESI-MS metabolomics datasets (95, 96). This presents challenges for metabolite annotation (Section 1.4.5).

1.4.3.2 Orbitrap-based mass analysis

In untargeted metabolomics, mass resolution, typically defined by the full width half maximum (FWHM), i.e., the width of a spectral peak at 50% of its maximum height, is integral. With higher resolution, or narrower spectral peaks, the number of signals detected is increased since ions with similar *m/z* are more likely to be resolved into unique signals. Ultimately, this means increased sensitivity and more confidence in feature annotation. For this reason, high resolution mass spectrometry (HRMS), mainly employing Fourier Transform (FT) mass analysers, is favoured in metabolomics research (66, 67).

Of the FT analysers in existence, the Orbitrap, first proposed in 2000 by Alexander Makarov (97), and later made commercially available (Thermo Scientific, 2005), is one of the most prominent, owing to its reduced complexity and size, enabling it to be integrated into a benchtop instrument, compared to its HRMS competitor, the previous state-of-the-art FT ion cyclotron resonance (FT-ICR) analyser, which requires a superconducting magnet (98). The Orbitrap determines *m/z* based on an ion's frequency of motion. Specifically, ions are injected into the space between two outer electrodes, and a central spindle-like electrode. Voltage is applied to the central spindle electrode, forming an electrostatic field of quadro-logarithmic potentials, inducing the ions to orbit the central electrode. Orbiting ions harmonically oscillate along the electrode; the frequency of these axial oscillations for a given ion is dependent on its mass according to Equation 1, thus *m/z* may be calculated by FT of these oscillations following image current detection by the outer electrodes (97, 99).

Equation 1 The frequency of ion axial harmonic oscillations in the Orbitrap

$$\omega = \sqrt{\frac{e}{(\frac{m}{z})} \times k}$$

ω = frequency of axial oscillation; e = elementary charge; m = mass; z = charge; k = field curvature constant

The addition of the C-trap, a “modified bent storage quadrupole” adjacent to the Orbitrap enables decoupling of the Orbitrap from the rest of the system (Figure 1.5). By providing pulsed injections of accumulated ions (ion packets), the number of which is controlled by the Automatic Gain Control (AGC), the Orbitrap operates with a more optimal number of charges, thus maximising the sensitivity, accuracy of mass measurements (by limiting space-charge effects) and dynamic range possible, with mass accuracy <5 parts-per-million (ppm) (98, 100).

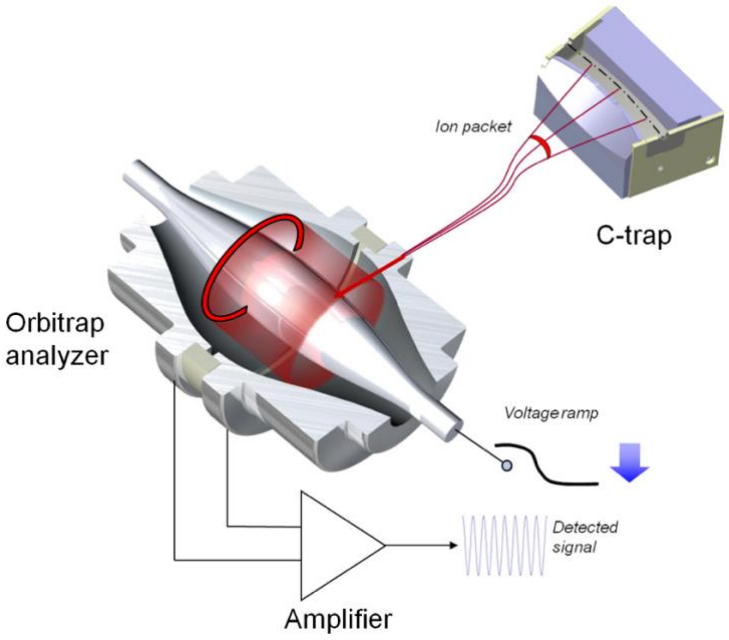


Figure 1.5 Graphical representation of a C-trap coupled to an Orbitrap mass analyser. Taken from Thermo Scientific (Bremen).

Since its commercial introduction, a range of Orbitrap instruments have been released, each combining an Orbitrap with additional mass analysers, ion transfer

devices and/or collision cells. Noteworthy for this thesis, the QE-Focus couples an Orbitrap to a quadrupole (Figure 1.3a), the Elite couples an Orbitrap to a dual-pressure linear ion trap (LIT) (Figure 1.3b), while the ID-X has both a quadrupole and an LIT, in addition to its Orbitrap (Figure 1.3c).

Each of the configurations offers advantages to the acquisition of mass spectral data for metabolomics:

- Considering the Orbitrap; modification of the Orbitrap between instrument releases, with progression from the original design through the high field Orbitrap, to the ultra-high field Orbitrap, has given rise to improved performance by enabling increased mass resolution or acquisition speeds, largely through reducing the size of the Orbitrap and increasing the voltage applied to the central electrode (Table 1.1) (101).

Table 1.1 Summary of Orbitrap characteristics for the three Thermo Scientific mass spectrometers used in this thesis.
Adapted from (102) using additional data from www.thermofisher.com.

Instrument	Release year	Orbitrap design	Orbitrap analyser size (mm)	Orbitrap central electrode voltage (kV)	Maximum resolution at *m/z* 200	Maximum scan speed (Hz)
Q-Exactive Focus Orbitrap	2015	Original	30	3.5	70,000	12
Orbitrap Elite	2011	High field	20	3.5	240,000 at *m/z* 400	12
Orbitrap ID-X Tribrid	2019	Ultra-high field	20	5.0	500,000	30

- The S-lens, a set of stacked rings to which a radio frequency (RF) is applied to focus ions, is found within all three instruments, enabling more efficient ion transmission through the ion optics, thus increasing sensitivity (98, 99).

- The collision cell for higher-energy collisional dissociation (HCD), also available in all three instruments, enables precursor fragmentation prior to analysis. Employing this fragmentation capability in metabolomics enables structural elucidation of analytes, providing confidence in compound annotation.

- The coupling of the Orbitrap to a segmented quadrupole, as in the QE-Focus and ID-X instruments, enables filtering of ions based on mass prior to the C-trap/Orbitrap. The quadrupole, which is composed of four hyperbolic profile round rods arranged to form a square cross section, achieves this by applying opposing RF and direct current (DC) voltages with specific ratio to the rod pairs, such that only select ions pass through. This mass filtering capability enables enhanced transmission and sensitivity of target ions.

- The dual-LIT within the Elite and ID-X instruments, is capable of not only ion isolation, which is typically less efficient than quadruple-based mass filtering, but also MS^n fragmentation through collision-induced dissociation (CID), thereby offering a complementary fragmentation mechanism to HCD provided by the collision cell, giving rise to additional structural information that can increase confidence in compound annotation. These functions use the high-pressure cell. Meanwhile, the low-pressure cell of the LIT is capable of faster mass analysis, albeit at lower resolution and mass accuracy compared to the Orbitrap. This enables parallelisation such that fragmentation data might be acquired at lower resolution in the LIT without compromising the acquisition of high resolution MS^1 data, thus permitting reduced cycle times and higher throughput acquisition.

Taken together, the use of high-resolution Orbitrap mass spectrometers in untargeted metabolomics enables highly sensitive analysis, thus maximising coverage of metabolomes despite large variation in analyte concentrations, which range from pico- to milli-molar. Furthermore, the high mass accuracy that can be achieved, coupled with capacity to acquire MS/MS and MS^n fragmentation data to aid structural elucidation, facilitates more confident metabolite annotation.

1.4.3.3 Sample separation by liquid chromatography coupled mass spectrometry

In metabolomics, mass spectrometers are typically coupled to chromatographic separation as so-called hyphenated techniques, enabling separation of complex mixtures in the time domain prior to MS analysis. This separation yields less complex spectra, enhances resolution of isobaric compounds and reduces matrix effects including ion suppression, thus increasing the signal-to-noise ratio (SNR) of analytes. Furthermore, separation in the time domain provides an orthogonal measurement, retention time (RT), for use in more confident metabolite annotation (68).

The coupling of liquid chromatography (LC) to mass spectrometry is currently the most favoured hyphenated MS approach in metabolomics. The principle of separation by LC is that different analytes, carried by a liquid mobile phase, will interact with a solid stationary phase to varying degree depending on their physicochemical properties; an analyte with physicochemical properties that support a stronger interaction with the stationary phase will elute from an LC column slower than an analyte which interacts with the stationary phase to a lesser extent, thus the analytes are separated in the time domain (68). In practice, this is achieved using a pump system to push mobile phases from solvent reservoirs through capillaries to the column, where separation occurs, and on to the detector. The sample is mixed with

the mobile phase via an autosampler syringe before it reaches the column (Figure 1.6).

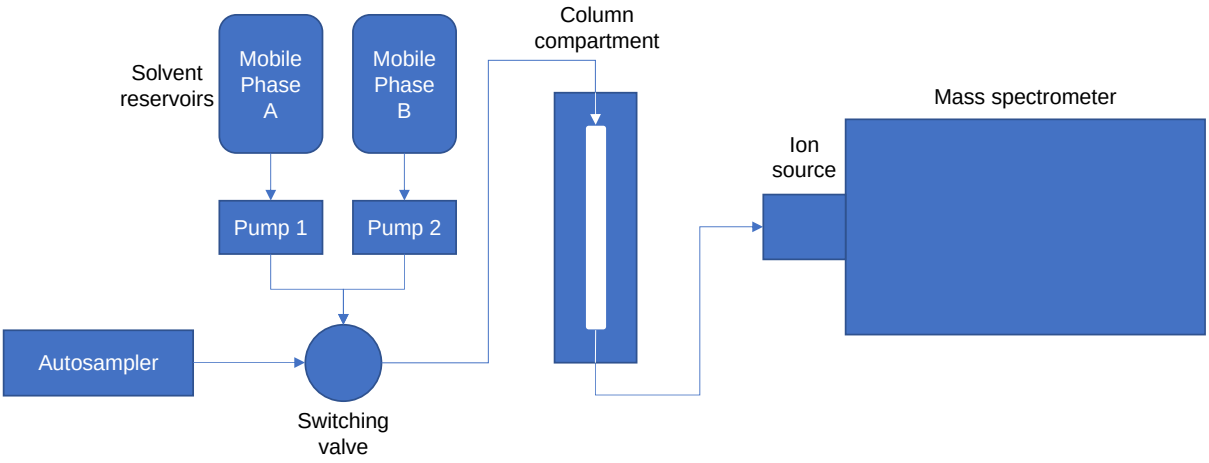


Figure 1.6 Schematic of a typical ultra-high performance liquid chromatography instrument coupled to a mass spectrometer.
Arrows indicate direction of flow. Mobile phases stored in solvent reservoirs are pumped at the user-defined flow rate through the system by high-pressure pumps. Samples, stored within the autosampler at a stable user-defined temperature, are injected into the system via the switching valve. The analytes within the sample are separated in the time domain by the analytical column contained within a temperature-controlled compartment, before being sent to the detector, i.e., mass spectrometer coupled to an electrospray ionisation ion source, for mass analysis.

Chromatographic resolution, as defined by the FWHM of chromatographic peaks, is a key metric in evaluating performance of LC for metabolomics. Higher resolution means better separation, thus improved sensitivity by reduced ion suppression and increased SNR, and improved specificity by better separation of isomers. Chromatographic resolution, and thus LC performance, may be enhanced through use of smaller stationary phase particles and narrower (i.e., smaller internal diameter) or longer columns. However, the chromatographic resolution that can be achieved is ultimately limited by the back pressure than can be handled by the instrument, with the aforementioned changes all increasing back pressure as defined by the Kozerny-Carman equation (Equation 2), where change in back pressure (ΔP) is proportional to the product of solvent viscosity (η), solvent flow rate (F), and the length of the column

(L), and inversely proportional to the product of the permeability constant (K^0), column radius (r) and stationary phase particle size (d_p).

Equation 2 Kozerny-Carman equation

$$\Delta P = \frac{\eta F L}{K^0 \pi r^2 {d_p}^2}$$

As such, the advent of ultra-high-performance LC (UHPLC) instruments, which can operate at back pressures up to 1000-1500 bars, was a significant technological advancement in LC-MS-based untargeted metabolomics. It has driven the development and use of columns with narrower internal diameters (typically 2.1 mm) and smaller particles sizes (< 2.6 µm), enabling higher resolution and sensitivity, and shorter analytical run times (66, 67, 88, 103).

The choice of LC stationary phase defines the selectivity of an LC-MS assay. Stationary phases commonly applied in untargeted metabolomics include reversed-phase (RP) and hydrophilic interaction (HILIC) phases (67). The former are composed of hydrocarbon chains, typically C_{18}, attached to silica beads. They are used with polar mobile phases, e.g., acetonitrile, methanol, or isopropanol, and are selective for more hydrophobic molecules (67, 88). The latter possess polar functional groups attached to silica which selectively interact with polar and charged molecules. The separation mechanism relies on hydration of the stationary phase head groups, thus aqueous/organic mix mobile phases, e.g., 50-80% aqueous acetonitrile, are used (88). It is common for both types of stationary phase to be employed in separate assays within a metabolomics study, such that coverage of the metabolome is increased. For example, Verheijen *et al*., applied a RP-C_{18} and HILIC method to measure the lipids and polar metabolites, respectively, in the spent culture media of liver and cardiac microtissues as part of the EU/FP7 HeCaToS project to

develop an *in-silico* prediction system for human drug safety assessment (104). Meanwhile, the use of RP-C_{30} stationary phase offers enhanced selectivity toward, and better resolution of, lipophilic molecules compared to more routinely used RP-C_{18} columns, making them well suited to applications seeking more in-depth characterisation of the lipidome (105).

Despite the benefits offered by coupling MS to UHPLC, the approach does not lend itself to analysis of samples with low biomass since chromatographic dilution limits the sensitivity which can be achieved. Furthermore, considering 15-30-minute mobile phase gradients are typically required to achieve adequate resolution of complex mixtures (i.e., representing the analysis time per UHPLC-MS assay per sample), analytical throughput of this approach is relatively slow. As such, UHPLC-MS-based metabolomics is less amenable to large-scale discovery-based studies, where thousands of samples are analysed.

1.4.3.4 Higher sensitivity by direct infusion mass spectrometry

An alternative MS-based metabolomics approach which overcomes the limitations of UHPLC-MS both in terms of sensitivity and throughput is direct infusion mass spectrometry (DIMS). Direct injection of sample into the ion source, i.e., in absence of diluting mobile phase, results in higher concentration of analytes at the point of ionisation (88). Furthermore, the application of nESI limits sample consumption, and minimises ion suppression induced from relatively complex matrices typically analysed in metabolomics, as discussed previously (Section 1.4.3.1).

The TriVersa Nanomate system (Advion Biosciences) is a nESI ion source commonly used for DIMS applications. It is composed of a sample compartment, robotic arm, and silicon nESI chip (Figure 1.7). It operates as follows: a liquid sample is aspirated

from a well of a microplate stored within the temperature-controlled sample compartment, into a conductive tip. The loaded tip is subsequently aligned to a nozzle, or microcapillary, on the silicone nESI chip, itself located in front of MS inlet. A high voltage and gas pressure is supplied to the positioned tip, encouraging formation of the electrospray from the nozzle and facilitating forward movement of gaseous ions into the MS (Advion Biosciences; (106).



Figure 1.7 Image of a TriVersa Nanomate system and a conductive silicone nano-electrospray ionisation chip containing small nozzles which facilitate sample spray.
The chip is slotted into the front of the system for analysis (Advion Biosciences).

An approach termed ‘spectral stitching’ further increases the analytical sensitivity of nESI-DIMS. The principle of the approach lies in reducing the proportion of ions, via a narrower target mass range, such that ion competition within the trap is minimised, and dynamic range is increased. Overall, this gives rise to a method composed of several selected ion monitoring (SIM) scans, each covering sequential regions of the complete target mass range, e.g., *m/z* 50-620 for polar metabolomics, which are subsequently ‘stitched’ together post-acquisition, offering a fivefold increase in sensitivity. Small overlaps in adjacent windows (ca. 5 *m/z*) addresses a problematic

phenomenon termed “edge effects”, whereby intensities of ions found close to the edge of windows are lower than if the same ion was in the centre of a window (107, 108). The applicability of this approach for untargeted toxico-metabolomics has been demonstrated across diverse test systems including roach testes (109), *Chlamydomonas reinhardtii* algae (110), *Daphnia magna* (111) and HepaRG cell line (87). The approach is particularly well suited where sample biomass is limited. More recently, further improvement to the spectral stitching approach, mainly reduced ion competition and increased sensitivity (e.g., *ca.* 50% more features measured in serum), has been achieved by defining SIM windows of variable widths across the full mass range based on ion count or total ion intensity, with the aim of detecting a consistent number of features in each scan range, thus accounting for the irregular distribution of ions (112, 113).

1.4.4 Interrogating metabolomics data by statistical analysis

Once acquired, highly complex untargeted metabolomics datasets must be processed to convert raw spectral data into a data matrix to enable statistical analysis. This involves extracting non-noise peaks, often termed peak picking, and aligning, or grouping, measurements across samples (66-68, 114) (Figure 1.8). There are a number of open source and commercial software to achieve processing of UHPLC-MS metabolomics data; XCMS (115), and Compound Discoverer (Thermo Scientific) were employed to process data presented in this thesis. Meanwhile, processing SIM-based nESI-DIMS data requires an analytical method-specific additional step to ‘stitch’ together spectra of adjacent SIM windows. The python package, DIMSpy, was specifically designed for this purpose (116).

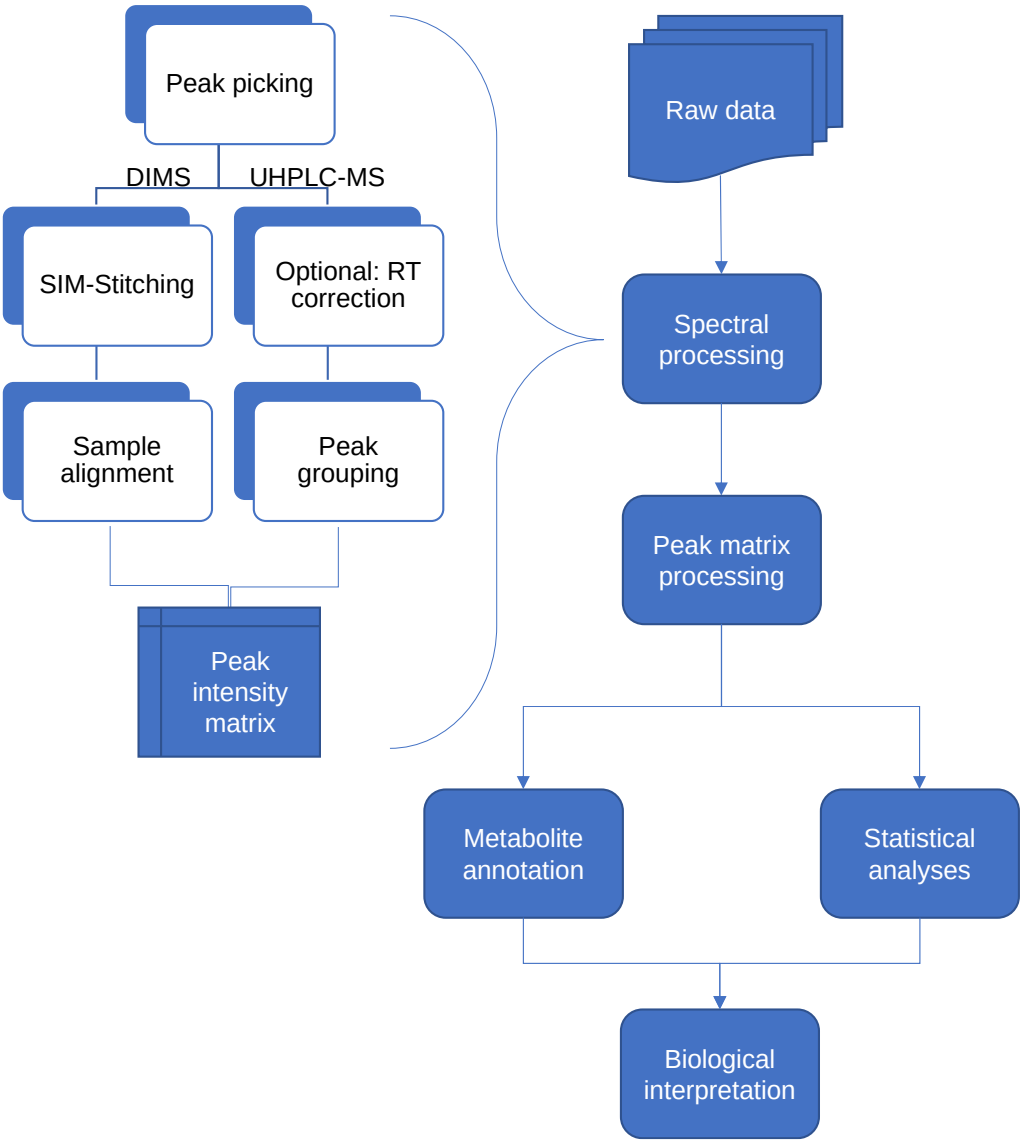


Figure 1.8 Schematic of a typical workflow for processing and analysing mass spectrometry-based untargeted metabolomics data.

UHPLC-MS data can sometimes require an additional step, RT alignment, prior to peak grouping to correct for shifts in RT of analytes across the run, which can be introduced by a variety of instrument variables (67, 68, 114) (Figure 1.8). The OBI-warp algorithm, which can be implemented within the XCMS pipeline, is one approach, performing non-linear correction based on a warp path calculated from a spectral similarity matrix (115, 117).

Once generated, the peak-intensity matrix, i.e., a matrix containing the relative intensities of all features in all samples, undergoes additional processing including correction of systemic errors, e.g., signal drift and batch effects, removal of features of non-biological origin (blank filtering), filtering of features by incidence and reproducibility, filtering of samples based on number of missing values, and normalisation against biomass- or technical-based variation (67) (Figure 1.8). Many of these steps, specifically signal drift and batch correction (SBC) by robust spline correction (RSC) (118), feature filtering by incidence and reproducibility, and probabilistic quotient normalisation (PQN) employ data from intra-study quality control samples (QCs). These are representative samples, often generated from a pool of study sample aliquots, measured at regular intervals over the analytical run. As such, QC measurements inform on technical reproducibility and analytical drift, independent of biological variation (67, 69). While these post-acquisition steps help to ensure only the highest quality data of biological origin absent of confounding factors, e.g., variation correlating with order of sample preparation, are considered in statistical analyses, it is best practice to avoid introducing bias through robust study design, particularly appropriate randomisation and batching of samples for sample preparation and analysis (66, 67, 69, 75).

At this point, the peak-intensity matrix is considered ready for statistical analysis (Figure 1.8). For high-dimension datasets such as those produced by untargeted metabolomics, i.e., where number of features, or variables, is typically much larger than number of samples, analysis may be univariate, i.e., consider variables independently, or multivariate, i.e., consider all variables simultaneously (114). Univariate analyses typically include Student's or Welch's *t*-test or analysis of

variance (ANOVA), in cases where a normal distribution is assumed, or non-parametric equivalents, e.g., Mann-Whitney *U* test or Kruskal-Wallis one-way analysis of variance, in attempt to identify features whose abundance is considered significantly different between sample groups (68). Applying a correction term to account for the repeated testing performed on a multivariate dataset is important to reduce the proportion of false positives, e.g., false discovery rate (FDR) correction by Benjamini-Hochberg (119) method or Bonferroni correction (68). Meanwhile, the magnitude of change may be quantified by calculating the fold change, or ratio, of the feature's average intensity in the sample groups. The power and reliability of these approaches to discover features (metabolites) that have been perturbed within the system is dependent on the level of replication within the study, and whether it is sufficient to allow accurate prediction of the true distributions, accounting for technical variation. Best practice recommendations suggest for *in vitro* experiments, at least three replicates are required, but more than five is preferable (120).

Multivariate statistical approaches commonly applied in metabolomics are based on the principle of dimension reduction, i.e., they summarise the multivariate dataset into fewer simulated latent variables. These approaches typically cannot handle missing values common in metabolomics data matrices (52). As such, it is common practice to impute these, although approaches vary from simple imputation with zero, or minimum expected value, to more complex machine learning-based approaches. The *k*-nearest neighbour (KNN) approach, which imputes missing values based on intensities of the *k* most similar samples or features has been recommended for UHPLC-MS and DIMS datasets (108, 121). Furthermore, to address heteroscedasticity and limit bias towards features of greater abundance, it is

recommended to transform peak intensities by generalised log (glog) transformation (52, 108, 121).

Principal components analysis (PCA) is one such dimension-reducing approach often used to explore the dataset, identifying outliers and reveal trends in the variation between samples. PCA models are calculated such that each successive principal component maximises the variation explained in an orthogonal direction, without considering sample group labels, i.e., it is a form of unsupervised multivariate analysis (52, 68, 114). Scores plots, showing the distribution of samples along the displayed principal components, may be used to visualise the model (Figure 1.9a). Hierarchical clustering analysis (HCA) is an alternative unsupervised approach with similar applications as PCA. It reveals relative level of similarity between samples (or features) which may be visualised by a dendrogram, where branch length is proportional to dissimilarity (Figure 1.9b). Pair-wise similarity is calculated using a distance metric, e.g., Euclidean distance, to identify pairs of highest similarity, i.e., a cluster, and the distance between clusters is determined by a linkage method, e.g., Ward's method (52, 68, 114).

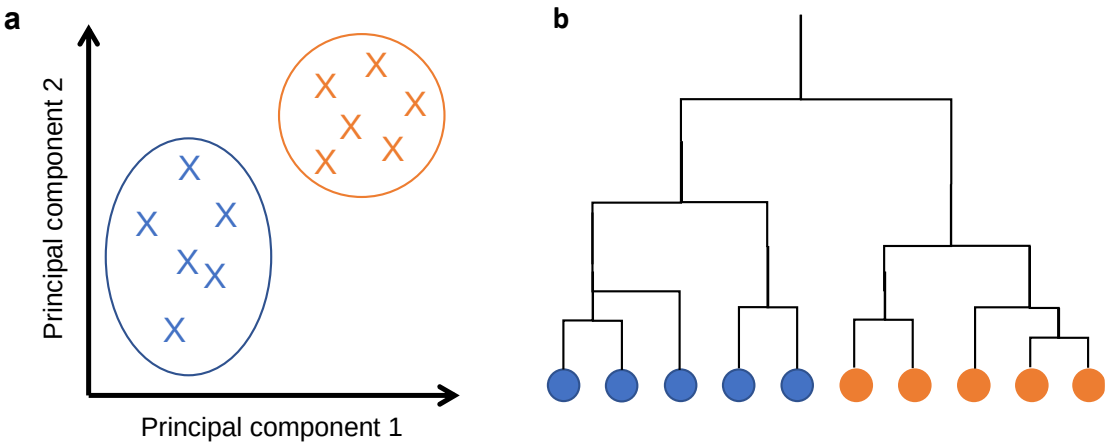


Figure 1.9 Graphical representation of unsupervised multivariate analysis outputs.

a Graphical representation of a principal components analysis scores plot showing distribution of samples (X) along the first two principal components of the model and the 95% confidence interval per class label (shaded regions). **b** Graphical representation of a hierarchical clustering analysis dendrogram showing the dissimilarity between samples (circles). Dissimilarity is proportional to height of the dendrogram branches.

Alternatively, supervised dimension-reduction approaches, e.g., partial least-squares discriminatory analysis (PLS-DA), consider sample class labels to build latent variables with maximal inter-class variation. As such, they are suitable for building multivariate predictive models and for discovering putative biomarkers, by identifying the original variables most important to the model, i.e., using the variable importance in project (VIP) scores (52, 68, 122). Orthogonal PLS-DA (OPLS-DA) is an extension of PLS-DA that incorporates an orthogonal signal correction (OSC) filter to isolate variation in the measured data (**X**-matrix) predictive of class labels (**Y**-matrix) from uncorrelated (orthogonal) variation which enhances the interpretability of the resultant model, making it a particularly powerful approach for the aforementioned applications (68, 123). A caveat of applying PLS approaches to metabolomics datasets where number of variables considerably exceeds the number of samples, is that they are prone to overfitting, i.e., the trained model does not perform as well on independent test data. Cross-validation and permutation methods should be applied to evaluate the model in this regard (68, 122).

The final step in the workflow (Figure 1.8), the translation from a list of perturbed or most important metabolic features to biological insights, e.g., a mechanistic hypothesis, is one of the most challenging aspects of untargeted toxico-metabolomics, owing largely to the difficulty in annotating mass spectral features (see Section 1.4.5). Where at least some metabolite annotation has been achieved, a common approach for deriving biological hypotheses is based on mapping metabolite

changes revealed by statistical analyses to metabolic networks, e.g., the Kyoto Encyclopaedia of Genes and Genomes (KEGG) (124). Applying Fisher's exact test to assess significance, pathway overrepresentation analysis may reveal metabolic and biochemical pathways that are perturbed, thus enabling deeper biological insight into toxic responses. Caution should be taken when implementing these approaches, with particular consideration for (1) confidence in metabolite annotations, (2) use of the 'right' metabolite reference background and (3) an appropriate threshold for selection of differentially abundant metabolites, since each impacts the accuracy and reliability of the results (52, 68, 125, 126).

1.4.5 Challenges of metabolite annotation and identification

Metabolite annotation and identification is ultimately required to derive biological insight from untargeted metabolomics datasets yet it remains a significant bottleneck, driven by (1) complexities of ESI and consequential data redundancy– recent estimates suggest up to 90% signals are due to contaminants, artifacts and degeneracy (127); (2) the existence of isomers such that a single neutral mass can correspond to multiple molecular formulae and multiple biological molecules can have the same molecular formula, e.g., glucose, galactose, maltose share the common molecular formula $C_6H_6O_6$; (3) the vast number of previously reported metabolites that might be present and detected, e.g., >200,000 compounds stored within the Human Metabolome Database (HMDB, version 5.0) (128) and 47,800 lipids within LIPID MAPS Structure Database (LMSD) (129); and (4) an unknown number of detectable compounds which have not previously been reported (67, 68, 130). In a typical untargeted metabolomics dataset, only a small proportion of features will be annotated and many of these will be putative, with a low degree of

confidence, while absolute identification is difficult to achieve (67, 130). Confidence in metabolite annotations is often reported using the Metabolomics Standards Initiative's (MSI) four confidence levels, which describe the accuracy and robustness of a given annotation based on the data used to derive it (Table 1.2) (120). More recently, Schymanski *et al*., proposed an alternative framework composed of five levels for communicating confidence in metabolite annotation (Figure 1.10) (131).

Table 1.2 The levels of metabolite identification confidence, as defined by the Metabolomics Standards Initiative.
Taken from (120).

Level	Confidence of identity	Level of evidence
1	Confidently identified compound	Comparison of two or more orthogonal properties with an authentic chemical standard analysed under identical conditions.
2	Putatively annotated compounds	Based upon physicochemical properties and/or spectral similarity with public/commercial spectral libraries, without reference to chemical standards.
3	Putatively annotated compound classes	Based upon characteristic physicochemical properties of a chemical class of compounds, or by spectral similarity to known compounds of a chemical class.
4	Unknown compounds	Although unidentified and unclassified, these metabolites can still be differentiated and quantified based on spectral data.

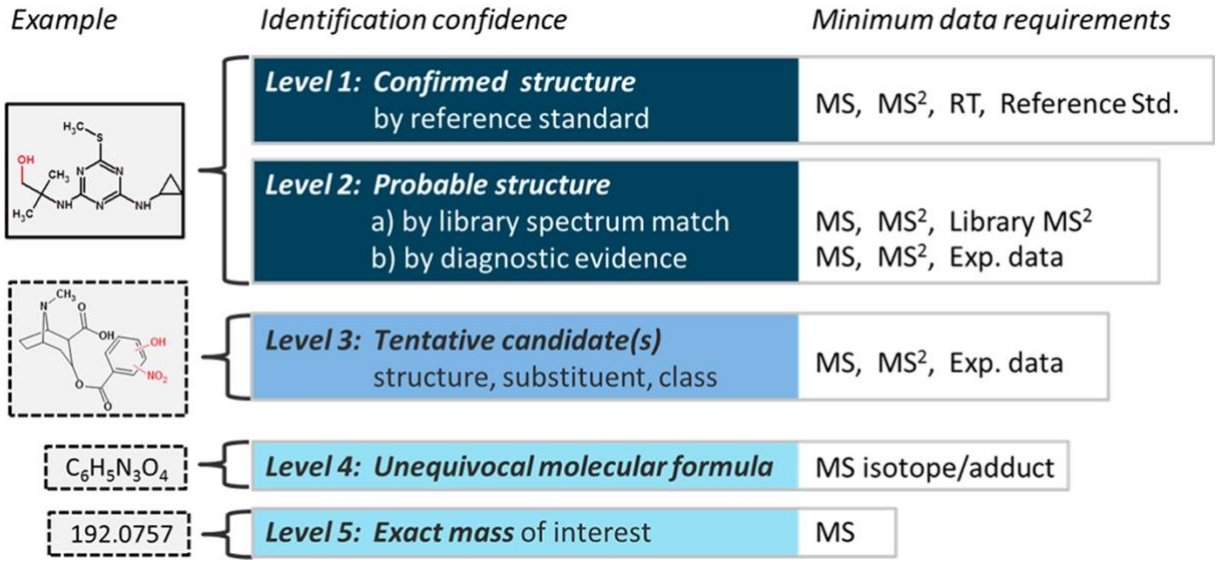


Figure 1.10 Levels of confidence in small molecule identification using high resolution mass spectrometry data.

The highest level of confidence (Level 1, confirmed structure) requires a match of accurate *m/z,* MS/MS, and retention time to that of a reference standard. Probable structure annotations are possible by match of MS/MS to spectrum within a library (Level 2a) or to (*in silico)* fragmentation predictions (Level 2b). Level 3 (tentative candidate(s)) is achieved where MS/MS evidences substructures of class, but unambiguous elucidation of complete structure is not possible. The lowest levels of confidence arise where only *m/z* data are available, which either enables annotation with molecular formula (Level 4) or is insufficient to assign any compound information (Level 5). Figure copied from (131).

The process of assigning metabolite annotations to untargeted metabolomics data typically comprises the deconvolution of full-scan (MS^1) accurate mass *m/z* measurements which considers the complexity of ESI, including adduct formation, in-source fragmentation, neutral losses, multiply charged species, and presence of naturally occurring elemental isotopes (e.g., ^{13}C), and the specific mass differences between possible features of a single compound, and the co-responsiveness of features, i.e., correlation of intensity measurements across all samples, to group *m/z* features corresponding to a single compound and calculate its monoisotopic neutral mass. Taking this neutral mass, the molecular formula of the compound can be calculated, and metabolite annotations assigned accordingly. Alternatively, the *m/z* of a single feature can be directly matched to metabolites within a metabolomic database. Here, prior assignment of ion form and isotopic composition limits the number of possible molecular formulae and putative metabolite annotations (66, 95, 96, 130, 132-135).

The accuracy of ion form, molecular formula and metabolite assignment is dependent on the mass accuracy and resolution of measurements and the mass error tolerance considered during feature annotation (95, 130). The degree of mass error introduced during data acquisition is influenced by the instrument used, the accuracy of its calibration and the concentration of analytes. It is measured in ppm and calculated

using Equation 3. A mass error tolerance of ±5 ppm is typically applied, which is consistent with specifications of HRMS (95, 136).

Equation 3 Calculating the error of *m/z* measurement by mass spectrometry in parts-per-million (ppm).

$$\boldsymbol{Mass\ error\ (ppm)} = \frac{(\boldsymbol{experimentall\ measured\ m/z - theoretical\ m/z})}{\boldsymbol{theoretical\ m/z}} * \boldsymbol{1e6}$$

The acquisition of orthogonal data can enhance the accuracy and robustness of metabolite feature annotation (67, 95, 120). First, RT, e.g., as measured in UHPLS-MS, can assist the grouping of *m/z* features since all signals from the same metabolite will have the same RT (66, 95, 96, 130, 132). RTs may also be compared to those of an authentic chemical standard for higher confidence in compound assignment. However, the RT of the standard typically must be measured 'in-house', since RT is strongly dependent on instrumentation and assay (stationary phase, mobile phase composition and gradient) used, which can be an expensive and time-consuming task (95, 130).

Secondly, fragmentation, i.e., MS^2-MS^n, data can be employed to filter molecular formula and/or metabolites assigned to full scan MS^1 data (95, 130). For the former, this is achieved through assigning molecular formula to fragment ions, thus constraining the molecular formula possible for the precursor. Considering metabolite annotation, fragmentation spectra can be compared to those of defined metabolites contained with metabolite database to reduce the list of possible annotations and/or provide confidence in the compound assignment (66, 130). These databases may be experimentally acquired from authentic chemical standards, e.g., such as mzCloud (Thermo Scientific), MassBank , and MassBank of North America (MoNA) (137), or predicted by *in silico* approaches, e.g., LipidBlast. The spectral similarity is typically assessed using the dot product score between aligned experimentally measured and

reference spectra (95, 138). Alternatively, measured fragments may be compared to *in silico* predicted fragments of compounds putatively assigned based on full scan data, allowing putative annotations to be ranked based on a match score, an approach applied by MetFrag (130, 139, 140).

Given the value of fragmentation data in metabolite annotation, maximising the coverage of its acquisition is a key objective in MS-based metabolomics data acquisition. Strategies for MS^n acquisition include data dependent (DDA) and data independent (DIA) acquisition. In DDA, the top *n* highest intensity features measured by a preceding MS^1 scan are selected as the precursors for fragmentation, where *n* is defined by the user but limited by instrument capabilities, and, in UHPLC-MS, the need for sufficient (i.e., at least eight) MS^1 data points across a chromatographic peak (95, 138). With this approach, precursors are isolated using a narrow *m/z* window such that resulting fragmentation spectra are relatively pure, i.e., most or all the fragment ions are derived from a single precursor (141). The selection criteria of DDA means that it is biased toward features of highest intensity, thus fragmentation data for many biologically relevant metabolites of lower intensity will not be acquired, limiting the coverage of this approach (95, 138). The coupling of this approach with user-defined inclusion lists, whereby features with *m/z* defined in the inclusion list are selected for fragmentation if detected, can increase coverage of biologically relevant metabolites, although this is limited to those that are expected (142). Other 'intelligent' use of DDA methods, e.g., use of smaller precursor selection windows in separate experiments, have shown to increase the depth coverage (143). More recently, software, e.g., AcquireX (Thermo Scientific), has been developed which enables on-the-fly generation and modification of inclusion lists, i.e., peak detection

and deconvolution to predict which features are molecular ions and subsequently prioritise these features for fragmentation, and exclusion lists, i.e., to avoid fragmenting features that have already been fragmented, with the aim of reducing the redundancy and maximising coverage of MS^n data acquisition. In DIA, larger isolation windows, e.g., sequential medium-width (*ca.* 20-25 Da wide) windows as in Sequential Windowed Acquisition of All Theoretical Fragment Ions (SWATH), are applied for precursor filtering such that the fragmentation spectra acquired are the product of many parent ions. This aim of DIA is complete unbiased coverage, with any precursor above a certain intensity threshold fragmented, however the loss of association between the precursors and their fragment ions and the difficulties faced in deconvoluting the MS/MS spectra makes the ultimate goal of metabolite annotation a challenge (95, 138).

Despite acquiring data with high mass accuracy and resolution, implementing deconvolution strategies, and exploiting orthogonal data, the number of false positive compound assignments can remain high, due ultimately to matching *m/z* or neutral masses to very large databases, e.g., HMDB (128), many of which will not be present or detected in a study sample. Curating biological test system-specific metabolite libraries has been proposed as a strategy to reduce the search space and limit the proportion of false positive annotations in untargeted metabolomics datasets (95, 130, 144), an approach explored further in this thesis.

1.5 Importance and measurement of xenobiotic toxicokinetics

As recognised by regulatory bodies, e.g., ICH, both the effect of the model system on the exposure xenobiotic, i.e., toxicokinetics (TK), and the effect of the xenobiotic on the model system, i.e., toxicodynamics are important factors when considering the

safety of a xenobiotic (145). Considering the former: TK describes the absorption, distribution, metabolism (biotransformation) and excretion (ADME) of a xenobiotic within a test system, properties which are dependent on the type of test system, i.e., *in vivo*, *ex vivo*, or *in vitro*, its capacity for biotransformation and, for *in vivo* systems, the route of exposure (146, 147). Meanwhile, the ADME properties of a given xenobiotic will influence its effects on the test system (i.e., TD). For example, in an *in vivo* model, the extent of distribution to a target organ will influence the magnitude of potentially toxic side effects on that organ. As a further example, less or absent biotransformation of a xenobiotic to a more or less toxic compound in one test system, e.g., *in vitro* model, compared to another, e.g., *in vivo* test species, may explain disparity in xenobiotic toxicity between the test systems. Scenarios such as this make extrapolation of findings between test systems and humans particularly complex and challenging. By characterising xenobiotic ADME properties in test systems, and through relating systemic exposure to dose levels and toxicity, more informed and accurate *in vitro* to *in vivo* extrapolation (IVIVE) and cross species extrapolation for prediction of human safety is enabled (146, 148, 149).

In drug development, the ADME properties of a NCE are typically characterised in test species through application of targeted MS (150), often with stable-isotope labelling (151, 152), or, in later stages of drug development, using (^{14}C)-radiolabelling, e.g., (153), to measure circulating levels of xenobiotics over a series of time points after dosing (i.e., systemic exposure), discover xenobiotic biotransformation products, and determine the distribution of the xenobiotic into tissues of interest. However, these analyses are not typically applied in *in vitro* toxicity evaluations, giving rise to a lack of understanding in a drug's disposition,

making interpretation and extrapolation (to *in vivo* systems) of endogenous responses more challenging (146, 147, 154).

The untargeted, high sensitivity nature of MS-based untargeted metabolomics measurements means that xenobiotics and related compounds, i.e., biotransformation products, present within analytical samples are typically measured alongside endogenous metabolites (53, 155). As such, efforts to develop and apply approaches to mine relevant ADME/TK data from untargeted metabolomics datasets, acquired for the purpose of interrogating effects of xenobiotics on the test system, could enable characterisation of xenobiotic ADME properties (1) within *in vitro* systems, which are otherwise typically overlooked, and (2) within *in vivo* systems without the need for additional experiments, test subjects and/or measurements, as is currently routine. This was explored further in this thesis.

1.6 Research objectives

Untargeted metabolomics is a favourable approach in toxicology, providing comprehensive data on molecular responses to xenobiotic perturbation which may be used to build greater understanding in mechanisms of toxicity and discover biomarkers for predictive purposes. In particular, it has great potential in tackling the challenge of early and accurate prediction of the cardiotoxicity potential of NCEs during drug development.

However, while the benefits of using more physiologically relevant *in vitro* models, *e.g.,* cardiac microtissues, for investigative toxicology is well recognised, their preparation for and analysis by MS-based untargeted metabolomics requires development and application of more appropriate methods. Furthermore, gaining biological insight from untargeted metabolomics datasets can be burdensome due to

the major bottleneck surrounding metabolite annotation and identification. Without efforts to overcome these obstacles, the potential impact of untargeted metabolomics within drug safety assessment is limited. Meanwhile, the use of untargeted metabolomics datasets to derive understanding of xenobiotic toxicokinetics in model systems is so far underdeveloped, despite the potential benefits to IVIVE, cross species extrapolation, and ultimately, prediction of drug safety in humans.

This thesis aims to develop and apply untargeted metabolomics approaches and tools to characterise metabolic perturbations induced by structural cardiotoxins in model systems, with a focus on cardiac microtissues, to ultimately discover a predictive metabolic signature of drug-induced structural cardiotoxicity. The following research objectives were established to achieve this aim. Each is addressed in a subsequent chapter of this thesis.

1. (Chapter 2) To address the unfulfilled potential of routine untargeted metabolomics datasets to inform on xenobiotic TK/ADME properties in test systems: develop an integrative method to discover extensive xenobiotic-related data within untargeted metabolomics datasets, and subsequently demonstrate the types of information which might be attained. This includes using the data to (1) derive information on xenobiotic disposition over time, (2) uncover toxicologically relevant endogenous perturbations, (3) reveal metabolic competency of an *in vitro* model, and (4) discover exposure to xenobiotics and subsequently characterise their metabolic fate.

2. (Chapter 3) Develop and demonstrate an extensive metabolomics workflow for investigating drug-induced perturbations in cardiac microtissues, incorporating

nESI-DIMS-based untargeted metabolomics of intracellular extracts and UHPLC-MS-based analysis of spent culture medium, both to profile the metabolic footprint and quantify drug exposure concentrations. The ultimate aim of this is to enable the application of a highly physiologically relevant *in vitro* system and untargeted metabolomics to discover predictive biomarkers of drug-induced structural cardiotoxicity.

3. (Chapter 4) Facilitate higher confidence metabolite annotation in nESI-DIMS studies using cardiac microtissues, thus addressing the major bottleneck in untargeted metabolomics studies and striving towards biological mechanistic insight. To achieve this, systematically measure and annotate the detectable polar metabolome and lipidome of cardiac microtissues using UHPLC-MS^n , then generate a polar metabolite and lipid library specific to the test system.

4. (Chapter 5) Investigate the response of cardiac microtissues following exposure to eight structural cardiotoxins and four non-structurally cardiotoxic xenobiotics at two concentrations for 6-, 48- and 72-hours. To achieve this, measure the relative levels of intracellular metabolites and lipids, and extracellular metabolites in exposed and biological control samples by application of four nESI-DIMS and two UHPLC-MS-based metabolomics assays to intracellular extracts and spent culture medium, respectively. Additionally, quantify the free extracellular concentrations of the twelve xenobiotics, using the same UHPLC-MS measurements, and discover their metabolic fate. Subsequently, using the extensive metabolomics data acquired, discover a metabolic signature predictive of drug-induced structural cardiotoxicity in cardiac microtissues.

CHAPTER 2: SIMULTANEOUSLY DISCOVERING THE FATE AND BIOCHEMICAL EFFECTS OF PHARMACEUTICALS THROUGH UNTARGETED METABOLOMICS

2.1 INTRODUCTION

Untargeted metabolomics is increasingly applied across a wide range of fields including toxicology (53, 64, 156). This approach uses an untargeted analytical detector, typically MS, to measure large numbers of low molecular weight biochemicals (metabolites and lipids) in a biological sample (66). In toxicology, such information can be utilized to discover MoA (53, 57, 69, 156, 157); derive molecular points-of-departure from baseline as a means to calculate safety thresholds (53, 69, 156); and group chemicals into categories based on similarities of metabolic responses to increase the reliability of read-across in chemical risk assessments (69, 156, 158). A consequence of the untargeted nature of the analytical detector is that xenobiotics and related compounds are typically measured alongside endogenous metabolites (53, 156). Simultaneous measurement of the exposure xenobiotic(s) and its biotransformation products can confuse the interpretation of endogenous metabolic responses if they remain unidentified. Consequently, it is recommended to identify and discard these xenobiotic-related data prior to statistical analyses (109). Yet measurements of xenobiotics can provide valuable information, revealing insights into the exposome, i.e., the chemical environment to which an individual has been exposed (156, 159, 160), and into their fate and metabolism (53, 145, 161-166). While stable isotope and untargeted MS-based approaches have successfully discovered biotransformation products of xenobiotics (152, 160, 167-171), the integration of untargeted endogenous metabolomics data with measurements of

internal dose and biotransformation to simultaneously understand the fate *and* effects of xenobiotics is limited (172).

Characterising the exposure to, and biotransformation of, a xenobiotic are key factors in the safety assessment of pharmaceuticals, biocides and industrial chemicals (145, 161-166), anti-doping testing (173), and environmental risk assessment (156, 159). Internal dose measurements disclose information on a xenobiotics disposition (absorption, distribution, metabolism and elimination; ADME) (174), e.g., by confirming distribution to target organ(s), indicating the time and concentration of peak internal dose, and revealing steady-state levels (after repeated dosing) (145, 161, 162, 165). Such information can help to enable accurate prediction of human risk from the responses of model species (145, 161, 164, 165). Biotransformation of a xenobiotic may result in compounds that are more toxic than the parent and, consequently, the toxicity of biotransformation products to which humans are exposed – either through pharmacological intervention or unwanted exposure – must be evaluated (162, 163, 166). This requires the measurement of complete biotransformation maps of xenobiotics (162, 163, 166). Knowledge of biotransformation maps is also important for risk assessment of industrial chemicals, e.g., serving as a basis for chemical grouping to support read-across of toxicity data (175).

Standardised methods for measuring xenobiotic internal dose and/or biotransformation are described in guidance documents that support regulatory safety legislation for pharmaceuticals, biocides and industrial chemicals (145, 165). Methods typically rely on [^{14}C]-labelling (gold-standard) (153), or more recently, stable isotopic labelling ([^{13}C] or [^{2}H]) (152, 169), to track xenobiotic biotransformation, limiting their application to pre-defined exposures. Additionally,

while these methods are not intended to provide insights into the impacts of a xenobiotic on endogenous biochemistry, the potential to acquire information simultaneously on the disposition of a xenobiotic alongside its biological impacts is tantalising. This could enable a deeper assessment of the covariance of systemic or organ-specific exposure and endogenous response, revealing otherwise undiscovered toxicological insights. Furthermore, there is an unmet need for rapidly and affordably characterising xenobiotic biotransformation *in vitro*, yet knowledge of such characteristics could enhance the *in vitro*-*in vivo* extrapolation of dose-response relationships, helping to promote the use of *in vitro* models for safety assessments and contributing to a reduced need for expensive and time-consuming *in vivo* toxicology studies (147, 154). The overarching aim of the current study was to demonstrate an integrative method to discover extensive xenobiotic-related data from routine untargeted metabolomics datasets and subsequently derive information on the disposition of an exposure substance, over time, obtained from the same biological samples and analytical measurements used to discover the endogenous metabolic responses. This type of analysis may be termed “untargeted toxicokinetics” (69) (TK) or untargeted ADME/TK. The first objective was to develop a computational open-source workflow to semi-automatically discover and visualise the measurements of a xenobiotic and its biotransformation products within untargeted metabolomics datasets – here demonstrated using pharmaceuticals. Secondly, I sought to demonstrate the capability of this workflow to discover fingerprints of xenobiotic biotransformation within the plasma (with temporal resolution) and at a site of toxicity (the heart), in rats exposed to two cardiotoxins, sunitinib and KU60648. The third objective was to reveal the capacity, by association of measured internal relative doses with the endogenous biochemical responses, to

uncover toxicologically relevant perturbations, including at a site of toxicity. Next, I attempted to demonstrate the capability to reveal the metabolic competencies of *in vitro* models by applying the workflow to sunitinib-exposed human induced pluripotent stem cell-derived cardiomyocytes (hiPSC-CMs). The final objective was to highlight the ability to discover exposures of humans to several pharmaceuticals and, through implementation of the workflow, characterise their metabolic fate.

2.2 Materials and Methods

2.2.1 Chemicals

Sunitinib malate was purchased from Carbosynth Ltd (UK). KU60648 was synthesised in-house at AstraZeneca. Amitriptyline hydrochloride, lansoprazole, Paracetamol (acetaminophen) and ramipril were purchased from Merck Life Sciences (UK). The purity of all chemicals was ≥ 98%.

2.2.2 In vivo rat studies: animals, treatment and sampling

Animal studies were performed by AstraZeneca in accordance with the United Kingdom Animal (Scientific Procedures) Act 1986, were subject to local ethics committee (AstraZeneca Animal Welfare Review Board and Babraham Institute Animal Welfare and Ethical Review Board) approval and in line with project and personal license conditions.

Rats (Han-Wistar – Crl:WIST; 240-260 g or 220-240 g for male and female, respectively) were purchased from Charles River Laboratories (UK). Animals were housed as previously described (176).

Animals were grouped randomly for the purposes of the study: groups 1-4 were formed of N = 5 male rats, groups 5-8 were formed of N = 5 female rats. Sunitinib and KU60648 were formulated in 20% w/v aqueous (2-hydroxypropyl)-β-cyclodextrin and administered orally. Sunitinib-exposed rats (groups 6 and 8) were dosed with 25

mg/kg/day (10 mL/kg/day) of sunitinib malate for 14-days. KU60648-exposed rats (groups 2 and 4) were dosed with 150 mg/kg/day (10 mL/kg/day) for 2-days, then with 225 mg/kg/day (10 mL/kg/day) on day 3. These doses were selected as doses that were likely to elicit toxicologically relevant molecular responses while considered suitable for investigation based on previous studies demonstrating tolerance to these doses, i.e., approximately the maximum tolerated dose.

TK analysis was carried out on plasma samples collected on day 1 (groups 2, 4, 6 and 8) at 1-, 4-, 6- and 24-hours post-dose, day 3 (groups 2 and 4) pre-dose and 4-hours post-dose and day 14 (groups 6 and 8) at 1-, 4-, 6- and 24-hours post-dose. Sample collection and analysis was performed as described previously (176).

Blood samples for untargeted metabolomics were taken on days 1 and 2 (groups 1-4), day 1 and 4 (groups 5-6) or days 2 and 8 (groups 7-8) at 4-hours post-dose. Terminal samples were also taken 24-hours post-dose (day 4, groups 1-4) and 28-hours post-dose (day 15, groups 5 – 8). 300 µL whole blood was collected via the tail vein, mixed with Lithium-Heparin anticoagulant, and used to derive approximately 150 µL of plasma for analysis.

KU60648-exposed rats (groups 2 and 4) and corresponding vehicle controls (groups 1 and 3) were terminated on day 4. Sunitinib-exposed rats (groups 6 and 8) and corresponding vehicle-controls (groups 5 and 7) were terminated on day 15. Following termination, the whole heart was removed (groups 3, 4, 7 and 8), with the apex sectioned for untargeted metabolomics analysis.

2.2.3 CARDIOMYOCYTE STUDY

Cardiomyocyte culturing, exposures and sampling was performed by Dr. Andrew Hall (AstraZeneca). Cardiomyocytes (hiPSC-CMs, Cellular Dynamics International,

Fujifilm, US (CDI)) were defrosted according to manufacturer's instructions and plated at 500,000 cells per well in 6-well plates pre-coated with 0.1% gelatine. (Each well formed a time-point N and was repeated from three separate vials). After plating in Cardiomyocyte plating media, cells were cultured in Cardiomyocyte maintenance media from 48-hours post plating, until end of experiment. Ten days post-plating, the cardiomyocytes were treated with either 0.1% dimethyl sulfoxide (DMSO, control) or 5 µM sunitinib (treated), for either 1-, 6- or 24-hours, added as part of a media change. This concentration was selected as one that would elicit a toxicologically relevant molecular response without significant loss in cell viability, i.e., approximately the maximum tolerated dose, based on previous studies. Once the exposure time had elapsed, plates were placed on wet ice, the media was removed (to microcentrifuge tubes), then wells were washed twice with 1 mL ice-cold 0.9% sodium chloride (NaCl). Plates were then immediately frozen on dry ice. Media samples were spun at 10,000-*g* for 5-minutes at 4°C to remove any cell debris. The supernatants were then transferred to new microcentrifuge tubes. All samples were stored at -80°C prior to metabolomic analyses.

2.2.4 HUMAN PLASMA SAMPLES

Plasma from 21 healthy human volunteers (18 females, 3 males; age 24-62) was obtained from the University of Birmingham's Human Biomaterials Resource Centre (HBRC), which holds ethical approval from a UK National Health Service (NHS) Research Ethics Committee (NRES Committee North West – Haydock; Ref 20/NW/0001) to provide human biomaterials and associated data for a broad spectrum of biomedical research. Human biomaterials and associated data were obtained in accordance with the Human Tissue Act 2004 and associated Codes of Practice, and project specific use of human biomaterials and associated data were

subject to the HBRC Access Review panel for ethical approval and sponsorship under the UK Policy Framework for Health and Social Care Research.

Plasma samples selected for analysis were from donors (healthy volunteers) who reported to have taken some common medication in the 24-hours prior to sampling. Plasma was prepared from peripheral blood samples mixed with EDTA and stored at -80°C until analysis.

2.2.5 EXTRACTION OF POLAR METABOLITES AND LIPIDS FROM CARDIAC TISSUE

Preparation of cardiac tissue samples was performed by Dr. Andrew Southam (Phenome Centre Birmingham (PCB)) according to previous studies (77, 86), with some minor changes. Tissue sizes ranged from 54-124 mg. 8 µL/mg wet tissue mass of ice-cold methanol (LC-MS grade, VWR International, UK) and 3.2 µL/mg ice-cold water (LC-MS grade, VWR International) was added to frozen tissue samples, which were homogenised in a bead-based homogenisation system (Precellys 24 with CK28 tubes, Stretton Scientific, UK). The homogenate was transferred to a 1.8 mL glass vial and 8 µL/mg ice-cold chloroform (HPLC grade, Fisher Scientific) and 4 µL/mg water were added. Sample was vortexed (30-seconds), left on ice (10-minutes, for extraction) and centrifuged (2,500-*g*, 4ºC, 10-minutes). Sample was set at room temperature (approximately 20ºC) for 5-minutes to complete phase partitioning. Fixed volumes of the polar (400 µL – equivalent to 30 mg extracted tissue) and non-polar (250 µL – equivalent to 30 mg extracted tissue) were removed and dried in a SpeedVac sample concentrator (Savant SPD111V230, Thermo Scientific) or a nitrogen blow down drier (Techne FSC400D), respectively. Samples were stored at -80ºC until analysis. To create polar intra-study QCs an extra 300 µL of the polar extract (post-bi-phase partition) was taken from each sample, mixed (vortexed 30-seconds) and aliquoted (400 µL) before drying by

SpeedVac. To create non-polar intra-study QCs an extra 200 µL of the non-polar extract (post-bi-phase partition) was taken from each sample, mixed (vortexed 30-seconds) and aliquoted (250 µL) before drying by nitrogen blow down drier. Extract blank samples were created by carrying out the above procedure in the absence of tissue. Prior to UHPLC-MS analysis, dried samples were resuspended in 300 µL 3:1 acetonitrile/water (polar extracts) or 300 µL 3:1 isopropanol/water (non-polar extracts), vortexed (30-seconds), centrifuged (20,000-*g*, 4ºC, 20-minutes) and 100 µL supernatant loaded into an LC vial (Chromatography Direct, UK).

2.2.6 Extraction of polar metabolites and lipids from cardiomyocytes

Cardiomyocyte (hiPSC-CM) intracellular extracts were prepared by Dr. Andrew Southam (PCB). 6-well plates (containing saline-washed cardiomyocytes with all liquid removed) were placed on dry-ice and 600 µL of 2:0.8 methanol/water (prechilled on dry ice for 1-hour) was added to each well. Cardiomyocytes were dislodged into the solvent using a cell scraper (Corning, UK) and all cardiomyocytes and liquid were removed into a fresh 1.8 mL glass vial. A further 240 µL of prechilled 2:0.8 methanol/water was added to the well, scraped and all contents added to the 1.8 mL glass vial. 600 µL ice-cold chloroform and 300 µL ice-cold water were added to the 1.8 mL glass vial and sample was vortexed (30-seconds), left on ice (10-minutes, for extraction) and centrifuged (2,500-*g*, 4ºC, 10-minutes). Sample was set at room temperature (approximately 20ºC) for 5-minutes to complete phase partitioning. Fixed volumes of the polar (900 µL) and non-polar (600 µL) were removed and dried in a SpeedVac sample concentrator or a nitrogen blow down drier, respectively. Samples were stored at -80ºC until analysis. Extract blank samples were created by carrying out the above procedure in the absence of cells. Prior to UHPLC-MS analysis, dried samples were resuspended in 150 µL 3:1

acetonitrile/water (polar extracts) or 150 µL 3:1 isopropanol/water (non-polar extracts), vortexed (30-seconds), centrifuged (20,000-*g*, 4ºC, 20-minutes) and 100 µL supernatant loaded into an LC vial. To create the intra-study QCs, the remaining 50 µL liquid from each centrifuged resuspended sample was pooled (for polar and non-polar separately), vortexed and moved to an LC vial for direct analysis.

2.2.7 Extraction of polar metabolites and lipids from biofluids

Samples were prepared in accordance with previous studies (76), with some minor changes. Rat plasma and cardiomyocyte spent culture media were prepared by Dr. Andrew Southam (Phenome Centre Birmingham). I prepared the human plasma samples. Biofluids (rat plasma, human plasma or cardiomyocyte spent culture media) were thawed on ice and briefly vortexed (5-seconds). 50 µL of the biofluid was mixed with either (i) 150 µL 100% ice-cold acetonitrile (LC-MS grade, VWR International; polar metabolite extraction), or (ii) 150 µL 100% ice-cold isopropanol (LC-MS grade, VWR International; lipid extraction). Samples were vortexed and centrifuged (20,000-*g*, 4ºC, 20-minutes) and 100 µL supernatant removed into an LC vial for direct analysis. To create the intra-study QCs, 50 µL of each plasma sample (plasma QC) or 50 µL of each media sample (media QC) was pooled, vortexed (30-seconds) and split into several 50 µL aliquots. Each aliquot was prepared as for the samples (above).

2.2.8 Untargeted ultra-performance liquid chromatography-mass spectrometry

Analysis of samples from the rat and cardiomyocyte studies was performed by Dr. Andrew Southam (PCB) as described previously (76) using an Q-Exactive Focus mass spectrometer (Thermo Scientific, Hemel Hempstead, UK) coupled to a Dionex Ultimate 3000 UHPLC (Thermo Scientific), employing HILIC and RP-C_{18} chromatography. For the HILIC method, an Accucore 150 Amide column (100 × 2.1

mm, 2.6 µm, Thermo Scientific) was used. Mobile phase A was 95% acetonitrile/water (10 mM ammonium formate, 0.1% formic acid) and mobile phase B was 50% acetonitrile/water (10 mM ammonium formate, 0.1% formic acid). The gradient was as follows: t = 0.0, 1% B; t = 1.0, 1% B; t = 3.0, 15% B; t = 6.0, 50% B; t = 9.0, 95% B; t = 10.0, 95% B; t = 10.5, 1% B; t = 14.0, 1% B. All changes were linear (curve = 5). The flow rate was 0.5 mL/min, and the column temperature was 35 °C. For the RP-C_{18} chromatography, a Hypersil GOLD C_{18} column (100 × 2.1 mm, 1.9 µm, Thermo Scientific) was employed. Mobile phase A was 60% acetonitrile/40% water (10 mM ammonium formate, 0.1% formic acid) and mobile phase B was 85.5% propan-2-ol/9.5% acetonitrile/5% water (10 mM ammonium formate, 0.1% formic acid). The gradient was as follows: t = 0.0, 20% B; t = 0.5, 20% B, t = 8.5, 100% B; t = 9.5, 100% B; t = 11.5, 20% B; t = 14.0, 20% B. All changes were linear (curve = 5). The flow rate was 0.4 mL/min, and the column temperature was 55 °C. In all cases analysis was performed in positive and negative ionisation modes separately at a resolution of 70,000, between 70-1050 *m/z* (HILIC) and 150-2000 *m/z* (RP-C_{18}). The sample injection volume was 2 µL. MS/MS fragmentation data was collected by DDA (using ‘Discovery Mode’) of QCs using HCD with stepped collision energies (CEs) (HILIC 25, 60, 100; RP-C_{18} 20, 50, 80). For HILIC and RP-C_{18} separately, MS/MS data was collected for three different *m/z* ranges from three separate injections. Scan ranges were: HILIC *m/z* 70-200, *m/z* 200-400, and *m/z* 400-1000; RP-C_{18} *m/z* 200-400, *m/z* 400-700 and *m/z* 700-1500. Additional MS/MS fragmentation data of putative xenobiotic-related features was collected by DDA, using targeted inclusion lists across multiple injections of selected xenobiotic-exposed samples, using HCD with stepped cEs (HILIC 25, 60, 100; RP-C_{18} 20, 40, 100). For MS/MS fragmentation

data acquisition, analysis was performed at a of resolution of 35,000 and 17,500 for full scan (MS^1) and MS/MS, respectively.

The analysis of human plasma extracts was performed using a positive ion HILIC UHPLC-MS method as described above, but deployed on an Orbitrap ID-X Tribrid mass spectrometer (Thermo Scientific) coupled to a Vanquish Horizon UHPLC (Thermo Scientific) (with method gradient: t = 0.0, 1% B; t = 2.1, 1% B; t = 4.1, 15% B; t = 7.1, 50% B; t = 10.1, 95% B; t = 11.0, 95% B; t = 11.5, 1% B; t = 15.0, 1% B). Analysis was performed at a resolution of 120,000, over a scan range of m/z 70–1050. MS/MS fragmentation data was collected by DDA (ddMSnScan) from pooled samples using HCD with stepped normalised-CEs (20, 40, 130%), and inclusion lists targeting SyGMa predicted biotransformation products ($[M+H]^+$, $[M+Na]^+$ and $[M+NH_4]^+$ ion forms). Analysis was performed at resolutions of 60,000 and 30,000 for full scan and MS/MS, respectively, for fragmentation data acquisition.

2.2.9 Untargeted metabolomics raw data processing

Vendor format raw data files (.RAW) were converted to mzML file format using ProteoWizard software (v3.0.11392) (177). Full scan (MS^1) data deconvolution was performed by XCMS operated in Galaxy (115), as reported previously (76) (settings: min. peak width (HILIC = 4; RP-C_{18} = 6); max. peak width (30); ppm (HILIC = 12; RP-C_{18} = 14); mzdiff (0.001); bw (0.25); mzwid (0.01); minfrac (0.2 for rat and cardiomyocyte datasets, 0.05 for human dataset)). A data matrix of peak intensities for metabolite features (*m/z*-RT pairs) *vs*. samples were constructed. MS/MS data files were processed, filtered and averaged using the R/Bioconductor package msPurity (141) (settings: XCMS (as described above except minfrac (0.1)), plim (0.5), ppm (5.0)). Processed MS/MS spectra were aligned to metabolite features in

the peak matrix generated from full scan (MS^1) data files using 5 ppm mass error and 10-second RT tolerance window.

2.2.10 XENOBIOTIC-BASED DATA ANALYSIS AND ANNOTATION

Exposure to suspect xenobiotics, i.e., any of the Top 20 pharmaceuticals prescribed by the UK NHS between 2014-2020, was defined for human samples with unknown exposures as follows. First, measured features corresponding to each of the ten suspect xenobiotics (pharmaceuticals) were identified by (i) match of measured *m/z* to theoretical *m/z*, for a low confidence annotation (MSI Level 3 / Schymanski level 3), (ii) match of selected MS/MS fragmentation data to MS/MS spectrum contained within a public database (MassBank, GNPS), for a mid-confidence annotation (MSI Level 2 / Schymanski level 2) and/or (iii), match of MS/MS fragmentation pattern and RT to that of a chemical standard measured using the same instrument and analytical method, for a high-confidence annotation (MSI Level 1 / Schymanski level 1). Using the annotated features, samples were defined as exposed to a given xenobiotic if the relative intensity of the representative feature was > 10-fold the median intensity across all samples and intra-study QCs, after imputing missing values with the lowest measured relative intensity across all features. Where relative intensity was below this value, the sample was defined as 'control'.

In the case of laboratory model-based experiments (*in vivo* rat & *in vitro* cardiomyocyte studies), the 'exposed' and 'control' sample labels were defined as per the experimental conditions.

Putative xenobiotic-related features were discovered by applying the following filters: feature present in ≥80% (for rat and cardiomyocyte datasets) or ≥50% (human datasets) of exposed samples; feature present in ≤50% biological control samples;

and the median intensity of a feature in exposed samples is ≥10-fold its median intensity in biological control samples. This was implemented using the R/Bioconductor package structToolbox (178) (v1.6.0, https://bioconductor.org/packages/release/bioc/html/structToolbox.html). Ion form annotation and feature grouping of the putative xenobiotic-related features was carried out using the functions ‘Group features’ and ‘Annotate Peak Patterns’ in the python package BEAMSpy (v1.0.0, https://github.com/computational-metabolomics/beamspy), using 5 ppm mass error, 5-second RT tolerance window.

Pearson’s correlation analysis was carried out using the R/cran package RcmdrMisc (https://cran.r-project.org/web/packages/RcmdrMisc/index.html) on combined data from all UHPLC-MS assays following normalisation of intensity measurements by PQN, applying coefficients calculated for the endogenous datasets. A given pair of features were defined as co-responsive when Holm adjusted p-value < 0.05 and R ≥ 0.75. A network diagram of the correlation matrix was analysed and visualised in Cytoscape v3.7.2 (179).

Biotransformation products of parent xenobiotics (sunitinib, KU60648, paracetamol, omeprazole, atorvastatin, lansoprazole, bisoprolol, and amitriptyline were predicted using SyGMa (180) and the “Generate Expected Compounds” tool in Compound Discoverer (v3.0, Thermo Scientific, sunitinib and KU60648, only). For SyGMa, both number of Phase I and Phase II transformation steps: 3. The outputs were filtered to predictions with a SyGMa score ≥0.01% and predictions where molecular formulae of predicted biotransformation products were identical were combined. For Compound Discoverer predictions, the standard software transformation library was used to predict biotransformation products for both xenobiotics, with maximum

number of dealkylation steps: 1, maximum number of Phase II steps: 1 and maximum number of all steps: 3. Predicted biotransformation products were aligned to putative xenobiotic-related features using the R programming language (https://www.R-project.org), using ±5 ppm mass error.

The molecular formula/structures associated with the measured fragmentation peaks of parent xenobiotics and their putative biotransformation products were annotated *in silico* using MetFrag in command line (140) with the candidate molecule(s) a given spectra user-defined as the annotation from SyGMa and/or Compound Discoverer, or parent xenobiotic where features were not annotated (settings: fragment peak match mass deviation = 5 ppm)

K-means cluster analysis, a type of unsupervised clustering, was carried out using the R programming language (https://www.R-project.org). Prior to analysis, data was scaled by unit variance. An elbow plot was generated for each dataset to select the optimal value of *k* prior to execution of *k*-means cluster analysis using the median intensity of feature across biological replicates at each time point.

2.2.11 Endogenous metabolite and lipid-based data analysis

Prior to data analysis, datasets were filtered as follows: any feature whose median intensity in biological samples is <20x its median intensity in blank samples was removed; features with relative standard deviation (RSD) ≥30% across the QCs were removed; samples with >50% missing values were removed; features which were missing in ≥10% QCs and/or ≥50% of all samples were removed; features present in the list of putative xenobiotic features were removed. Univariate statistical analysis (*t*-test) was applied after PQN. PCA was carried out after PQN, missing value imputation (MVI) by KNN (*k* = 5) and glog transformation. These steps were executed using the R/Bioconductor packages pmp (v1.6.0,

https://bioconductor.org/packages/release/bioc/html/pmp.html) and structToolbox (178) (v1.6.1, https://bioconductor.org/packages/release/bioc/html/structToolbox.html).

Endogenous polar metabolite annotation was performed using Compound Discoverer (Thermo Scientific). Metabolite features within the UHPLC-MS/MS data were searched against the mzCloud database. Only annotations with spectral match score >0.6 were used. Endogenous lipid annotation was performed using LipidSearch (Thermo Scientific). Lipid features within the UHPLC-MS/MS data were searched against the entire *in silico* HCD database (±5 ppm mass error). Only annotations graded A-C were used for annotation purposes (Grade A: all fatty acyl chains and class were completely identified; Grade B: some fatty acyl chains and the class were identified; Grade C: either the lipid class or some fatty acyls were identified). These approaches provided annotations consistent with reporting level 2 of the MSI recommendations (120). Annotations were aligned to the XCMS outputs using the R programming language (https://www.R-project.org), using ±3 ppm mass error and ±10-second RT tolerance window.

Spearman's correlation analysis of annotated lipids and parent xenobiotics (sunitinib or KU60648) in the cardiac tissue of exposed rats was carried out using PQN-normalised peak intensity measurements. This was executed using the R/cran package RcmdrMisc (https://cran.r-project.org/web/packages/RcmdrMisc/index.html). A network diagram of the resulting correlation matrix was analysed and visualised in Cytoscape v3.7.2 (179). Over-representation analysis of lipid classes significantly correlated with sunitinib or KU60648 (p <0.05) was carried out by one-way Fisher's Exact test, using full list of annotated lipids as the reference set.

2.3 Results and Discussion

2.3.1 Development of untargeted workflow to discover xenobiotics

Untargeted metabolomics datasets are measured to provide information on endogenous biochemistry but can also reveal insights into the fate and metabolism of xenobiotics. Here we developed a data processing and analysis workflow to discover information arising from exposure to a xenobiotic and its biotransformation products using data that can be measured routinely by state-of-the-art ultra-high performance liquid chromatography mass spectrometry (UHPLC-MS) untargeted metabolomics (Figure 2.1).

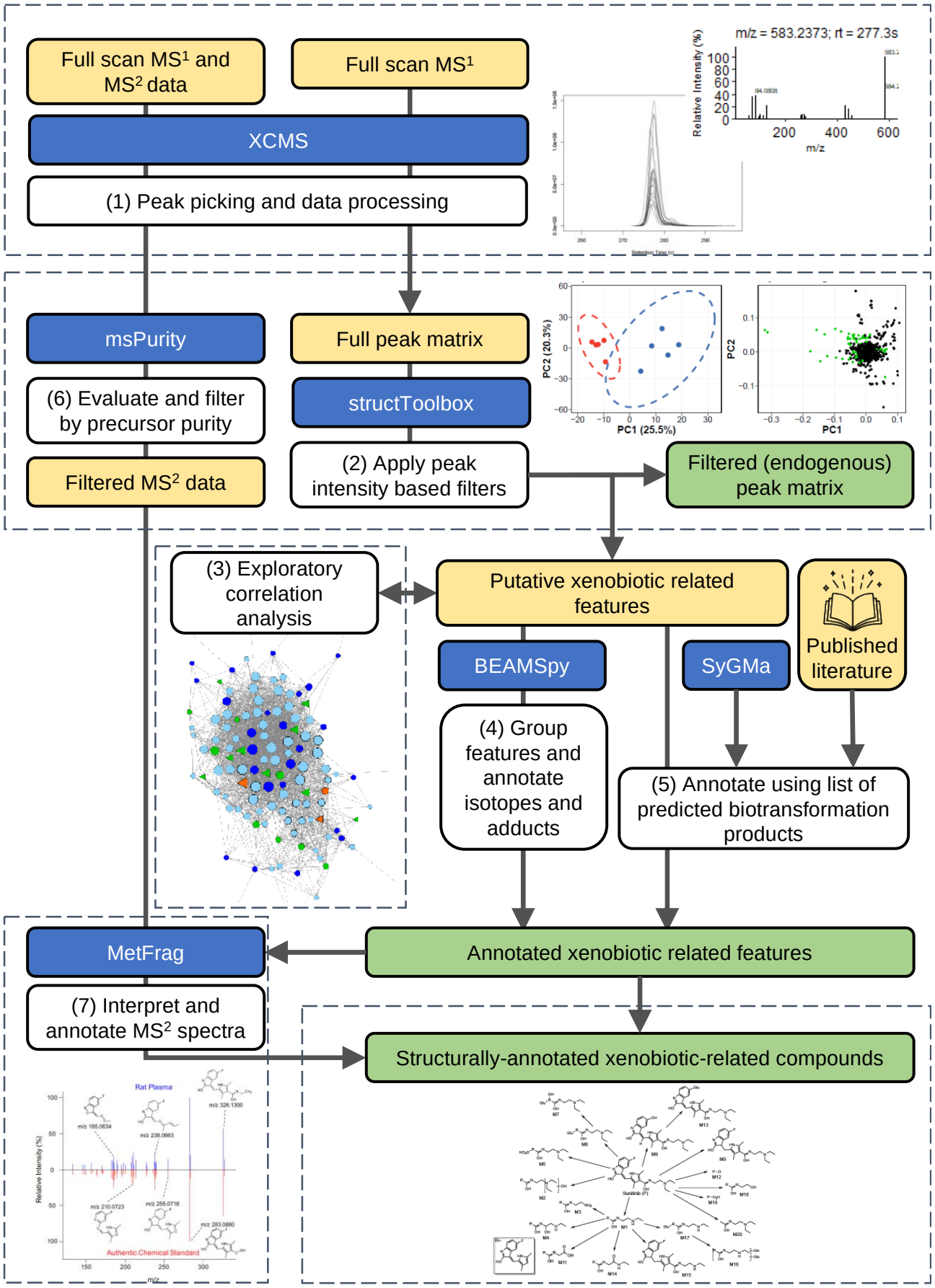


Figure 2.1 Schematic of the untargeted ADME/TK workflow.

An open-source workflow to semi-automatically discover and visualise xenobiotics and their biotransformation products from UHPLC-MS untargeted metabolomics dataset. (1) Full scan MS^1 data are peak-picked and processed using XCMS (115) to produce a 'full peak matrix'. (2) A series of three peak intensity-based filters are applied using structToolbox (178) to reduce this matrix to generate a subset matrix of 'putative xenobiotic-related features' which can be explored initially by (3) correlation analysis to reveal relationships between features. (4) Grouping of features and annotation of peak patterns, followed by (5) annotation of compounds using a list of predicted biotransformation products, yields a matrix of annotated xenobiotic-related compounds and their relative intensities. Confidence in identifying the xenobiotics and their biotransformation products can be increased by incorporating MS/MS data measured for these annotated compounds. (6) MS/MS data are processed and filtered using msPurity (141) and (7) compared against *in silico* predicted assignments using MetFrag (140) to generate a list of 'structurally annotated xenobiotic-related compounds'. Green shading indicates the outputs of the workflow. Putative xenobiotic-related features are removed from the full peak matrix, generating a filtered (endogenous) peak matrix for endogenous data analysis.

With the demonstration of this workflow to discover rich and extensive information on the disposition of pharmaceuticals and related toxicodynamic knowledge presented in the following five results sections, here I describe the rationale for the computational workflow and selection of processing parameters. First, the workflow applies three intensity-based filters to the acquired MS^1 data, following peak picking, to refine the dataset towards a list of putative xenobiotic-related features: (1) Only features present in at least 80% of all xenobiotic-exposed biological samples are retained. In principle, xenobiotic-related features should be present in all samples taken from exposed biological system(s), however, considering the low concentrations of some analytes and routine occurrence of missing values in UHPLC-MS untargeted metabolomics datasets (181), some leniency is incorporated into the filter to reduce the false-negative rate. (2) Features present in more than 50% of biological control samples are removed. Although xenobiotic-related features should not be present in control samples, peak detection can occur in cases of system carry-over (182), or in the event of co-eluting peaks, hence leniency was introduced through this filter to reduce the false-negative rate. (3) Only features with ≥10-fold median intensity in exposed samples relative to control samples are retained (in principle the fold-change should be infinite for xenobiotic-related

features). This threshold was derived based on an extensive review of toxicity datasets, which concluded that a ≥10-fold intensity change is highly unlikely for endogenous biochemicals (Figure 2.2). Subsequent exploratory correlation analysis of the putative xenobiotic-related features, i.e., those that pass these three filters, provides confidence that the features are closely related based on their co-responsiveness (183).

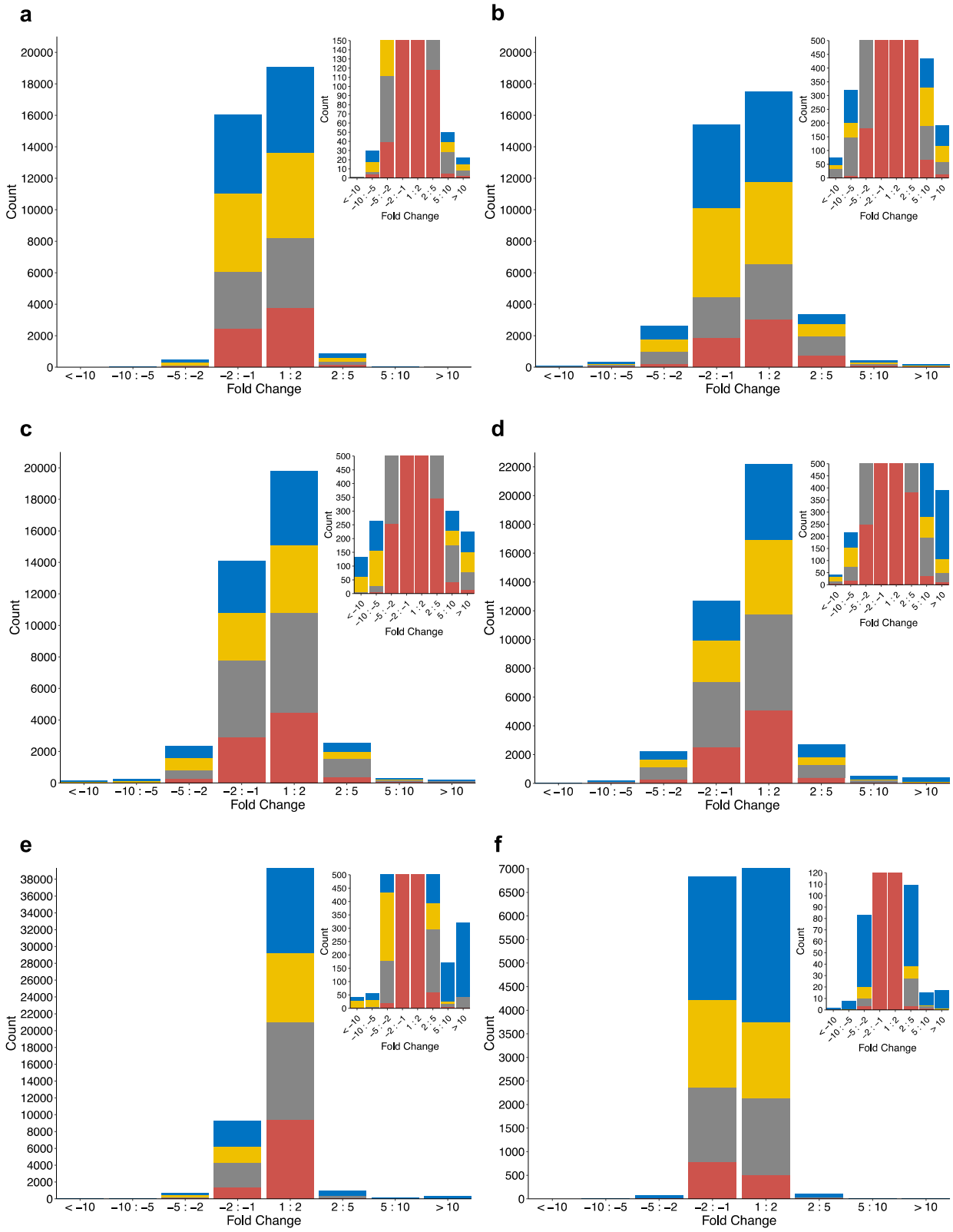


Figure 2.2 Distribution of peak intensity fold changes observed in untargeted metabolomics toxicity datasets.

The distribution of fold changes (median exposed peak intensity compared to median biological control peak intensity per feature) observed in the untargeted metabolomics toxicity datasets measured by HILIC UHPLC-MS in positive ion mode (blue), HILIC UHPLC-MS in negative ion mode (yellow), RP-C_{18} UHPLC-MS in positive ion mode (grey), and RP-C_{18} UHPLC in negative ion mode

(red) discussed in this thesis chapter: a plasma from rats exposed to sunitinib (n = 29), b plasma from rats exposed to KU60648 (n = 19), c cardiac tissue of rats exposed to sunitinib (n = 5), d cardiac tissue of rats exposed to KU60648 (n = 5), e intracellular extracts of hiPSC-CMs exposed to sunitinib (n = 9), and f culture medium of hiPSC-CMs exposed to sunitinib (n = 9). Inset figures display the chart zoomed-in on y-axis. At least 98% of fold changes are below the 10-fold threshold across the 6 datasets.

The list of putative xenobiotic-related features is then annotated and grouped to unveil features common to a single compound (132). This includes consideration that features may arise from in-source modification, including adduct formation, heterodimerisation and fragmentation. The use of retention time data here enables the distinction between products of analytical and biological transformation, i.e., chromatographically separated features likely arise from unique compounds produced in biological test systems. Comparison of the grouped features to a list of predicted biotransformation products, generated by combining outputs of *in silico* prediction engines (e.g., SyGMa (180)) with previously reported experimental data, allows for putative compound annotation. Further confidence in these annotations can be gained from inspection of corresponding MS/MS fragmentation spectra. Since preparing analytical standards for each of the biotransformation products of >100,000 compounds (184, 185) is impossible, the application of *in silico* fragmentation predictor tools (e.g., MetFrag (140)) is essential to attempt to assign partial or complete chemical structures to the measured MS/MS spectra. The structure corresponding to the putative compound annotation(s) and/or exposure xenobiotic structure is used as the input for these tools, since many xenobiotic biotransformation products will not be documented in publicly available databases. Annotation of a compound's MS/MS spectrum with substructures of the parent xenobiotic is consistent with it being related, via biotransformation, to the parent. The differences between the MS/MS spectra of the parent and suspected biotransformation product may elucidate the site of modifications (186, 187).

The final output of the workflow is a list of detected exposure xenobiotic(s) and their biotransformation products, annotated with putative molecular formula, partial or complete chemical structures, and corresponding peak intensity data. These data can be further analysed to discover the fate of the xenobiotic, investigate associations between exposure and effects on endogenous biochemistry, and contrast the metabolic competency of biological test systems, as described below.

The above summarised workflow is centred on three principles: (1) unbiased data-driven discovery of unknown biotransformation products. This is facilitated by exploiting the high sensitivity of HRMS, enabling discovery of lower abundance molecules, and the application of three intensity-based filters to untargeted metabolomics datasets, which were designed to reduce the frequency of false-positive (fold-change filter) and false-negative (exposed and biological control sample filters) outputs, and requires no prior knowledge of xenobiotic biotransformations. Unlike other strategies for measuring xenobiotic biotransformations, this approach does not require stable isotope-labelling, opening the door to discovering unknown exposures to xenobiotics and their internal fate. (2) Targeted detection of known and/or predicted biotransformation products. Primarily achieved through the application of *in silico* biotransformation prediction engines, to aid annotation of xenobiotic biotransformation products. (3) Maximising confidence in the identity of detected xenobiotics and biotransformation products, largely through MS/MS-based structural elucidation. In the absence of MS/MS fragmentation data, e.g., for low intensity or low purity precursor ions, the combination of an accurate mass match to a predicted biotransformation product (“targeted”) along with passing filtering thresholds (“data driven”), provides substantial evidence that compounds are xenobiotic-related. Taken together, the untargeted ADME/TK workflow has the

potential to discover predicted and novel biotransformation products of unlabelled xenobiotics as well as provide confidence in their annotation or identity. The use of open-source software (115, 140, 141, 178, 180) following application of published UHPLC-MS-based untargeted metabolomics analytical methods (76) makes this approach amenable to application by the wider metabolomics community.

2.3.2 UNTARGETED WORKFLOW DISCOVERS FATE OF SUNITINIB IN RAT

To test the ability of the workflow to discover pharmaceuticals and their biotransformation products from an untargeted metabolomics dataset, I applied it to an investigation of the metabolic perturbations induced in rats exposed to sunitinib (Table A.1). This dataset was originally measured to characterise endogenous metabolic changes only and comprised four assays, HILIC UHPLC-MS in positive and negative ion modes to study the polar metabolome, and RP-C_{18} UHPLC-MS in both ion modes to investigate the lipidome, for both plasma and cardiac samples. Application of the three intensity-based filters (Figure 2.1) to 12,197 features in the full peak matrix from HILIC positive ion mode acquisition of plasma yielded 107 putative xenobiotic-related features. Similar filtering applied to the HILIC negative, RP-C_{18} positive and RP-C_{18} negative datasets isolated 7, 30 and 2 features, respectively (Table 2.1).

Table 2.1 Number of features in rat plasma and cardiac tissue untargeted metabolomics datasets before and after application of the three untargeted ADME/TK workflow filters. Separate full peak matrices per metabolomics assay were produced for sunitinib-exposed and corresponding biological control rat plasma samples, and KU60648-exposed and corresponding biological control rat plasma samples. Also, a single full peak matrix per metabolomics assay comprising data from both sunitinib-exposed and KU60648-exposed, and their corresponding biological control, rat cardiac tissue samples was produced. The number of putative xenobiotic-related features discovered by application of the three intensity-based filters for each xenobiotic are presented, and the number of features retained after removal of those features from the full peak matrices to generate the filtered (endogenous) peak matrices.

		HILIC positive	HILIC negative	RP-C_{18} positive	RP-C_{18} negative
Sunitinib exposed/biological control rat plasma	Number of features in full peak matrix	12,197	10,920	8,339	6,297
	Number of putative sunitinib-related features	104	7	30	2
	Number of features in filtered (endogenous) peak matrix	12,093	10,913	8,309	6,295
KU60648 exposed/biological control rat plasma	Number of features in full peak matrix	12,493	12,318	8,142	5,318
	Number of putative KU60648-related features	147	41	71	17
	Number of features in filtered (endogenous) peak matrix	12,346	12,277	8,071	5,301
Sunitinib exposed/KU60648 exposed/biological control rat cardiac tissue	Number of features in full peak matrix	8,202	7,585	11,832	6,273
	Number of putative sunitinib-related features	68	41	137	53
	Number of putative KU60648-related features	71	57	217	63
	Number of features in filtered (endogenous) peak matrix	8,063	7,487	11,478	6,157

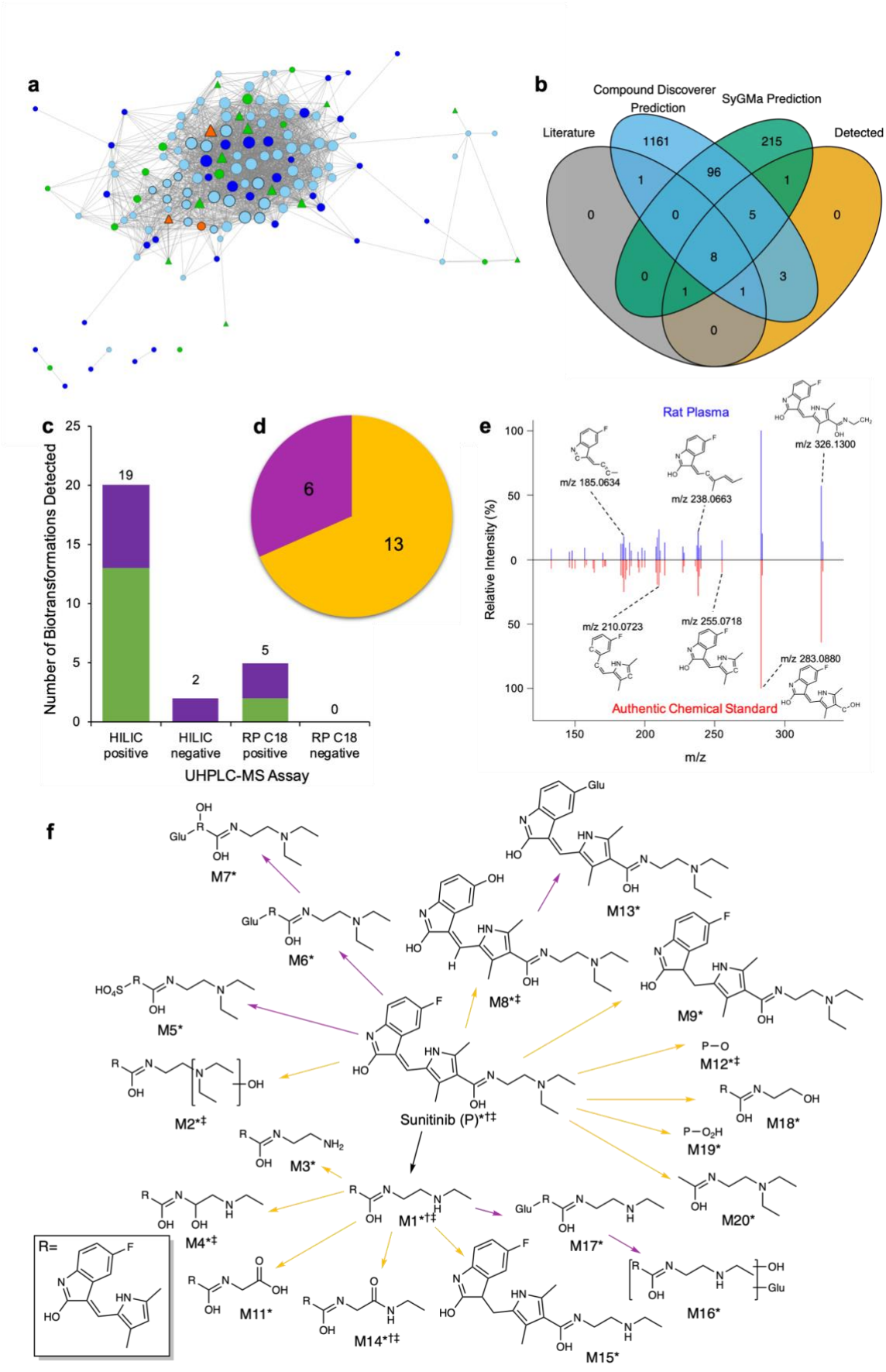


Figure 2.3 Application of the untargeted ADME/TK workflow to plasma of rats exposed to sunitinib.

a Pearson's correlation-based network of putative sunitinib-related features (n = 29). Edges present when Holm adjusted *p*-value <0.05 and R ≥0.75, node size is proportional to its degree of connectivity. Node colour highlights molecular ions ($[M+H]^+$/$[M-H]^-$) of sunitinib (orange), molecular ions of biotransformation products of sunitinib (green), alternate ion forms (adducts and isotopes) of sunitinib or biotransformation products (pale blue), and unannotated features (dark blue). Node shape distinguishes between annotations based on MS^1 data only (circle) vs. more confident annotations also based on MS/MS data (triangle). The high density of this network is implicit of the expected strong correlations between features representing a single compound and chemically related compounds. **b** The overlap of sunitinib biotransformation products reported in published literature (153), predicted by the "Generate Expected Compounds" tool of Compound Discoverer (Thermo Scientific), and by SyGMa (180), and detected by untargeted metabolomics. **c** Number of molecular formulae-annotated (putative annotation) (purple) and structurally annotated (MSI level 2) (green) biotransformation products of sunitinib detected by each UHPLC-MS metabolomics assay. The bars are annotated with the total number of biotransformation products detected by each UHPLC-MS metabolomics assay. **d** The proportion of Phase I (yellow) and Phase II (magenta) biotransformation products of sunitinib detected across all assays. **e** Representative comparison of measured MS/MS fragmentation spectra for sunitinib in rat plasma (top) vs authentic chemical standard of sunitinib (bottom) and the corresponding MetFrag-annotated structures of major peaks. **f** A biotransformation map of sunitinib showing the biotransformation products discovered in the rat plasma UHPLC-MS untargeted metabolomics dataset (data from four assays – HILIC positive (*)/negative (†), RP-C_{18} positive (‡)/negative (§)) by the untargeted ADME/TK workflow. The colour of the arrow denotes type of transformation– phase I (yellow) or phase II (magenta). Extracted ion chromatograms and MS/MS fragmentation spectra for these compounds are displayed in Figure A.1 and Figure A.2

Correlation analysis of the putative sunitinib-related features (data from the four assays combined) discovered the majority of features are highly associated (R ≥ 0.75, Pearson's), forming a dense cluster with representative features of sunitinib (Figure 2.3a). The observation of this co-responsive behaviour provides further confidence that those features are sunitinib-related. Features peripheral to the core cluster are likely not related to sunitinib, or represent biotransformation products who's rate of synthesis is limited by other factors beyond the availability of sunitinib (183).

A list of predicted biotransformation products of sunitinib was generated from literature sources (153) and two *in silico* prediction tools, comprising 1492 unique molecular formulae (Table A.2, Table eA.1). Of these, 109 were predicted by both prediction engines, 217 were uniquely predicted by SyGMa (180), and 1166 were predicted by only the "Generate Expected Compounds" tool in Compound

Discoverer (Thermo Scientific) (Figure 2.3b). Comparison with the metabolomics data revealed 19 of the predicted biotransformation products, plus sunitinib, could be annotated in the HILIC positive dataset (Figure A.1, Table A.2). Additionally, 2 and 5 products were annotated against the filtered HILIC negative and RP-C_{18} positive datasets, respectively, with some redundancy across datasets. No biotransformations were annotated within the RP-C_{18} negative dataset (Figure 2.3c). Taken together, 19 predicted biotransformation products of sunitinib were detected and annotated, comprising 13 Phase I and 6 Phase II transformations (Figure 2.3d). As such, the workflow successfully revealed all except one (M10, previously only reported in monkey faeces) of the 11 sunitinib biotransformations previously reported by Speed *et al.* (153) (Table A.2). Of note, the workflow discovered a further 9 biotransformations of sunitinib not reported in the gold-standard pharmacokinetics study using ^{14}C-radiolabelling (153) (M12-M20; Figure 2.3b).

The identity of features annotated as the molecular ions ($[M+H]^+$/$[M-H]^-$) of sunitinib were confirmed by comparison against an authentic chemical standard. *In silico* structural annotation of the experimentally acquired MS/MS spectra of sunitinib (from analysis of an authentic chemical standard and exposed rat plasma) using MetFrag (140) revealed that peaks at *m/z* 185, 210, 238, 255, 283 and 326 represent substructures of sunitinib (Figure 2.3e). To increase confidence in the putative biotransformation product annotations derived from accurate mass matching, and to elucidate structural information, the experimentally acquired MS/MS spectra of features corresponding to the molecular ions of putative sunitinib biotransformation products were structurally annotated using MetFrag (140). MS/MS spectra were acquired successfully for 12 of the 19 biotransformation products reported here (Figure A.2). The acquired spectra confirmed all 12 compounds were sunitinib-

related given the annotation of at least three of the substructures of sunitinib described above (Figure 2.3e, Table eA.2). Deviations of the MS/MS spectra of biotransformation products from that of sunitinib provided insights into the location of modifications, thus contributing to the structural elucidation of the previously unreported biotransformations. As such, I report the presence of sunitinib to MSI (120) and Schymanski (131) confidence level 1 (using accurate *m/z*, RT and MS/MS spectral match to authentic standard), 12 biotransformation products of sunitinib to MSI level 2 (Schymanski confidence level 2-3, i.e., probable or tentative structure, using accurate *m/z* and *in silico* structural annotation of MS/MS spectra), and 7 biotransformation products with putative molecular formulae (Schymanski confidence level 4, unequivocal molecular formula, using accurate *m/z*), in the plasma of rats exposed to sunitinib (Figure 2.3f, Table eA.2). Eight of the biotransformation products detected included N-dealkylation of sunitinib (M1, M3, M4, M11, M14, M15, M16, M17) while half are the result of sunitinib oxygenation (M2, M4, M7, M8, M11, M12, M14, M16, M18, M19). M9 and M15 are products of saturation of the exocyclic double bond of sunitinib and M1, respectively. M20 results from the hydrolysis of the cyclic head from the tail. Considering the Phase II biotransformations detected, glucuronidation (M6, M7, M13, M16, M17) appears as the preferred conjugation reaction, while only a single sulphate conjugate (M5) was detected.

Taken together, the untargeted ADME/TK approach has supported and furthered prior knowledge on the biotransformation of sunitinib in rats using a dataset primarily intended to provide insights into endogenous metabolic responses. The discovery of novel biotransformation products of sunitinib was enabled through the use of HRMS which offers enhanced sensitivity over [^{14}C]-labelling-based approaches.

The workflow was also applied to data acquired from analysis of cardiac tissue collected from the same rats. In total, 68, 41, 137 and 53 putative sunitinib-related features were isolated from the HILIC positive, HILIC negative, RP-C_{18} positive and RP-C_{18} negative datasets, respectively (Table 2.1). These lists included six predicted biotransformation products that were also detected in the plasma: M1, M2, M4, M6, M7 and M8 (Table eA.2). The detection of sunitinib in cardiac tissue of rats builds on previous findings that demonstrated distribution of sunitinib-related material to the heart following dosing with ^{14}C-sunitinib (153). Moreover, the distribution of sunitinib, M1, M2 and M9 to the liver, kidney and tumour tissue has been reported in syngeneic subcutaneous mouse tumour models by MALDI-MS (188); the application of the workflow has furthered the knowledge on the distribution of sunitinib biotransformation products by discovering the presence of Phase I (M1, M2, M4, M8 - de-ethylation, oxidation, oxidative defluorination) and Phase II (M6, M7- glucuronidation) biotransformation products in rat heart.

2.3.3 Untargeted workflow discovers fate of KU60648 in rat

To further demonstrate the ability of the developed workflow to discover novel biotransformation products of an exposure pharmaceutical from an untargeted metabolomics dataset, it was applied to a second experiment designed to investigate the endogenous metabolic perturbations induced in rats exposed to KU60648 (Table A.1).

Through application of the workflow, 147, 41, 71 and 17 putative KU60648-related features were extracted from datasets collected by four untargeted metabolomics assays: HLIIC positive, HILIC negative, RP-C_{18} positive and RP-C_{18} negative, respectively (Table 2.1). Exploratory correlation analysis highlighted the strong

association of these features across the exposed rat samples, adding confidence to their predicted relationship to KU60648 (Figure 2.4a).

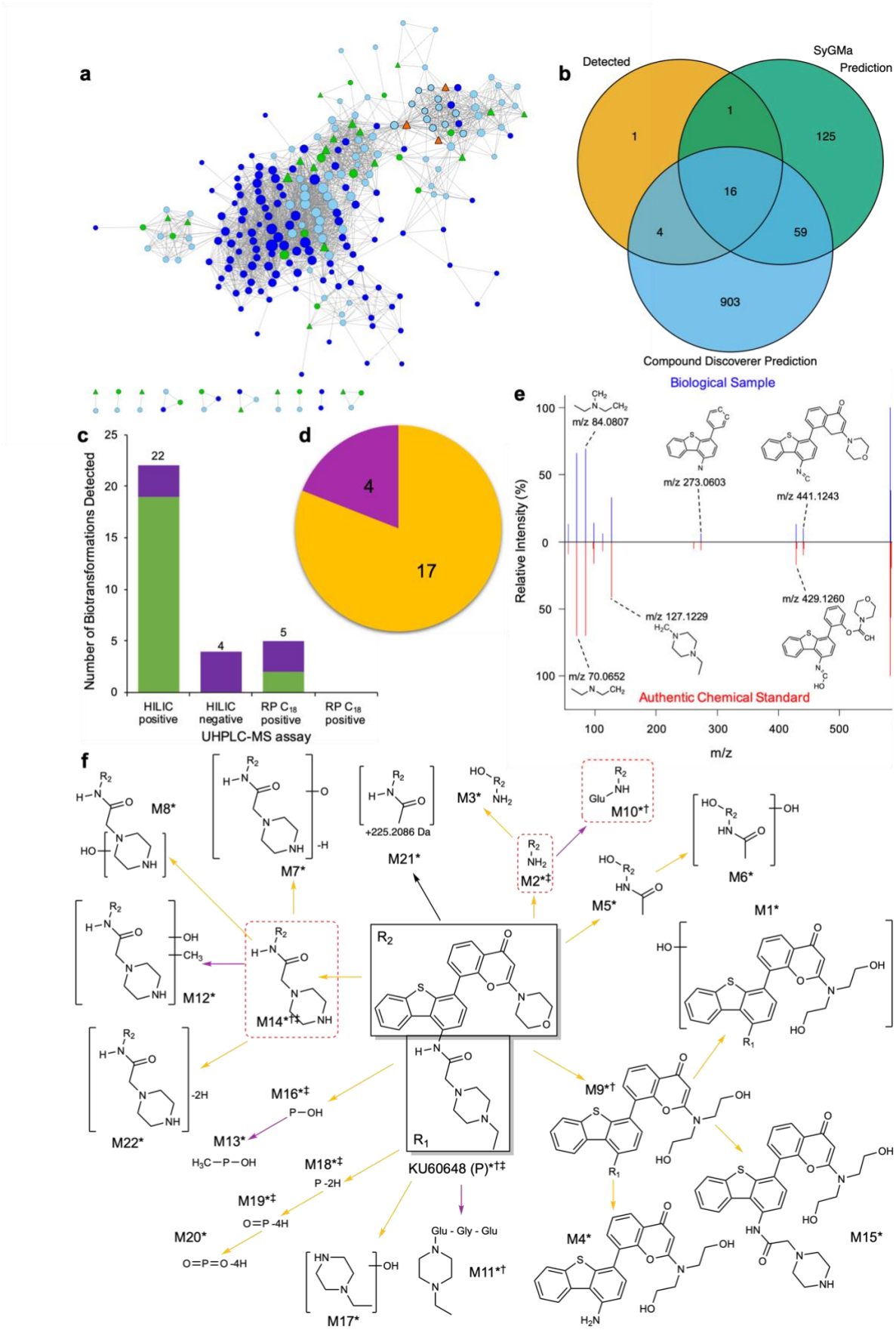


Figure 2.4 Application of the untargeted ADME/TK workflow to plasma of rats exposed to KU60648.

a Pearson's correlation-based network of putative KU60648-related features (n = 19). Edges present where Holm adjusted *p*-value <0.05 and R ≥0.75, size of node is proportional to its degree connectivity. Node colour highlights molecular ions ($[M+H]^+$/$[M-H]^-$) of KU60648 (orange), molecular ions of biotransformation products (green), alternate ion forms (isotopes and adducts) of KU60648 or biotransformation products (pale blue), and unannotated features (dark blue). Node shape distinguishes between annotations based MS^1 data only (circle) vs annotations using MS/MS data also (triangle). The high density of this network is implicit of the expected strong correlation between features representing a single compound and chemically related compounds. **b** The overlap of KU60648 biotransformation products predicted by the "Generate Expected Compounds" tool of Compound Discoverer (Thermo Scientific), and by SyGMa (180), and detected by untargeted metabolomics. **c** Number of molecular formulae-annotated (putative annotation) (purple) and structurally annotated (MSI level 2) (green) biotransformation products of KU60648 detected by each UHPLC-MS metabolomics assay. The bars are annotated with the total number of biotransformation products detected by each UHPLC-MS metabolomics assay. **d** The proportion of Phase I (yellow) and Phase II (magenta) biotransformation products of KU60648 detected across all assays. **e** Representative comparison of measured MS/MS fragmentation spectra for KU60648 in rat plasma (top) vs authentic chemical standard of KU60648 (bottom) and the corresponding MetFrag-annotated structures of major peaks. **f** A biotransformation map of KU60648 showing biotransformation products discovered in the rat plasma UHPLC-MS untargeted metabolomics dataset (data from four assays – HILIC positive (*)/negative (†), RP-C_{18} positive (‡)/negative (§)) by the untargeted workflow. The colour of the arrow denotes type of transformation– phase I (yellow) or phase II (magenta). Outlined (red dashed line) are the biotransformation products also detected in the cardiac tissue of exposed rats. Extracted ion chromatograms and MS/MS fragmentation spectra for these compounds are displayed in Figure A.3 and Figure A.4.

A list of 1108 predicted biotransformation products was generated by *in silico* predictions (Table eA.1) enabling the annotation of 20 biotransformation products from the lists of putative KU60648-related features, as well as KU60648 itself. One further biotransformation product was detected that was not predicted by either SyGMa (180) or the "Generate Expected Compounds" tool of Compound Discoverer (Thermo Scientific) (Figure 2.4b). The majority of biotransformation products were detected by the HILIC positive assay (Figure 2.4c; Figure A.3). Furthermore, 17 of the detected biotransformation products were Phase I modifications of KU60648 and 4 were Phase II modifications (Figure 2.4d), while the biotransformation step(s) that result in the formation of M21 was not elucidated. The identity of features corresponding to KU60648 itself were confirmed by comparison against the MS/MS fragmentation spectra of an authentic chemical standard (Figure 2.4e). The MS/MS spectra of KU60648 (from analysis of an authentic chemical standard and exposed

rat plasma) were structurally-annotated using MetFrag (140), discovering that peaks at *m/z* 70, 84, 127, 273, 429 and 441 represent major substructures of KU60648. Of the 22 biotransformation products annotated using accurate mass measurements, MS/MS spectra were successfully acquired for 14 and used to confirm the presence of KU60648 substructure(s) and elucidate sites of metabolism by *in silico* structural annotation using MetFrag (140) (Figure 2.4f, Table eA.3, Figure A.4). This included the four compounds (M18, M19, M21, M22) from the list of measured putative KU60648-related features that were not predicted *in silico*. Thus, applying the untargeted ADME/TK workflow, I report the presence of KU60648 to MSI and Schymanski confidence level 1 (using accurate *m/z*, RT and MS/MS spectral match to authentic standard), and discovery of 14 biotransformation products to MSI level 2 (Schymanski confidence levels 2-3, i.e., probable or tentative structure, using accurate *m/z* and *in silico* structural annotation of MS/MS spectra) and a further 8 biotransformation products with putative molecular formulae (Schymanski confidence level 4, using accurate *m/z*) in the plasma of rats exposed to KU60648 (Figure 2.4f, Table eA.3).

In summary, this is the first published report on the biotransformation of KU60648. The discoveries made through the untargeted ADME/TK workflow evidence biotransformation of KU60648 in rats by de-ethylation, oxidation, dehydrogenation, methylation and glucuronide and glycine conjugations.

The workflow was also applied to untargeted UHPLC-MS metabolomics data collected from cardiac tissue samples taken from the same KU60648-exposed rats, to demonstrate its capability to discover fingerprints of pharmaceutical biotransformation at the site of toxicity. Following data filtering, three of the 22 biotransformations detected in plasma were also detected in cardiac tissue (Figure

2.4f, Table eA.3). These biotransformations include Phase 1 modifications, amide hydrolysis (M2, M10) and de-ethylation (M14), and a Phase II modification, glucuronide conjugation (M10). This demonstrated capability to examine the distribution of a pharmaceutical and its biotransformation products to a site of toxicity could, for example, improve the ability to decipher the causative agent of toxicity by providing compound-specific evidence of tissue exposure.

2.3.4 Temporally tracking pharmaceuticals and biotransformation products

In addition to providing qualitative data regarding the presence of a xenobiotic and its biotransformation products, untargeted metabolomics measurements also yield relative amounts of those compounds. For the experimental design reported here, this enables changes in relative levels of each pharmaceutical and its biotransformation products in rat plasma to be tracked over time. Additionally, comparisons of relative amounts of the pharmaceuticals (and their biotransformation products) between individual test subjects allows judgement on the inter-individual variability in their disposition (Table A.1).

First, the reliability of the metabolomics UHPLC-MS peak intensity measurements of the parent substances, made while simultaneously measuring thousands of endogenous features, were verified by comparison to conventional quantification of the pharmaceuticals using single compound targeted LC-MS/MS. A strong correlation of the intensities of sunitinib measured in the HILIC positive metabolomics assay with those from the fully quantitative approach, for plasma samples collected on day 15 (samples for metabolomics taken 4-hours after targeted measurements, from the same individuals), was observed ($R = 0.90$; Figure 2.5a). High correlation coefficients were also calculated for the HILIC negative and RP-C_{18}

positive assays relative to the conventional targeted approach (Figure 2.5b-c). Comparable analysis using intensity measurements from untargeted metabolomics, and quantitative measurements from targeted LC-MS/MS of KU60648 provided further evidence of the reliability of intensity data from untargeted metabolomics (Figure 2.5d-f).

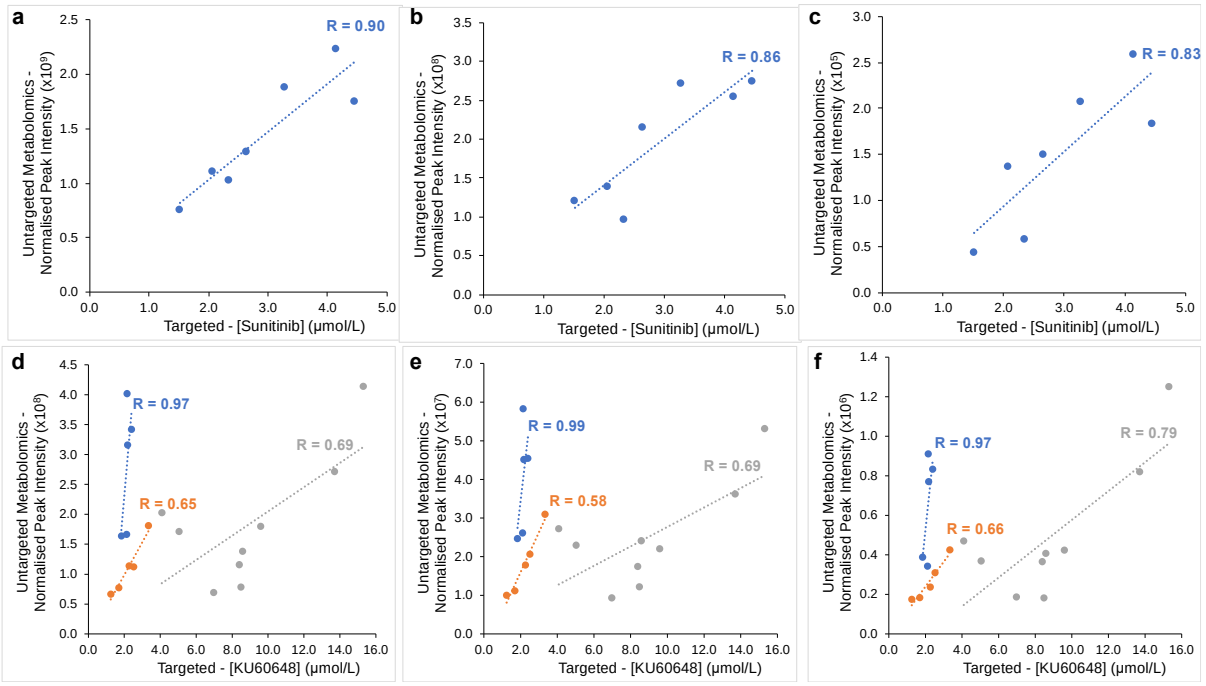


Figure 2.5 Reliability of untargeted metabolomics relative peak intensity measurements of pharmaceuticals in rat plasma.
Relationship between UHPLC-MS untargeted metabolomics peak intensity measurements of **a-c** sunitinib and **d-f** KU60648, measured by **a, d** HILIC positive, **b, e** HILIC negative and **c, f** RP-C_{18} positive assay, and the absolute quantification of **a-c** sunitinib and **d-f** KU60648 using conventional targeted LC-MS/MS. For **a-c** sunitinib measurements, rat plasma was sampled 4-hours later on day 15 (blue) for UHPLC-MS untargeted metabolomics compared with plasma for targeted LC-MS/MS. For **d-f** KU60648 measurements, rat plasma for both analyses was sampled at the same time on day 1 (orange). Rat plasma for UHPLC-MS untargeted metabolomics was sampled 20-hours earlier, and 20 hrs later on days 2 (blue) and 4 (grey), respectively, compared to plasma for targeted LC-MS/MS analysis. Pearson correlation coefficients (R) of n = 5 (day 1 and day 2), n = 8 (day 4) or n = 7 (day 15) measurements from separate animals are displayed.

The metabolomics measurements – originally intended to investigate the endogenous biochemical changes over time – were used to track the relative temporal changes in sunitinib systemic exposure over the 15- and 4-day studies, respectively (Figure 2.6a). Sunitinib intensities increase towards steady state with

repeated daily dosing between days 1 and 4. At day 15, 28-hours after the last dose on day 14, average levels of sunitinib are significantly two-fold less than those measured 4-hours post-dose on day 8, providing evidence of effective elimination upon completion of dosing. Comparison of relative sunitinib levels across individual rats revealed greatest variability at the points of greatest systemic exposure (days 4 and 8; Figure 2.6a).

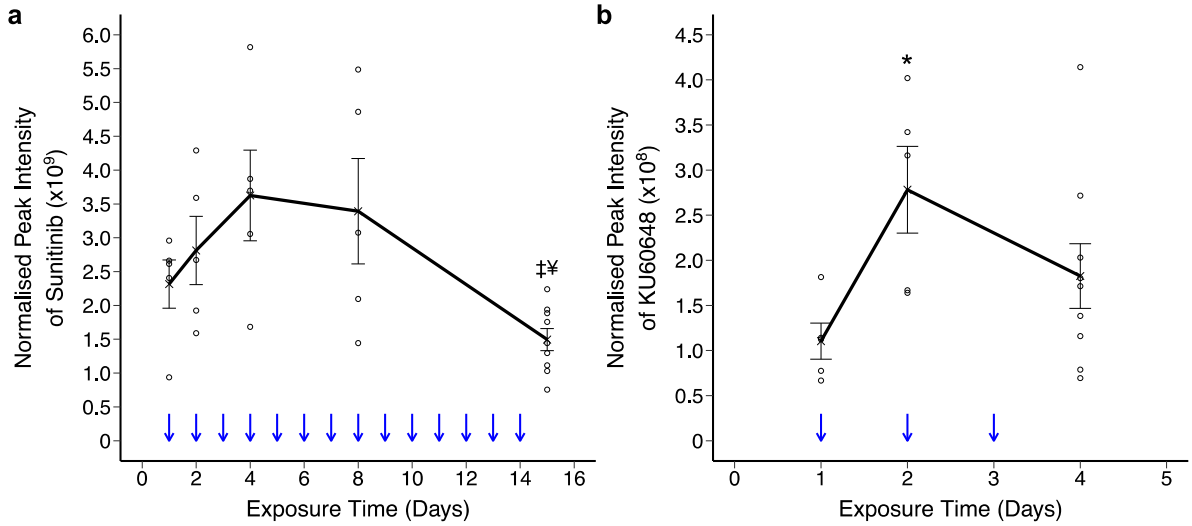


Figure 2.6 Temporal distribution of pharmaceuticals in plasma of exposed rats.
Mean peak intensity (cross) of **a** sunitinib over the duration of the 15-day study and **b** KU60648 over the duration of the 4-day study, as measured by UHPLC-MS untargeted metabolomics. **a** N = 5 individual animals on days 1, 2, 4, and 8; n = 9 individual animals on day 15, **b** n = 5 individual animals on days 1 and 2; n = 9 individual animals on day 4. Individual data points are also displayed open circle. Error bars show standard error. Arrows indicate time of dosing. Statistical analysis was conducted by one-way ANOVA followed by Tukey's post-hoc test (*p <0.05 vs. day 1, ‡p <0.05 vs. day 4, ¥p <0.05 vs. day 8).

Similar analyses were conducted for KU60648 over the course of the 4-day rat exposure study (Figure 2.6b). Significantly greater systemic exposure of KU60648 is achieved after a second dose. Meanwhile, levels measured in the plasma on day 4 indicate some elimination by 24-hours post-dose. The largest inter-individual variation is observed on day 2, when systemic levels of KU60648 are at their highest.

The untargeted ADME/TK workflow also provides peak intensity measurements for the discovered biotransformation products, representing additional information that is not measured in conventional toxicokinetic studies. K-means clustering of the temporal responses of sunitinib and its biotransformation products (Figure 2.3f) discovered commonality between the temporal variation in the systemic exposure of sunitinib and the responses of the products of its simplest routes of metabolism: M1 (de-ethylation), M2 (hydroxylation) and M9 (saturation) ((Figure 2.3f; cluster 2, Figure 2.7). These compounds display significantly greater systemic exposure on days 2, 4 and 8 compared with day 1. A significant drop in levels is observed on day 15 to levels comparable to day 1, evidencing effective elimination once dosing is ceased. Five other clusters of biotransformation products diverge from the behaviour of the parent xenobiotic. Cluster 1 (M11, M15, M17 and M19) and cluster 6 (M3, M4, M6, M12, M14 and M18) show similar trends to cluster 2, with a significant increase from day 1 levels observed on days 4 and 8, and just day 8, respectively. The majority of detected biotransformation products resulting from Phase II conjugation reactions, excluding M6 and M17, do not show any significant changes in systemic levels across the measured time points (clusters 3, 4 & 5). M8 (product of oxidative de-fluorination) and M20 (product of parent cleavage), also in cluster 5, displayed similar trends (Figure 2.3f; Figure 2.7). This suggests the steady state of these compounds is reached following the initial dose.

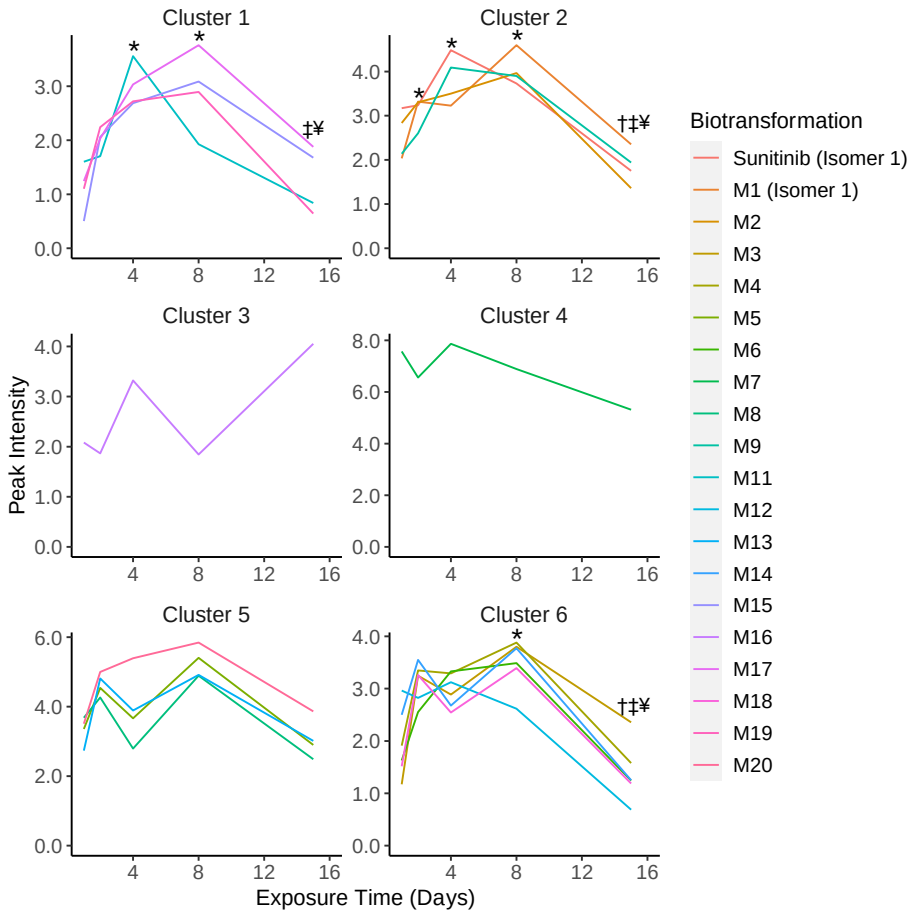


Figure 2.7 Temporal distribution of sunitinib and its biotransformation products in plasma of exposed rats.
Median peak intensities, measured by UHPLC-MS untargeted metabolomics and scaled by unit variance, of sunitinib and its biotransformation products over the duration of the 15-day exposure study, clustered by an unsupervised *k*-means approach (*k* = 6, optimal value determined by the Elbow Method). Cluster 1: M11, M15, M17, and M19. Cluster 2: sunitinib, M1, M2 and M9. Cluster 3: M16. Cluster 4: M7. Cluster 5: M5, M8, M13 and M20. Cluster 6: M3, M4, M6, M12, M14, and M18. Statistical analysis was conducted by one-way ANOVA followed by Tukey's post-hoc test (* p <0.05 vs. day 1, $^{\dagger}p$ <0.05 vs. day 2, $^{\ddagger}p$ <0.05 vs. day 4, $^{¥}p$ <0.05 vs. day 8). N = 5 individual animals on days 1, 2, 4, and 8; n = 9 individual animals on day 15.

Temporal responses of the biotransformation products of KU60648 discovered in the plasma of exposed rats were also investigated. K-means clustering revealed six clusters of responses (Figure 2.8). The responses of M4, M6, M9, M11, M18 and M19 were found to be most similar to that of KU60648, forming cluster 2, while five other clusters of biotransformation products diverge to varying degrees from the behaviour of the parent.

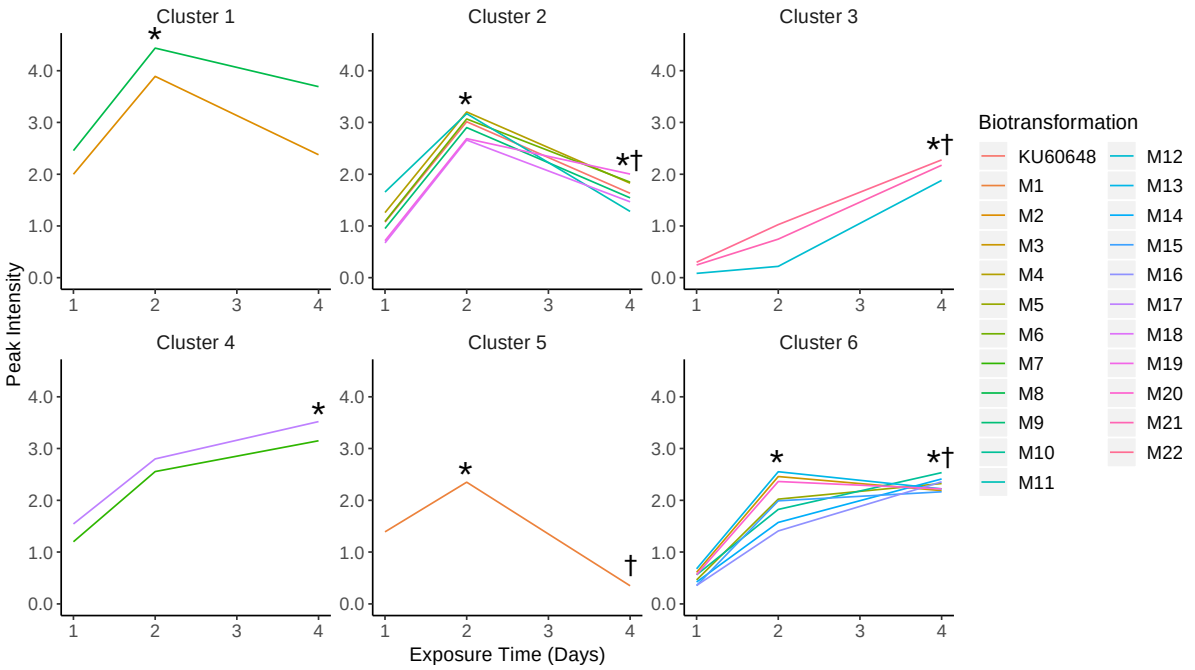


Figure 2.8 Temporal distributions of KU60648 and its biotransformation products in plasma of exposed rats.
Median peak intensities, measured by UHPLC-MS untargeted metabolomics and scaled by unit-variance, of KU60648 and its biotransformation products over the duration of the 4-day study, clustered by unsupervised *k*-means clustering (k = 6, optimal value determined by the Elbow Method). Statistical analysis was conducted by one-way ANOVA followed by Tukey's post-hoc test (* p <0.05 vs. day 1, † p <0.05 vs. day 2, ‡ p <0.05 vs. day 4. N = 5 separate animals on days 1 and 2; n = 9 separate animals on day 4. KU60648 is clustered with 6 of its biotransformation products: M4, M6, M9, M11, M18 and M19 (cluster 2). The average response of these compounds shows a significant and large increase (2.8-fold) in systemic levels between days 1 and 2 followed by a slight, but significant, decline by day 4, although levels remain significantly 1.5-fold greater than those measured on day 1. Cluster 1 (M2 and M8) shows a similar temporal trend to Cluster 2, however the increase between day 1 and 2 is to a lesser extent (1.8-fold compared to 2.8-fold). Cluster 3 (M12, M21, and M22) shows consistent accumulation throughout the experiment. The accumulation is significant by day 4 where levels were 9-fold greater than those measured on day 1. Cluster 4 (M7 and M17) has a similar response to Cluster 3, with significant change occurring by day 4. However, this accumulation is lesser, with day 4 levels 2.5-fold greater than those measured on day 1. M1 does not cluster with any other KU60648 biotransformation products (cluster 5). Its systemic levels significantly increase between days 1 and 2 to levels 1.7-fold greater but returns to levels comparable to day 1 by day 4. Cluster 6 (M3, M5, M10, M13, M14, M15, M16 and M20) systemic levels are significantly 4-fold greater on day 2 than on day 1, with a further 2-fold increase by day 4.

Time-resolved measurements of relative systemic exposure of a pharmaceutical made by the same analysis, within the same samples, as the endogenous response, such as those demonstrated here, could, by association, help to explain the temporal trends detected in toxicological response(s) of the test subjects. Thus, through application of our workflow, untargeted metabolomics offers an effective route for

discovering dose-response associations. Furthermore, analysis of the time-resolved responses of the biotransformation products revealed clusters of co-responsiveness. Such analysis of temporal changes in relative systemic levels of biotransformation products is not usually investigated. However, it provides potentially important insight into the fate of biotransformation products, some of which may possess efficacious or toxic activities, which could aid explanation of temporal toxicological responses.

2.3.5 Lipid responses associate with internal dose

The capability of the untargeted ADME/TK workflow to reveal the identities and relative levels of xenobiotic-related features from an untargeted metabolomics dataset may be beneficial to the analysis of the endogenous responses. First, by accurately removing the xenobiotic-related features from the metabolomics dataset, a more reliable multivariate statistical analysis of the endogenous data can be achieved. This is demonstrated by PCA (Figure 2.9). Where putative sunitinib-related features (Table 2.1) are not removed from the metabolomics dataset, these features are primarily responsible for the separation of exposed plasma samples from biological controls along PC1, as evidenced by the loadings plots. This influence of exposure substance-related features leads to the false conclusion of a strong perturbation of the plasma metabolome in response to sunitinib on day 1 (Figure 2.9a). At day 15, although sunitinib-related features have the highest magnitude loadings, separation of sample classes remains along PC1 after their removal, indicating a strong perturbation of the endogenous fraction of the detected plasma metabolome as a consequence of sunitinib exposure (Figure 2.9e). Similar analysis of day 2, day 4 and day 8 measurements reveals a trend of increasing perturbation over time, which is only discernible when sunitinib-related features are excluded (Figure 2.9b-d). In summary, xenobiotic-related features can be considered

confounding factors in the analysis of endogenous biochemical responses so must be excluded from the dataset prior to analysis.

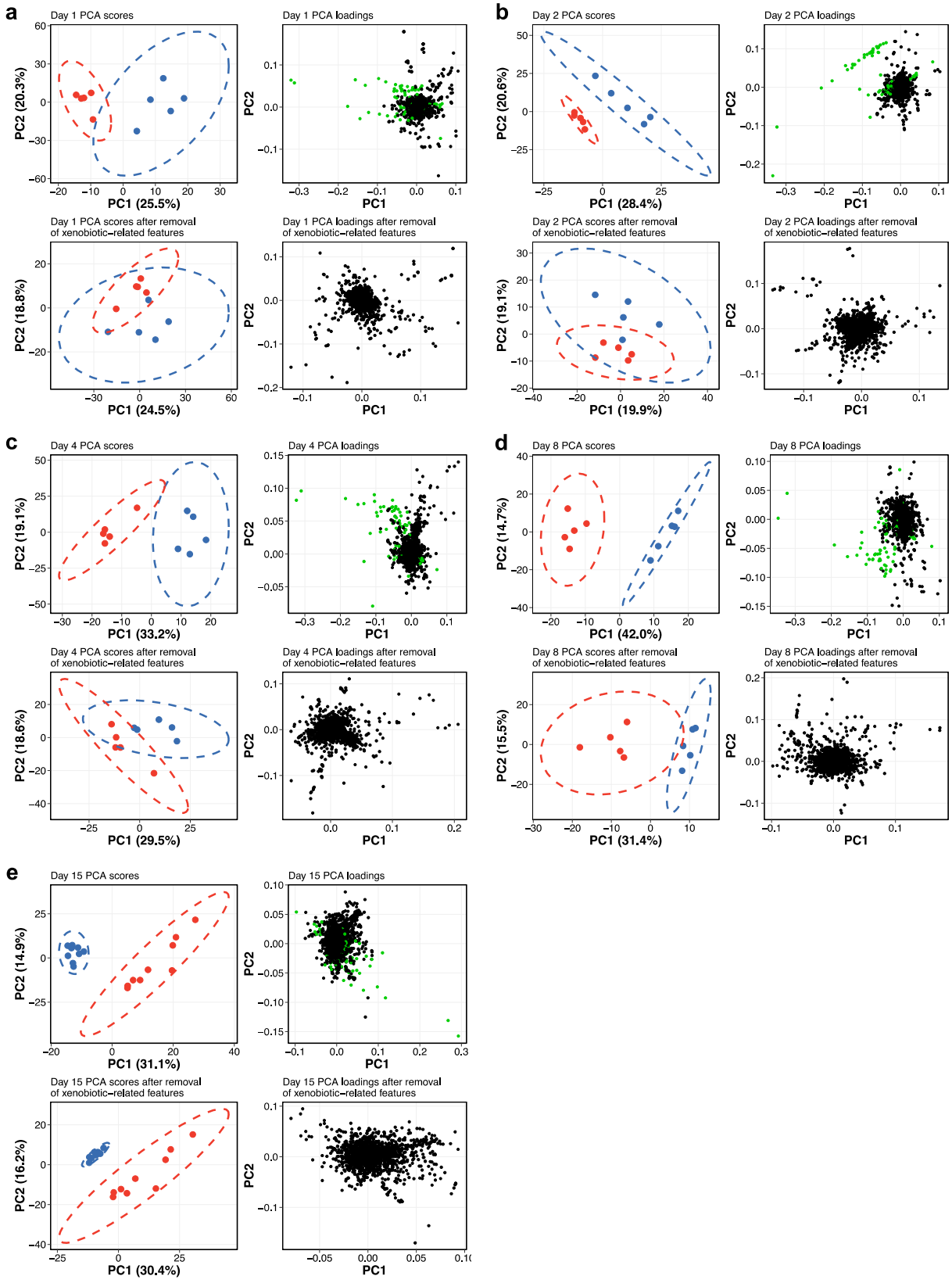


Figure 2.9 Sunitinib-induced perturbation of the plasma metabolome of rats.

PCA scores (left) and loadings (right) plots of data acquired from plasma of rats exposed to sunitinib (red) and biological control rats (blue), after **a** 1-day, **b** 2-days, **c** 4-days, **d** 8-days and **e** 15-days, measured by HILIC UHPLC-MS in positive ion mode before (top) and after (bottom) removal of putative sunitinib-related features (green in the loadings plots).

The trend of an increasing magnitude of perturbation to the endo-metabolome was also revealed by univariate statistical analyses conducted on the filtered (endogenous) peak matrices (Table 2.1). Specifically, a total of 40, 121, 131, 463, and 3494 features were significantly perturbed across the four assays on day 1, 2, 4, 8, and 15, respectively (Table 2.2). Changes are observed across a broad array of metabolite and lipid classes (Table eA.4).

Table 2.2 Number of significantly changing features in plasma and cardiac tissue of rats exposed to sunitinib compared to biological controls.
Reported are the number of features per time point (plasma only) and analytical assay with significantly different intensities in exposed compared to time-matched biological control samples. Significance was evaluated using two-tailed Student's *t*-test with FDR correction (N = 5 separate animals for plasma days 1, 2, 4 and 8 and cardiac tissue, N = 9 separate animals for plasma day 15). A significant difference was defined as *q*-value <0.1.

Assay	Number of significant features					
	Day 1	Day 2	Day 4	Day 8	Day 15	Cardiac tissue
HILIC positive	25	38	9	109	524	8
HILIC negative	3	81	1	52	518	69
RP-C_{18} positive	12	2	38	75	1389	222
RP-C_{18} negative	0	0	83	227	1063	156

PCA and univariate analyses conducted on the cardiac filtered (endogenous) peak matrices (Table 2.1) indicate a distinct perturbation of the cardiac metabolome by sunitinib (Figure 2.10). A total of 455 features were significantly perturbed across the four assays (Table 2.2) with effects on the lipidome dominating, including changes to ceramides, phospholipids, sphingolipids and di- and tri-acylglycerols (Table eA.5). This is consistent with the known association of perturbed lipid uptake and metabolism with cardiomyopathy (189, 190).

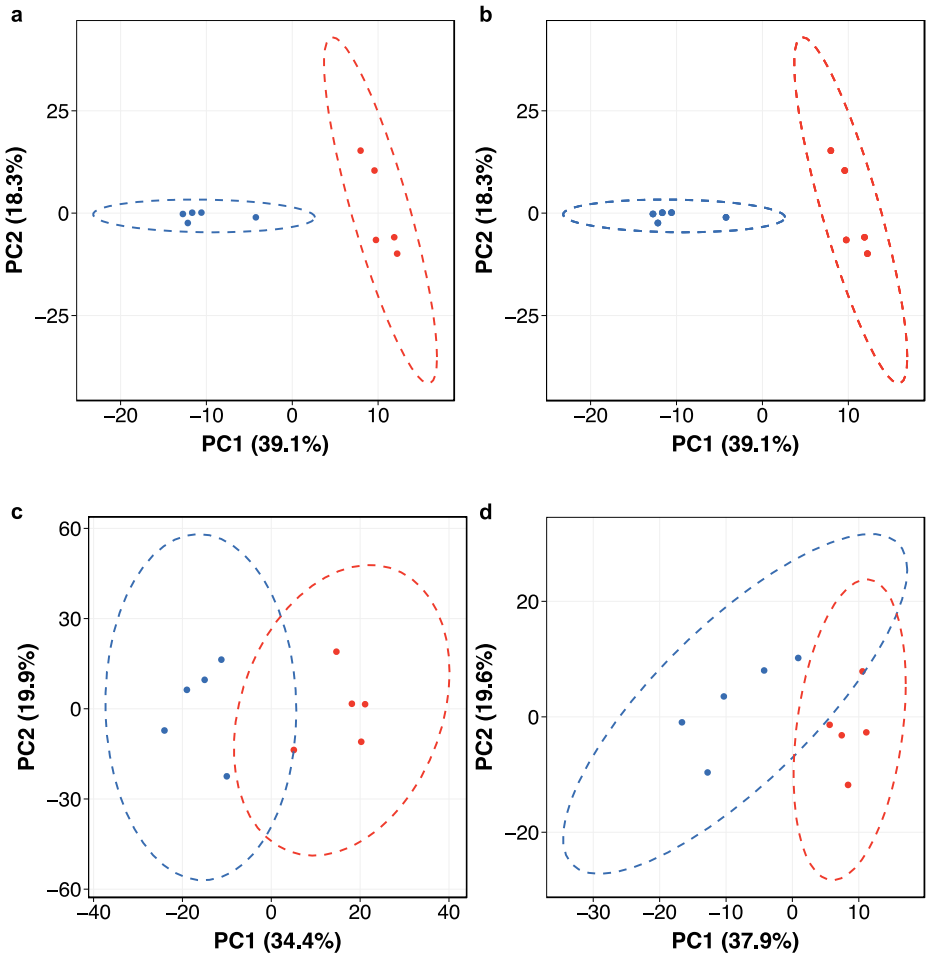


Figure 2.10 Sunitinib-induced perturbation of the cardiac tissue metabolome of rats. PCA scores plots of cardiac tissue samples from rats exposed to sunitinib (red) compared to biological control rats (blue), as measured by four untargeted metabolomics assays: **a** HILIC UHPLC-MS in positive ion mode, **b** HILIC UHPLC-MS in negative ion mode, **c** RP-C_{18} UHPLC-MS in positive ion mode and **d** RP-C_{18} UHPLC-MS in negative ion mode. Analysis was carried out on the endogenous data matrices following removal of putative sunitinib-related features.

Inter-individual differences in internal xenobiotic dose should in principle relate strongly to the magnitude of change of the endogenous metabolome, thereby offering an effective route for discovering xenobiotic-induced perturbations. To this end, measurements of the relative levels of pharmaceutical were used to explore the endogenous responses, i.e., to attempt to discover direct associations between exposure substance levels at a target site and endogenous lipids. This would not be possible with nominal dose values which do not account for inter-individual differences in xenobiotic bioavailability and distribution. Specifically, correlation

analysis revealed a dense network of direct associations between sunitinib levels and subsets of multiple lipid classes in the cardiac tissue of exposed rats (Figure 2.11, Table eA.6).

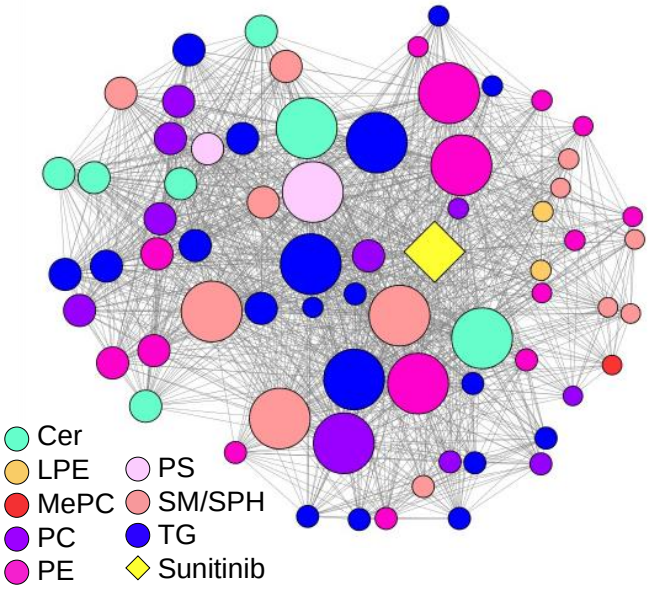


Figure 2.11 Association of internal relative dose of sunitinib with the cardiac tissue lipidome of exposed rats.
Correlation network of sunitinib and MSI level 2 annotated lipids: ceramides (Cer), lysophosphatidylethanolamines (LPE), methyl phosphatidylcholine (MePC), phosphatidylcholines (PC), phosphatidylethanolamines (PE), phosphatidylserines (PS), sphingomyelins (SM/SPH) and triacylglycerols (TG), in cardiac tissue of rats exposed to sunitinib (N=5). Node size is proportional to its degree of connectivity. Edges represent significant Spearman's correlation (p <0.05 and, $|\rho| \geq 0.9$) between compounds. All nodes displayed are significantly correlated to sunitinib.

Nine sphingomyelins negatively correlated with the relative internal levels of sunitinib; over-representation analysis confirming that this lipid class is significantly overrepresented (p <0.1) amongst those lipids whose responses correlate with levels of sunitinib (Table 2.3). This finding is supported by the conventional statistical analyses of the endogenous cardiac data for which seven sphingomyelins decreased significantly upon exposure, with a mean fold-change of 0.71 (Table eA.5). These analyses have provided the first direct evidence of a role for sphingomyelins in sunitinib-induced cardiotoxicity. This is accordant with previous reports of a decrease in sphingomyelin in isolated primary rat cardiomyocytes exposed to doxorubicin, a

model cardiotoxin, concurrently with an increase in ceramide levels (191). Pathologically, sphingomyelins, through their catabolism to ceramides, have been linked to the induction of apoptosis (190, 192).

Related to this discovery, levels of seven sphingomyelins were significantly higher in the plasma of exposed rats compared to biological controls on day 15 (Table eA.4). Of note, four of those overlap with the nine that negatively correlated to sunitinib levels at the site of toxicity (Figure 2.12). Assuming circulating levels of sphingomyelins are a direct consequence of cardiac changes, these discoveries suggest sphingomyelins could be successfully employed as biomarkers for drug-induced cardiotoxicity. Supporting this, previous studies have reported increases in circulating levels of sphingomyelins following myocardial infarction, and demonstrated a direct correlation with clinical biomarkers of cardiac pathologies, including high-sensitive-troponin and C-reactive protein, and lower left ventricular ejection fraction (LVEF) (193, 194).

Table 2.3 Over-representation analysis of lipids significantly correlated to sunitinib levels in the cardiac tissue of exposed rats.
The number of lipid species per lipid class annotated to MSI level 2 (Reference List Count), and number of those lipids significantly correlated (Spearman's, p <0.05) to sunitinib levels in exposed samples (network count) are reported. Expected network count refers to the number of species per lipid class expected to be significantly correlated to sunitinib levels in exposed samples in the case of no lipid class enrichment. The fold enrichment of lipid classes significantly correlated (Spearman's, p <0.05) to sunitinib levels in exposed samples was calculated as the ratio of network count to expected network count, and the significance assessed by a one-sided Fisher's Exact test (p-value).

Lipid Class	Reference List Count	Network Count	Expected Network Count	Fold Enrichment	*p*-value
Cer	28	7	3.94	1.78	0.064
LPE	3	2	0.42	4.76	0.053
MePC	6	1	0.84	1.19	0.595
PC	107	10	15.1	0.66	0.828
PE	101	15	14.2	1.06	0.174
PS	7	2	0.99	2.02	0.252
SM	43	11	6.05	1.82	0.014
SPH	1	1	0.14	7.14	0.140
TG	142	19	20.0	0.95	0.174

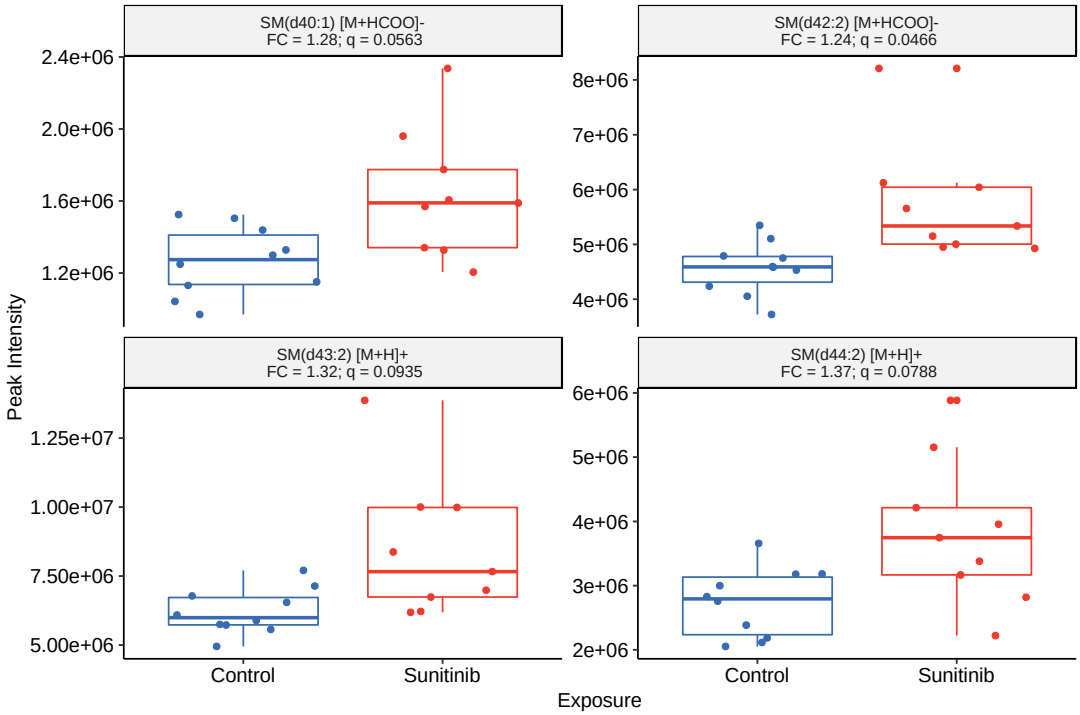


Figure 2.12 Four sphingomyelins associated with sunitinib levels at the site of toxicity have significantly increased levels in plasma of exposed rats.
Box plots show significantly increased plasma levels of four sphingomyelins found to be associated with sunitinib levels at the site of toxicity, in rats exposed to sunitinib (red) for 15 days, compared to time-matched biological controls (blue). Fold change and *q*-values (FDR-corrected *p*-values calculated by Student's *t*-test) are displayed.

A significant perturbation of the plasma and cardiac metabolome of rats exposed to KU60648 was also observed following removal of putative KU60648-related features (Table 2.1, Figure 2.13, Figure 2.14, Table 2.4). In the plasma, a total of 5771 and 5696 features were significantly perturbed across the four assays on days 2 and 4, respectively, indicating extreme effects of KU60648 exposure (Table 2.4, Table eA.7). At the site of toxicity (cardiac tissue), perturbation of lipids dominated the response to KU60648 exposure (Table 2.4, Table eA.8).

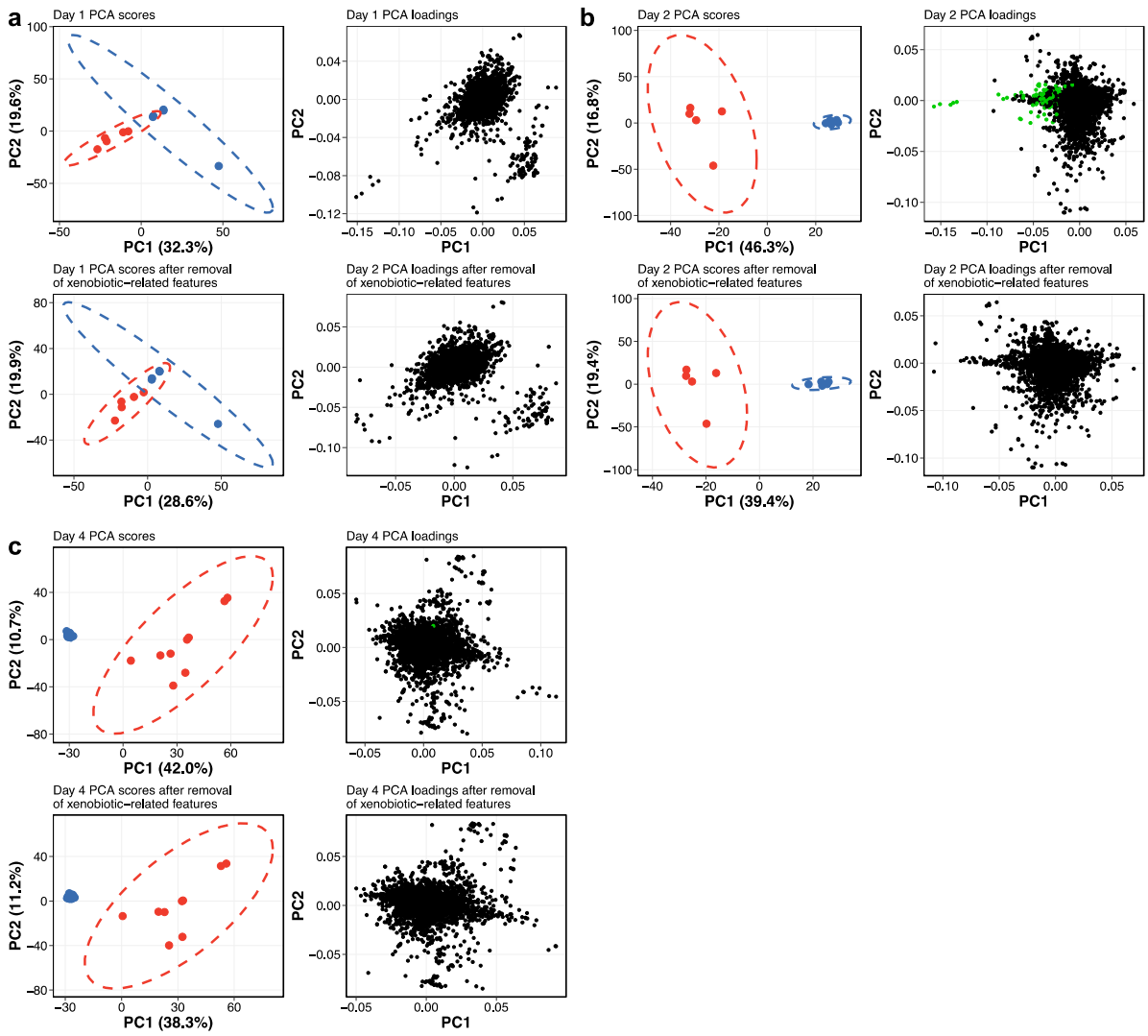


Figure 2.13 KU60648-induced perturbation of the plasma metabolome of rats.
PCA scores and loadings plots of data acquired from plasma of rats exposed to KU60648 (red) and biological control rats (blue), after **a** 1-day, **b** 2-days and **c** 4-days, measured by HILIC UHPLC-MS in positive ion mode before and after removal of putative sunitinib-related features (green in the loadings plots).

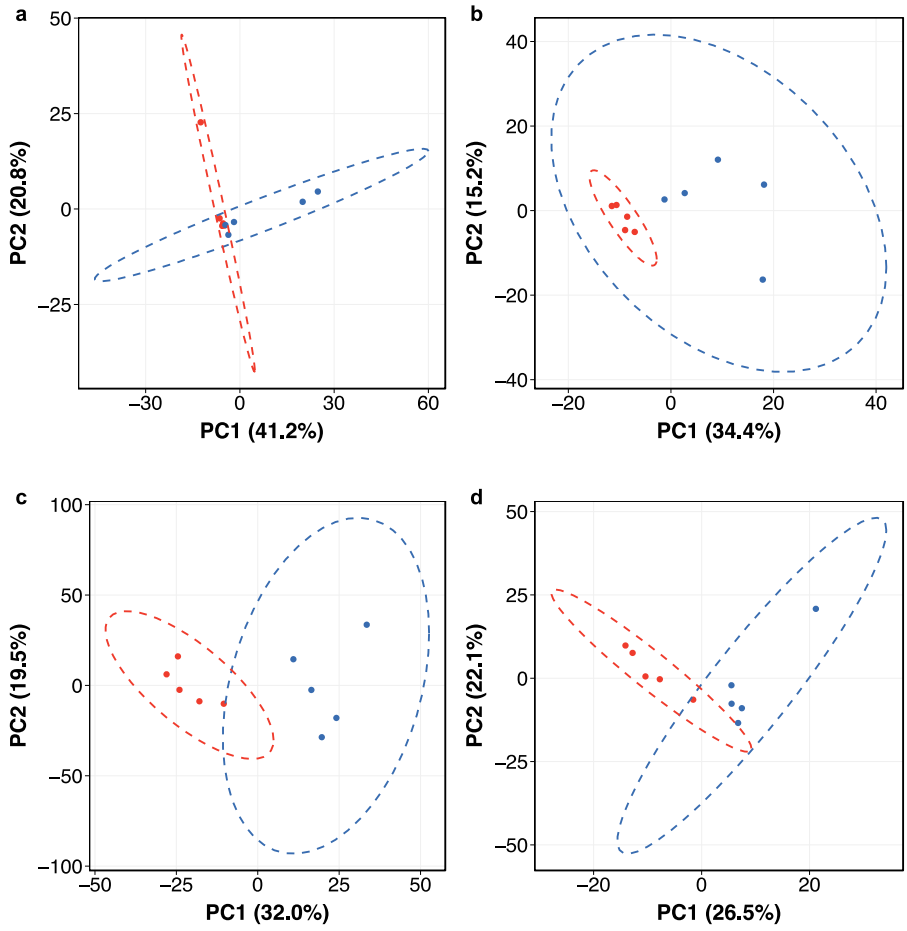


Figure 2.14 KU60648-induced perturbation of the cardiac tissue metabolome of rats.
PCA scores plots of cardiac tissue samples from rats exposed to KU60648 (red) compared to biological control rats (blue), as measured by 4 untargeted metabolomics assays: **a** HILIC UHPLC-MS in positive ion mode, **b** HILIC UHPLC-MS in negative ion mode, **c** RP-C_{18} UHPLC-MS in positive ion mode and **d** RP-C_{18} UHPLC-MS in negative ion mode. Analysis was carried out on the endogenous data matrices following removal of putative KU60648-related features.

Table 2.4 Number of significantly changing features in plasma and cardiac tissue of rats exposed to KU60648 compared to biological controls.
Reported are the number of features per time point (plasma only) and analytical assay with significantly different intensities in exposed compared to time-matched biological control samples. Significance was evaluated using two-tailed Student's *t*-test with FDR correction (N = 5 separate animals for plasma days 1 and 2 and cardiac tissue, N = 9 separate animals for plasma day 4). A significant difference was defined as *q*-value <0.1.

Assay	Number of significant features			
	Day 1	Day 2	Day 4	Cardiac tissue
HILIC positive	137	1429	2420	26
HILIC negative	91	1000	2368	81
RP-C_{18} positive	161	2244	2920	944
RP-C_{18} negative	1	1098	2014	496

A correlation-based approach was used to seek associations between levels of KU60648 in the cardiac tissues of exposed rats and the responses of MSI level 2 annotated lipids in the same samples (Figure 2.15). Significant correlations were observed, mostly for acylcarnitines, phosphatidylcholines and triacylglycerols (Table eA.9). Direct association of these lipids to KU60648 levels explains the inter-individual variation of their relative levels amongst exposed samples.

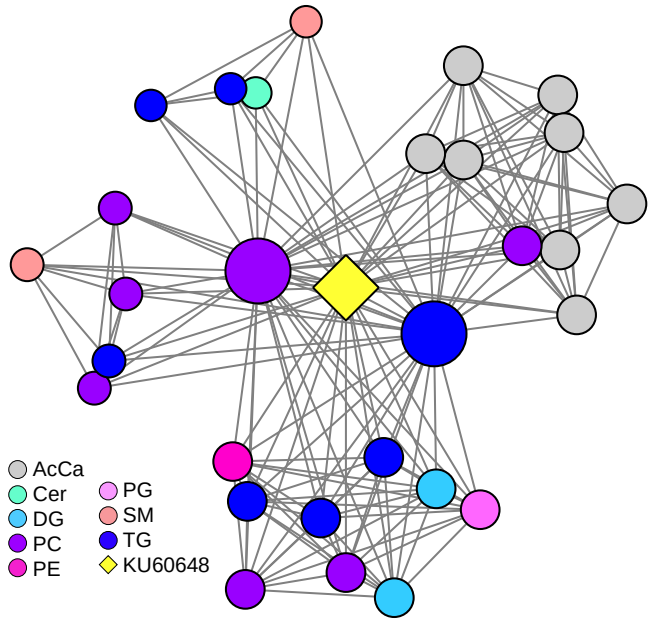


Figure 2.15 Association of internal relative dose of KU60648 with the cardiac tissue lipidome of exposed rats.
Correlation network of KU60648 and MSI level 2 annotated lipids: acylcarnitines (AcCa), ceramides (Cer), diacylglycerols (DG), phosphatidylcholines (PC), phosphatidylethanolamines (PE), phosphatidylglycerol (PG), sphingomyelins (SM) and triacylglycerols (TG), in cardiac tissue of rats exposed to KU60648 (N = 5). Node size is proportional to its degree of connectivity. Edges represent significant Spearman's correlation (*p*-value <0.05 and, |ρ| ≥0.9) between compounds. All nodes displayed are significantly correlated to KU60648.

Over-representation analysis identified the negative correlation of a subset of eight acylcarnitines to relative amounts of KU60648 within the cardiac tissue of exposed rats as significant (Table 2.5). Of note, conventional univariate analysis (*t*-test) of this dataset did not reveal acylcarnitines in the cardiac tissue of exposed rats as significantly different compared to controls. This is likely due to the large inter-

individual variation amongst exposed samples. The explicit coupling of individual- and site-specific KU60648 levels (i.e., internal dose) with measurements of the lipidome was therefore required to reveal that the response of acylcarnitines is highly sensitive to the relative exposure of cardiac tissue to KU60648, and thereby to discover the involvement of acylcarnitines in KU60648-induced cardiotoxicity. Since acylcarnitines have previously been proposed as biomarkers of dysregulated fatty acid metabolism and/or mitochondrial dysfunction (195, 196), a commonly proposed mechanism in the progression of xenobiotic-induced cardiotoxicity (197), our discovery implicates mitochondrial dysfunction in the progression also of KU60648-induced cardiotoxicity.

Levels of five of these acylcarnitines, alongside four others, were further found to be significantly increased in the plasma of exposed rats on days 2 and 4, with median fold changes of 7.80 and 12.94, respectively (Table eA.7, Table eA.9, Figure 2.16). Significant increases in levels of acylcarnitines have been associated with heart failure, including correlation with LVEF (198), while it has also been reported that plasma acylcarnitine levels reflect the acylcarnitine profile in the cardiac tissues (199). Taken together, the evidenced direct association with KU60648 levels at the site of toxicity, coupled with large and significant disruption in the plasma, and supported by literature reports, identify acylcarnitines as tantalising putative biomarkers for drug-induced cardiac metabolic dysfunction.

Table 2.5 Over-representation analysis of lipids significantly correlated to KU60648 levels in the cardiac tissue of exposed rats.
The number of lipid species per lipid class annotated to MSI level 2 (Reference List Count), and number of those lipids significantly correlated (Spearman's, p <0.05) to KU60648 levels in exposed samples (network count) are reported. Expected network count refers to the number of species per lipid class expected to be significantly correlated to KU60648 levels in exposed samples in the case of no lipid class enrichment. The fold enrichment of lipid classes significantly correlated (Spearman's, p <0.05) to KU60648 levels in exposed samples was calculated as the ratio of network count to expected network count, and the significance assessed by a one-sided Fisher's Exact test (p-value).

Lipid Class	Reference List Count	Network Count	Expected Network Count	Fold Enrichment (Actual/ Expected)	p-value
AcCa	15	8	0.8	10.0	1.467×10^{-7}
Cer	28	1	1.6	0.63	0.794
DG	13	2	0.7	2.86	0.156
PC	107	7	6.0	1.17	0.217
PE	101	1	5.7	0.18	0.995
PG	6	1	0.3	3.33	0.292
SM	42	2	2.4	0.83	0.661
TG	142	7	8.0	0.88	0.442

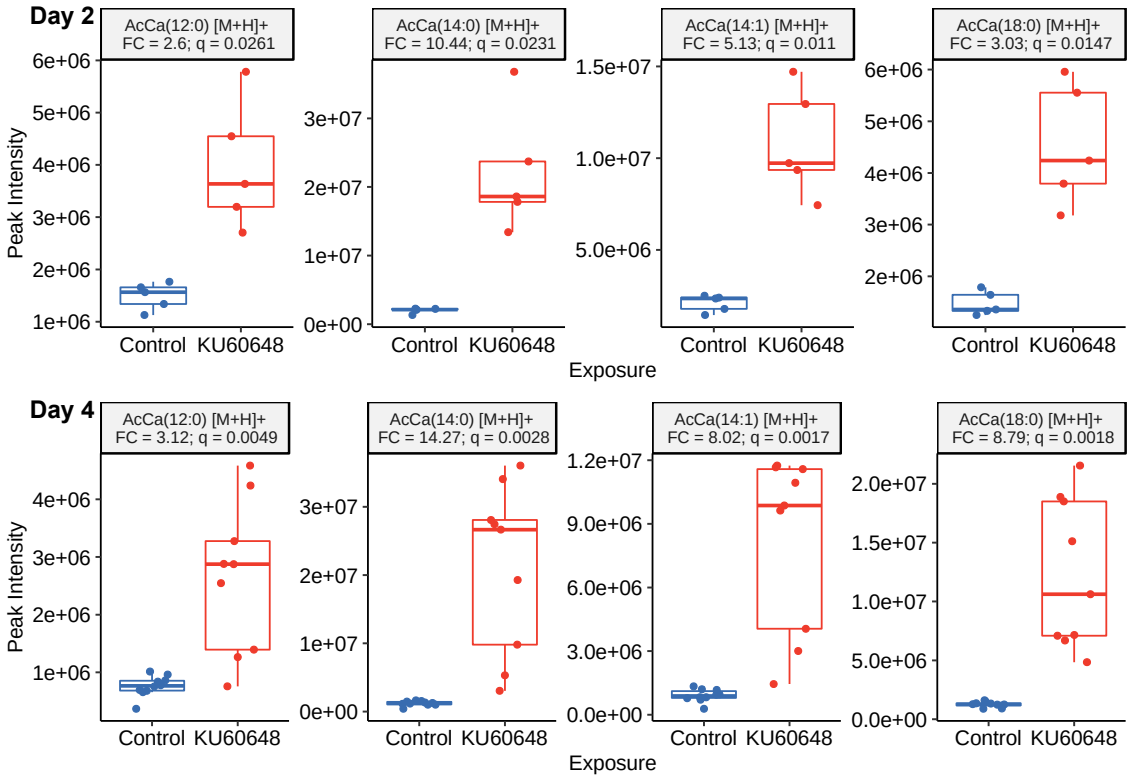


Figure 2.16 Four acylcarnitines associated with KU60648 levels at the site of toxicity have significantly increased levels in plasma of exposed rats.
Boxplots showing the peak intensity values of four acylcarnitines; AcCa(12:0), AcCa(14:0), AcCa(14:1) and AcCa(18:0), in the plasma of rats exposed to KU60648 for either 2- or 4-days, compared to time-matched biological controls. The levels of the same four acylcarnitines were found to be significantly correlated with levels of KU60648 in the cardiac tissue of rats exposed to KU60648 for four days. Fold changes and q-values (FDR-corrected p-values from Student's two-tailed t-test) are also displayed.

2.3.6 CONTRASTING METABOLIC COMPETENCIES OF EXPERIMENTAL MODELS

In vitro models for assessing organ toxicities are becoming increasingly common in accordance with the 3Rs concept (20, 32, 53) and the advantages of human-relevant test systems (154). Xenobiotic biotransformations can play a major role in toxicity, however many *in vitro* model systems remain uncharacterised in terms of their metabolic competencies (200, 201). Here the untargeted ADME/TK workflow was applied to metabolomics datasets that were originally collected to investigate the effects of sunitinib on hiPSC-CMs. By comparison to biotransformation of sunitinib in rat, the ability to reveal the metabolic competences of experimental model *in vitro* systems was demonstrated.

Untargeted metabolomics measurements of both intracellular extracts and culture medium of hiPSC-CM cultures were acquired by the same four assays and processed using the workflow (Figure 2.1). A total of 356 and 87 putative sunitinib-related features were identified in intracellular extracts and culture medium, respectively (Table 2.6). This included sunitinib and its biotransformation products M1, M2, M3, M4, M12, M14 and M20 within the intracellular extracts, and sunitinib, M1, M2, M12 M14 and M18 in the culture medium (Figure 2.17, Table eA.10). The observation of products of sunitinib de-ethylation, oxidation and/or hydrolysis demonstrates that cardiomyocytes possess metabolic competency, yet this appears to be limited to a subset of Phase I biotransformations. Meanwhile, investigation of the temporal distribution of sunitinib levels provides evidence, through lack of significant change, that hiPSC-CMs were exposed to a consistent level of sunitinib over the duration of the 24-hour experiment (Figure 2.18).

Table 2.6 Number of features in the untargeted metabolomics datasets of hiPSC-CM cultures before and after application of the three untargeted ADME/TK workflow filters.
Separate full peak matrices per metabolomics assay were produced for sunitinib-exposed and corresponding biological control samples of hiPSC-CM intracellular extracts and spent culture medium. The number of putative xenobiotic-related features discovered by application of the three intensity-based filters for each xenobiotic are presented, and the number of features retained after removal of those features from the full peak matrices to generate the filtered (endogenous) peak matrices.

		HILIC positive	HILIC negative	RP-C_{18} Positive	RP-C_{18} Negative
Intracellular extracts	Number of features in full peak matrix	12,028	5,924	8,025	3,690
	Number of putative sunitinib-related features	217	12	102	25
Culture medium	Number of features in full peak matrix	6,027	3,426	3,168	1,195
	Number of putative sunitinib-related features	71	3	13	0

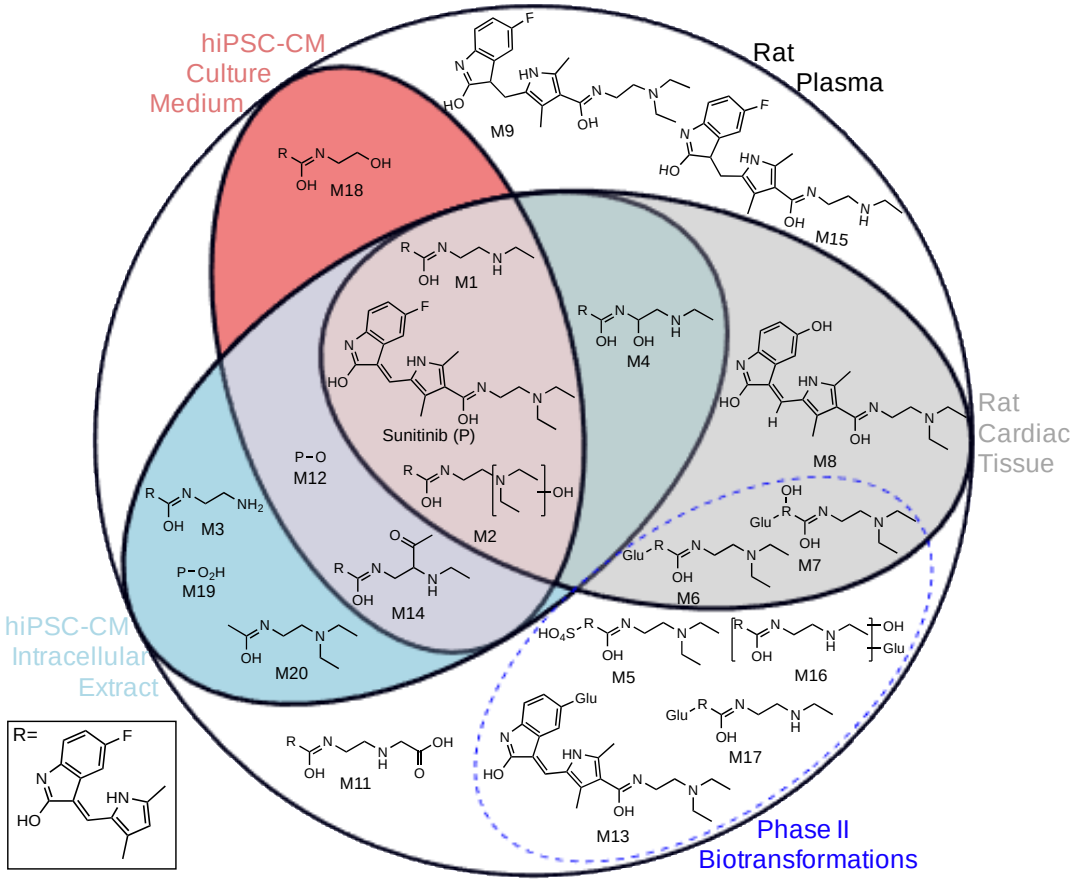


Figure 2.17 Comparison of the metabolic competencies of cardiomyocyte (hiPSC-CM) *in vitro* cultures and rat by applying the untargeted ADME/TK workflow to four UHPLC-MS metabolomics datasets.
Euler diagram depicting in which biological samples (rat plasma, rat cardiac tissue, the intracellular extracts and culture medium of hiPSC-CM cultures) sunitinib and its biotransformation products were detected.

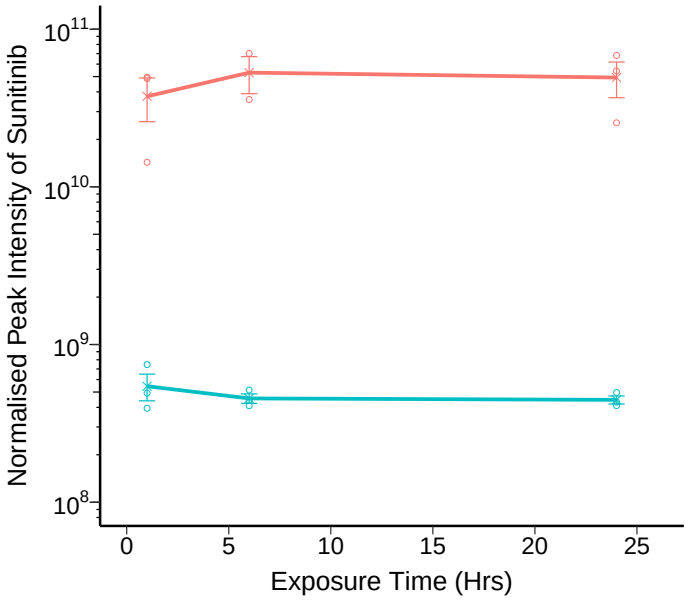


Figure 2.18 Temporal distribution of sunitinib in the intracellular extracts (coral) and culture medium (light blue) of hiPSC-CM cultures exposed to sunitinib.
Mean (cross) peak intensity of sunitinib, measured by UHPLC-MS untargeted metabolomics, over the duration of the 24-hour study. N = 3 from separate vials of hiPSC-CMs. Individual data points are also displayed (open circle). Error bars show standard error. Neither intracellular nor extracellular levels of sunitinib significantly change over the duration of the 24-hour exposure (one-way ANOVA, p >0.05).

Some overlap in the biotransformation products detected in cardiomyocyte cultures and cardiac tissue of rats was observed, mainly M1, M2 and M4. However, three products were unique to cardiac tissue, including two glucuronidation biotransformations (M6 and M7). Five biotransformation products were detected in the cardiomyocytes but not the cardiac tissue. Although this comparison may be confounded by differences in detection limits between matrices, it has revealed distinct patterns in the biotransformations of the pharmaceutical.

Taken together, through application of the untargeted ADME/TK workflow, a previously unreported capacity of hiPSC-CMs for Phase I-type oxidative and hydrolytic reactions, but no indications of Phase II reactions, is revealed. Such discoveries of *in vitro* biotransformation, by comparison to *in vivo* biotransformation, could help to explain discrepancies between *in vitro* and *in vivo* toxicological

responses to a pharmaceutical (154), without requiring additional time-consuming and expensive analysis.

2.3.7 UNTARGETED WORKFLOW DISCOVERS FATE OF PHARMACEUTICALS IN HUMANS

The ability to characterise the exposure to, and biotransformation of, xenobiotics in humans as a component of an untargeted metabolomics assay of biochemical effects could enhance mechanistic safety assessments of pharmaceuticals, biocides, and industrial chemicals. Additionally, characterising unknown and/or unintended human exposure to xenobiotics is important in environmental health research, e.g., to identify populations exposed through the environment to xenobiotics of concern. Here the capability of our workflow to detect human exposure to pharmaceuticals, from a list of suspects, and discover their metabolic fates was demonstrated (Table A.1, Figure 2.19**).**

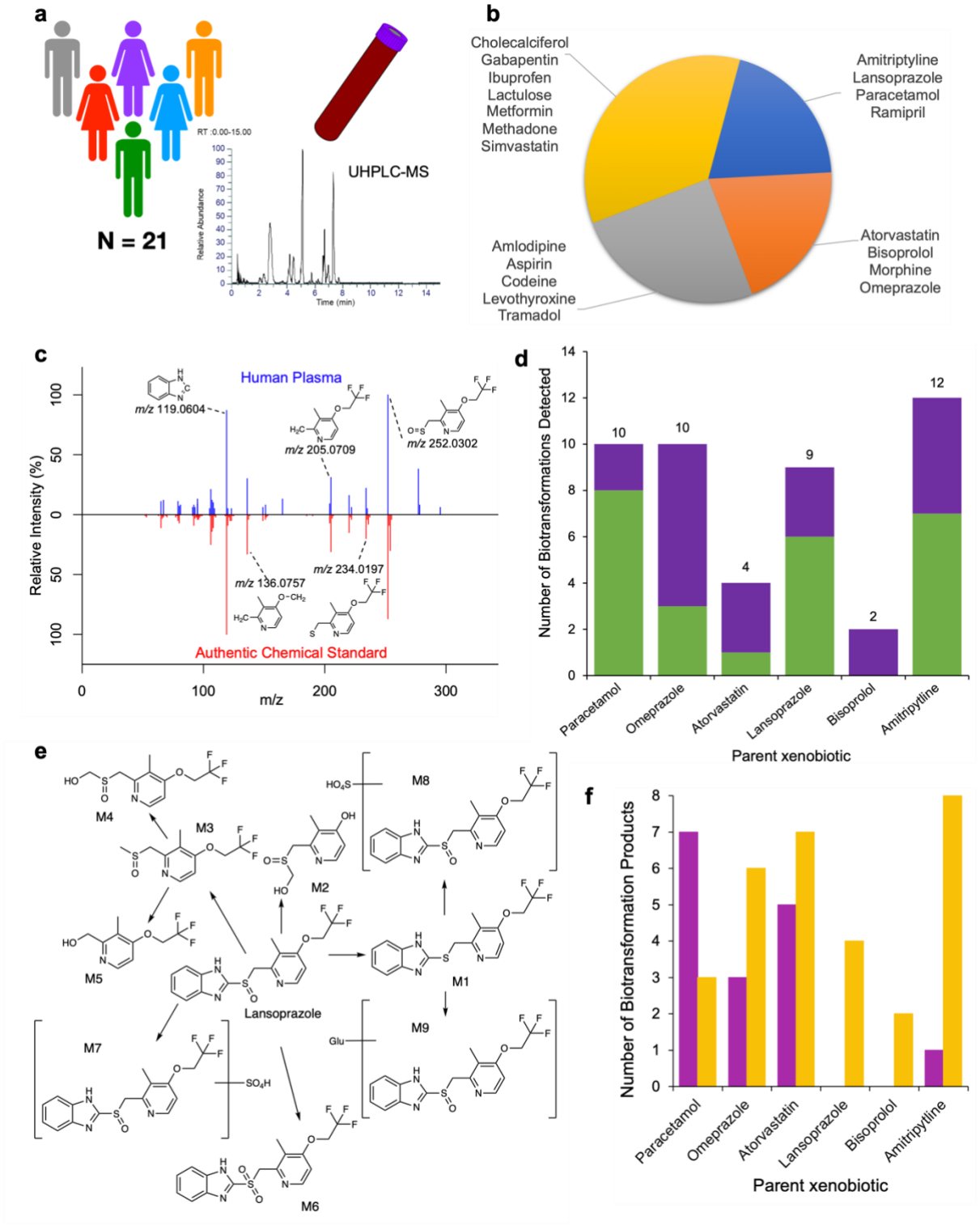


Figure 2.19 Discovery of pharmaceuticals and their biotransformation products in a human plasma untargeted metabolomics dataset.

a Summary of approach. **b** Pie chart displaying detection of UK NHS Top 20 most prescribed pharmaceuticals within the human plasma UHPLC-MS untargeted metabolomics dataset: blue - pharmaceuticals that were detected, with identity confirmed by matching retention time and MS/MS to analytical standard, orange - pharmaceuticals detected, with confidence in annotation from matching MS/MS to public database, yellow - pharmaceuticals detected according to putative MS^1-based annotation, grey - not detected. **c** Representative comparison of measured MS/MS fragmentation

spectrum for lansoprazole in human plasma (top) vs. its authentic chemical standard (bottom) and the corresponding MetFrag-annotated structures of major peaks. **d** Number of molecular formulae-annotated (putative annotation) (purple) and structurally annotated (MSI level 2) (green) biotransformation products of detected and confidently annotated parent pharmaceuticals. **e** Map showing the biotransformation products of lansoprazole discovered in plasma of healthy humans by UHPLC-MS untargeted metabolomics using our untargeted ADME/TK workflow. **f** Number of Phase I (yellow) and Phase II (magenta) biotransformation products derived from 6 confidently annotated parent pharmaceuticals discovered by the workflow.

A list of the UK NHS top 20 most prescribed pharmaceuticals was selected as an appropriate 'suspect' list for demonstrating this application of the workflow (Table A.3). All 20 of the suspect xenobiotics are considered emerging chemicals of concern and listed within the NORMAN (202) and CECscreen (203) databases. Eight of these pharmaceuticals were confidently detected (MSI Level 1 or 2, or Schymanski confidence level 1 - 3) within the human plasma untargeted metabolomics dataset (Figure 2.19b-c, Table A.3, Figure A.5). Subsequent labelling of each sample as either 'exposed' or 'control' for each of the eight confidently detected pharmaceuticals, followed by application of the three intensity-based filters (Figure 2.1) generated matrices of putative xenobiotic-related features for six parent substances (each detected in at least two human plasma samples).

Annotation of these features using BEAMSpy and SyGMa predictions revealed 10, 10, 4, 9, 2, and 12 biotransformation products of paracetamol (acetaminophen), omeprazole, atorvastatin, lansoprazole, bisoprolol, and amitriptyline, respectively (Figure 2.19d, Tables eA.10-16, Figure A.6). Of the total of 47 biotransformation products detected, 31 are products of Phase I transformations, while 16 result from Phase II transformations, mainly glucuronidation (Figure 2.19f). Corresponding MS/MS spectra for 53% of the biotransformation products were measured and interpreted, providing confidence in their annotation (Figure 2.19d-e, Table 2.7, Tables eA.10-16, Figure A.7, Figure A.8).

Table 2.7 Implementing the untargeted ADME/TK workflow on human plasma UHPLC-MS untargeted metabolomics data.
The number of samples defined as either 'exposed' or 'control', number of putative xenobiotic-related features remaining after implementing the three intensity-based filters, and the number of annotated biotransformation products annotated to either MSI Level 3 (MS^1 match only) or MSI Level 2 (supporting MS/MS spectrum) are reported for each pharmaceutical confidently detected in the dataset.

Pharmaceutical	Number of 'exposed' samples	Number of 'control' samples	Number of putative xenobiotic-related features	Number of molecular formulae annotated biotransformation products (MS^1 only)	Number of structurally annotated biotransformation products (MetFrag)
Paracetamol (Acetaminophen)	7	14	70	2	8
Omeprazole	3	18	89	7	2
Atorvastatin	2	19	201	3	1
Ramipril	0	21	0	N/A	N/A
Lansoprazole	6	15	74	3	6
Bisoprolol	1	20	73	2	0
Amitriptyline	3	18	51	5	7
Morphine	0	21	0	N/A	N/A

Taken together, the approach described here has revealed insights into the pharmaceutical exposomes of the tested individuals. In future, there is an opportunity for such measurements (i.e., relative internal dose of pharmaceuticals and their biotransformation products) to be associated with (relative) levels of endogenous metabolites and lipids, measured in the same analysis, as an approach to relate exposure and internal fate to biological effect.

2.4 Conclusions

The ability to measure xenobiotics and their biotransformation products in the same UHPLC-MS analysis used to probe endogenous biochemical effects enables insights into both the external chemical environments to which individuals are exposed and the internal fate and effects of xenobiotics, without the need for additional samples and analytical measurements, and hence associated costs (155). To this end, a data processing workflow was developed and implemented to semi-automatically discover

measurements corresponding to a xenobiotic and its biotransformation products within untargeted UHPLC-MS metabolomics datasets. The workflow addresses caveats of other xenobiotic biotransformation product identification strategies, including overcoming a need for prior knowledge of xenobiotic biotransformations and avoiding the requirement for stable isotope-labelling. Despite this, there are some limitations of the workflow: first, the workflow uses datasets acquired by UHPLC-MS-based metabolomics, i.e., analytical methods which are optimised to measure biochemicals using ESI. However, many xenobiotics have physicochemical properties that are not compatible with ESI and will not be detectable (66). As biotransformation products are typically more polar than parent substances, the detectability of such products using UHPLC-MS based metabolomics is anticipated to be higher. Furthermore, xenobiotics and their biotransformation products can occur at very low concentrations in biological samples, particularly when originating from unintended environmental exposure (159, 204). Detection of low abundant compounds is challenging, particularly in complex matrices from crude extraction of biological samples (66). Where biotransformation products are measured, only partial structural formulae may be assigned.

Implementation of the workflow on two routine UHPLC-MS untargeted metabolomics datasets designed to explore the effects of sunitinib and KU60648 treatment on rats demonstrated its capabilities to discover extensive biotransformation maps of pharmaceuticals, including previously reported, predicted and novel biotransformation products, and provide confidence in their annotation or identity. Further analysis of the discovered xenobiotic-related data revealed the ability of untargeted metabolomics to inform on tissue distribution, e.g., distribution to sites of

toxicity, and temporal distribution, i.e., relative systemic exposure over experiment duration, of both parent substances and their biotransformation products.

In addition to the discoveries on xenobiotic fate, the metabolomics datasets were mined to investigate the endogenous biochemical responses of rats, in both plasma and at a site of toxicity (cardiac tissue), following exposure to sunitinib and KU60648. First the importance of discovering and removing xenobiotic-related features, i.e., confounding factors, from the endogenous peak matrix was highlighted. Subsequently, going beyond conventional analysis, the availability of relative internal dose and untargeted metabolomics measurements from the same samples was exploited to discover dose-response associations within the cardiac tissue. Results, e.g., discovery of direct association between sunitinib and ceramide cardiac levels, and separately, KU60648 and acylcarnitine cardiac levels, demonstrated that this approach is pertinent to toxicological MoA elucidation and biomarker discovery.

Implementation of the workflow was extended to an untargeted metabolomics dataset from a study into the effects of sunitinib on hiPSC-CMs, revealing previously unreported capacity for Phase I-type oxidative and hydrolytic reactions, but no indications of Phase II reactions. The metabolic capacity of *in vitro* test systems is an important consideration for more accurate IVIVE. Thus, this demonstrated capability has potential to transform the translational accuracy of *in vitro* toxicity testing.

Finally, the workflow was applied to reveal exposure to suspect pharmaceuticals (Top 20 UK NHS most prescribed) from human plasma UHPLC-MS dataset, and subsequently map the biotransformation of the detected substances. Through this implementation of the workflow, its broader applicability beyond (targeted) toxicological studies, e.g., for pharmaceutical or chemical risk assessment, to

exposomics-based research was established. However, the workflow is limited to discovering only features related to identifiable suspects.

CHAPTER 3: AN EXTENSIVE METABOLOMICS WORKFLOW TO DISCOVER CARDIOTOXIN-INDUCED MOLECULAR PERTURBATIONS IN MICROTISSUES

3.1 INTRODUCTION

Drug-induced cardiotoxicity is a major cause of attrition during preclinical and clinical drug development and post-approval withdrawal of medicines (2, 4, 18, 19). Consequently, there is an urgent need to develop effective preclinical assays to evaluate the cardiac safety risk of lead compounds (18). *In vitro* approaches, when coupled with molecular assays, are considered promising for this purpose given their relatively low cost, capability for high throughput and ethical benefits, i.e., 3Rs. The effectiveness of preclinical *in vitro* screens is well evidenced by the successes of the hERG assay, which evaluates the risk that a compound will induce QT prolongation, an electrical disturbance in the heart (13, 14, 16, 18). Furthermore, the ability of assays employing stem cell-derived cardiomyocytes to predict the risk of cardiotoxicity has been demonstrated (20, 30-32). However, these *in vitro* models do not take into consideration the role of non-cardiomyocytes, which contribute approximately 70% of the cell mass and have important roles in cardiac physiology and functionality (35, 36). Furthermore, monolayer cultures are considered to lack physiological relevance given the absence of cell–cell and cell–ECM interactions which are important regulators of cell morphology (205-207). The recent development and use of more complex *in vitro* models encompassing hiPSC-CMs in 3D co-cultures alongside fibroblasts and endothelial cells, which together represent the majority of non-cardiomyocytes in the heart, has enhanced the specificity and sensitivity of assays which aim to predict the cardiac safety risk of screened

compounds (21, 36). These spontaneously beating 3D co-cultures, composed of approximately 500 cells, are termed cardiac microtissues (21).

The majority of screening assays developed over recent years have focused on predicting functional cardiotoxicity, i.e., change in the mechanical function of the myocardium, while molecular biomarkers that can predict drug-induced morphological damage of the myocardium and loss of cardiac viability (structural cardiotoxicity) are still lacking (32, 36, 61). As such, mechanistic insight and predictive biomarkers of structural cardiotoxicity remain a significant unmet need (18, 32, 36, 61). Untargeted metabolomics is a promising approach in toxicology for generating hypotheses on toxicity MoA (52, 53, 57, 69, 157) and for discovering metabolic biomarkers (61). Metabolomics-based *in vivo* studies have previously detected metabolic perturbations associated with drug-induced cardiotoxicity (208, 209). Furthermore, the technology has successively been applied to measure changes to the extracellular metabolome, termed the 'metabolic footprint', of hiPSC-CMs induced by cardiotoxins, with the responses of four metabolites (arachidonic acid, lactic acid, 2′-deoxycytidine and thymidine) proposed as biomarkers predictive of the cardiotoxicity potential of drugs (61). Measurement of the metabolic footprint of an *in vitro* model can be achieved by conventional UHPLC-MS-based analyses of spent culture medium, which can be relatively simply and non-invasively sampled (61, 74). However, although it provides an indication of molecular disruption to the *in vitro* model, the metabolic footprint does not represent all intracellular responses (74, 75). Thus, profiling intracellular metabolic perturbations, in addition to the metabolic footprint in the culture medium, offers a more promising platform for gaining mechanistic insight and discovering predictive biomarkers of structural cardiotoxicity.

Profiling drug-induced intracellular metabolic perturbations, particularly of more advanced *in vitro* models such as microtissues, is challenging. For example, conventional metabolomics technologies such as UHPLC-MS typically require more than a million cells per sample (74), while 3D microtissue cultures are limited to just a few hundred cells (36). Greater sensitivity may be achieved through application of a spectral stitching nESI-DIMS-based approach, which offers an enhanced detection sensitivity while maintaining high reproducibility and minimising ion suppression and/or enhancement (108). However, this approach is thus far untested on *in vitro* samples consisting of $<5x10^5$ cells (HepaRG) (87). Furthermore, harvesting cells in a manner that ensures the metabolomics analysis accurately measures the levels of intracellular physiological metabolites is challenging, particularly for suspended cultures including cardiac microtissues (79). Optimally, sample harvesting removes the culture medium, including extracellular metabolites, while limiting leakage of intracellular metabolites (79). Sample harvesting of suspended cell cultures is often achieved by centrifugation to first separate the cells from their culture medium before quenching metabolism. However, it can take up to several minutes before metabolism is quenched, particularly when washing steps are included to ensure thorough removal of extracellular metabolites. This is deemed unacceptable for metabolites with relatively fast turnover rates (79). Filtration has been proposed as an alternative approach which can allow more rapid isolation of cells from their culture medium, although this has only been tested on relatively large-scale cultures (79).

Characterising a drug's disposition is commonplace in *in vivo* studies to aid the prediction of human risk from the responses of model species (145, 164). However, comparable analyses are not typically applied in *in vitro* toxicity evaluations, despite

their potential for enhancing the interpretation of endogenous responses and subsequently aiding IVIVE. An ‘untargeted toxicokinetics’ workflow capable of extracting information on xenobiotic disposition from UHPLC-MS untargeted metabolomics datasets, including extraction of relative extracellular levels of an exposure xenobiotic, sunitinib, in an *in vitro* cardiomyocyte-based model over a 24-hour toxicity study, was developed and implemented in Chapter 2. Moving beyond this, absolute quantification of drug concentrations in the spent culture medium of *in vitro* models over the duration of a toxicity experiment would enable validation of drug exposure levels and may contribute to greater certainty in IVIVE.

The aim of this study was to develop and subsequently demonstrate an extensive metabolomics workflow for investigating drug-induced cardiotoxicity in cardiac microtissues, incorporating nESI-DIMS-based untargeted metabolomics of intracellular extracts and UHPLC-MS-based analysis of spent culture medium, both to profile the metabolic footprint and quantify drug exposure concentrations. Firstly, approaches for harvesting and washing cardiac microtissues for intracellular metabolomics were evaluated with respect to the *m/z* feature count, data reproducibility and effectiveness of culture medium removal. Additionally, an experimentally feasible sample biomass for intracellular nESI-DIMS metabolomics was determined by assessing the sensitivity and reproducibility of measurements across a gradient of cardiac microtissue biomasses. The third objective was to demonstrate the suitability of this workflow for assessing drug-induced cardiotoxicity in microtissues. Cardiac microtissues were exposed to sunitinib, a synthetic drug and established structural cardiotoxin, at two concentrations, for up to 72-hours. Time-resolved intracellular metabolic perturbations and changes to the metabolic footprint were discovered by nESI-DIMS and UHPLC-MS analysis, respectively. The final

objective was to integrate quantitative measurements of the extracellular concentrations of the exposure drug, sunitinib, into the same UHPLC-MS metabolomics assay.

3.2 Materials and Methods

3.2.1 Cell culturing and sunitinib exposure

Cell culturing was performed by Dr. Andrew Hall (AstraZeneca). Cardiac microtissues were cultured as described previously (36). Briefly, primary human cardiac microvascular endothelial cells (hCMECs, Lonza, Basel, Switzerland) and primary human cardiac fibroblasts (hCFs, Lonza) were grown and maintained in EGM-2 MV Endothelial Med BulletKit (CC-3202), and FGMTM-3 Cardiac Fibroblast Growth Medium-3 BulletKit (CC-4526), respectively. On the day of microtissue synthesis, hiPSC-CMs (iCell Cardiomyocytes, CDI) were thawed in plating media according to manufacturer's instructions, and hCMECs and hCFs were detached to obtain a single suspension. Microtissues were formed by combining cell suspensions of hiPSC-CMs, hCFs and hCMECs to obtain 285 hiPSC-CMs, 142 hCFs and 71 hCMECs in a total of 40 µL (20 µL hiPSC-CM thaw medium (CDI), and 20 µL EGM-2 MV medium (Lonza)) per well. Microtissues were plated into 384 ultra-low attachment U-bottom plates (Corning), and the medium was topped up to 80 µL with maintenance medium (50% iCell maintenance medium (CDI), 50% EGM-2 MV (Lonza)) after 48-hours. Note, microtissues were not plated on the outer edge of the 384-well plates due to the higher medium evaporation rates here. Microtissues were maintained for a minimum of 14-days prior to experimentation by removal of 40 µL medium, which was replaced by fresh maintenance medium twice weekly.

Microtissues were treated with either 0.1% DMSO (control), 1.1 µM sunitinib (low concentration) or 3.3 µM sunitinib (high concentration) by the removal of 40 µL

medium, and addition of drugs at a 2x stock. Microtissues were treated for either 2-, 6-, 48- or 72-hours prior to sampling/imaging.

3.2.2 HIGH CONTENT BIOLOGY ASSAY

The high content biology (HCB) assay was performed by Dr. Andrew Hall (AstraZeneca). Briefly, microtissues were stained for with fluorescent probes by removal and replacement of 40 µL cell culture maintenance medium containing two dyes: ER-Tracker (2 µM final) and TMRE (0.5 µM final) for ER integrity and mitochondrial membrane potential analysis, respectively. Microtissues were imaged live on a Cell Voyager 7000 (Yokogawa, Japan) using a 20x objective in a temperature (37°C)- and CO_2 (5%)-controlled chamber. ER-Tracker was imaged using a 405 nm excitation laser (405 ± 5 nm, 100 mW, Coherent, UK) and an Andor Neo sCMOS camera with a 445/45 nm band pass emission filter. TMRE was imaged using a 561 nm excitation laser (561 ± 2 nm, 200 mW, Coherent) and a 600/37 nm band pass emission filter. Transmitted light images were acquired using a 100 W halogen lamp as an illumination source. Images were captured over a 60 µm range in the Z-axis with a 5 µm interval between slices. Z-stack images were output as a maximal projection of multiple z-planes.

Maximum projection images were imported and analysed in the Columbus Platform (v2.7, Perkin Elmer Inc., UK). Objects were identified using the transmitted light image and the object of interest selected based on morphological and intensity-based features from the fluorescence channels. Quantitative measurements of morphological, texture and intensity features from the microtissues were captured for all parameters and exported for data analysis.

3.2.3 MICROTISSUE SAMPLE COLLECTION

3.2.3.1 Microtissue sampling by centrifugation

Microtissues and their culture media were aspirated from either 14 wells (1 column) or 154 wells (11 columns, corresponding to ½ plate) of the 384-well culture plate and pooled. Samples were centrifuged at 400-*g* for 3-minutes, the supernatant (culture medium) was discarded, and the pellet (microtissues) was resuspended in 0.5 mL ice-cold 0.9% NaCl. Washed samples were centrifuged again (5000-*g*, 3-minutes). The supernatant was discarded, and the saline wash step repeated. Finally, the pellet was resuspended in 0.5 mL ice-cold ultra-pure (18.2 mQ) water. Resuspended samples were spun until 5000-*g* was reached, and then the supernatant was rapidly discarded before quenching the microtissues in dry ice/ethanol. Harvested microtissue samples were stored at −80°C until extraction. Process blanks were generated by sampling of media only (no microtissues) by the same approach.

3.2.3.2 Microtissue sampling by filtration

Microtissues and their culture media were aspirated from either 7 (½ column), 14 (1 column), 21 (1½ columns) or 28 (2 columns) neighbouring wells of a 384-well culture plate and added to one side of a cell strainer (37 µm reversible strainer, StemCell Technologies, Cambridge, UK). The culture medium was allowed to drain, before successive ice-cold 0.9% NaCl and ultra-pure water washes (either 2x 0.5 mL 0.9% NaCl, 1x 0.5 mL water for the experiments described in Sections 3.3.1 and 3.3.2, or 3x 1 mL 0.9% NaCl, 1x 1 mL water for the experiments described in Section 3.3.3) were conducted, with the cell strainer allowed to drain. The microtissue-containing cell strainer was then rapidly frozen in dry ice/ethanol and stored on dry ice during the collection of remaining samples. Harvested microtissue samples were stored at −80°C until extraction. Samples of spent culture media were spun to remove cellular debris and then stored at −80°C until extraction.

Process blanks were generated by sampling of media only (no microtissues) using the same approach. To evaluate the effect of washing on the amount of residual medium remaining on the cell strainers after sampling, process blanks were generated using media only (no microtissues). Specifically, 2.24 mL culture medium was added to a cell strainer and allowed to drain. The strainer was then either not washed, or washed with 2x 0.5 mL, 2x 1 mL, 3x 1 mL or 4x 1 mL 0.9% NaCl. Each washing protocol was concluded with a single water wash of equivalent volume to a single NaCl wash.

3.2.4 Intracellular nESI-DIMS Untargeted Metabolomics and Lipidomics

3.2.4.1 Extraction of intracellular metabolites

Intracellular polar metabolites were extracted from harvested microtissues by either addition of 200 µL ice-cold 4:1 (v/v) methanol/water (LC-MS grade, VWR International) to each sample in a microcentrifuge tube or, for samples harvested by filtration, addition of 200 µL ice-cold 4:1 (v/v) methanol/water to the surface of the cell strainer (held in a microcentrifuge tube, creating an airtight seal which prevents the solvent from passing through the filter), followed by re-aspiration of the solvent and microtissues, and transferred to a microcentrifuge tube. For the experiment described in Section 3.3.3, methanol was supplemented with 0.2 µM L-tryptophan-(indole-d5) (Merck Life Sciences), added as an internal standard to assess technical error resulting from sample preparation and analysis. Samples were vortexed for 2-minutes and then centrifuged (20,000-*g*, 4°C) for 20-minutes. Either 180 µL of the supernatant was transferred to a microcentrifuge tube (experiments discussed in Section 3.3.1) or 90 µL of the supernatant was transferred to two microcentrifuge tubes (experiments described in Sections 3.3.2 and 3.3.3). Extracts were then dried in a SPD11V SpeedVac sample concentrator (Thermo Scientific, UK) for 4-hours.

Extraction blanks were generated by applying the same extraction procedure to fresh cell strainers.

3.2.4.2 Extraction of intracellular lipids

Intracellular lipids were extracted from samples by either addition of 160 µL ice-cold methanol to each sample in a microcentrifuge tube or, for samples harvested by filtration, addition of 160 µL ice-cold methanol to the surface of the cell strainer (held in a microcentrifuge tube, creating an airtight seal which prevents the solvent from passing through the filter). The solvent and microtissues in the microcentrifuge tube or cell strainer were then aspirated and transferred to a 1.75 mL glass vial. An amount of 80 µL ice-cold chloroform (HPLC grade, Merck) was added, for a final solvent ratio of 2:1 (v/v) methanol/chloroform. For the experiment described in Section 3.3.3, methanol was supplemented with 0.2 µM dodecylphosphorylcholine-d38 (Merck), added as an internal standard to assess technical error resulting from sample preparation and analysis. Samples were vortexed for 2-minutes and then centrifuged (1500-*g*, 4°C) for 20-minutes. Either 200 µL of the supernatant was transferred to a 1.75 mL glass vial (experiments discussed in Section 3.3.1) or 100 µL of the supernatant was transferred to 200 µL conical glass inserts (experiments described in Sections 3.3.2 and 3.3.3). Extracts were then dried by nitrogen blowdown for 10-minutes. Dried extracts were stored at −80°C prior to analysis.

3.2.4.3 Resuspension of dried extracts

Dried intracellular polar metabolite extracts were resuspended in either 25 µL 4:1 (v/v) methanol/water containing 0.25% (v/v) formic acid (98%, Honeywell, UK) or 25 µL 4:1 (v/v) methanol/25 mM aqueous ammonium acetate (≥99.9% trace metal basis, Honeywell), for positive and negative ion metabolomics, respectively, and then centrifuged (20,000-*g*, 4 °C) for 10-minutes. For the experiment described in Section

3.3.1, dried extracts were resuspended in 20 µL 4:1 (v/v) methanol/water containing 0.25% (v/v) formic acid. Dried intracellular lipid extracts were resuspended in 35 µL 2:1 (v/v) 7.5 mM methanolic ammonium acetate/chloroform for lipidomics in positive and negative ionisation and then centrifuged (1500-*g*, 4°C) for 10-minutes.

Technical replicates for each sample class in the experiments described in Section 3.3.1 were generated from a pool of aliquots from the resuspended biological replicates per sampling approach. For the experiment described in Section 3.3.2, intra-study QCs per sample biomass were derived from a pool of aliquots from the resuspended extracts of samples with equivalent biomass. Intra-study QCs for experiments described in Section 3.3.3 were derived from a pool of additional biological control extracts.

Either 15 µL or 20 µL of the resuspended intracellular polar metabolite or lipid extracts, respectively, including biological samples, process blanks and intra-study QCs, were transferred to a 384-well Eppendorf twin-tec analysis plate for analysis.

3.2.4.4 *Data acquisition by nESI-DIMS*

Data were acquired using an Orbitrap Elite mass spectrometer (Thermo Scientific) with an nESI source (TriVersa Nanomate, Advion, Ithaca, USA) and the spectral stitching nESI-DIMS method and parameters reported previously (108), with some modifications. Mainly, each sample was infused once, with each *m/z* window collected four times, generating 'internal replicate' measurements (87).

3.2.4.5 Processing and annotation of nESI-DIMS data

Data were processed using DIMSpy tools (116) via the Galaxy interface as described previously (108), with some modifications. Mainly, in place of the replicate filter, only features measured in ≥ 75% internal replicates were retained per sample.

Samples for which electrospray ionisation failed were excluded, based on ion injection times and total peak count (as calculated after DIMSpy peak picking, spectral stitching, and internal replicate filtering). For the metabolomics (positive and negative ionisation) and lipidomics (positive ionisation only) nESI-DIMS datasets described in Section 3.3.3, samples were additionally filtered based on the response of the internal standard (L-tryptophan-indole-d5 and dodecylphosphorylcholine-d38 for metabolomics and lipidomics, respectively), whereby samples with an outlying internal standard peak intensity (after DIMSpy peak picking, spectral stitching and internal replicate filtering) were removed (Figure 3.1). The remaining samples were aligned using ±3 ppm mass error tolerance for data presented in Sections 3.3.1 and 3.3.2, and ±2 ppm for data presented in Section 3.3.3, and data matrices of peak intensities for *m/z* features vs. samples were constructed. Features whose intensities in ≤80% non-blank samples were <10x their median intensity in process blanks were removed. For data presented in Section 3.3.3, the sample filter DIMSpy tool was also applied, removing any feature present in ≤80% across all biological samples and intra-study QCs.

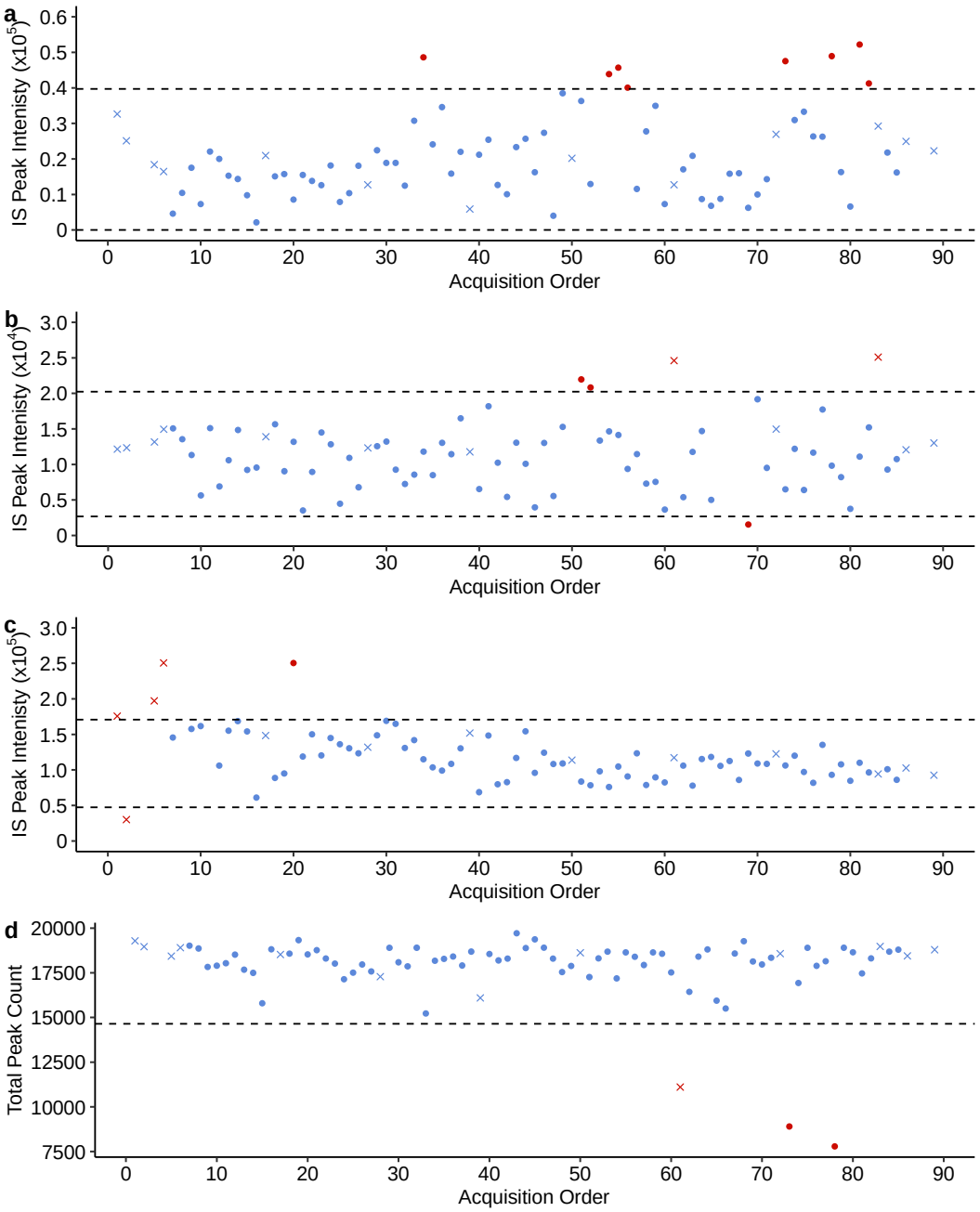


Figure 3.1 Peak intensity of internal standard.
Intensities of peaks annotated as **a** L-tryptophan-indole-d5 $[M+Na]^+$, **b** L-tryptophan-indole-d5 $[M+Na-2H]^-$ and **c** dodecylphosphorylcholine-d38 $[M+Na]^+$, in biological samples (●) and intra-study quality control samples (×) across analytical sequences as measured by polar metabolomics in positive and negative ionisation, and lipidomics in positive ionisation, respectively. Dotted line shows threshold for sample and/or intra-study QC removal, derived from median ± 2.97*MAD (median absolute deviation) of peak intensity across all injections. Accepted and rejected QCs/samples are coloured blue and red, respectively. **d** In the absence of internal standard peaks in the negative ionisation lipidomics data, poor quality samples were removed based on total peak count after spectral stitching. Here the threshold was derived at 80% median peak count across all injections.

Further data pre-processing was carried out using the R/Bioconductor package structToolbox (178). Sample filters of 75% and 80% were applied across biological

and technical replicates/intra-study QCs per sample class (either sample biomass or sampling methodology) for data presented in Sections 3.3.1 and 3.3.2, respectively, generating separate peak matrices for each sample class. For data presented in Section 3.3.3, samples with >30% missing values were removed from the peak matrix, and data were corrected for signal drift by QC-RSC (118). All peak matrices were normalised by PQN, using the mean intra-study QCs as the reference. For data presented in Figure 3.4, the peak matrix generated by the DIMSpy 'Align Samples' tool was filtered so that only features present in 100% of the 'no washing' samples were retained. No further data pre-processing was applied.

Putative annotation of *m/z* features was achieved by application of the Python package BEAMSpy (Birmingham mEtabolite Annotation for Mass Spectrometry, v0.1.0, available at https://github.com/computational-metabolomics/beamspy, accessed on 4th July 2019), by accurate mass matching to HMDB (210), KEGG (211) and LMSD (129) metabolite and lipid databases, using a ±5 ppm mass error window.

3.2.5 UHPLC-MS(/MS) UNTARGETED METABOLOMICS AND QUANTITATION OF SUNITINIB

3.2.5.1 Extraction of polar metabolites from culture medium

Samples of spent culture medium were prepared as described previously (76), with some minor changes. Samples were thawed on ice and briefly vortexed (5-seconds). An amount of 50 µL of medium was mixed with 150 µL ice-cold 1:1 (v/v) acetonitrile/methanol (LC-MS grade, VWR international). Samples were vortexed and centrifuged (20,000-*g*, 4 °C, 20-minutes), and 100 µL was transferred to an LC vial (Chromatography Direct) for analysis. Process blanks were generated from 50 µL H_2O, in place of media. Intra-study QC samples were created by pooling an

aliquot of each sample, vortexing (30-seconds) and then splitting into several 50 µL aliquots. Each aliquot was prepared as for the samples.

3.2.5.2 Preparation of sunitinib calibration standards, quantitation QCs and blanks

Duplicate sunitinib calibration standards with final concentrations of 0.0625, 0.125, 0.25, 0.5, 1, 2, 4 and 8 µM were prepared in fresh microtissue culture media containing 0.1% DMSO (Honeywell) from an initial stock solution of 50 mM sunitinib in DMSO. Duplicate sunitinib quantitation QCs (quant-QCs) with final nominal concentrations of 0.1875, 0.75 and 6.25 µM (high, mid, and low quant-QCs, respectively) were also prepared in media containing 0.1% DMSO. Triplicate 'quant-blanks' were prepared as 0.1% DMSO in media. Then, 50 µL aliquots of the calibration standards, quant-QCs and quant-blanks were prepared for analysis as described in Section 3.2.5.1.

3.2.5.3 Data acquisition by UHPLC-MS(/MS)

Samples were analysed using an existing method (76) implemented on a ID-X Tribrid Orbitrap mass spectrometer (Thermo Scientific) coupled to a Vanquish Horizon UHPLC (Thermo Scientific), using an Accucore 150 Amide column (100 x 2.1 mm, 2.6 µm, Thermo Scientific) with a pre-column UHPLC filter (2.1 mm ID x 0.2 µm filter cartridge, Thermo Scientific). Mobile phase A was 95% acetonitrile/water (10 mM ammonium formate, 0.1% formic acid), and mobile phase B was 50% acetonitrile/water (10 mM ammonium formate, 0.1% formic acid) for the positive ionisation mode. For the negative ionisation mode, mobile phase modifiers were 10 mM ammonium acetate and 0.1% acetic acid, in place of ammonium formate and formic acid, respectively. The gradient was as follows: t = 0.0, 1% B; t = 2.1, 1% B; t = 4.1, 15% B; t = 7.1, 50% B; t = 10.1, 95% B; t = 11.0, 95% B; t = 11.5, 1% B; t = 15.0, 1% B. All changes were linear (curve = 5). The flow rate was 0.4 mL/min, and

the column temperature was 35 °C. Analysis was performed in positive and negative ionisation modes separately at a resolution of 120,000, between 70 and 1050 *m/z*. Ion source parameters are detailed in Table 3.1. The sample injection volume was 2 µL.

Table 3.1 Ion source parameters for data acquisition by two UHPLC-MS(/MS) assays.

Assay	Sheath Gas (Arb)	Aux gas (Arb)	Sweep gas (Arb)	Spray voltage (kV)	Ion transfer tube temperature (°C)	Vaporizer temperature (°C)
HILIC Positive	40	8	1	3.2	200	300
HILIC Negative	40	8	1	2.7	200	300

MS/MS fragmentation data were collected by applying the AcquireX intelligent data acquisition workflow ('Deep Scan mode', Thermo Scientific). Briefly, an initial inclusion list consisting of protonated or de-protonated ion forms of toxicologically relevant metabolites was built manually. This was added to by AcquireX using full scan data acquired from an injection of an intra-study QC. AcquireX also generated an exclusion list using full scan data acquired from an injection of a process blank. MS/MS data were then acquired using HCD with stepped normalised-CEs of 20, 40 and 100% and 40, 60 and 130% for positive and negative ionisation, respectively, from three iterative injections of an intra-study QC using the inclusion and exclusion lists, which were modified by AcquireX after each iterative injection. Analysis was performed at a resolution of 60,000 and 30,000 for full scan (MS^1) and MS/MS, respectively, over a scan range of *m/z* 70–1050.

MS^1, RT and MS/MS fragmentation data of sunitinib, hypoxanthine, inosine and L-glutamine were also collected from chemical standards prepared in 1.5:1.5:1.0 acetonitrile/methanol/water using identical methods and instrumentation, as detailed above.

3.2.5.4 Processing and annotation of UHPLC-MS(/MS) untargeted metabolomics data

Vendor format raw data files (.RAW) were converted to mzML file format using ProteoWizard software (177). Full scan (MS^1) data deconvolution was performed by XCMS (v3.6.1) (115) operated in Galaxy, as reported previously (76). XCMS parameters were as follows: ppm (12), min. peak width (3), max. peak width (30), mzdiff (0.001), bw (0.25), minfrac (0.5), mzwid (0.01), OBI-warp RT correction (negative ionisation data only). A peak-intensity matrix for metabolite features (m/z–RT pairs) vs. samples was constructed.

Prior to data analysis, datasets were filtered as follows: any features whose median intensity in biological samples is <20x its median intensity in process blank samples were removed; features with RSD ≥30% across the intra-study QCs were removed; samples with >50% missing values were removed; features which were missing in ≥10% QCs and/or ≥50% of all samples were removed. Data were corrected for signal drift by QC-RSC (118). Peak matrices were then PQN normalised using the mean intra-study QCs as the reference. These steps were executed using the R/Bioconductor package structToolbox (178).

Putative metabolite annotation was performed using BEAMSpy, operated in Galaxy, using a ±5 ppm mass error and ±5-second RT tolerance window for feature grouping. More robust compound annotations were generated through matching of MS/MS data to the mzCloud spectral database using Compound Discoverer 3.2 (Thermo Scientific). Annotations were graded by the HighChem HighRes algorithm and aligned to XCMS outputs using the R programming language, using ±5 ppm mass error and ±20-second RT tolerance window. Further confidence in metabolite annotations was achieved by comparison of the MS^1 accurate m/z, RT, and MS/MS

spectrum of the specific adduct to data acquired for chemical standards using the same analytical method and instrumentation. Metabolite identification was confirmed using the following criteria: accurate mass error <5 ppm, RT tolerance ±30-seconds and MS/MS spectrum similarity score (dot product cosine) >0.9, as calculated using the R package, OrgMassSpecR (212), with a baseline threshold of 10% and *m/z* alignment tolerance of ±0.001 Da.

3.2.5.5 Quantitation of Sunitinib

The concentration of sunitinib in spent culture medium of cardiac microtissues was quantified using TraceFinder (Thermo Scientific). Absolute quantitation was performed using the peak area of the $[M+H]^+$ ion form of sunitinib, with the identity of this peak confirmed by matching of accurate *m/z*, RT and MS/MS fragmentation spectra to those of an analytical standard of sunitinib, measured as part of the same analytical sequence, i.e., MSI Level 1 identification (120). The response of sunitinib was calibrated against an 8-point calibration curve, using linear regression with $\frac{1}{X^2}$ weighting to fit the curve. Accuracy of the calibration was deemed sufficient with the calculated amount of all but one of the eight duplicated calibration points <20% of their theoretical amount. Sufficient accuracy and precision of the calibration were confirmed, with the calculated amount of five of six quant-QCs <20% of their theoretical amount (accuracy) and the coefficients of variation (CVs) per quant-QC level <15% (precision).

3.2.6 Statistical Analysis

Supervised (PLS-DA) and unsupervised (PCA) multivariate analyses of nESI-DIMS metabolomics and lipidomics data were performed using the R/Bioconductor package structToolbox (178). Prior to the analyses, MVI was performed on the peak

matrices MVI using the KNN algorithm (k = 5) and glog transformed, also using the structToolbox package (178).

Univariate data analysis (ANOVAs with Tukey's honestly significant difference test (HSD)), to discover metabolic/lipid features with significantly different intensities between sample classes, and Spearman's correlation analysis, to evaluate the association between *m/z* feature intensities and sample biomasses, were performed using the PQN-normalised peak matrices with the R/Bioconductor package structToolbox (178). The q-values were calculated by FDR correction.

ANOVAs with Tukey's HSD, to test the significance between the number of features detected per sample class (washing protocol), and two-sided t-tests, to test the significance in changes to percentage response of ER stress and Δψm between sample classes, and the concentration of sunitinib between time points, were all performed using the R programming language (https://www.R-project.org).

K-means cluster analysis was executed using the R programming language (https://www.R-project.org). An elbow plot was generated to select the optimal value of k prior to execution of k-means cluster analysis using the $\log_2$ fold change for each *m/z* feature calculated per time point.

Pathway over-representation analysis was performed using putative annotations of significantly perturbed *m/z* features as input to the 'Pathway Analysis' tool of MetaboAnalyst (213).

3.3 Results and Discussion

3.3.1 Comparison of approaches for the sampling of cardiac microtissues for untargeted metabolomics

A rapid filtration-based microtissue sampling approach using cell strainers was evaluated by comparison against a more routine, slower centrifugation-based approach, with respect to the efficiency in isolating the microtissues from the culture medium, impact on the cells (i.e., do they induce cell lysis) and overall metabolic reproducibility. These characteristics were assessed by examining the number of *m/z* features detected as well as their variability across biological replicates. Comparing the time scales for the two sampling approaches (outlined in Figure 3.2), the filtration method required ca. 60-seconds from collecting the microtissues from their culture plate through to the quenching of metabolism, while the centrifugation method required over 10-minutes, opening the potential for significant and unwanted metabolic changes. PCA of nESI-DIMS measurements of the metabolome and lipidome revealed that somewhat more consistent (less variable) intracellular metabolic and lipidomic signatures can be obtained when the microtissues are sampled rapidly via filtration (Figure 3.3). This finding is further evidenced by the lower median RSD (mRSD); an established metric for describing the variance of metabolic features (214), measured across filtered, vs. centrifuged, biological replicates (Table 3.2). Sampling microtissues by filtration resulted in a 1.9x and 1.6x higher number of *m/z* features in the intracellular polar metabolite and lipid extracts, respectively, compared to when microtissues were sampled by centrifugation. This improved coverage of the metabolome and lipidome is believed to be a consequence of the shorter handling times and reduced strain placed on cells during sampling, which likely minimises metabolite degradation and cell lysis prior to quenching.

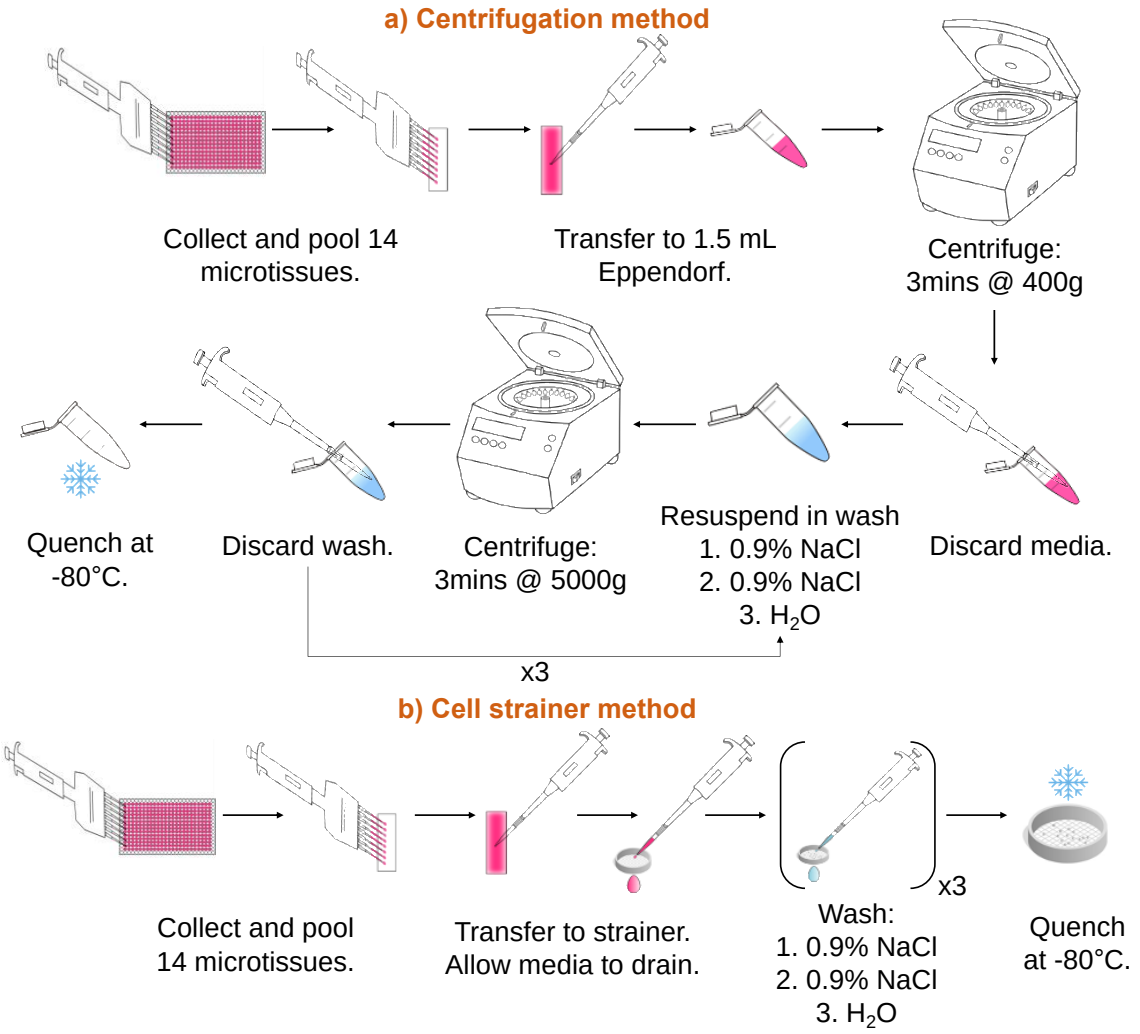


Figure 3.2 Graphical summary of two approaches for sampling cardiac microtissues, incorporating isolation from culture medium, washing, and quenching of metabolism. **a** centrifugation-based method and **b** filtration-based method employing cell strainers. Both methods begin by collecting the microtissues and their culture medium from the culturing 384-well microplate and pooling into a reservoir. For isolation from the media by centrifugation, **a**, the pooled material (media and microtissues) is dispensed into a microcentrifuge tube, then centrifuged for 3-minutes to pellet the cellular material, allowing the media/supernatant to be discarded. Washing is achieved by resuspending the cell pellet with 0.9% sodium chloride (NaCl) or water (H_2O), and repetition of the centrifuge/discard supernatant cycle until the cellular material has been washed twice with 0.9% NaCl and once with H_2O. For isolation of the microtissues from the media by filtration, **b**, the pooled material (media and microtissues) is dispensed onto a cell strainer. The media is allowed to drain through the filter, while the microtissues are retained on the surface. Subsequent washing is achieved by addition of either 0.9% NaCl or H_2O to the cell strainer, which also drains to waste, diluting and removing any residual media. The final step for both approaches is to quench metabolism by flash-freezing the samples, contained, **a**, within a microcentrifuge tube or, **b**, on the filter mesh of a cell strainer, in dry ice/ethanol bath (*ca*. -78°C) and storing at -80°C until analysis.

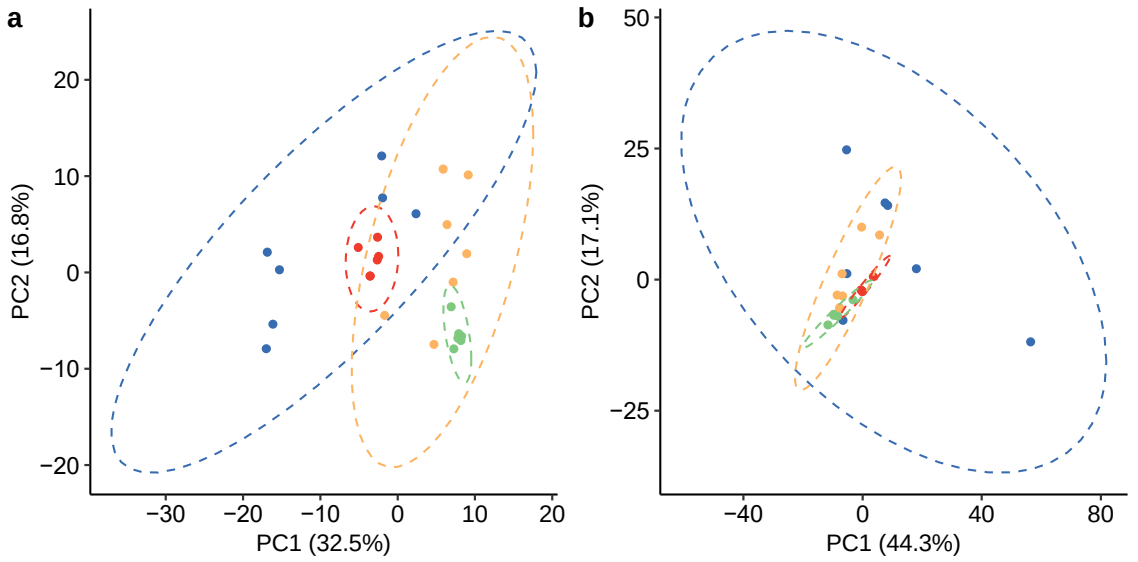


Figure 3.3 PCA score plots visualising the metabolic differences between samples harvested by centrifugation or filtration.
Data shown were measured by **a** nESI-DIMS polar metabolomics (positive ion mode) and **b** nESI-DIMS lipidomics (positive ion mode). Replicate samples are colour coded as: ● centrifugation—biological replicates; ● centrifugation—technical replicates; ● filtration—biological replicates; and ● filtration—technical replicates. Dashed lines show 95% confidence intervals for each group of samples.

Table 3.2 Coverage, technical and total reproducibility of metabolomics datasets from microtissues harvested by either centrifugation or filtration.
Summary metrics to evaluate the relative coverage of the microtissue metabolome/lipidome (*m/z* feature count), technical reproducibility (mRSD across technical replicates) and total reproducibility (mRSD across biological replicates) for pooled microtissues sampled by either centrifugation- or filtration-based approaches and all analysed by nESI-DIMS metabolomics and lipidomics (positive ion mode).

Assay	Metabolomics		Lipidomics	
Sampling Method	Centrifugation	Filtration	Centrifugation	Filtration
Feature count	1697	3169	3173	4919
Technical variation: mRSD across technical replicates (%)	17.0	12.9	13.0	20.4
Total variation: mRSD across biological replicates (%)	42.1	35.5	50.2	31.6

Thorough removal of residual culture medium from cells is preferable to limit contamination of intracellular extracts (79). This is particularly important for nESI-DIMS measurements where high-concentration, highly ionisable compounds in the media (potentially including the exposure chemical) can induce ion competition in the MS source, suppressing detection of the intracellular metabolome and lipidome (112). The use of isotonic washing solutions, e.g., 0.9% NaCl, is preferable in order

to minimise metabolite leakage by osmotic shock to the cells (79). However, residual salts in analytical samples can interfere with nESI-DIMS measurements; thus, a final water wash, rapid enough to minimise osmotic shock (<20-seconds), is recommended (215).

Consequently, I sought to optimise the procedures for washing harvested microtissues as part of the filtration-based sampling approach. This was achieved by evaluating the impact of the number and volume of saline wash steps on the nESI-DIMS measurement of process blanks, and thus the effectiveness of residual media removal, by comparing the total number of features detected per group and the relative intensities of features per group. Washing was shown to impact the amount of residual media removed from the cell strainers, demonstrated by the significant decrease in the number of features detected from washed strainers compared to no washing (Figure 3.4a) and a significant reduction in the intensities of between 71 and 117 features, depending on the washing protocol, that were detected in at least two of three replicates per group (q <0.1, one-way ANOVA with Tukey's HSD post-hoc test and FDR correction; Figure 3.4b). Included in the features with significantly reduced intensities are constituents of cell culture media (e.g., putatively annotated lactic acid, amino acids; Table eB.1). Upon examining a range of washing options, 3x 1 mL 0.9% NaCl followed by 1x 1 mL water yielded the least number of detected features and, of those, the most features with significantly reduced intensities compared to no washing. It was concluded to wash with 3x 1 mL 0.9% NaCl, plus 1x 1 mL water, to limit the residual culture medium contamination on the cell strainers during sampling of cardiac microtissues for metabolomics analysis.

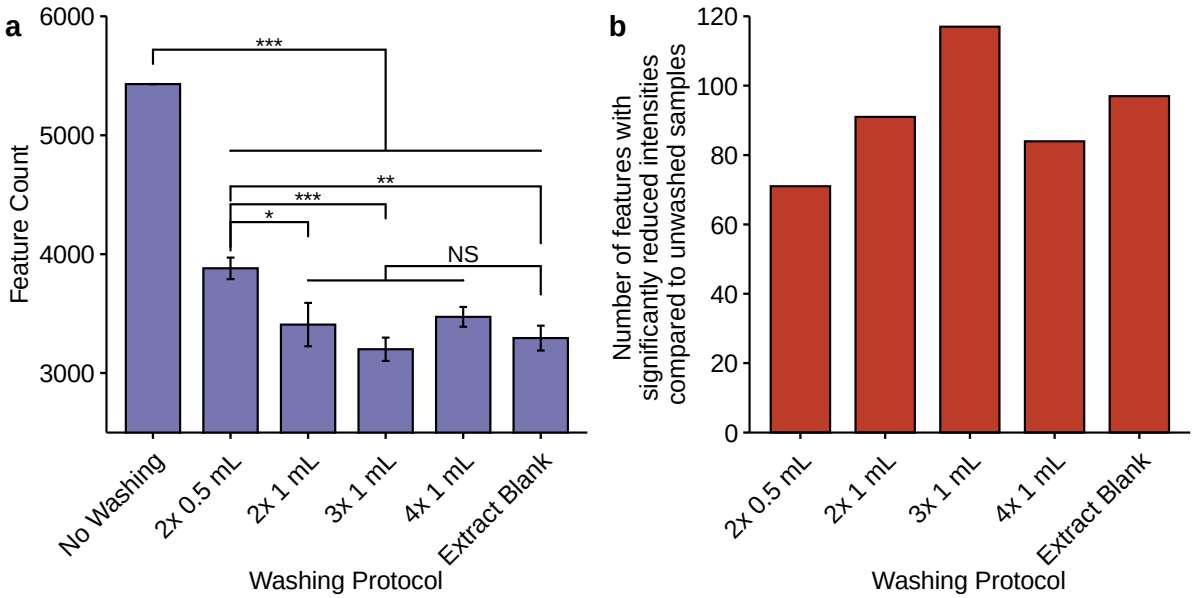


Figure 3.4 Evaluation of washing procedures for filtration-based sampling of microtissues. **a** Bar chart showing the total number of features detected in process blanks prepared without washing, or with 2x 0.5 mL, 2x 1 mL, 3x 1 mL or 4x 1 mL 0.9% NaCl washes, followed by 1x 1 mL water wash. Negative control data were acquired from extraction blanks (i.e., no medium was passed through the cell strainer prior to extraction). Error bars display standard error across three replicates. Significant differences between groups (one-way ANOVA with Tukey's HSD post-hoc test) are displayed: *** p <0.01, ** p <0.05, * p <0.1, NS, not significant. **b** Bar chart showing the number of features (of 2023 features detected in ≥2 of 3 replicates in each group) whose intensities are significantly reduced by each washing protocol compared to no washing. Significant reduction in feature intensity is defined where fold change of median intensity in washed samples compared to non-washed samples is <1 and q <0.1, calculated by one-way ANOVA with Tukey's HSD post-hoc test and FDR correction.

Thus, here, a filtration-based approach which allows for rapid, reproducible, and efficient harvesting of suspended cell cultures for untargeted metabolomics is presented. Although only demonstrated for cardiac microtissues, I propose this approach would be appropriate for other suspended cell cultures of low biomass.

3.3.2 Sensitivity and reproducibility of nESI-DIMS untargeted metabolomics measurements using very low biomass samples

Following the demonstration of an improved methodology for the sampling of cardiac microtissues relative to a more conventional centrifugation-based approach, I sought to characterise the sensitivity and reproducibility of nESI-DIMS untargeted metabolomics measurements across a gradient of cardiac microtissue biomasses, with the aim to determine which biomass to use in subsequent toxicology studies.

Specifically, four biomasses were selected based on practical feasibility, corresponding to 28-, 21-, 14- and 7-pooled microtissues.

The sensitivity of the nESI-DIMS untargeted metabolomics was assessed according to the number of features detected in ≥80% of samples (biological replicates and intra-study QCs that were composed of an equivalent number of microtissues as the biological samples) after blank subtraction, at each sample biomass. As expected, the *m/z* feature count increased with increasing sample biomass (Table 3.3). Specifically, there was a 1.7-fold and 1.8-fold increase in the number of features detected by the metabolomics and lipidomics assays, respectively, when samples consisting of 28-pooled microtissues were compared to just 7-pooled microtissues. I concluded that the maximum feasible number of microtissues per sample, 28 (ca. 14,000 cells), should be employed to maximise detection of the metabolome and lipidome.

Table 3.3 Sensitivity, technical and total reproducibility of metabolomics datasets from microtissue samples of varying biomass.
Summary metrics to evaluate the detection sensitivity (feature count), technical reproducibility (mRSD across intra-study QCs) and total reproducibility (mRSD across biological replicates) of measurements are reported for samples of 7, 14, 21 or 28 pooled cardiac microtissues analysed by nESI-DIMS metabolomics and lipidomics (positive ion mode).

Assay	Metabolomics				Lipidomics			
Sample biomass (Number of pooled cardiac microtissues)	7	14	21	28	7	14	21	28
Feature count	796	817	1030	1321	1427	1765	2336	2507
Technical variation: mRSD across intra-study QCs (%)	13.7	10.6	18.0	20.5	17.6	16.9	15.1	12.4
Total variation: mRSD across biological replicates (%)	37.1	39.0	40.5	31.9	33.4	37.9	34.7	27.6

It is noteworthy that of the 367 metabolite and 914 lipid features detected consistently across all four sample biomasses, the intensities of 45% and 50% of these features, respectively, showed a significant positive correlation (Spearman's, $p < 0.05$) with the sample biomass. This association evidences the biological origin of

those features, thus demonstrating that a reduced feature metabolic and lipidomic signature could, in fact, be measured using nESI-DIMS analysis of as little as seven pooled microtissues (ca. 3,500 cells).

The technical reproducibility of the nESI-DIMS measurements was assessed by mRSDs across replicates derived from intra-study QCs for each sample biomass. The mRSD values were ≤20.5% for all four microtissue biomasses (Table 3.3), which were deemed acceptable based on the mRSDs reported for cell-based samples of a larger biomass, e.g., technical mRSD of 14% for human immortalised K562 cells analysed by nuclear magnetic resonance spectroscopy (214).

Variation measured across biological replicates can originate from any step in the workflow from cell culturing through to the analytical measurement. Minimising this variation can improve statistical power in comparative analyses, e.g., in the discovery of metabolic features perturbed by chemical exposure. Our data show no clear trend in the total variation as a function of the sample biomass; however, the most reproducible peak intensities, as indicated by the lowest mRSD across biological replicates, are observed for samples composed of 28-pooled microtissues for both metabolomics and lipidomics measurements (Table 3.3), further supporting the selection of 28-pooled microtissues per sample for subsequent studies.

Thus, I have demonstrated that implementation of spectral stitching nESI-DIMS enables reproducible untargeted metabolomic analysis of samples composed of as little as ca. 3,500 cells. This discovery may encourage the application of untargeted metabolomics to other sample types which suffer from a limited biomass.

3.3.3 PROBING MOLECULAR RESPONSES OF CARDIAC MICROTISSUES TO SUNITINIB EXPOSURE

With validation of a filtration-based sampling approach for cardiac microtissues and confirmation that the nESI-DIMS analytical method is sufficiently sensitive and reproducible for untargeted analyses of intracellular extracts from 28-pooled microtissues, I next sought to demonstrate the capability of this approach to discover time-resolved intracellular metabolic responses of cardiac microtissues following exposure to sunitinib, a synthetic drug and clinically labelled cardiotoxin. Additionally, I implemented UHPLC-MS(/MS) analysis of the spent culture medium from the same samples both to characterise changes to the metabolic footprint of cardiac microtissues following exposure to sunitinib and to quantify extracellular concentrations of sunitinib over the duration of exposure.

The responses to two concentrations of sunitinib were investigated: 3.5 μM ('high') and 1.1 μM ('low'), where the high concentration is phenotypically anchored to the 30% maximal inhibitory concentration (IC_{30}) of adenosine triphosphate (ATP) depletion after 72-hour of exposure (36), i.e., a concentration known to induce some metabolic disruption, and the low concentration is a half-log dilution of the high concentration.

3.3.3.1 Phenotypic measurements demonstrate adversity at 72-hours

HCB measurements (36) conducted on a subset of microtissues provided confirmation that phenotypic perturbations are induced by both concentrations of sunitinib after 72-hours. Specifically, the high exposure to sunitinib (3.5 μM) induced an 83.9% and 24.8% reduction in ER integrity and Δψm, respectively (Figure 3.5). Meanwhile, the low exposure (1.1 μM) induced a slight change (−9.5%) to Δψm and a more significant 63.1% loss of ER integrity by 72-hours (Figure 3.5). These results are consistent with previously reported dose–response relationships of sunitinib-

exposed cardiac microtissues, thus demonstrating the high reproducibility of the *in vitro* model (36).

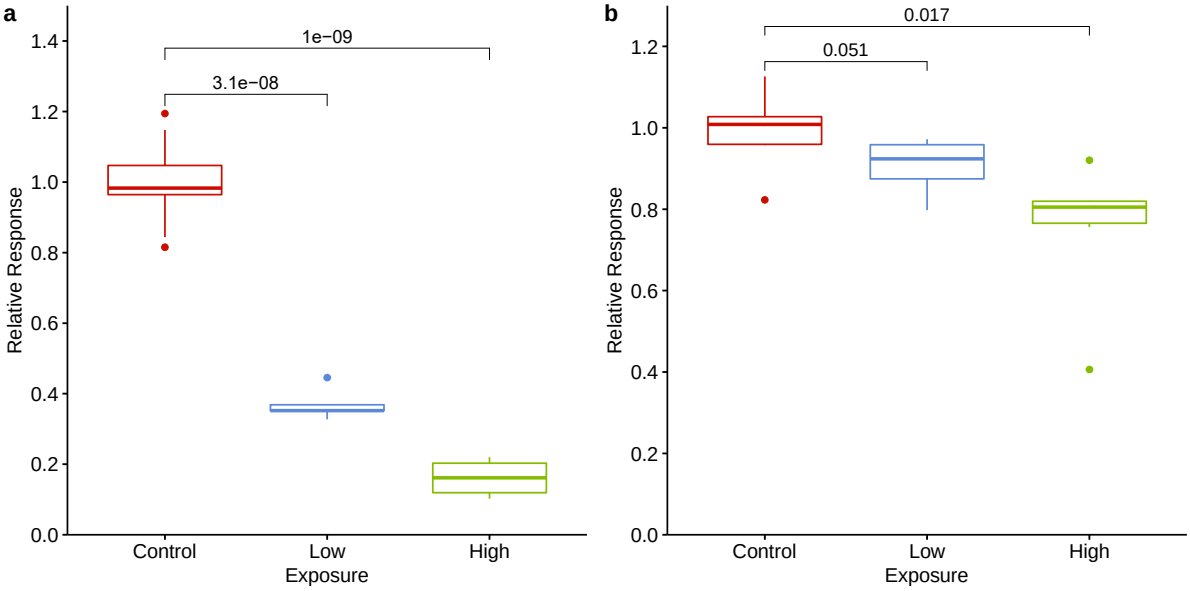


Figure 3.5 Phenotypic perturbations induced by 72-hour exposure to a low and high dose of sunitinib in cardiac microtissues.
Box plots showing the relative change to **a** endoplasmic reticulum integrity and **b** mitochondrial membrane potential of cardiac microtissues exposed to either low (1.1 µM) or high (3.5 µM) concentration of sunitinib, compared to controls, as measured by high content biology imaging assays. *p*-values calculated by two-sided *t*-tests are displayed.

3.3.3.2 Quantitation of extracellular sunitinib in spent culture medium indicates uptake into microtissues

Targeted absolute quantitation of sunitinib as part of the same UHPLC-MS(/MS) analytical run applied for untargeted metabolomics (described later), using an external sunitinib calibration curve (Figure 3.6a), allowed us to confirm and evaluate the variability of sunitinib exposure concentrations across biological replicates, and to estimate the extent of uptake into the microtissues. The measurements showed extracellular sunitinib concentrations reached an equilibrium of 77% and 69% of the nominal low and high concentrations, respectively, by 2-hours and remained consistent at least up to 48-hours (Figure 3.6b). This suggests a 23% and 31% uptake of sunitinib at low and high exposures, respectively, into the cardiac microtissues, assuming the nominal exposure concentrations were accurate and

negligible nonspecific binding of sunitinib occurred, e.g., to plasticware. This second assumption is substantiated by there being no significant difference between the nominal and measured concentrations of sunitinib in 'negative control' samples that include media and sunitinib but lack microtissues. At 72-hours, extracellular levels were restored to 132% and 90% of the nominal high and low exposures, respectively, a significant increase from the levels measured at 48-hours (p < 0.0001, two-sided t-test), suggesting efflux of the drug from microtissues may occur between 48- and 72-hours (Figure 3.6b). The variability in exposure concentrations between samples was low, with mRSDs across biological replicates (sum of biological and technical variability) of <20% for both exposure concentrations at all time points.

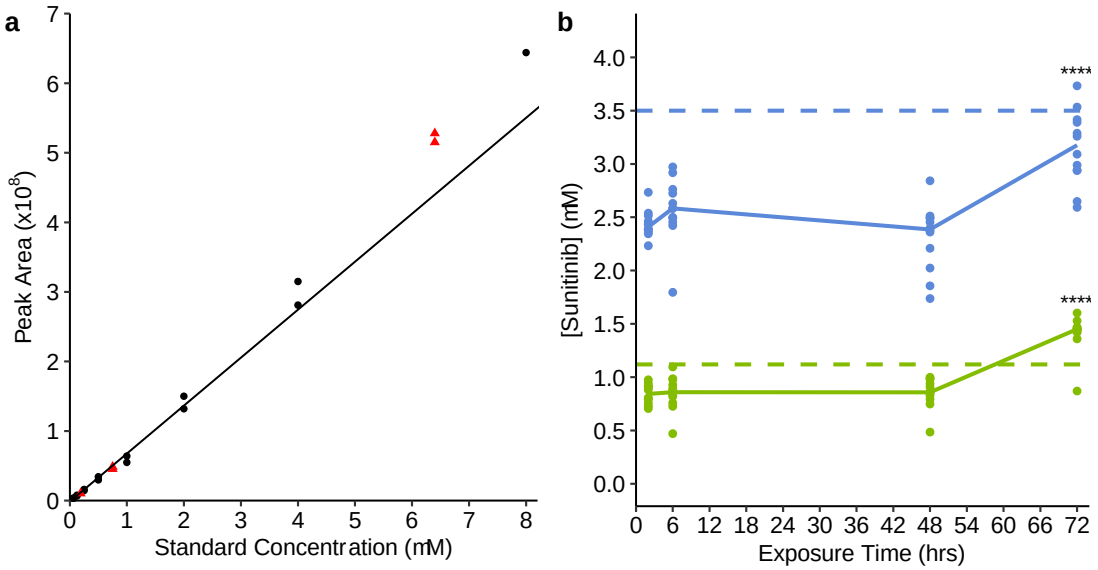


Figure 3.6 Quantitation of sunitinib concentrations in spent culture media of cardiac microtissues.
a External calibration curve for sunitinib. Black points show measured peak areas of accepted external calibration standard samples and red points show peak areas of accepted quantitation quality control samples (quant-QCs) (acceptance criteria for calibration standards and quant-QCs are described in Section 3.2.5.5). A $\frac{1}{x^2}$ linear curve with formula $\boldsymbol{y = 6.90 \times 10^7 x - 1.15 \times 10^6}$ was fitted to the external calibration standard data. The calibration curve fits the data with R^2 = 0.99. **b** Absolute sunitinib concentrations in spent media of pooled microtissues collected at 2-, 6-, 48- and 72-hours after initial exposure as calculated from measured peak areas using an external calibration curve. Solid lines show the median extracellular sunitinib concentration at each time point for low (green) and high (blue) exposures separately. Nominal low and high exposure concentrations are displayed

as a dashed line, green and blue, respectively. **** p <0.0001, for comparison of concentrations at 48- vs. 72-hours, per concentration (two-sided t-test). All other comparisons of concentrations at consecutive time points (2- vs. 6-hours, 6- vs. 48-hours) were not significant (p > 0.05).

Absolute quantitation of exposure drugs in *in vitro* studies is not routinely obtained, and while measurements of an exposure drug in the same biological samples as those used to probe endogenous metabolic responses have been demonstrated previously (Chapter 2), these were limited to relative exposure levels only. Here, I demonstrate that by including an external calibration curve in the analytical sequence, it is possible to absolutely quantify exposure drug concentrations using the same UHPLC-MS(/MS) untargeted measurements used to probe endogenous responses. In *in vitro* toxicology studies, such measurements offer the opportunity to enhance IVIVE by providing confidence in actual exposure concentrations and to make evidence-based predictions on the amount of drug uptake.

3.3.3.3 Untargeted metabolomics and lipidomics reveal time-dependent sunitinib-induced intracellular and extracellular perturbations in cardiac microtissues

Four nESI-DIMS assays were implemented to measure the intracellular polar metabolome and lipidome, both in positive and negative ion modes, of cardiac microtissues exposed to sunitinib (high concentration—3.5 µM; low concentration—1.1 µM) or 0.1% (v/v) DMSO (control), sampled at 2-, 6-, 48- and 72-hours after initial exposure. Intra-study QCs were derived from a single pool of control cardiac microtissue extracts. Biological feature counts, after data processing, were 1874 and 1559, and 2106 and 2456, for positive and negative ion metabolomics, and positive and negative ion lipidomics assays, respectively. The technical variability of the datasets was estimated from QCs, with mRSDs of 33.8% and 6.8%, and 9.0% and 14.0%, for positive and negative ion metabolomics, and positive and negative ion lipidomics assays, respectively, indicating high technical reproducibility in three of the four assays. The positive ion metabolomics dataset was deemed of poor

technical quality and thus not considered further. The total metabolic variability was assessed for each group of biological replicates, with mRSDs ranging between 20.0% and 49.6% for all groups and assays (Figure 3.7). No clear trend in the total metabolic variability with respect to treatment class or time point was observed.

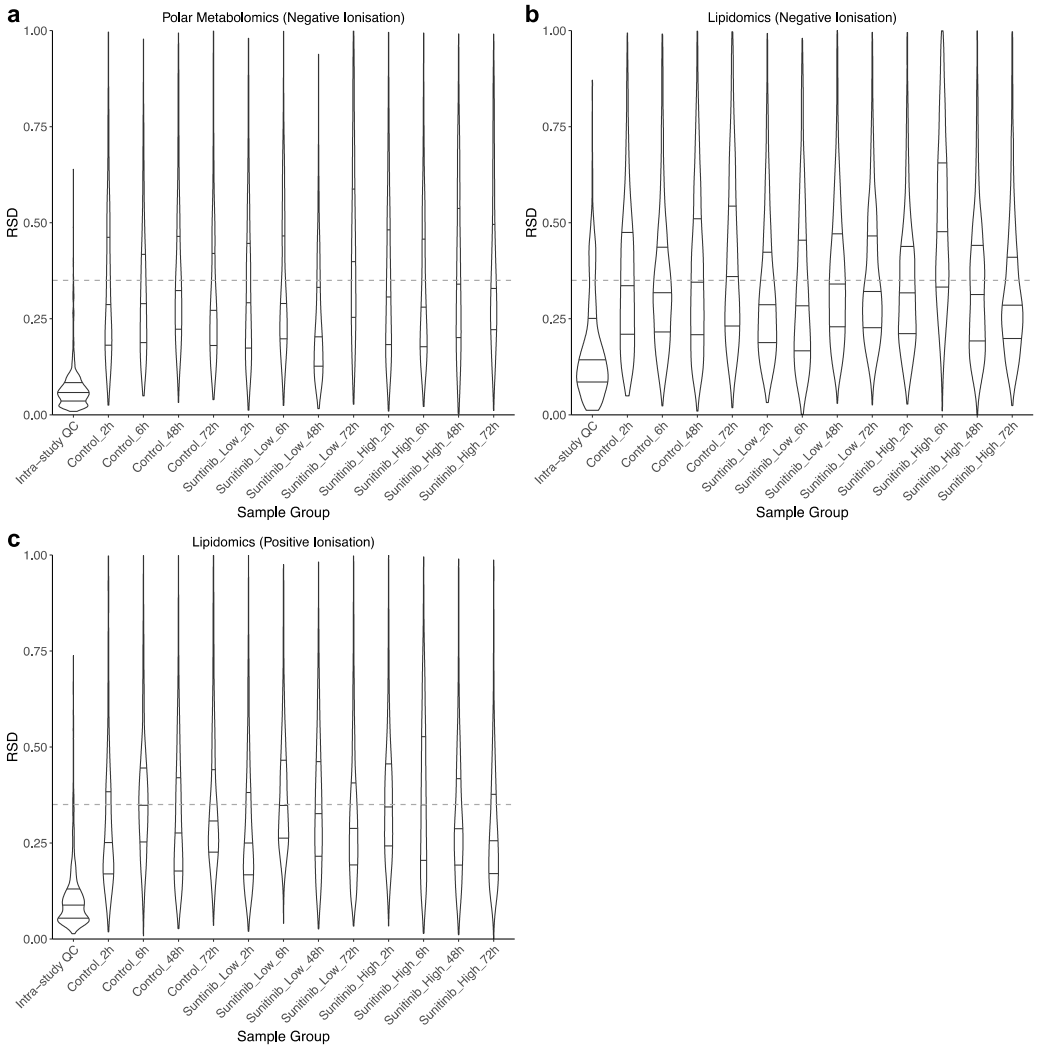


Figure 3.7 Assessment of total metabolic variability.
Violin plots displaying the distribution of feature intensity RSDs measured per sample group for nESI-DIMS **a** negative metabolomics, **b** positive lipidomics and **c** negative lipidomics assays.

Univariate statistical analysis (one-way ANOVAs with Tukey's HSD post-hoc testing) comparing measured levels of intracellular features in sunitinib-exposed vs. control microtissues revealed a significant perturbation of the cardiac microtissue metabolome after 6-, 48- and 72-hours (Figure 3.8a). The greatest perturbation of

the intracellular metabolome was observed in response to low sunitinib exposure after 6-hours, where the intensities of 315 features changed significantly (*q*-value <0.1, one-way ANOVA with Tukey's HSD post-hoc testing) compared to time-matched controls. At 48-hours, the levels of 69 and 47 polar features were significantly different in microtissues exposed to low and high concentrations of sunitinib, respectively, compared to controls. Meanwhile, at 72-hours, significant differences were only detected in microtissues exposed to the higher concentration of sunitinib.

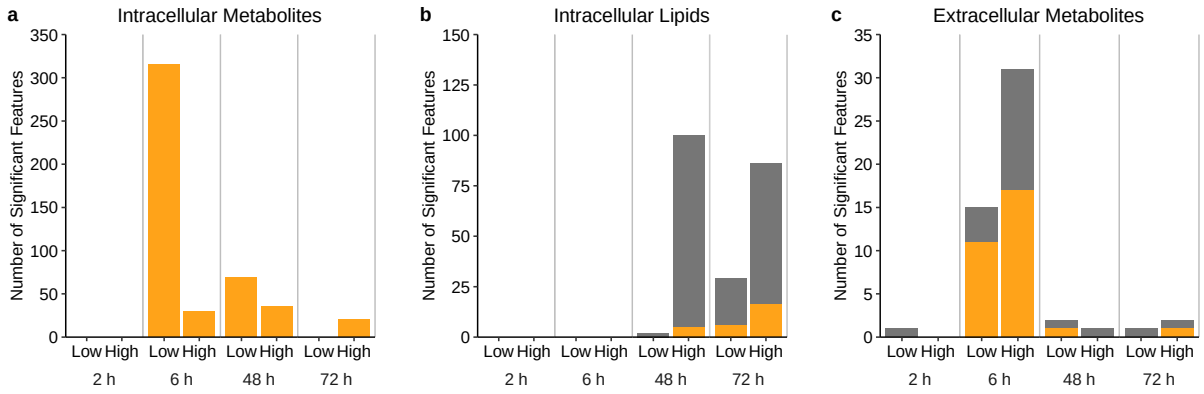


Figure 3.8 Univariate data analysis reveals significant perturbation of intracellular and extracellular features.
Bar charts summarising the number of significantly changing *m/z* features following the exposure of cardiac microtissues to sunitinib. Number of **a** intracellular metabolite, **b** intracellular lipid and **c** extracellular metabolite features whose intensities changed significantly upon exposure to two concentrations of sunitinib for 2-, 6-, 48- or 72-hours, relative to controls. Stacked bars show contribution of measurements from positive (grey) and negative (yellow) ionisation-based assays. Significance defined as *q* <0.1, one-way ANOVA with Tukey's HSD post-hoc test and false discovery rate correction.

The largest response of the intracellular lipidome was observed at 48-hours following high exposure to sunitinib. Here, the intensities of 100 features were significantly different compared to the control. A significant lipidomic response to the lower concentration of sunitinib was not apparent until 72-hours, when the intensities of 29 features were significantly perturbed compared to the control. In contrast, the intensities of 86 features were significantly perturbed in microtissues exposed to the

higher concentration of sunitinib at 72-hours (Figure 3.8b). Further analysis, by *k*-means cluster analysis, revealed five subclusters of intracellular lipids displaying distinct temporal responses when exposed to the higher concentration of sunitinib. A subset of lipids in three of the five subclusters showed dose dependency in their response, with comparable temporal trends of lower magnitude observed in response to the lower concentration of sunitinib (Figure 3.9).

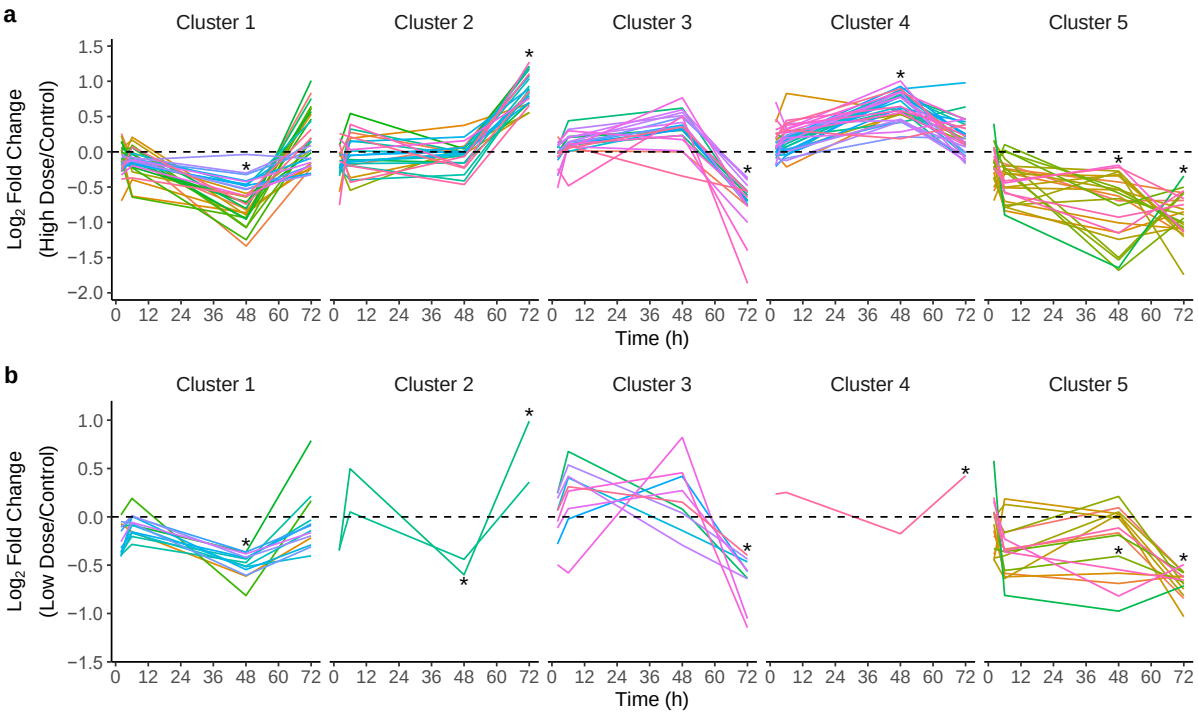


Figure 3.9 *k*-means cluster analysis reveals similarities in the temporal responses of intracellular lipid features.
a Clusters of temporal response (log_2 fold change, treated compared to control, at 2-, 6-, 48- and 72-hours) of annotated lipid features showing significant change (*p*-value < 0.05, 1-way ANOVA with Tukey's HSD) in relative levels in microtissues exposed to high concentration of sunitinib were calculated by *k*-means cluster analysis (*k* = 5, selected using elbow method). These response patterns correspond to a reduction at 48 h but with recovery to normal levels by 72-hours, increase in levels at 72-hours, reduction at 72-hours, increase at 48-hours but with recovery to normal levels by 72-hours and a reduction at 48- and 72-hours for clusters 1, 2, 3, 4, and 5, respectively. **b** Analysis of the same lipids following exposure to low concentration sunitinib reveals comparable time-dependent significant responses of smaller magnitude for 12 of 30, 9 of 21, and 15 of 24 lipids belonging to clusters 1, 3 and 5, respectively, revealing a dose-dependency of these temporal patterns. Only one of the lipids aligning to cluster 4 displayed a significant response to low exposure, with the significantly different levels occurring at 72-hours. Furthermore, only two of the lipids aligning to cluster 2 significantly responded to the low concentration of sunitinib, one at 48-hours, and one at 72-hours. * *p* <0.05 at specified time point for the majority of features shown in the cluster as measured by one-way ANOVA with Tukey's HSD post-hoc test.

In addition to nESI-DIMS untargeted metabolomics and lipidomics of the intracellular extracts, UHPLC-MS(/MS) untargeted metabolomics was conducted on spent culture medium from the same cardiac microtissues. Feature counts after data processing and peak matrix filtering were 756 and 548 for the positive and negative ion modes, respectively. Univariate statistical analyses (one-way ANOVA with Tukey's HSD post-hoc test) revealed significant differences (q <0.1) in the intensities of 18 and 28 features following exposure to low- and high-concentration sunitinib, at 6-hours. Meanwhile, only 1, 2 and 1 feature(s) significantly responded to low-sunitinib exposure at 2-, 48- and 72-hours, respectively, and 0, 2 and 1 feature(s) significantly responded in response to high-sunitinib exposure at 2-, 48- and 72-hours, respectively (Figure 3.8c). The time of this maximal effect on the extracellular footprint is consistent with the largest response of the intracellular polar metabolome.

I further sought to discover intracellular metabolic perturbations in cardiac microtissues induced by exposure to sunitinib using supervised multivariate analyses. PLS-DA was conducted separately for each treated (either high or low concentration of sunitinib) vs. control comparison across all assays and time points. Acceptable models were built which separated the low-exposure negative ion metabolome at 2-, 6- and 48-hours, and high-exposure negative ion lipidome at 48- and 72-hours, from the time-matched controls (Figure 3.10; Table 3.4).

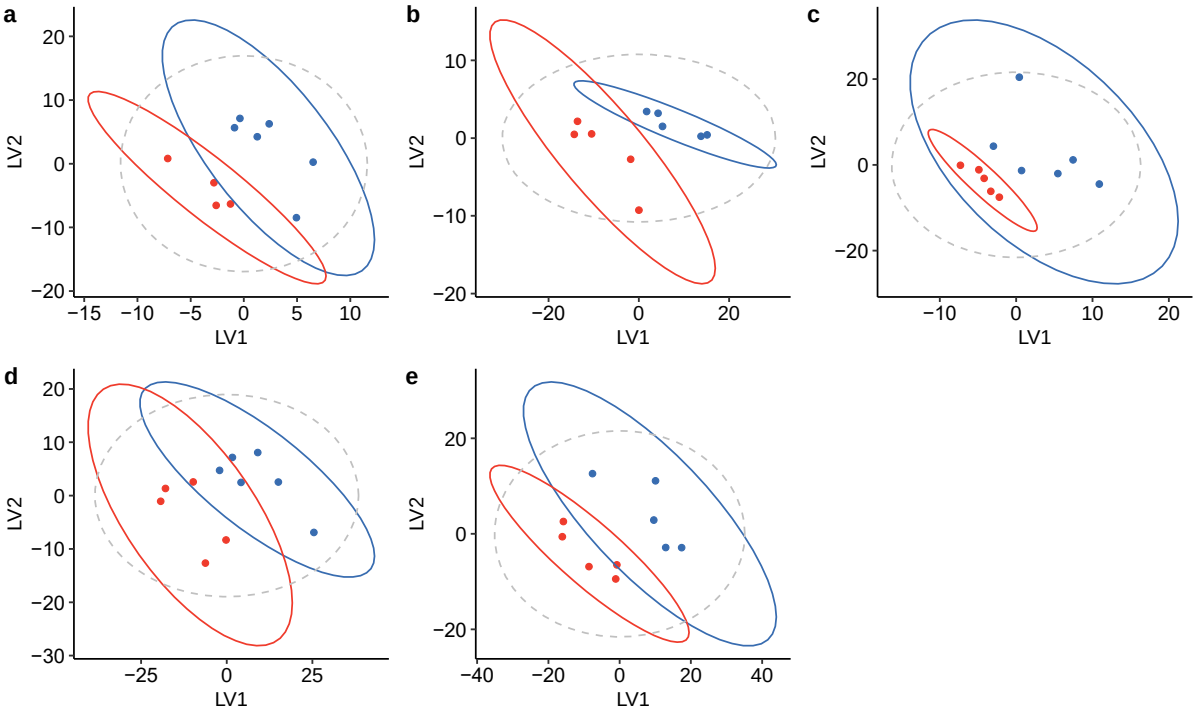


Figure 3.10 PLS-DA scores plots discriminating between sunitinib exposed and control samples.
Scores plots of PLS-DA models (latent variables 1 and 2) discriminating between the negative ion metabolome, of microtissues exposed to a low concentration (1.1 μM) of sunitinib (red) and control microtissues (blue) at **a** 2-hours, **b** 6-hours and **c** 48-hours after initial exposure. Scores plots of PLS-DA models (latent variables 1 and 2) which discriminate between the negative ion lipidome of microtissues exposed to a high concentration (3.5 μM) of sunitinib (red) and control microtissues (blue) at **d** 48-hours and **e** 72-hours are also displayed. Solid lines show 95% confidence interval of each group. The dashed grey line shows the 95% confidence interval of all samples.

Table 3.4 Performance metrics for PLS-DA models.
The mean R^2 ± standard deviation (SD) as calculated by 10-fold cross-validation (using the leave-one-out method), Q^2, balanced error rate (BER) and BER *p*-value, as calculated using the formula $\boldsymbol{P = \frac{1+\#(NMC_p \leq NMC)}{N}}$, where $\boldsymbol{NMC}$ is the number of misclassifications, $\#(\boldsymbol{NMC_p \leq NMC})$ is the number of elements in the null distribution which are smaller or equal to the $\boldsymbol{NMC}$ for the original dataset and $\boldsymbol{N}$ is the number of permutations (100), are reported for each PLS-DA model.

Metabolomics assay	Comparison	Time (hours)	R^2 ± SD	Q^2	BER	BER *p*-value
Polar Negative	Low Dose vs Control	2	0.94 ± 0.04	0.51	0.083	0.02
Polar Negative	Low Dose vs Control	6	0.94 ± 0.02	0.65	0.1	0.03
Polar Negative	Low Dose vs Control	48	0.91 ± 0.02	0.70	0	0.01
Non-Polar Negative	High Dose vs Control	48	0.95 ± 0.02	0.64	0.18	0.05
Non-Polar Negative	High Dose vs Control	72	0.96 ± 0.01	0.51	0.1	0.02

Comparison of features important to the models (VIP score >1) at each time point revealed a relatively high level of consistency, suggesting the same set of metabolites and lipids is capable of discriminating a sunitinib-perturbed intracellular

microtissue metabolome or lipidome from that of controls at any time point (Figure 3.11). Specifically, 191 and 388 features were consistently important in discriminating the effects of sunitinib on the metabolome and lipidome, respectively.

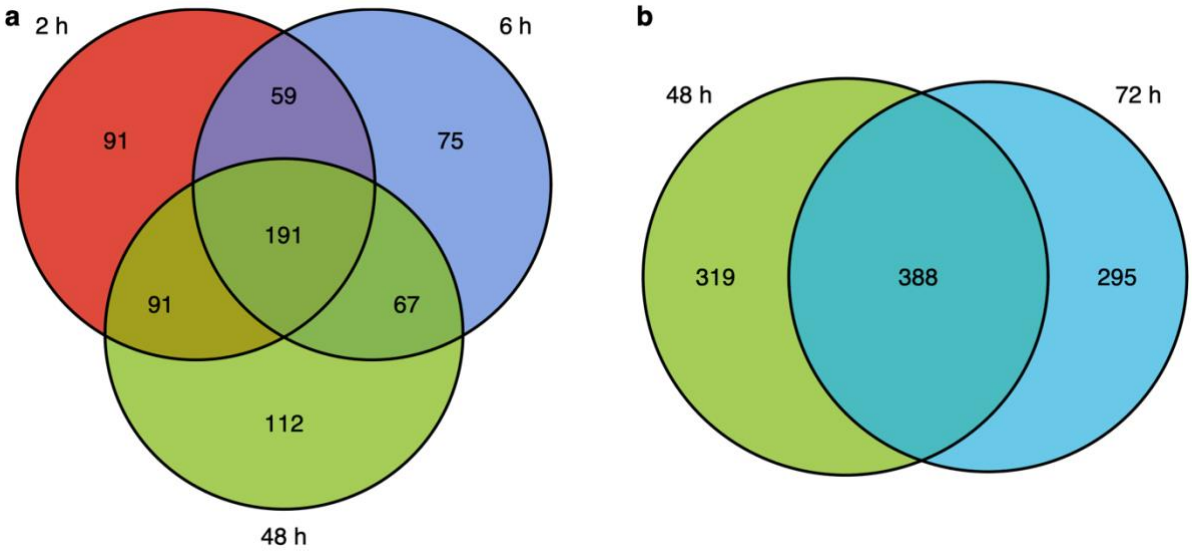


Figure 3.11 Consistency in features important to PLS-DA models.
Venn diagrams displaying the overlap in features with VIP scores >1 in PLS-DA models discriminating **a** between the polar metabolome, as measured by polar negative assay, of microtissues exposed to low-dose sunitinib and control microtissues at 2-, 6- and 48-hours after initial exposure, and **b** between the lipidome, as measured by lipid negative assay, of microtissues exposed to high-dose sunitinib and control microtissues at 48- and 72-hours after initial exposure.

Annotation of biological features can allow hypotheses to be generated with respect to the perturbations induced at the pathway level. Here, a statistical enrichment (FDR-corrected *p*-value, hypergeometric test) of polar metabolites associated with purine metabolism was observed, in response to sunitinib exposure for 6-hours, as determined by univariate analyses (Table eB.2, Table 3.5).

Table 3.5 Results of over-representation pathway analysis of metabolites significantly perturbed by sunitinib exposure in cardiac microtissues.
The number of metabolites (putatively annotated) that were significantly perturbed by sunitinib exposure which align to each KEGG metabolic pathway (211) (Number of hits) and the total number of metabolites in each KEGG metabolic pathway (Total number of metabolites in pathway) are reported. The expected number of hits refers to the number of metabolites within a given pathway expected to be within the list of significantly changing metabolites in the case of no enrichment (depends on number of significantly changing metabolites and number of metabolites in pathway). The fold enrichment of significantly changing metabolites (putative annotations) aligning to each KEGG metabolic pathway was calculated as the ratio of number of hits to expected number of hits, and the significance assessed by a hypergeometric test (p-value, q-value with FDR correction). The top four enriched pathways are displayed.

Pathway	Total number of metabolites in pathway	Expected number of hits	Number of hits	Fold Enrichment	*p*-value	*q*-value (FDR correction)
Purine metabolism	65	1.26	7	5.6	0.0002	0.0131
Pyrimidine metabolism	39	0.75	3	4.0	0.0374	1.000
Lysine degradation	25	0.48	1	2.1	0.389	1.000
Galactose metabolism	27	0.52	1	1.9	0.413	1.000

Additionally, the intensities of three metabolites - hypoxanthine, inosine and L-glutamine (MSI level 1 annotation, using accurate *m/z*, RT and MS/MS fragmentation match to reference standards, Figure B.1, Figure B.2, Figure B.3) - were discovered to be significantly different in the spent medium of sunitinib-exposed microtissues relative to untreated controls, at 6-hours (Figure 3.11). These metabolites are all constituents of the purine metabolism pathway (map00230, KEGG PATHWAY (211)), thereby supporting the hypothesis from the intracellular metabolomics that sunitinib perturbs purine metabolism in cardiac microtissues within 6-hours of initial exposure.

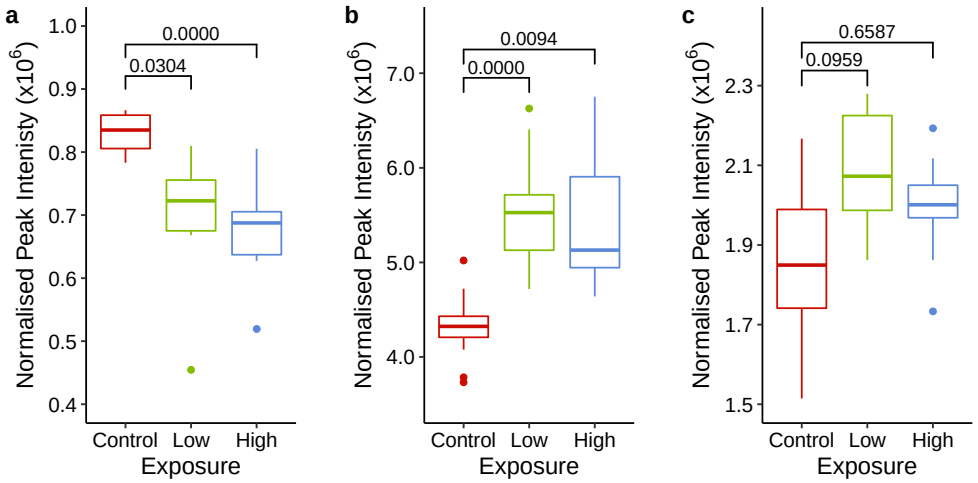


Figure 3.12 Responses of extracellular metabolites following sunitinib exposure. Peak intensities of **a** hypoxanthine ($[2M-H]^-$), **b** inosine ($[M+H]^+$) and **c** L-glutamine ($[M-H-H_2O]^-$) measured using HILIC UHPLC-MS in the spent culture medium of control (exposed to 0.1% DMSO), low (1.1 µM sunitinib) and high (3.5 µM sunitinib) cardiac microtissues at 6-hours after exposure. The *q*-values (one-way ANOVA with Tukey's HSD post-hoc test and FDR corrected) are displayed.

Disruption of purine metabolism has also been linked with doxorubicin-induced cardiotoxicity *in vitro*. Specifically, an enrichment of purine metabolism pathway (hsa00230, KEGG) constituents was discovered amongst significantly down-regulated genes in doxorubicin-treated hiPSC-CMs (216). Thus, our results, coupled to previous findings, implicate purine metabolism dysfunction in the progression of drug-induced structural cardiotoxicity.

Furthermore, putative annotation of the features with a VIP score >1 across multiple PLS-DA models revealed a notional importance for the response of polyunsaturated fatty acids, amongst other metabolites and lipids, in discriminating sunitinib-perturbed microtissues from controls (Table eB.3, Table eB.4) This poses these molecules as of interest for further characterisation as potential biomarkers of drug-induced structural cardiotoxicity. Polyunsaturated fatty acids have previously been shown to impact the development of drug-induced structural cardiotoxicity. Specifically, pre-treatment with eicosapentaenoic or docosahexaenoic acid significantly attenuated activation of the NF-ϰB/iNOS/NO signalling pathway,

increased ROS, change to mitochondrial membrane potential, cytotoxicity and inflammation induced by doxorubicin, a structural cardiotoxin, in H9C2 cells (217, 218).

These results demonstrate the capability of our workflow, involving nESI-DIMS untargeted metabolomics and lipidomics of intracellular extracts, and UHPLC-MS(/MS) untargeted metabolomics of spent culture medium, to reveal metabolic and lipidomic perturbations in cardiac microtissues induced by a structural cardiotoxin, in this case, sunitinib. The time dependency of these effects reveals the importance of incorporating temporal resolution into the design of toxicity studies. Furthermore, through annotation of perturbed biological features, it is possible to develop evidence-based hypotheses on the mode of action and discover putative metabolic and/or lipid biomarkers of drug-induced structural cardiotoxicity in cardiac microtissues.

3.4 Conclusion

A filtration-based approach for the sampling of cardiac microtissues for nESI-DIMS untargeted metabolomics was shown to minimise handling times, reduce metabolic variation and, with an optimised washing protocol, sufficiently remove media. Furthermore, the nESI-DIMS analytical method was deemed sufficiently sensitive and reproducible to measure intracellular metabolic and lipid *m/z* features in samples consisting of as few as 7-pooled microtissues (ca. 3,500 cells), while samples consisting of 28-pooled microtissues (ca. 14,000 cells) resulted in higher feature counts and more reproducible data and thus were selected for our subsequent toxicology study. I also demonstrated an extensive metabolomics-based workflow incorporating untargeted intracellular metabolomics and lipidomics by nESI-DIMS, and UHPLC-MS(/MS) analysis of spent culture medium for untargeted measurement

of metabolic footprints and absolute quantitation of the exposure drug, together capable of discovering time-resolved cardiotoxin-induced perturbations in a highly relevant *in vitro* model, cardiac microtissues. The observed metabolic and lipid perturbations provide sufficient evidence to hypothesise toxicological modes of action, including perturbation of purine metabolism and a role for polyunsaturated fatty acids, and may be further characterised for use as molecular biomarkers of drug-induced structural cardiotoxicity.

CHAPTER 4: CHARACTERISING THE CARDIAC MICROTISSUE METABOLOME AND LIPIDOME

4.1 INTRODUCTION

The metabolite annotation of spectral features is integral to the application of untargeted metabolomics for toxicology and safety assessment. In a confidence-in-identification (CII) framework which considers the use of untargeted metabolomics in regulatory toxicology, Malinowska and Viant propose that metabolic predictive biomarkers, if to be used individually, would need to be identified to MSI level 1, but a range of confidence levels could be acceptable for a panel of markers (126). Meanwhile mechanistic interpretation of metabolomics data through pathway enrichment analysis, e.g., for discovery of molecular KEs, relies on achieving correct annotations with good coverage (125). Yet despite its importance to biomarker and molecular KE discovery in toxicology, metabolite annotation remains a significant bottleneck in untargeted metabolomics (95).

The challenge of annotation in MS-based metabolomics is a consequence of multiple factors. First, annotation approaches must deconvolute the highly redundant data, integrating the multiple signals pertaining to single metabolites that arise by ESI (95, 130). Second, a single, resolved, monoisotopic mass may be annotated with multiple chemical structures due to the existence of several types of isomers within biology. Meanwhile, accounting for a degree of mass error in the measurement means searches often span a range of ±5 ppm around the measured mass, further extending the list of putative metabolite annotations for a single feature (95, 130). Finally, the public metabolite databases, e.g., HMDB (128), KEGG (124, 211), LMSD (129), often used as the ‘search space’ for annotation purposes contain many compounds that are either not present or not detectable in the sample type that has

been analysed. The use of larger search spaces, containing metabolites that are unlikely to be present, gives rise to increased number of putative annotations associated with a single feature and greater probability of false positive annotations (95, 130).

In UHPLC-MS-based metabolomics, RT measurements may be used to tackle some of the aforementioned challenges associated with metabolite annotation. For example, the fact that signals for the same metabolite will be positively correlated and have the same RT across samples may be applied to aid feature deconvolution (95, 130, 132). RT may also be used, by comparison either to RTs of authentic chemical standards or to *in silico* predicted RTs, e.g., (219), to rank and filter lists of putative metabolite annotations per feature (95, 130). However, the use of some *in vitro* models, e.g., cardiac microtissues, in untargeted metabolomics, chosen for their greater translational relevance and ethical benefits (21, 36), requires the application of analytical approaches with higher sensitivity, e.g., nESI-DIMS, to overcome the limited available biomass (108). The lack of sample separation associated with nESI-DIMS exacerbates the challenge of metabolite annotation.

A proposed solution to overcome, in part, the challenge of annotation in untargeted metabolomics is the replacement of large, diverse metabolite databases, e.g., HMDB (128), with smaller, accurately defined lists of metabolites known to be present and detectable within the specific sample type, for use as the search space. In principle, this would reduce the proportion of false positive annotations attained (95). To this end, Deep Metabolome Annotation (DMA) of test systems, i.e., experimentally and accurately define which metabolites are present and detectable within a specific sample type, has been recommended (144). Consistent with this recommendation, a comprehensive approach combining solid phase extraction, untargeted UHPLC-

MS(/MS), gas chromatography-MS (GC-MS), NMR and nESI-DIMS^n was applied for DMA of *Daphnia magna* (220). Taken further, the Model Organism Metabolomes task group of the international Metabolomics Society proposed the deep investigation of the metabolomes of eleven model organisms spanning the microbial, plant and animal kingdoms, to ultimately tackle the paucity of metabolite annotation, one of the “critical weaknesses of metabolomics”, and to build a better understanding of the evolutionary conservation of metabolic pathways (221). However, the approaches typically implemented for DMA, e.g., as applied by Jones (2018) are time-consuming and expensive, limiting its feasibility. Other, less comprehensive, attempts at annotating metabolomes extend to the human adult urinary metabolome (222), zebrafish embryo metabolome (223), *Escherichia coli* metabolome (127), and bovine liver and heart lipidomes (224) where researchers have achieved good metabolome coverage through use of complementary LC-MS(/MS) assays, for example, the application of a pentafluorophenyl (PFP)-based stationary phases to separate isomers which co-eluted by RP-C_{18}-based LC (222) or the implementation of both HILIC and PFP-based LC assays (223); intelligent DDA strategies for MS^n acquisition (224); and thorough annotation approaches which exploit credentialing (127).

This study’s aim was to generate a library of polar metabolites and lipids present in cardiac microtissues and which are detectable by ESI-MS, to facilitate higher confidence annotation of untargeted metabolomics datasets derived from cardiac microtissues. To achieve this aim, concentrated intracellular polar metabolite and lipid extracts, each from the equivalent of ca. $1.9x10^5$ cells, were analysed by HILIC and RP-C_{30} UHPLC-MS^n, respectively, using an intelligent DDA acquisition workflow (AcquireX) to maximise the coverage of fragmentation data. The second objective

was to employ in-house RT and MS/MS libraries of toxicologically-relevant metabolites, i.e., metabolites found within the MTox700+ biomarker list (225), two publicly-available spectral databases, mzCloud (Thermo Fisher) and MoNA (137), and two *in silico* lipid spectral databases, LipidSearch (Thermo Fisher) and LipidBlast (226), to annotate the detectable polar metabolome and lipidome of cardiac microtissues, curating lists for the purpose of later annotating metabolomics datasets.

4.2 Materials and Methods

4.2.1 Materials

Solvents and chemicals used for sample preparation and UHPLC mobile phases were as follows: LC-MS grade methanol (Honeywell) and isopropanol (Honeywell), purchased from Fisher Scientific; LC-MS grade acetonitrile and water, purchased from VWR International; HPLC grade chloroform, purchased from Merck Life Sciences; ammonium acetate (≥99.99% trace metals basis, Honeywell), LC-MS grade ammonium formate (Fisher Chemicals), LC-MS grade acetic acid (Fisher Chemicals) and formic acid (for MS, ~98%, Honeywell Fluka), purchased from Fisher Scientific.

Microcentrifuge tubes (Eppendorf), glass micro-inserts (Fisherbrand) and glass polyspring inserts (Thermo Scientific) were purchased from Fisher Scientific. Glass vials (Trident) were purchased from Scientific Laboratory Supplies (Hessle, UK). LC vials and caps were purchased from Chromatography Direct.

4.2.2 Cell culturing and sample collection

Cardiac microtissues were cultured and sampled by Dr. Andrew Hall (AstraZeneca). Briefly, 14-day mature microtissues were sampled 2- and 72-hours after a media change as described previously (Sections 3.2.1 and 3.2.3.2). Specifically, 154

microtissues and their spent culture medium were aspirated from neighbouring wells (½ plate) of the 384-well culture plate. Each sample of 154 microtissues was isolated on the filter surface of a cell strainer (37 µm reversible strainer, StemCell Technologies) and washed with 3x 1.0 mL 0.9% NaCl, followed by 1.0 mL ultrapure water. Suction was applied to ensure removal of any residual wash solution before rapid freezing of the microtissue-containing cell strainer in dry ice/ethanol. Samples were kept on dry ice during collection before being transferred to a freezer maintained at −80°C. Samples were later shipped on dry ice then returned to -80°C storage conditions until preparation for metabolomics analyses.

Process blanks were generated by sampling of media only (no microtissues) by the same approach.

4.2.3 Extraction of intracellular polar compounds and lipids

Polar compounds were extracted from 15 samples, each 154 microtissues isolated on a cell strainer, in 200 µL 4:1 (v/v) methanol/water, as described previously (Section 3.2.4.1). After centrifugation, a single pooled sample was created by combining 180 µL supernatant from each of the 15 samples. The pooled sample was vortexed, then split between four microcentrifuge tubes, 490 µL in each (equivalent to ca. 377 cardiac microtissues, or ca. 1.9×10^5 cells) before drying in a SpeedVac concentrator (Savant SPD111V, Thermo Scientific). Dried extracts were stored at -80°C.

Intracellular lipids were extracted from 15 samples, each 154 microtissues isolated on a cell strainer, in 240 µL 2:1 (v/v) chloroform/methanol as described previously (Section 3.2.4.2). After centrifugation, 200 µL supernatant from each sample was combined to form a single pooled sample which was subsequently vortexed then split between four 250 µL glass micro-inserts held in 1.75 mL glass vials, 590 µL in

each (equivalent to ca. 379 cardiac microtissues, or ca. $1.9x10^5$ cells). Aliquots were dried under N_2 (Techne Dri-Block DB100/3 sample concentrator), then stored at -80°C.

Process blanks were prepared as described for samples. Extracts from three separate process blank samples were pooled to form a single dried extract.

4.2.4 Resuspension of dried extracts

Dried polar extracts were resuspended in 38 µL 1.5:1.5:1.0 (v/v/v) acetonitrile/methanol/water. Each resuspended sample was vortexed for 30-seconds then centrifuged at 20,000-*g* for 20-minutes at 4°C. Similarly, dried lipid extracts were resuspended in 38 µL 3:1 (v/v) isopropanol/water, vortexed, and centrifuged at 4000-*g* for 20-minutes at 4°C. 33 µL of supernatant from each resuspended extract was transferred to a separate 300 µL polyspring glass insert within an LC vial for analysis.

4.2.5 Data acquisition by UHPLC-MS^N

Data was acquired using an Orbitrap ID-X Tribrid mass spectrometer coupled to a Vanquish Horizon UHPLC (Thermo Scientific). During analysis, samples were stored within the autosampler module, maintained at 4°C. Previously reported methods employing HILIC (76, 77) and RP-C_{30} chromatography (105) were implemented, with some modifications.

4.2.5.1 HILIC UHPLC-MS^n

Chromatographic separation was performed as described in 3.2.5.3, using a sample injection volume of 2 µL.

Full scan data acquisition was performed in positive and negative ionisation modes separately, at a resolution of 120,000, between 70 and 1050 *m*/*z*. The AGC target

was $1x10^5$ and maximum injection time set at 75 ms. Ion source and ion optics settings are detailed in Table 4.1.

Table 4.1 Ion source and ion optics settings for data acquisition by UHPLC-MS^n.

Assay	Sheath Gas (Arb)	Aux gas (Arb)	Sweep gas (Arb)	Spray voltage (kV)	Ion transfer tube temperature (°C)	Vaporizer temperature (°C)	RF lens voltage (%)
HILIC positive	40	8	1	3.2	300	350	30
HILIC negative	40	8	1	2.7	300	350	30
RP-C_{30} positive	40	8	1	3.2	300	350	70
RP-C_{30} negative	40	8	1	2.7	300	350	70

An AcquireX Deep Scan (Thermo Scientific) workflow was implemented for the acquisition of MS^n fragmentation data. Three cycles of a sequence were executed, the sequence being composed of: two full scan injections of a process blank, the second of which was used to generate an exclusion list; a full scan injection of a column equilibration sample; a full scan injection of a study sample, used to modify the user-generated inclusion list of protonated or de-protonated ion forms of toxicologically relevant metabolites (MTox700+ biomarker list (225)); and five iterative injections for MS^n acquisition using the inclusion and exclusion lists, which were modified by AcquireX software after each injection, removing features from the inclusion list and adding them to the exclusion list if they had been used as a precursor ion. Injections of study sample within a cycle were from the same vial, with a different vial used for each cycle. Regarding acquisition settings of MS^n data: MS^1 and HCD MS/MS (MS^2) data were acquired by the Orbitrap; CID MS/MS/MS (MS^3) data were acquired for the three most intense fragments measured in the HCD spectra by the ion trap. Further details are provided in Figure 4.1.

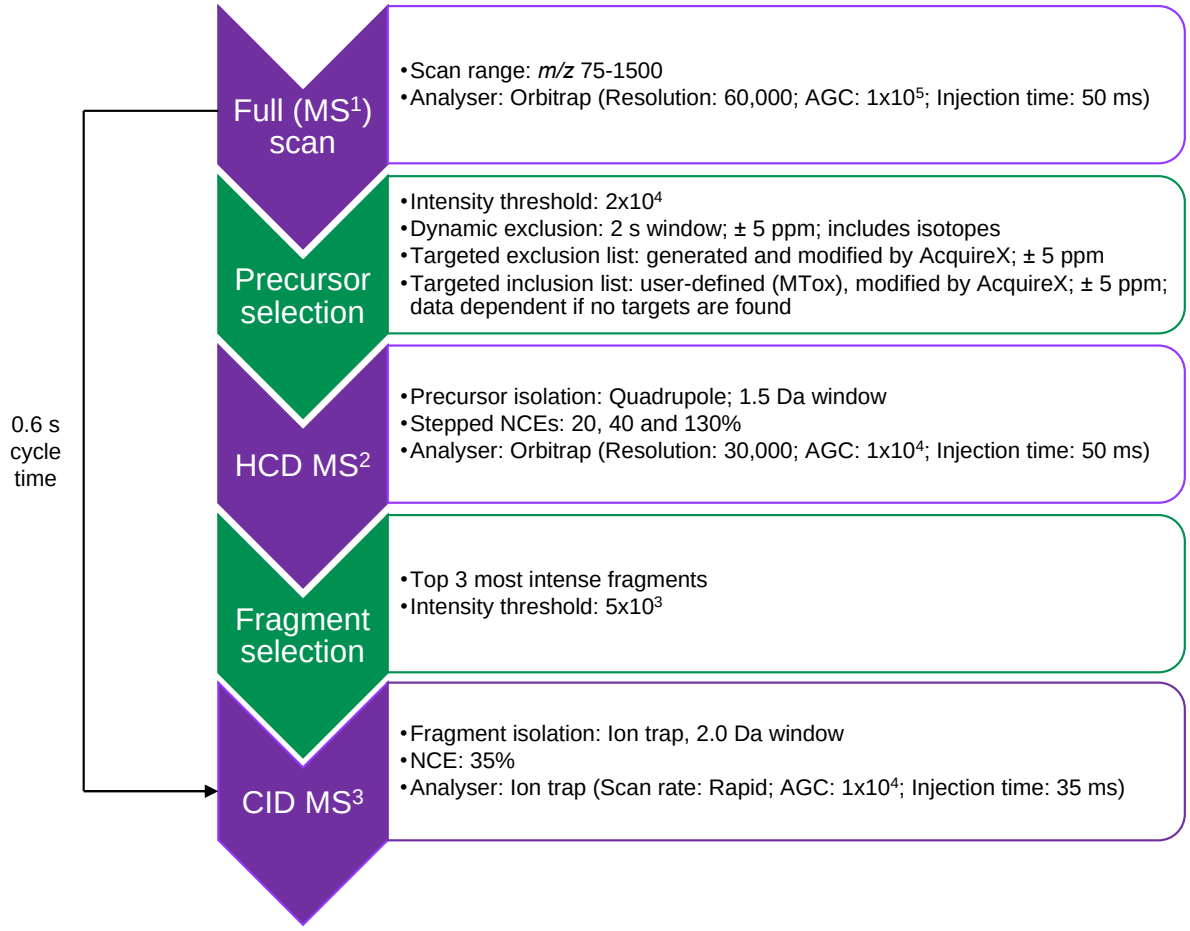


Figure 4.1 Flow chart describing MS^n data acquisition method when coupled to HILIC chromatography.
Each scan cycle begins with full (MS^1) scan by the Orbitrap, measurements from which are used to select precursors which meet defined criteria for subsequent fragmentation by higher-energy collisional dissociation (HCD) at three stepped normalised collision energies (NCEs). The resulting MS^2 fragments are detected in the Orbitrap. Subsequent collision-induced dissociation (CID) is performed in the high-pressure cell of the dual-pressure linear ion trap on the three most intense MS^2 fragments, provided they pass the defined intensity filter. The resulting MS^3 fragments are detected in the low-pressure cell of the dual-pressure linear ion trap. The MS^2 and subsequent MS^3 is repeated for as many MS^1 precursors as possible within the 0.6-second cycle time, before proceeding to the next MS^1 scan, at which point the cycle repeats.

4.2.5.2 Reversed-Phase C_{30} UHPLC-MS^n

Chromatographic separation was performed on an Accucore C_{30} column (2.1 x 150 mm, 2.6 µm, Thermo Scientific), maintained at 55°C. Mobile phases A and B were 60:40 acetonitrile/water (20 mM ammonium formate) and 85.5:9.5:5 isopropanol/acetonitrile/water (20 mM ammonium formate). A 30-minute gradient elution was applied as follows: t = 0.0, 20% B; t = 2.5, 20% B; t = 2.6, 55% B; t = 12.0, 60% B; t = 12.1, 80% B; t = 19.0, 90% B; t = 21.0, 100% B; t = 23.0, 100% B; t

= 23.1, 20% B, with all changes linear (curve = 5). The flow rate was 0.4 mL/min, and the injection volume was 2 µL.

Data was acquired in positive and negative ionisation modes separately, over a mass range of 150-2000 *m/z*, at a resolution of 120,000. The AGC target was $4x10^5$ and maximum injection time set at 100 ms. Ion source and ion optics settings are detailed in Table 4.1.

AcquireX was implemented for acquisition of MS^n data as described in section 4.2.5.1. Regarding data acquisition settings: MS^1 and HCD MS^2 data were acquired in the Orbitrap; subsequent CID MS^2, triggered by detection of a fragment ion at *m/z* 184.0733 or *m/z* 168.0431 in positive and negative ionisation, respectively, or CID MS^3, triggered by detection of fragment ions formed as a result of one of 32 targeted neutral losses, were measured in the Orbitrap (Figure 4.2).

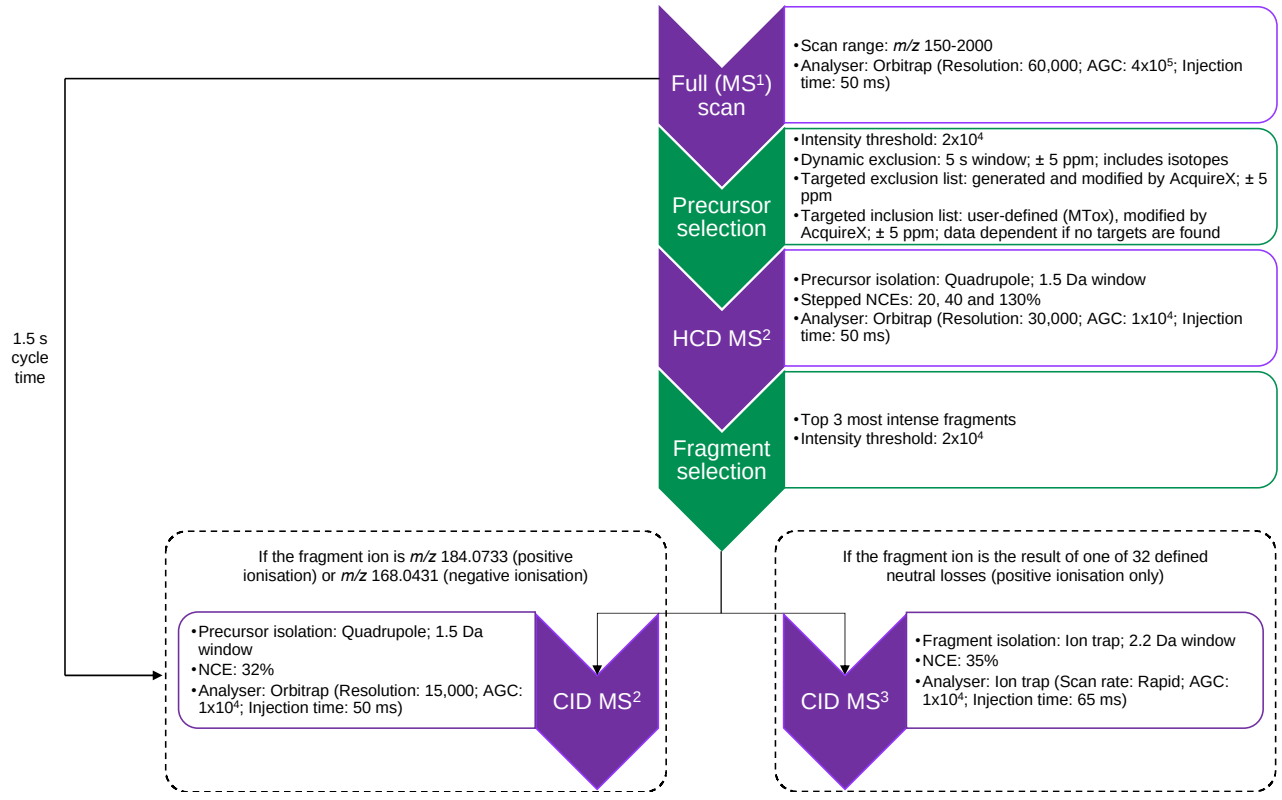


Figure 4.2 Flow chart describing MS^n data acquisition when coupled to RP-C_{30} chromatography.

Each scan cycle begins with full (MS^1) scan by the Orbitrap. The MS^1 measurements are used to select precursors which meet defined criteria for subsequent fragmentation by higher-energy collisional dissociation (HCD), at three stepped normalised collision energies (NCEs). The resulting MS^2 fragments are detected in the Orbitrap. Subsequent collision-induced dissociation (CID) is performed in the high-pressure cell of the dual-pressure linear ion trap on the same precursor (MS^1) ion if a fragment at *m/z* 184.0733 or *m/z* 168.0431 is detected in the HCD spectrum in positive and negative ionisation, respectively. These fragment ions correspond to the phosphocholine head group (protonation or de-methylation, respectively) of phosphatidylcholines, lysophosphatidylcholines and sphingomyelins. Alternatively, collision-induced dissociation (CID) may be performed on the three most intense MS^2 fragments if they are formed by a defined neutral loss from the precursor ion. The defined neutral losses correspond to the loss of fatty acyls, typically observed in MS^2 of triacylglycerols. The resulting MS^2 or MS^3 fragments are detected in the low-pressure cell of the dual-pressure linear ion trap. The HCD MS^2 and subsequent CID MS^2 or MS^3 is repeated for as many MS^1 precursors as possible within the 1.5 s cycle time, before proceeding to the next MS^1 scan, at which point the cycle repeats.

4.2.6 DATA PROCESSING AND COMPOUND ANNOTATION

4.2.6.1 XCMS

Vendor format raw data files (.RAW) were first converted to mzML file format using ProteoWizard (v3.0.21215) (177). XCMS (v3.14.0) (115) was then used to detect and group MS^1 peaks, generating a peak-intensity matrix for features (*m/z*-RT pairs) vs. samples for each dataset. The XCMS parameter values used for each dataset are defined in Table 4.2.

Table 4.2 XCMS parameters used for full scan (MS^1) peak picking and grouping.

Function	Parameter	HILIC chromatography	RP-C_{30} chromatography
Peak detection – centwave algorithm	ppm	7.5	5
	peakwidth	5,40	5,40
	snthresh	10	10
	prefilter	3,100	3,100
	mzCenterFun	wMean	wMean
	mzdiff	0.001	0.001
Peak grouping - PeakDensity	bw	0.25	0.25
	Minfrac	0.5	0.5
	binSize	0.001	0.01
	maxFeatures	50	50

The data matrices were subsequently filtered to remove features of non-biological origin and those that were not reproducibly detected. Specifically, only features detected in full scan injections of microtissue extract from at least two of three

AcquireX cycles, with intensity greater than 10x the median intensity in process blanks, were retained.

4.2.6.2 msPurity

The Bioconductor/R package msPurity (v1.18.0) (141) was implemented to process, filter (precursor ion purity >0.5; SNR of fragment ions >3), and average (across all samples, keeping only fragment ions in at least 50% contributing spectra) MS^2 data, generating a database of MS^2 spectra per assay. Annotations were subsequently assigned by comparison of the generated databases to in-house databases of MS^2 spectra using the msPurity spectral matching function (precursor match: ±5 ppm, product ion match: ±10 ppm). Only annotations where the dot product cosine score was >0.6 were retained.

4.2.6.3 Compound Discoverer

All data were processed using Compound Discoverer (v3.3.0, Thermo Scientific). The implemented workflow included the following processing nodes and settings: Detect peaks (SNR >1.5); Align Retention Times (Adaptive curve model, mass tolerance: ±5 ppm; maximum shift: 2-minutes); Detect Compounds (mass tolerance: ±5 ppm; min. peak intensity: $1x10^4$; min. scans per peak: 5; chromatographic SNR >1.5; max. peak width: 1-minute; gap ratio threshold: 0.35; isotope pattern detection: default settings; ions: all available, except '3M' species; base ions: $[M+H]^+$ and $[M-H]^-$; remove singlets: True), Group Compounds (use intensity (area integration) from most common ion; mass tolerance: ±5 ppm; RT tolerance: ±0.2-minutes; peak rating contributions: default; not filtered according to peak rating), Mark Background Compounds (max. sample/blank: 5); Search mzCloud (search MS^n tree: True; precursor mass tolerance: ±5 ppm; fragment mass tolerance, FT: ±10 ppm; fragment mass tolerance, IT: ±0.4 Da; search autoprocessed & reference libraries; HighChem

HighRes score threshold: 0.6); Search mzVault (precursor mass tolerance: ±5 ppm; fragment mass tolerance, FT: ±10 ppm; fragment mass tolerance, IT: ±0.4 Da; search two libraries contributed by Prof. Bamba (Kyushu University), and one built using data from LipidBlast (226); HighChem HighRes score threshold: 0.6); Assign Compound Annotations (mass tolerance: ±5 ppm, source #1: mzCloud, source #2: mzVault).

The reported compounds tables were subsequently filtered such that only compounds detected in full scan injections of microtissue extract from at least two of three AcquireX cycles, with at least MS^2 data, a RT >1-minute, and an assigned annotation from either mzCloud or mzVault, were retained. Results were then manually interrogated, keeping only annotations corresponding to endogenous metabolites assigned from matches, minimally, at both MS^1 and MS^2 (match of at least two fragment ions), and optionally, at MS^3 level. Here, some expertise was required to ensure correct ion form assignment to accurately assess, and filter on, the mass error at the MS^1 level, e.g., account for incorrect automated assignment of a given precursor as $[M+H]^+$ instead of $[M+NH_4]^+$ by Compound Discoverer, indicated by mass error of 17 Da.

4.2.6.4 LipidSearch

Data acquired by RP-C_{30} assays were processed and annotated using LipidSearch (v5.0, Thermo Scientific). Lipids within the LipidSearch *in silico* database (all lipid classes, substituents and adduct ion definitions) were assigned to detected peaks and their deconvoluted MS^2 spectra (default parameters) using precursor and product ion mass error tolerances of ±5.0 and ±8.0, respectively, and a product ion intensity threshold of 5.0. Annotations were then aligned across all samples, grouping peaks assigned the same sum composition lipid molecule (RT tolerance:

±0.2-minutes; SNR[1] threshold: 3.0; intensity ratio (IR)[2] threshold: 1.5; valid peak ratio (VPR)[3] threshold: 0.5) within and between samples.

Annotations reported by LipidSearch were subsequently filtered, retaining only those annotated in at least two of the three AcquireX cycles, and assigned a grade of A, B or C (see Section 2.2.11 for definitions).

4.2.6.5 Retention time matching

Compounds within the MTox700+ list of metabolic biomarkers (225) were assigned to features reported by XCMS (section 4.2.6.1) and compounds reported by Compound Discoverer (section 4.2.6.3) by matching *m/z* (±5 ppm) and RT (±40-seconds) to data within an in-house RT library.

4.2.6.6 Aligning annotations and curation of compound lists

Lists of all annotated polar metabolites and lipids detected in intracellular extracts of cardiac microtissues were curated by combining annotations assigned by either spectral matching using msPurity, Compound Discoverer and LipidSearch, or RT matching against an in-house RT library. All annotations were assigned a HMDB identifier, based on compound name where this was not already assigned by the software or database used, or an abbreviated lipid name. These identifiers were used to align annotations from different sources.

4.2.7 PATHWAY MAPPING

Compounds recorded in the curated list of polar compounds were mapped to KEGG pathways using MetaboAnalyst (v5.0, https://www.metaboanalyst.ca/MetaboAnalyst/) Pathway Analysis function.

[1] Height ratio of each chromatographic peak to the average baseline intensity.
[2] Ratio of the total number of points at the top (>50% peak intensity) to the total number of points at the bottom (<50% peak intensity) of each chromatographic peak.
[3] Fraction of peaks detected in the group that pass both the SNR and IR thresholds.

Compound names were first mapped to PubChem, HMDB and KEGG identifiers, which were subsequently mapped to pathways within the *Homo sapiens* KEGG pathway library.

4.3 Results and Discussion

4.3.1 Analytical sensitivity and MS^N coverage

The UHPLC-MS^n measurements of intracellular metabolite and lipid extracts prepared from 14-day-mature cardiac microtissues were first assessed with respect to the analytical sensitivity and coverage of MS^n data.

Peak picking and alignment of samples using XCMS reported 2504 and 2008 features in HILIC positive and negative datasets, respectively, with 30-50% of these features subsequently removed by blank and replicate filtering. Meanwhile, 7454 and 7718 features were reported in the RP-C_{30} positive and negative datasets, respectively, with similar proportions removed by the filters (Table 4.3).

Table 4.3 Assessment of the analytical sensitivity and MS^n coverage of UHPLC-MS^n analyses of intracellular extracts from cardiac microtissues.
The table presents the number of features or compounds extracted from the raw data by XCMS and Compound Discoverer, respectively, how many features or compounds remained after removal of blank features and features present in less than two of three technical replicates, and for how many features or compounds was at least MS^2 fragmentation data measured.

Processing software	Description of data reported	HILIC positive	HILIC negative	RP-C_{30} positive	RP-C_{30} negative
XCMS & msPurity	Total number of features	2504	2008	7454	7718
	Number of features following blank and replicate filtering	1309	1387	4752	5406
	Number of features associated with MS^2 data	631	619	2942	2562
Compound Discoverer	Total number of compounds	4982	12142	35062	20289
	Number of compounds after blank and replicate filtering	961	1709	10264	7955
	Number of compounds with MS^2 data	825	1520	9233	6531

The raw data was also processed using Compound Discoverer which picks, aligns, filters and deconvolutes MS^1 peaks, and aligns MS^n spectral trees (i.e., all fragmentation spectra, including MS^2 and MS^3 derived from a single precursor ion) to the discovered compounds, where a compound is defined by one or more deconvoluted features (Section 4.2.6.3). The number of compounds reported before and after blank and replicate filtering exceeded the number of features picked by XCMS in all datasets, except for the HILIC positive dataset after filtering. The proportion of compounds removed by the two filters was 60-85% across the four datasets, indicating many of the discovered compounds were either not of biological origin, or not reproducible across technical replicates (Table 4.3).

Discrepancies between the results from the two processing routes may be explained by the differences in algorithms applied to pick peaks and highlights the usefulness of applying two complementary approaches for more complete metabolome annotation. Meanwhile, the greater number of features and compounds in the RP-C_{30} compared to HILIC datasets may be accounted for by one or the combined effect of the following: (1) the longer UHPLC method enables more effective sample separation, providing greater resolution in the time domain, (2) lipid extracts possess greater matrix complexity compared with polar extracts, or (3) greater analytical sensitivity is achieved by the assay-specific MS data acquisition settings.

While direct comparison with other datasets should be treated with caution due to differences in sample type, sample biomass, analytical instrumentation and settings, and data processing parameters, it can be concluded that results here indicate good analytical sensitivity since the number of features after filtering were within the expected range based on related datasets, e.g., 816, 266, 3736 and 2204 features within HILIC positive, HILIC negative, RP-C_{18} positive and RP-C_{18} negative

processed and filtered hiPSC-CMs-derived datasets, respectively; 1369, 2057, 6922, and 4320 features within HILIC positive, HILIC negative, RP-C_{18} positive and RP-C_{18} negative processed and filtered rat cardiac tissue-derived datasets, respectively (Table C.1).

Alignment of MS^2 fragmentation spectra processed and filtered by msPurity to the filtered XCMS-derived feature list provided 631, 619, 2942 and 2562 features from the HILIC positive, HILIC negative, RP-C_{30} positive and RP-C_{30} negative datasets, respectively, for which there were fragment ions available for compound annotation (Table 4.3). This is equivalent to approximately 44-62% coverage. Meanwhile, MS^2 data was acquired for 80-90% of filtered compounds reported by Compound Discoverer (Table 4.3). This may be considered very high coverage, consistent with previous reports of AcquireX coverage capabilities, and further demonstrating the benefits of applying AcquireX intelligent data acquisition. The greater coverage at the compound-level (Compound Discoverer) compared with the feature-level (XCMS and msPurity) is consistent with the capability of AcquireX to reduce the redundancy of fragmentation data by considering degenerate MS^1 features (i.e., multiple ion forms measured for single compound) during the curation and iterative modification of the inclusion lists.

Taken together, the UHPLC-MS^n analyses of intracellular polar metabolite and lipid extracts by HILIC and RP-C_{30} assays, respectively, employing AcquireX for intelligent MS^n acquisition, provided sufficient sensitivity and excellent MS^n coverage, ideal for the annotation of the cardiac microtissue polar metabolome and lipidome.

4.3.2 *Annotating compounds detected within polar intracellular extracts of cardiac microtissues by HILIC UHPLC-MS^N*

Combining annotations derived from spectral matching against mzCloud and an in-house spectral database, and RT matching against an in-house RT library of metabolic biomarkers for toxicology (225), a list of 315 compounds present in polar intracellular extracts of cardiac microtissues was curated (Table eC.1). The majority of annotations were derived from the matching of MS^n trees processed and aligned to compounds reported by Compound Discoverer to the mzCloud database in both positive and negative ionisation modes (Figure 4.3). This is consistent with both the greater number of compounds reported by Compound Discoverer compared with the number of features reported by XCMS (Table 4.3), and the size of the respective databases, with mzCloud containing spectra for >20,000 compounds (227), while the in-house databases are limited to just a few hundred compounds. The contribution of the positive and negative ionisation datasets to the curated list was relatively equal (Figure 4.3).

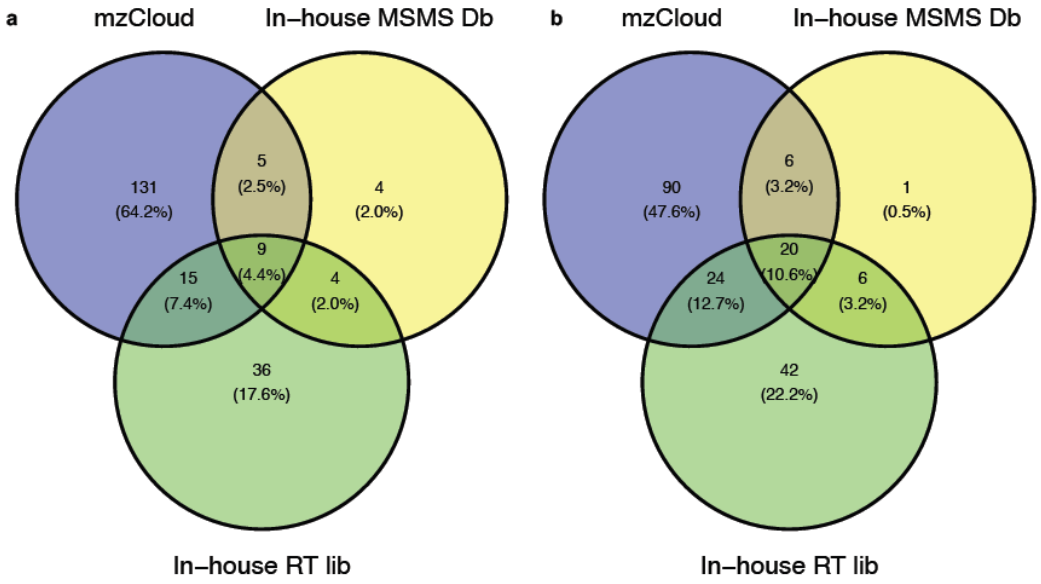


Figure 4.3 Contribution of different approaches to polar compound annotations.
Venn diagrams showing the contribution of each annotation approach, specifically MS^n-tree matching against the mzCloud database (blue), MS^2 matching against an in-house MS^2 database (yellow), and

RT matching against an in-house RT library (green), to the curated list of compounds present in intracellular polar extracts of cardiac microtissues detected by HILIC UHPLC in, **a** positive and **b** negative ionisation. Totals of 204 and 189 annotations were derived from the positive and negative datasets, respectively.

In some cases, despite the use of fragmentation and RT data, it was impossible to distinguish between isomers for annotation of a given feature. In such instances, all the likely assignments are included in the curated list, e.g., the listing of "Methionine||Racemethionine" as a single record. Future efforts to analyse authentic chemical standards by the exact same analytical method and instrumentation could help determine the correct annotations. In particular, this would enable the use of RT to distinguish between isomers with relatively similar MS^2 and MS^3 spectra, provided they are chromatographically resolved.

Examination of the curated list reveals the presence of metabolites associated with key functions in cardiac biochemistry (228). For example, the inclusion of the branched chain amino acids (BCAA), leucine, isoleucine and valine, an alternative group of substrates to fatty acids and glucose for cardiac energy metabolism and ATP synthesis. Impaired BCAA metabolism has been associated with multiple cardiovascular diseases, including myocardial hypertrophy, cardiomyopathies, and heart failure (229, 230). As a further example, the inclusion of creatine, which plays a key role in cardiac contraction via its phosphorylation to phosphocreatine, providing a mechanism for effective transportation and rapid synthesis of ATP. The creatine/phosphocreatine system is of particular importance at times of increased energy demand or oxygen deficiency (231).

Notably, the list also contains 126 lipids. This includes annotation of 11 acylcarnitines, 1 ceramide, 2 monogalactosyldiacylglycerols, 39 lysophospholipids, 64 phospholipids, and 9 sphingomyelins (Table eC.1). The presence of these

compounds in polar extracts is consistent with findings of (76), where lipids were also measured in acetonitrile/methanol/water-based monophasic extracts of heart, kidney and liver tissue by HILIC UHPLC-MS(/MS). This may be explained by the absence of a non-polar phase, as occurs in a biphasic extraction, into which most lipids would otherwise partition.

The list of polar compounds was interrogated further by mapping against the KEGG database of biochemical pathways. A total of 204 of the annotated metabolites were mapped, revealing representation of 57 (human) KEGG pathways (Table 4.4). Of the compounds which could not be mapped to the KEGG database, most are lipids, consistent with the general lack of organised knowledge covering lipid metabolism, particularly around the role of fatty acyl chain length, and the number and position of double bonds in fatty acyl chains (232). The most represented pathway, based on the number of mapped compounds, is the aminoacyl-tRNA biosynthesis pathway. Aminoacyl-tRNAs are molecules composed of an amino acid chemically bound to its cognate tRNA, responsible for delivering amino acids to the ribosome for synthesis of proteins by translation (233). The detection and annotation of 18 amino acids within polar intracellular extracts of cardiac microtissues is responsible for this being the most represented pathway (Table 4.4, Table eC.1). Other well represented pathways include purine metabolism and pyrimidine metabolism, both pathways of nucleotide metabolism (Table 4.4). The generation of nucleotides is essential for cell proliferation, with altered nucleotide metabolism recognised as a metabolic signature of tumours (234), and, pertinent to this thesis, associated with cardiotoxicity induced by anthracyclines (235). Furthermore, the representation of central energy metabolism pathways, including the citrate cycle, glycolysis / gluconeogenesis and pentose phosphate pathway, is promising for the intended application of untargeted

metabolomic analyses of cardiac microtissues to discover effects of structural cardiotoxins, many of which have previously been reported to disrupt cardiac energy metabolism (25, 236).

Table 4.4 Representation of metabolic pathways.
Listed are the names of KEGG biochemical pathways, the total number of metabolites within each pathway ('Total') and the number of metabolites within the curated list of polar metabolites detected in intracellular extracts of cardiac microtissues which mapped to each pathway ('Hits').

Pathway Name	Total	Hits
Aminoacyl-tRNA biosynthesis	48	18
Purine metabolism	65	16
Alanine, aspartate, and glutamate metabolism	28	12
Arginine biosynthesis	14	11
Amino sugar and nucleotide sugar metabolism	37	11
Pyrimidine metabolism	39	11
Arginine and proline metabolism	38	10
Glycine, serine, and threonine metabolism	33	9
Glyoxylate and dicarboxylate metabolism	32	8
Cysteine and methionine metabolism	33	8
Glycerophospholipid metabolism	36	8
Pantothenate and CoA biosynthesis	19	7
Citrate cycle (TCA cycle)	20	7
Galactose metabolism	27	7
Glutathione metabolism	28	7
beta-Alanine metabolism	21	6
Glycolysis / Gluconeogenesis	26	6
Valine, leucine, and isoleucine biosynthesis	8	5
Nicotinate and nicotinamide metabolism	15	5
Pentose phosphate pathway	22	5
Pyruvate metabolism	22	5
Lysine degradation	25	5
Inositol phosphate metabolism	30	5
Valine, leucine, and isoleucine degradation	40	5
Tyrosine metabolism	42	5
Butanoate metabolism	15	4
Histidine metabolism	16	4
Starch and sucrose metabolism	18	4
Fructose and mannose metabolism	20	4
Sphingolipid metabolism	21	4
D-Glutamine and D-glutamate metabolism	6	3
Ascorbate and aldarate metabolism	8	3
Pentose and glucuronate interconversions	18	3
Primary bile acid biosynthesis	46	3
Phenylalanine, tyrosine, and tryptophan biosynthesis	4	2
Synthesis and degradation of ketone bodies	5	2
Nitrogen metabolism	6	2
Taurine and hypotaurine metabolism	8	2
Vitamin B6 metabolism	9	2
Phenylalanine metabolism	10	2
Glycerolipid metabolism	16	2
Phosphatidylinositol signalling system	28	2
Porphyrin and chlorophyll metabolism	30	2
Tryptophan metabolism	41	2

Steroid biosynthesis	42	2
Neomycin, kanamycin, and gentamicin biosynthesis	2	1
Linoleic acid metabolism	5	1
Thiamine metabolism	7	1
Ubiquinone and other terpenoid-quinone biosynthesis	9	1
One carbon pool by folate	9	1
Biotin metabolism	10	1
alpha-Linolenic acid metabolism	13	1
Ether lipid metabolism	20	1
Propanoate metabolism	23	1
Folate biosynthesis	27	1
Arachidonic acid metabolism	36	1
Fatty acid degradation	39	1

The curated list of polar compounds was also compared against the MTox700+ list of 722 metabolic biomarkers for toxicology (225). This revealed 54.6% of the detected and annotated compounds have previously been associated with toxicity (Figure 4.4, Table eC.1). The presence of compounds considered to be predictive of toxicological endpoints within the list supports the use of cardiac microtissues for metabolomics-based discovery of metabolic biomarkers predictive of structural cardiotoxicity.

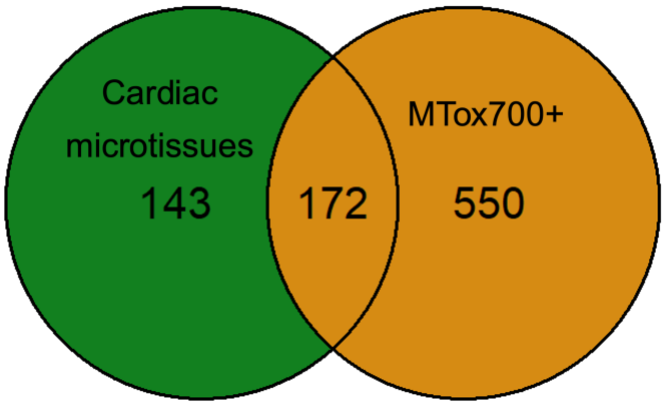


Figure 4.4 Proportion of toxicologically relevant metabolites.
A Venn diagram displaying the overlap between the curated list of polar compounds detected and annotated in intracellular extracts of cardiac microtissues and the MTox700+ list of metabolic biomarkers for toxicology (225).

4.3.3 Annotating compounds detected within lipid intracellular extracts of cardiac microtissues by RP-C_{30} UHPLC-MS^N

A list of 2450 unique lipid groups, i.e., reporting fatty acyl chains as total number of carbons and double bonds, equivalent to 'abbreviated names' in LMSD (129), present in intracellular lipid extracts of cardiac microtissues was curated from

annotations generated by spectral matching against LipidBlast *in silico* MS^2 database (226), MS^2 and MS^3-based annotation using LipidSearch, and msPurity-based spectral matching against an in-house MS^2 database (Table eC.2). The positive ionisation dataset contributed the most to the curated list with 2143 and 928 unique lipid group annotations derived in the positive and negative ionisation datasets, respectively (Figure 4.5).

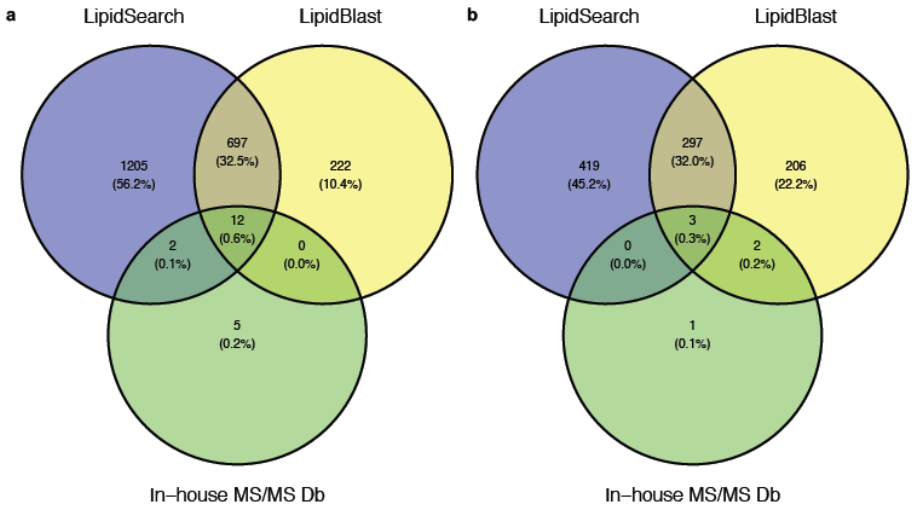


Figure 4.5 Sources of lipid annotations.
Venn diagrams showing the contribution of each annotation approach, specifically spectral matching against the LipidSearch *in silico* database (blue), MS/MS matching against the LipidBlast *in silico* database (yellow), and MS^2 matching against an in-house database (green), to the curated list of compounds present in intracellular lipid extracts of cardiac microtissues detected by RP-C_{30} UHPLC in, **a** positive and **b** negative ionisation. Totals of 2143 and 928 annotations were derived from the positive and negative datasets, respectively.

Amongst the 2479 lipids are 1593 unique molecular formulae, highlighting the presence of isomers. This is noteworthy when considering the annotation of nESI-DIMS datasets using the curated list of lipids as the search space since isomers cannot be resolved given the lack of chromatographic separation. As such, some features may be assigned multiple isomeric compounds. However, the incidence of multiple assignments will arguably be much lower than if a significantly larger database, *e.g.*, LMSD, was used as the search space.

The annotated lipids are reported as lipid groups, i.e., at the lipid sub-class or sum composition level, without fatty acyl fragment constituent information (237), to avoid otherwise anticipated high false positive rates associated with incorrect assignment of fatty acyls, including length, double bond location, stereochemistry and *sn*-position (238). In some cases, signatures in MS^2 and MS^3 data can provide evidence supporting presence of certain structural features, e.g., a neutral loss of 279.2 Da is indicative of the precursor possessing a fatty acyl chain with 18 carbons and 2 double bonds (239). However, the position of double bonds is not evidenced by typical MS^2 data. Furthermore, even with the more effective separation offered by RP-C_{30}-based chromatography compared with RP-C_{18} (105), structural isomers, e.g., TG 18:1/18:1/18:1 and TG 16:1/18:1/20:1, may not be fully resolved, with fragmentation spectra being the product of all co-eluting isomers. Future efforts to thoroughly interrogate the MS^n spectra and annotations derived from automated spectral matching approaches would enable reporting of many lipids at the fatty acyl level, e.g., PC 18:0/18:2 or PC 18:0_18:2, depending on whether the *sn*-position is evidenced, with high confidence. According to the annotation grades provided by LipidSearch, fatty acyl chains and class can be fully identified (i.e., grade A) for 733 of the reported lipid groups, and partial fatty acyl chain assignments can be added to a further 228 (Figure 4.6). Further confidence in fatty acyl assignments may also be achieved through the examination of RTs, whereby a positive correlation of RT with number of carbons and negative correlation of RT with number of double bonds is expected, as reported previously (105, 240).

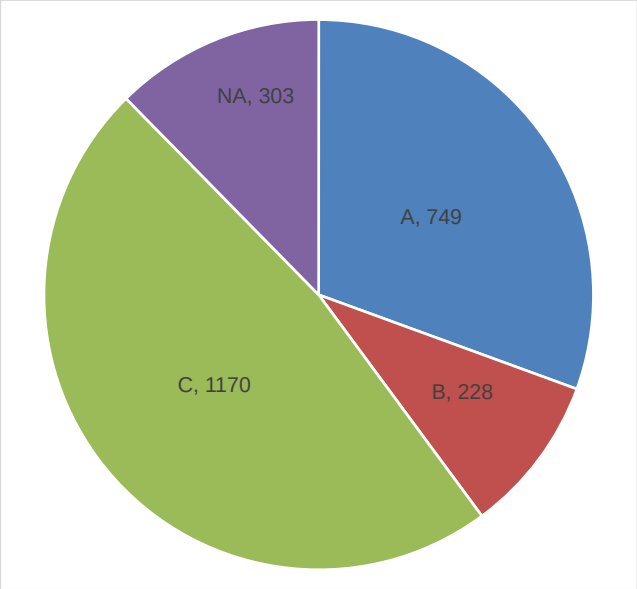


Figure 4.6 LipidSearch annotation grades.
The best LipidSearch annotation grade per lipid group reported in the curated list of compounds detected in intracellular lipid extracts of cardiac microtissues by RP-C_{30} UHPLC-MS^n. Grade A – all fatty acyl chains and class completely identified; Grade B – some fatty acyl chains and class identified; Grade C – either the lipid class or some fatty acyls identified; NA – lipid groups that were not annotated by LipidSearch.

The curated list of annotated lipids was further explored according to lipid class. The most abundant lipid class in terms of number of annotations was phosphatidylcholines, closely followed by triacylglycerols (Figure 4.7). These findings are consistent with the position of phosphatidylcholines as the most abundant phospholipid of mammalian cells and subcellular organelles. Recognised functions of phosphatidylcholines include regulation of energy metabolism (241). Meanwhile, triacylglycerols form the major cardiac energy supply, with alterations in their utilisation, including their accumulation due to reduced fatty acyl oxidation, associated with impaired cardiac function (190, 242). The accumulation of other lipid classes, including diacylglycerols and ceramides, both with roles in signalling, and acylcarnitines, responsible for shuttling fatty acyls into the mitochondria for β-oxidation, has also been linked to cardiotoxicity (190). The detection and annotation of these lipids within intracellular extracts of cardiac microtissues is thus pertinent to the aim of this thesis, to discover metabolic biomarkers of cardiotoxicity.

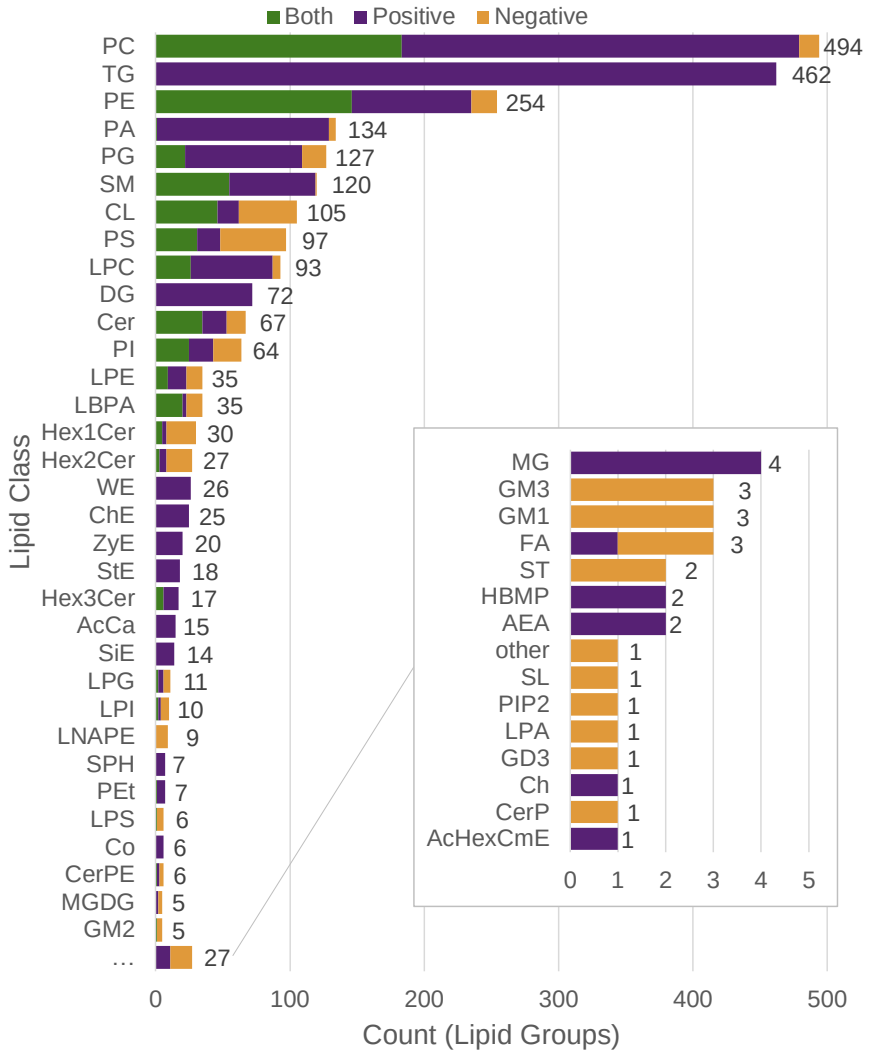


Figure 4.7 Abundance of lipids according to class.
The number of lipids (lipid groups) per lipid class (LipidSearch nomenclature) within the curated list of annotated compounds detected in lipid extracts of cardiac microtissues, and the ionisation mode by which they were measured (positive, negative or both). Common name definitions of lipid class acronyms are as follows, PC: phosphatidylcholine, TG: triacylglycerol; PE: phosphatidylethanolamine; PA: phosphatidic acid; PG: phosphatidylglycerol; SM: sphingomyelin; CL: cardiolipin; PS: phosphatidylserine; LPC: lyso-PC; DG: diacylglycerol; Cer: ceramide; PI: phosphatidylinositol; LPE: lyso-PE; LBPA: monoacylglycerophosphomonoacylglycerols; Hex1Cer: hexosylceramide; Hex2Cer: dihexosylceramide; WE: wax monoester; ChE: cholesterol ester; ZyE: zymosteryl ester; StE: ; Hex3Cer: trihexosyl ceramide; AcCa: fatty acylcarnitine; SiE: sitosterol ester; LPG: lyso-PG; LPI: lyso-PI; LNAPE: N-acyl phosphatidylethanolamines; SPH: sphingoid bases; PEt: glycerophosphoethanol; LPS: lyso-PS; Co: coenzyme; CerPE: PE-ceramide; MGDG: monogalactosyldiacylglycerol; GM2: ganglioside GM2; MG: monoacylglycerol; GM3: ganglioside GM3; GM1: ganglioside GM1; FA: fatty acyl; ST: sterol; HBMP: bis(monoacylglycero)phosphate; AEA: fatty amide; SL: saccharolipids; PIP2: phosphatidylinositol-bisphosphate; LPA: lyso-PA; GD3: ganglioside GD3; Ch: cholesterol; CerP: ceramide phosphate; AcHexCmE: acylhexosylcampesterol ester

4.4 Conclusions

This study aimed to characterise the polar metabolome and lipidome of cardiac microtissues, to curate a library of endogenous compounds both present within

intracellular polar and lipid extracts, and detectable by ESI-MS. To this end, HILIC and RP-C_{30} UHPLC-MS^n methods were applied to measure polar metabolites and lipids within intracellular extracts of cardiac microtissues. Measurements were deemed to have sufficient analytical sensitivity. Meanwhile, the coverage of MS^n across the determined features and compounds was considered very high, facilitating the annotation of a large proportion of the detected compounds.

Through the combination of multiple software, compound spectral databases and an in-house RT library, a total of 315 polar compounds and 2450 lipid groups were annotated. This encompassed major metabolites and lipids including cardiac energy substrates (e.g., BCAAs), intermediates (e.g., creatine, acylcarnitines) and stores (e.g., triacylglycerols), and central building blocks of macromolecules (e.g., amino acids, nucleotides) and cell membranes (e.g., phospholipids). The ability to detect and annotate such compounds with key roles in cardiac biology is promising for later attempts to discover metabolic biomarkers of drug-induced structural cardiotoxicity, since it is hypothesised, based on previous reports, that cardiac energy metabolism and proliferation is perturbed by structural cardiotoxins (243, 244). Future efforts to extend the curated library, such as through application of additional analytical assays with diverse compound selectivity's to the HILIC and RP-C_{30} assays already applied, e.g., measurement of polar ionic metabolites through ion exchange chromatography (245), would improve the effectiveness of its deployment in metabolomics studies using cardiac microtissues.

Use of the curated library as the search space for annotation of untargeted metabolomics datasets obtained from analysing cardiac microtissues intracellular extracts, in place of much larger public databases, e.g., HMDB, KEGG, LMSD, is expected to yield fewer false positives, thereby facilitating higher confidence in

annotations and consequently aiding discovery of biomarkers and mechanistic insight. Further work to incorporate spectral data acquired by analysing an authentic chemical standard of each of the listed compounds could facilitate even higher confidence in annotations, i.e., MSI level 1 identification by match of experimental MS^1 and MS^2 to data corresponding to an authentic chemical standard analysed by the same methods.

Taken together, this study has provided a valuable resource for metabolomics experiments utilising cardiac microtissues as the model system. In broader terms, the approaches described here, through their implementation to generate metabolite libraries specific to other toxicological test systems, have potential to enhance the value of untargeted and hybrid metabolomics across toxicology and safety assessment.

CHAPTER 5: DISCOVERING A PREDICTIVE METABOLIC SIGNATURE OF DRUG-INDUCED STRUCTURAL CARDIOTOXICITY IN CARDIAC MICROTISSUES

5.1 INTRODUCTION

Drug-induced cardiotoxicity poses a significant challenge in the development of safe and efficacious medicines, evidenced by the large proportion of market withdrawals and project closures driven by cardiac safety concerns (2, 19). A lack of ability to accurately predict cardiac safety liabilities during the earlier phases of drug development has been implicated in the costly cardiotoxicity-related market withdrawals and late-stage project closures. Such poor predictive capacity arises from a lack of mechanistic understanding across the broad spectrum of cardiotoxicity and relatively few translational predictive biomarkers (18). More specifically, while efforts to improve the prediction of functional cardiotoxicity, i.e., change in the electro-mechanical function of the myocardium, such as the introduction of the hERG assay, *in silico* models to predict effect on ion channels (13) and *in vitro* assays measuring the effect on cardiomyocyte contractility (20-23) have proven constructive, effective approaches to predict structural cardiotoxicity remains an unmet need (18). Recent attempts to address this challenge have focused on developing *in vitro* assays targeting established organelle-level pathologies associated with structural cardiotoxicity, e.g., HCB to measure the effect on mitochondrial membrane permeability, and ER (36), and other proposed key events, e.g., panel of biomarkers against apoptosis, oxidative stress, lipid accumulation and myocardial injury (30, 31). Notable is the use of hiPSC-CMs in 3D co-cultures with other major cardiac cell types, mainly endothelial cells and fibroblasts, to maximise the translation relevance of the *in vitro* test system employed in such assays (21, 26,

27, 35, 36). While these *in vitro* assays are promising steps toward improved prediction of drug-induced structural cardiotoxicity, consideration of its multi-factorial nature suggests that they may be limited in their screening to just a few of many possible contributing events. Further efforts are thus required to more comprehensively map, and discover biomarkers, of molecular mechanisms which culminate in the manifestation of structural cardiotoxicity.

Omics approaches are at the forefront of investigative toxicology, driven by their ability to measure molecular perturbations that can be used to elucidate MoA or discover biomarkers for predicting a phenotypic response (54, 55, 57, 58). Untargeted metabolomics is one such approach, measuring the collection of small molecules representing the substrates, intermediates, and end products of a systems metabolism within a biological sample (66, 68). The metabolome is often considered the most downstream “-ome” and closely related to phenotype, making metabolomics a particularly favourable tool in toxicology (53, 64, 69, 71). Untargeted metabolomics has previously been implemented in both *in vivo* and *in vitro* investigations of drug-induced structural cardiotoxicity. This includes profiling of doxorubicin-induced metabolic changes in the heart and plasma of B6C3F1 mice (246), plasma of rats (209), and footprint of hiPSC-CMs (247). Perturbation of the rat plasma metabolome induced by cyclophosphamide (248), and of the plasma, heart, muscle and liver metabolomes of rats following sunitinib and sorafenib treatment have also been explored (249, 250). However, these studies have been limited to investigating just one xenobiotic at a time. Consequently, the specificity and generalisability of any proposed biomarkers or mechanisms has not been evaluated with respect to the broad range of known structural cardiotoxins, limiting their application in drug discovery-based screening. Li *at al.* addressed this to some

extent by applying multivariate analysis to metabolic profiles induced by three structurally cardiotoxic xenobiotics in rat, discovering a cardiotoxicity-specific biomarker panel of 10 *m/z* features (208). More recently, Palmer *et al*. carried out a far more extensive study, implementing metabolomics to profile the metabolic response of hiPSC-CMs to 66 xenobiotics, including both structural and functional cardiotoxins and non-cardiotoxic xenobiotics. They used the data to develop a four-metabolite-based targeted assay and model that was predictive of cardiotoxicity potential, confirmed by test data on 88 xenobiotics (61). This study demonstrated the capability of untargeted metabolomics for discovering a predictive metabolite-based biomarker panel. However, it was limited by (1) the use of a test system with restricted translational relevance – 2D monolayers lack physiologically-relevant cell-cell and cell-ECM interactions, and non-myocytes which modulate the structure and function of myocytes *in vivo*, and (2) the measurement of the metabolic footprint only, which represents just a minor proportion of the total intracellular metabolic network. Addressing the limitations of this study may enable discovery of a more comprehensive biomarker panel with improved predictivity and translational relevance.

The fate of xenobiotics in *in vitro* systems used during drug discovery and preclinical screening is often overlooked. However, evidence demonstrates that free concentrations often differ significantly from nominal concentrations, which can have negative implications on concentration-response modelling and IVIVE (251). Furthermore, the biotransformation capacity of most non-hepatic test systems remains uncharacterised and usually assumed to be negligible, despite the relevance of xenobiotic biotransformation to predicting clinical toxicity outcomes (147, 200). A consequence of the unbiased nature of untargeted metabolomics is the

potential measurement of test xenobiotics and related compounds, i.e., biotransformation products. As demonstrated previously, these untargeted metabolomics-based measurements can be exploited to discover the fate of exposure xenobiotics in test systems (Chapter 2). Furthermore, absolute quantitation of parent xenobiotics can be incorporated into UHPLC-MS-based untargeted metabolomics experiment, enabling validation of exposure concentrations (Chapter 3, (251)). Inclusion of these established capabilities into an extensive untargeted metabolomics-based *in vitro* toxicology study is highly attractive toward maximising the potential translational relevance and accuracy of later IVIVE attempts.

The overall aim of this study was to apply untargeted metabolomics strategies to measure the fate and effects of eight (clinically recognised) structurally cardiotoxic and four non-structurally cardiotoxic small molecule xenobiotics in cardiac microtissues, ultimately, to discover a metabolic signature that is predictive of drug-induced structural cardiotoxicity. The first objective was to quantify the extracellular free concentrations of the twelve parent xenobiotics and discover their routes of biotransformation, to reveal the fate of the xenobiotics and evaluate the biotransformation competency of cardiac microtissues. The second objective was to characterise the response of cardiac microtissues induced by two concentrations of twelve parent xenobiotics after exposure for 6-, 48- and 72-hours. This included measuring the effects on the intracellular polar metabolic and lipid fingerprints, and on the extracellular metabolic footprint by application of four nESI-DIMS and two UHPLC-MS untargeted metabolomics assays, respectively. The final objective was to discover metabolic signature(s) in the cardiac microtissues predictive of drug-induced structural cardiotoxicity through multivariate analysis of the extensive metabolomics data.

5.2 Materials and Methods

5.2.1 Cell culturing

Cell culturing was performed by Dr. Andrew Hall (AstraZeneca), as described previously (Section 3.2.1).

5.2.2 Exposures

5.2.2.1 Xenobiotic selection

Test xenobiotics were selected from a list of 30 FDA approved and marketed small molecule drugs for which *in vitro* toxicity data was available in the form of HCB measurements (ER integrity and Δψm) in cardiac microtissues, measured after 72-hour exposures (36). To control, to some extent, against analytical variation induced by ion suppression and competition effects, which depend on the ionisation efficiency of the exposure xenobiotics, the list was filtered to contain only basic compounds. Related, structurally cardiotoxic xenobiotics with very low potency according to HCB data were filtered out since exposing at higher concentrations increases the likelihood of analytical challenges caused by the xenobiotics. A ratio of 1:2 non-structurally cardiotoxic/structurally cardiotoxic xenobiotics was chosen, such that there were sufficient structurally cardiotoxic xenobiotics to discover a relatively generalisable and consistent metabolic signature while having a sufficient 'out group' to reliably assess specificity.

Further criteria to select the eight structural cardiotoxic xenobiotics included:

1. Xenobiotics must be clinically recognised structural cardiotoxins, i.e., FDA approval label must include structural-based cardiovascular warnings.

2. Include subsets of xenobiotics which induced similar *in vitro* responses while maintaining diversity (based on HCA of HCB measurements, Figure D.1a).

3. Maintain chemical class diversity – include at least one anthracycline and one tyrosine kinase inhibitor (TKi).

Further criteria to select the four non-structurally cardiotoxic xenobiotics included:

1. Xenobiotics do not exhibit cardiotoxicity by any mechanism, i.e., no cardiovascular warnings on the FDA approval label.

2. Xenobiotics must not induce a response against HCB indicators at therapeutically relevant concentrations (<10x C_{max}, the maximum clinical blood concentration following treatment at therapeutic dose)

3. Include xenobiotics of the same chemical class or with structural similarity to the selected structurally cardiotoxic xenobiotics.

4. Maintain diversity in terms of *in vitro* response (based on HCA of HCB measurements – Figure D.1b).

5.2.2.2 Concentration selection

The nominal exposure concentrations (Table 5.1) were selected based on HCB measurements of cardiac microtissue responses to each xenobiotic for 72-hours (36). The high exposure concentration for each xenobiotic was the lowest value from (1) IC_{30} cell viability at 72-hours after initial exposure, as indicated by results of an ATP depletion assay, i.e., a phenotypically anchored concentration, (2) 15x C_{max}, to ensure therapeutic relevance, and (3) the lowest nominal concentration previously investigated by HCB. The low exposure concentrations were a half-log dilution of the high exposure concentrations. These are concentrations at which no ATP depletion was observed.

Table 5.1 Nominal concentrations of xenobiotic exposures.
The nominal low and high concentrations for each of the twelve xenobiotics to which cardiac microtissues were exposed in this study are reported. The reasoning for the selected nominal high concentration is reported, as per the selection criteria outlined in the main text. Also detailed is the batch in which exposure to each xenobiotic was carried out, and the structural cardiotoxicity label for each xenobiotic.

Batch	Xenobiotic	Structurally cardiotoxic	Nominal concentration - low (μM)	Nominal concentration - high (μM)	Reason for nominal high concentration
A	Acyclovir	False	15.8	99.9	15x C_{max}
A	Clozapine	True	2.23	7.05	15x C_{max}
A	Sorafenib	True	1.18	3.74	Cell viability IC_{30}
B	Buspirone	False	0.14	0.45	15x C_{max}
B	Doxorubicin	True	0.11	0.36	Cell viability IC_{30}
B	Lapatinib	True	1.75	5.53	Cell viability IC_{30}
C	Erlotinib	False	14.2	45.0	15x C_{max}
C	Idarubicin	True	0.095	0.30	Lowest investigated
C	Sunitinib	True	1.12	3.53	Cell viability IC_{30}
D	Mebendazole	False	9.63	30.5	15x C_{max}
D	Dasatinib	True	3.42	10.8	15x C_{max}
D	Fluorouracil	True	15.8	69.2	15x C_{max}

5.2.2.3 Batching

Exposures were carried out across four separate batches, using microtissue cultures originating from separate vials of hiPSC-CM. Each batch included exposure to two structurally cardiotoxic xenobiotics and one non-structurally cardiotoxic xenobiotic, each at two concentrations, for 6-, 48- and 72-hours. Sorting of xenobiotics amongst the four batches was otherwise random. Each batch also included a set of controls, where microtissues were exposed to 0.1% DMSO for 6-, 48- or 72-hours.

The treatment of 21-day mature cardiac microtissues in each batch was performed as described previously (Section 3.2.1).

5.2.3 SAMPLE COLLECTION

Microtissues and spent culture media were collected for metabolomics analysis as described previously (Section 3.2.3.2). Each sample of 28 microtissues was isolated on the filter surface of a cell strainer and washed with 3x 1.0 mL 0.9% NaCl, followed

by 1.0 mL ultrapure water. The corresponding filtered spent culture medium was collected into a microcentrifuge tube.

5.2.4 Extraction of intracellular polar compounds and lipids

Extraction of intracellular polar metabolites and lipids from cardiac microtissues was performed as described previously (Sections 3.2.4.1 and 3.2.4.2, respectively). Extraction solvents for biological samples were supplemented with 0.2 µM L-tryptophan-(indole-d5) (Merck, Gillingham, UK) and 0.2 µM dodecylphosphorylcholine-d38 (Merck) for polar metabolites and lipids, respectively.

Extraction was performed over five days for polar metabolites and lipids separately, with samples from a single exposure batch extracted per day. The extraction order of exposure batches was randomised. Samples were split by block randomisation into manageable ‘sub-batches’ of 21 for extraction. Extracts from each extraction sub-batch were transferred to two 96-well microplates, one each for positive and negative ionisation-based MS analysis, prior to drying. On the fifth day, 80 control samples designated for intra-study QCs and 8 process blanks, collected across the four exposure batches, were extracted in four sub-batches, assigned by block randomisation. Intra-study QC extracts from all sub-batches were pooled after centrifugation then aliquoted into 2x 88 separate wells across four 96-well microplates prior to drying. Dried aliquots of process blanks were prepared in the same way. Pooled extracts were stored at 4°C during extraction of subsequent sub-batches.

All dried extracts were stored at -80°C until analysis.

5.2.5 Resuspension of dried intracellular extracts

On a given day of metabolomics analysis, 18 96-well microplates, each containing 14 study sample dried extracts, *i.e.,* total of 252 study samples or two exposure

batches, plus one 96-well microplate containing intra-study QC and process blank dried extracts, were thawed on wet ice. Resuspension of a maximum of four microplates was performed in parallel using a Biomek i7 Hybrid Workstation (i7, Beckman Coulter). Polar and lipid dried extracts were resuspended in 30 or 40 µL resuspension solvent, respectively. Resuspension solvent for polar extracts was 4:1 (v/v) methanol/water with 0.25% formic acid and 4:1 (v/v) methanol/25 mM aqueous ammonium acetate, for positive and negative ion metabolomics, respectively, and 2:1 (v/v) 7.5 mM methanolic ammonium acetate/chloroform for lipid extracts. After addition of solvent, microplates were placed on the orbital shaker and shaken for 1-minute at 300 revolutions per minute (rpm), then transferred to a centrifuge for 3-minutes (3,622-*g* at 4℃). Spun plates were returned to the deck of the i7 and 20 or 30 µL polar or lipid resuspended extracts, respectively, were transferred to a 384-well Eppendorf twin-tec analysis plate. After transfer of all 252 study samples, intra-study QCs and process blanks, the analysis plate was sealed with heat-seal foil, centrifuged at 2,000-*g* for 10-minutes (4℃), then placed in a TriVersa Nanomate sample compartment, maintained at 10℃, ready for analysis.

5.2.6 Data acquisition by nESI-DIMS

Data were acquired using an Orbitrap ID-X Tribrid mass spectrometer (Thermo Scientific) with a nESI source (TriVersa Nanomate, Advion) and a modification of the spectral stitching nESI-DIMS method reported previously (108, 252).

The newly developed spectral stitching method consisted of either 19 or 33 SIM windows of variable width for analysis of the polar metabolites and lipids, respectively (Table 5.2, Table D.1). The widths of the SIM windows were defined using existing mass spectral measurements from cardiac microtissue intracellular extracts, i.e., data presented in Chapter 3, for each of the four assays separately.

Specifically, SIM windows were defined such that the total ion population was evenly distributed between SIM windows (112, 113). Furthermore, the size of the overlapping mass range between adjacent SIM windows was reduced from 10 Da to 5 Da, accounting for the improved ion isolation efficiency profile offered by the ID-X quadrupole compared with the Orbitrap Elite ion trap (original spectral stitching method).

Table 5.2 Spectral stitching nESI-DIMS method parameters.
Mass spectrometry parameters for the acquisition of untargeted metabolomics data by four nESI-DIMS assays performed on an Orbitrap ID-X Tribrid mass spectrometer.

Assay	Polar positive	Polar negative	Lipids positive	Lipids negative
Ionisation mode	Positive	Negative	Positive	Negative
Full mass range	50 – 620	50 – 620	190 – 2000	190 – 2000
Number of SIM windows	19	19	33	33
Number of internal replicates	3	3	3	3
Approximate method length (min)	3.9	3.9	3.9	3.9
Ion transfer tube temperature (°C)	200	200	200	200
RF lens voltage (%)	30	30	60	60
Isolation mode	Quadrupole	Quadrupole	Quadrupole	Quadrupole
Isolation window width	Variable	Variable	Variable	Variable
Mass analyser	Orbitrap	Orbitrap	Orbitrap	Orbitrap
Number of microscans	7	7	4	4
Resolution	240,000	240,000	240,000	240,000
AGC target	$5x10^4$	$5x10^4$	$5x10^4$	$5x10^4$
Maximum injection time (ms)	200	200	200	200

MS^n data were acquired using methods based on the spectral stitching full scan (MS^1) methods. For acquisition of MS^n data of endogenous features, the full mass ranges for polar or lipid assays were divided into three segments, each to be analysed by a separate sample injection. MS^1 data were acquired by SIM scans of the same mass ranges as the corresponding full scan method (Table D.1). After each SIM MS^1 scan, MS^n data were acquired for a defined period of time: either 4- or 2-minutes for polar and lipid assays, respectively, before analysis progressed to the next SIM MS^1 scan. Precursors for fragmentation were selected from measurements made in the preceding SIM MS^1 scan, guided by a user-defined target inclusion list

of toxicologically relevant metabolites (MTox700+ biomarker list (225)) and exclusion list of *m/z* features measured in a solvent blank sample. MS^n data acquired included HCD MS^2, using either three stepped normalised-CEs or single normalised-CE selected by 'Assisted CE', CID MS^2, and CID MS^3 for the three most intense fragments measured by single CE HCD MS^2 and, separately, for three most intense fragments measured by CID MS^2 (Figure 5.1). For acquisition of MS^n data corresponding to xenobiotic features, the same methods were implemented except shorter 1-minute or 30-second scan cycles for each SIM window in polar and lipid assays, respectively, to allow acquisition of data across the full mass ranges from a single sample injection.

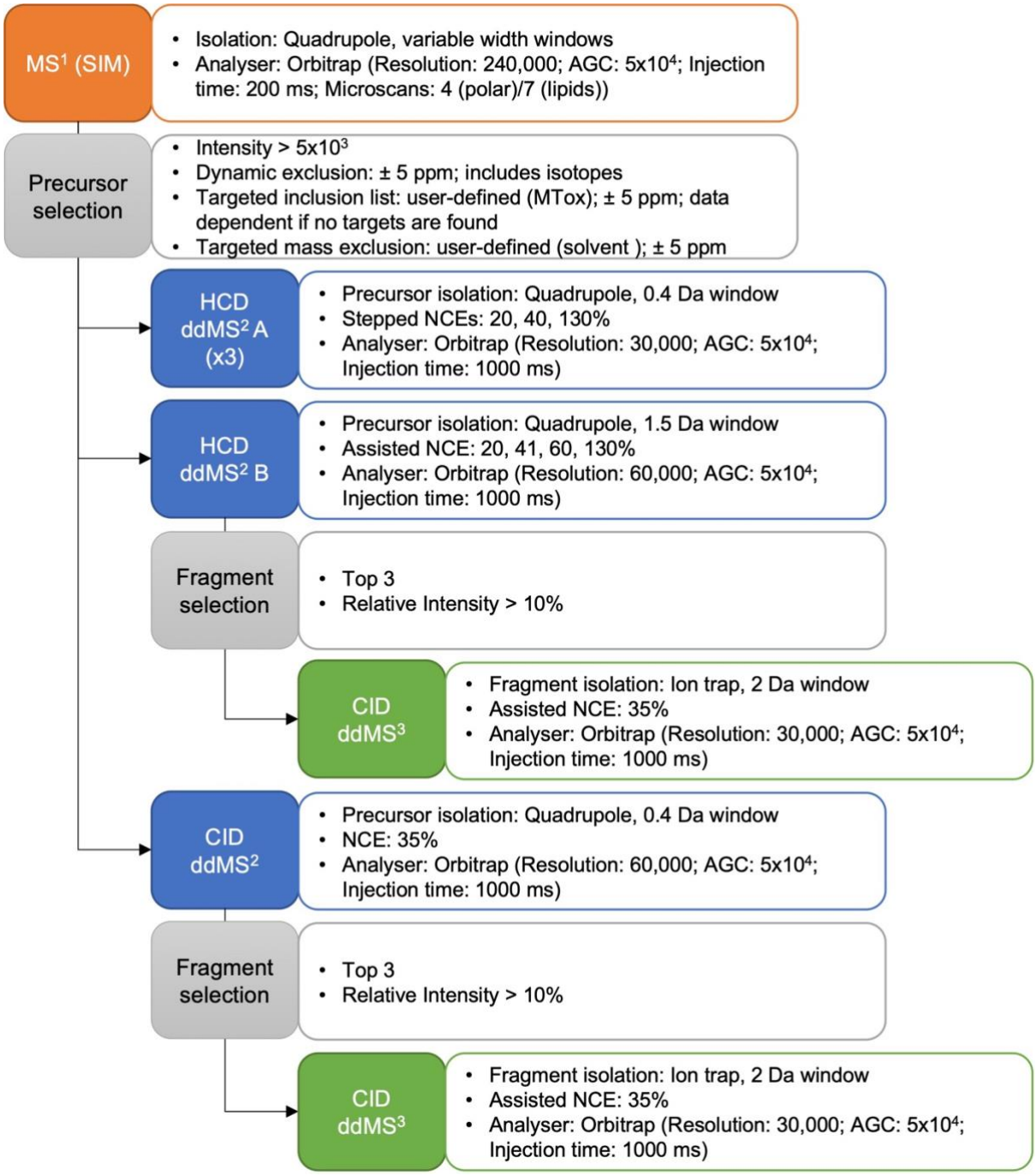


Figure 5.1 SIM-based nESI-DIMS^n data acquisition method.
The flow chart describes the method for acquiring MS^n data by nESI-DIMS using an Orbitrap ID-X Tribrid mass spectrometer. Each scan cycle begins with SIM (MS^1) scan by the Orbitrap, measurements from which are used to select precursors which meet defined criteria for subsequent fragmentation. Each selected precursor is analysed by SIM MS^1 scan, using an isolation window of 0.4 Da before fragmentation by higher-energy collisional dissociation (HCD) at three stepped normalised collision energies (NCE): 20, 40 and 130% in triplicate. The selected precursor is also fragmented by HCD at a single, optimal NCE, selected by 'Assisted CE' from a choice of 20, 41, 60 and 130%. Thirdly, the selected precursor is fragmented by collision-induced dissociation (CID) in the high-pressure cell of the dual-pressure linear ion trap using an NCE 35%. All MS^2 data are detected by the Orbitrap. Additionally, the three most intense MS^2 fragments resulting from HCD at the single, optimal, NCE, and the three most intense MS^2 fragments resulting from CID at NCE 35% undergo CID fragmentation, provided they pass the defined intensity filter. The resulting MS^3 fragments are

detected by the Orbitrap. This cycle is repeated for as many MS^1 precursors as possible within the 4- or 2-minute cycle time for polar and lipid assays, respectively, before proceeding to the next SIM MS^1 scan, at which point the cycle repeats.

Analysis was performed across two analytical batches, corresponding to two 384-well microplates of samples. Each analytical batch was composed of samples from two (random) exposure batches, maintained as separate blocks. The analysis order of samples within each exposure batch block was block randomised. Intra-study QCs were analysed after every eighth sample. Process blank data were acquired at the start and end of each exposure batch block. MS^n data were acquired at the end of each analytical batch. Between analytical batches, the MS ion transfer capillary was cleaned, and the nESI chip changed.

5.2.7 Processing and annotation of nESI-DIMS data

5.2.7.1 Raw data processing

Data were processed using the DIMSpy tools (116) in Galaxy interface as described previously (108), (Section 3.2.4.5). After an initial round of DIMSpy peak picking, spectral stitching and sample alignment, intra-study QCs and study samples with internal standard intensity outside defined thresholds (median ± 3x MAD, calculated separately for intra-study QCs and study samples per analytical plate) were removed. Features corresponding to the $[M+H]^+$ and $[M-H]^-$ ion forms of L-tryptophan-d5-indole, and the $[M+H]^+$ and $[M+acetate]^-$ ion forms of dodecylphosphorylcholine-d38 were used for the polar positive, polar negative, lipids positive and lipids negative datasets, respectively.

Following removal of outliers from the dataset, data were re-processed, including peak picking and spectral stitching (SNR>3, ±2 ppm mass tolerance, ≥2 internal replicates), sample alignment (±2 ppm mass tolerance), blank subtraction (features with intensity <10x median blank intensity in ≤80% non-blank samples removed) and sample filtering (features present in ≤50% non-blank samples were removed).

Processed data were subsequently spit into batch-specific peak-intensity matrices prior to further data filtering and pre-processing.

5.2.7.2 Discovery and annotation of xenobiotic-related features

Putative xenobiotic-related features within the processed datasets were discovered and annotated using the untargeted ADME/TK workflow presented in Chapter 2 (Figure 2.1). Mainly, three intensity-based filters were applied to the blank-filtered peak-intensity matrices for each of the twelve xenobiotics separately. These filters were (1) retain only features in >50% samples exposed to the high concentration of the given xenobiotic, (2) retain only features in <50% batch-matched control samples, and (3) where features were measured in both exposed and control samples, retain only those where the median intensity in samples exposed to the high concentration of the given xenobiotic is >10x median intensity in batch-matched control samples. Filters were applied to data across all three exposure durations simultaneously.

Putative xenobiotic-related features were annotated as described previously, using BEAMSpy and library of SyGMa-predicted biotransformation products for each of the twelve xenobiotics (Section 2.2.10).

5.2.7.3 Endogenous peak matrix processing

Further filtering and pre-processing of the peak-intensity matrices was applied using the R/Bioconductor package, structToolbox (178), to prepare the data for statistical analysis. Mainly, (1) putative xenobiotic-related features, (2) features corresponding to the internal standard, (3) features present in <50% of all non-blank samples, (4) samples with >50% missing values, and (5) features present in <70% intra-study QCs were all removed from the peak matrices. Data were then normalised by PQN, applied to subsets of features measured by each SIM window separately.

Subsequently, any features with RSD across intra-study QCs >30% after normalisation were removed.

5.2.7.4 Annotation of endogenous metabolites and lipids

Putative annotation of *m/z* features was achieved using the Python package BEAMSpy (v0.1.0). Ion forms were annotated against a list of common adducts, isotopes, neutral losses and multiply charged species, according to calculated mass differences, with mass tolerance of ±2 ppm. Compound annotation was performed using the curated lists of metabolites and lipids present in cardiac microtissues (Tables eC.1 and eC.2) and list of toxicity metabolic biomarkers (MTox700+ (225)) as the reference compound library and a ±2 ppm mass error window.

More confident annotations were derived by spectral matching of processed MS^n data to in-house library of toxicologically relevant compounds and public spectral databases (137). MS^n data were processed using the Python package MSnPy (https://github.com/computational-metabolomics/msnpy), operated in a Galaxy interface. This included (1) grouping of MS^n scans according to MS^1 precursor, i.e., grouping of stepped normalised-CE HCD MS^2, single normalised-CE HCD MS^2, CID MS^2, and CID MS^3 spectra, (2) peak picking across all grouped scans using SNR threshold of 10, mass tolerance of ±5 ppm, and 50% filter, where replicate scans were available, and (3) processed, grouped spectra were used to create database of spectral trees. Spectral matching was performed on each MS^2 spectra from each spectral tree separately after conversion to msp format using msPurity (141), with ±10 ppm mass tolerance for matching product ions.

Outputs of MSnPy processing and MS^2 spectral matching for each data file were filtered to remove any matches where the theoretical precursor *m/*z was outside the isolation window (± 0.2 Da) used by the instrument and to retain only matches where

either the dot product or reverse dot product score was >0.5. Where there were multiple compound annotations per spectrum, filtered outputs were collapsed to a single record per spectrum. Annotations were then matched to features of the MS^1 peak-intensity matrix where the theoretical precursor *m/z* was within ±2 ppm of MS^1 feature's measured *m/z*, with multiple annotations originating from separate raw data files collapsed into single records per feature.

5.2.8 Sample preparation for UHPLC-MS

Samples of spent culture medium were prepared as described previously (Section 3.2.5.1) with some modifications. Samples were thawed overnight at 4°C. Two 50 µL aliquots of every sample were added to separate 96-well plates. Additionally, an intra-study QC pool of aliquots from every study sample, twelve pools from aliquots of high concentration exposed samples, one for each test xenobiotic, and a pool of aliquots from every control sample were generated. Each of these pools were subsequently added to separate wells of 96-well microplates in 50 µL aliquots. Process blanks were generated from 50 µL water, in place of media.

Quantitation calibration standards, quant-QCs, and quant-blanks (Table 5.3) were prepared as described previously (Section 3.2.5.2). 50 µL aliquots of each were added to separate wells of 96-well microplates.

Table 5.3 Concentrations of calibration standards and QC preparations for quantitation of parent xenobiotics.
The table details the concentrations of the eight quantitation calibration standards and three quantitation quality controls (QCs) for each xenobiotic. The calibration samples were prepared per batch such that a given sample comprised the relevant concentration of three xenobiotics. Two aliquots of each calibration sample and QC were prepared for analysis.

Batch	Xenobiotic	[Quantitation calibration standards] (μM)								[Quantitation QCs] (μM)		
		1	2	3	4	5	6	7	8	Low	Mid	High
A	Acyclovir	2	4	8	16	32	64	128	256	6	24	204.8
A	Clozapine	0.125	0.25	0.5	1	2	4	8	16	0.0375	1.5	12.8
A	Sorafenib	0.0625	0.125	0.25	0.5	1	2	4	8	0.1875	0.75	6.4
B	Buspirone	0.008	0.016	0.0313	0.0625	0.125	0.25	0.5	1	0.0234	0.0938	0.8
B	Doxorubicin	0.008	0.016	0.0313	0.0625	0.125	0.25	0.5	1	0.0234	0.0938	0.8
B	Lapatinib	0.125	0.25	0.5	1	2	4	8	16	0.375	1.5	12.8
C	Erlotinib	1	2	4	8	16	32	64	128	3	12	102.4
C	Idarubicin	0.0080	0.0160	0.0313	0.0625	0.125	0.25	0.5	1	0.0234	0.0938	0.8
C	Sunitinib	0.0625	0.125	0.25	0.5	1	2	4	8	0.1875	0.75	6.4
D	Dasatinib	0.25	0.5	1	2	4	8	16	32	0.75	3	25.6
D	Mebendazole	2	4	8	16	32	64	128	256	6	24	204.8
D	Fluorouracil	0.5	1	2	4	8	16	32	64	1.5	6	51.2

All aliquots were prepared for analysis by addition of 150 μL 1:1 acetonitrile/methanol containing 1 μM L-tryptophan-(indole-d5). Mixing was performed by orbital shaking (200 rpm, 2-minutes, room temperature). Centrifugation was performed at 2600-*g* (10-minutes at 4°C). 150 μL supernatant of every extract was subsequently transferred to 96-well microplate analysis plates.

5.2.9 Data acquisition by UHPLC-MS

Samples were analysed as described previously (Section 3.2.5.3). Analysis of extracted spent culture medium was performed in one continuous sequence with the four exposure batches maintained as separate blocks. The analysis order of exposure batches and the order of samples within each exposure batch were randomised. Quantitation calibration standards, quant-QCs, and quant-blanks were analysed at the start and end of each exposure batch block. Intra-study QCs were analysed after every sixth sample. Process blank data were acquired at the start, middle and end of the analytical sequence. Xenobiotic-related MS/MS data were acquired at the end of each exposure batch block. Endogenous-related MS/MS data were acquired after the second and fourth blocks.

5.2.10 Quantitation of extracellular parent xenobiotic concentrations

Data processing for xenobiotic quantitation was performed using TraceFinder (v5.1, Thermo Scientific). Calibration functions were calculated by least-squares non-linear regression analysis with a weighting of $\frac{1}{x^2}$. The goodness-of-fit was evaluated according to R^2. Measurements of calibration standards were excluded from the final regression analysis if the absolute difference between the back-calculated and nominal concentrations was >40%.

Accuracy and precision of calibration was assessed using accepted quant-QCs (absolute difference between back-calculated and nominal concentrations ±40%), with accuracy defined as the mean calculated concentration relative to nominal concentrations, and precision defined as the mean CV across the calculated concentrations of duplicate quant-QCs.

5.2.11 Processing and annotation of UHPLC-MS untargeted data

5.2.11.1 Raw data processing

Raw UHPLC-MS untargeted metabolomics data were processed as described previously using XCMS (v3.12.0) after conversion to mzML file format using ProteoWizard software (v3.0.19198) (Section 2.2.9). Parameters were as follows; min. peak width: 3; max. peak width: 30; ppm: 10; mzdiff: 0.001; bw: 1; binSize: 0.005; min. frac.: 0.5 per sample group, where sample groups were defined according to batch and exposure conditions. OBI-warp RT alignment was also applied with following parameters: response: 10; gapInit: 0.6; gapExtend: 2.4.

Results of preliminary processing revealed substantial shifts in RT in the HILIC positive data which was not corrected by OBI-warp RT alignment (Figure D.2a). To correct this effect, and maximise accurate alignment of features between all samples, data were split into three groups of samples after peak deconvolution

(Figure D.2b). OBI-warp RT alignment was applied to each group separately. Functions were subsequently calculated by fitting smooth spline to RT error (difference in RT of reference features between reference sample from group two/three and the group one reference sample) against RT (Figure 5.2). Reference features were *m/*z-RT features with single peak in both reference samples after XCMS peak density-based feature correspondence using bw: 10 and binSize: 0.005. The calculated functions were used to align RTs of group two and three to those of group one, correcting the observed RT shifts. Data from the three aligned sample groups were merged into single XCMSSet object before XCMS feature correspondence, generating the aligned peak-intensity matrix.

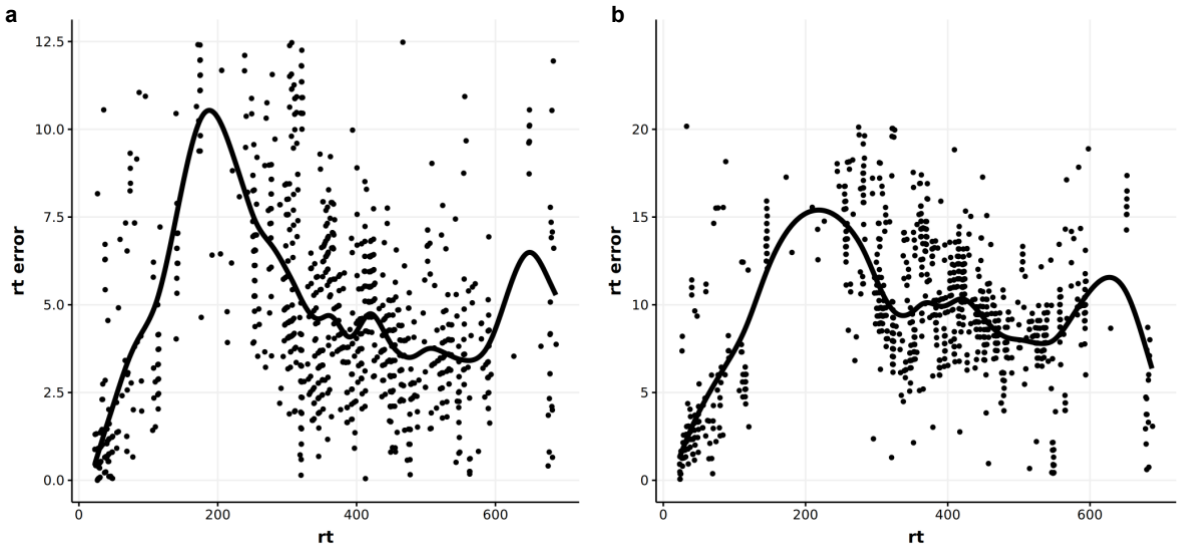


Figure 5.2 Smooth spline functions for retention time alignment of HILIC positive data. Smooth spline functions fitting retention time error of **a** 'group 2' samples (retention time in group 2 reference sample minus retention time in group 1 reference sample) and **b** 'group 3' samples (retention time in group 2 reference sample minus retention time in group 1 reference sample) against retention time in group 1 reference sample. Sample groups were defined based on visual inspection of peak count after XCMS with no retention time alignment as a function of injection order (Figure D.2b).

5.2.11.2 Discovery and annotation of xenobiotic-related features

As described in section 5.2.7.2, using peak-intensity matrices generated by XCMS as input.

5.2.11.3 Endogenous peak matrix processing

Endogenous peak matrix processing was performed as described previously (Section 3.2.5.4). QC-RSC (118) was applied to correct for drift in intensity as a function of injection order, after removal of blank and xenobiotic-related feature, and prior to other filtering.

5.2.11.4 Annotation of endogenous metabolites

Putative metabolite annotation was achieved using the Python package BEAMSpy (v0.1.0). Features were grouped according to RT (±5-second tolerance) and Pearson's correlation coefficient ($r \geq 0.7$) and *p*-value ($p \leq 0.01$). Ion forms were annotated against a list of common adducts, isotopes, neutral losses and multiply charged species, according to calculated mass differences, with mass tolerance of ±5 ppm. Compound annotation was performed using HMDB (v4.0, accessed 9th September 2020) as the reference compound library and a ±5 ppm mass error window.

More confident annotations were derived by RT matching to in-house RT library of toxicologically relevant metabolites, i.e., metabolites within MTox700+ list of biomarkers (225), with match defined if measured *m/z* and RT were within ±2.5 ppm and ±10-seconds of library reference values. More confident annotations were also derived by spectral matching of MS/MS data, processed using msPurity (141) as described in Section 4.2.6.2, to in-house spectral database of toxicologically relevant compounds, i.e., metabolites found within MTox700+ biomarker list (225), using ±5 ppm mass tolerance for matching of both precursor and product ions. Outputs were filtered to retain only annotations with dot product score >0.8 then aligned to *m/z*-RT features of the MS^1 peak-intensity matrices using tolerances of ±2.5 ppm and ±20-seconds for *m/z* and RT, respectively.

Additional ‘confident’ annotations were derived by spectral matching against mzCloud database, performed using Compound Discoverer (v3.3, Thermo Scientific). Outputs were filtered to retain only annotations where HighChem HighRes match score >60. Annotations were aligned to *m/*z-RT features of the MS^1 peak-intensity matrices using tolerances of ±2.5 ppm and ±20-seconds for *m/z* and RT, respectively.

Aligned annotations for each *m/z*-RT feature were all considered in defining a final compound annotation, with order of preference as follows: (1) MS/MS spectral and RT match to in-house databases of toxicologically relevant metabolites, (2) RT match only to in-house database of toxicologically relevant metabolites, and (3) mzCloud spectral match. Where available data could not distinguish between isomers, multiple compound annotations were collapsed into a single record per *m/z*-RT feature.

5.2.11.5 Statistical analysis

Univariate analyses (Welch’s *t*-test and fold change calculations) were performed on PQN-normalised peak-intensity matrices using the R/Bioconductor packages structToolbox (v1.6.1) (178). Intensity measurements in samples corresponding to each exposure condition (exposure xenobiotic, concentration, and duration) were compared to batch- and exposure duration-matched controls.

HCA was performed on matrices of *t*-statistics (features vs. exposure condition), calculated by the Welch’s *t*-tests described above. Matrices were first filtered to remove features with missing values. Matrices from each assay (four intracellular DIMS assays, or two extracellular UHPLC-MS assays) were then mean centred, scaled by hard block variance scaling (253), concatenated, and vector normalised. Distance matrices were calculated by Euclidean distance function, and clustering

performed by ward.D2 function using the R package pvclust (254). Multiscale bootstrap resampling (1000 permutations) was performed to estimate the stability of the clusters, retrieving an “Approximately Unbiased” (au) *p*-value as a metric of cluster stability.

OPLS-DA was performed using the R/Bioconductor packages struct and structToolbox (178) on matrices of control normalised responses, i.e., relative intensities in xenobiotic exposed samples were normalised against median intensity in batch- and exposure duration-matched controls, to correct for any batch- and baseline temporal-based variation. Prior to analysis, data were $\log_2$ transformed, missing values imputed by KNN (k = 5), and vector normalised.

5.3 Results and Discussion

5.3.1 Discovering the fate of xenobiotics in a cardiac microtissue test system

5.3.1.1 Quantifying the free concentration of parent xenobiotics

In this study, cardiac microtissues were exposed to one of twelve small molecule xenobiotics for 6-, 48- or 72-hours at two nominal concentrations: a ‘low’ and ‘high’ concentration (Table 5.1). Targeted absolute quantitation of the twelve xenobiotics, using measurements from the same UHPLC-MS analysis used to measure endogenous metabolites, enabled comparison of nominal exposure concentrations to the free, i.e., fully dissolved and not bound to medium constituents or adsorbed to plasticware, concentration of xenobiotics available in the environment to which microtissues were exposed, over the full duration of the experiment (Figure 5.3, Table 5.4, Figure 5.4).

Quantitation was performed using positive ionisation data for eleven of the twelve xenobiotics, and negative ionisation data for fluorouracil (Table 5.4). The identity of

peaks integrated for calibration and quantitation were confirmed by accurate mass, RT and MS/MS match to authentic reference standard measurements made during the same analytical run (Figure D.3, Figure D.4). Calibration precision and accuracy was deemed acceptable for all xenobiotics based on calculated amounts in at least three of six quant-QCs being ±40% to theoretical amounts (accuracy) and the CVs per quant-QC level <40% (precision). Comparison across the twelve xenobiotics reveals the external calibration of buspirone had the greatest accuracy (within ±4.2%), and precision (3.4%) (Table 5.4). Acceptance criteria for external calibration curves used in this study are less strict than the criteria defined for regulatory studies, e.g., according to FDA guidelines which state that accuracy and precision should be ±15% (255). This was to account for the inability to correct for analytical variability and drift, largely due to the absence of isotopically labelled internal standards. It is anticipated that the use of labelled internal standards would enable correction for analytical variability and thus improve the accuracy and precision of quantitation. However, this would come with the risk of negatively impacting, e.g., by ion suppression, the measurement of endogenous metabolites in study samples, which may impede the ability to achieve the primary aim of the study.

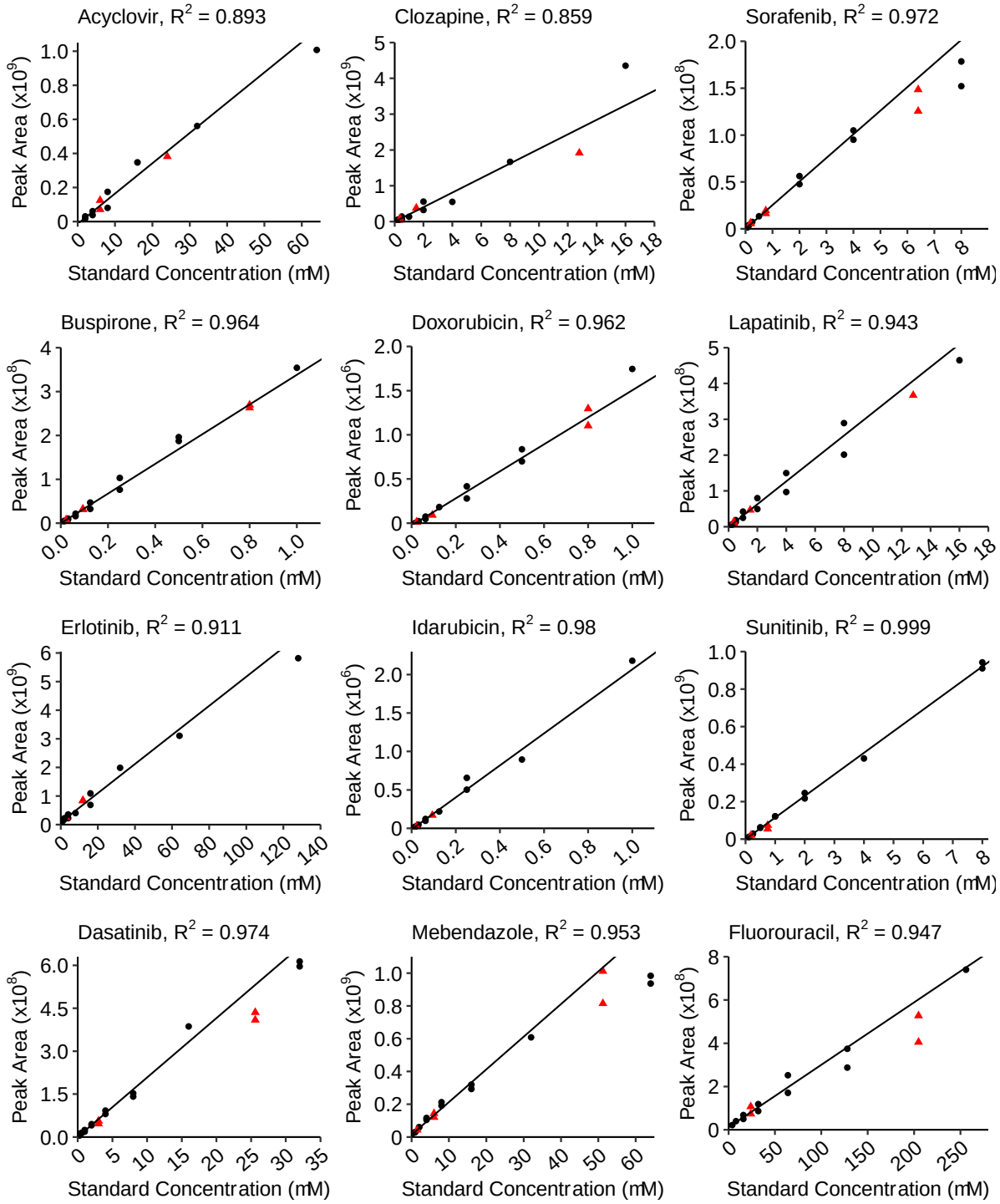


Figure 5.3 External calibration curves for quantitation of twelve parent xenobiotics.
Plots show the integrated area of MS^1 chromatographic peaks (MSI level 1 identifications based on matching of *m/z*, retention time and MS/MS to reference standards) against the nominal spiked concentration of duplicate quantitation calibration standards (•) for twelve parent xenobiotics. Also shown, are the measurements for duplicate quantitation quality controls (▲). Solid lines represent the calibration function calculated by least squares linear regression analysis with $\frac{1}{x^2}$ weighting. The R^2, describing the goodness-of-fit of the calibration function, are also reported. Excluded data points (calibration standards and quality controls) are not shown.

Table 5.4 External calibration metrics.
The ionisation mode of data used for calibration and quantitation, the lower and upper limits of quantitation (LLOQ and ULOQ, respectively) for each of the twelve parent xenobiotics, and the calibration function, as calculated by least squares linear regression, are reported. Also shown is the R^2 value, used to assess the goodness of fit of calibration standard measurements, the accuracy of quantitation, defined as average absolute difference between calculated concentration and nominal concentration of accepted quantitation quality controls, expressed as a percentage, and the precision of quantitation, defined as the average coefficient of variation across three quantitation quality control duplicates.

Xenobiotic	Batch	Ionisation mode	LLOQ (μM)	ULOQ (μM)	Calibration function	Goodness of fit (R^2)	Accuracy (%)	Precision (%)
Acyclovir	A	Positive	2	64	$1.78 \times 10^7 x - 1.26 \times 10^7$	0.893	78.7-129.2	38.8
Clozapine	A	Positive	0.125	16	$2.03 \times 10^8 x - 2.71 \times 10^6$	0.859	66.3-125.1	38.2
Sorafenib	A	Positive	0.063	8	$2.52 \times 10^7 x + 1.84 \times 10^5$	0.972	77.8-128.7	10.5
Buspirone	B	Positive	0.008	1	$3.39 \times 10^8 x - 5.26 \times 10^5$	0.964	97.0-104.2	3.4
Doxorubicin	B	Positive	0.016	1	$1.53 \times 10^6 x - 2.60 \times 10^4$	0.962	79.3-112.9	47.3
Lapatinib	B	Positive	0.125	16	$3.20 \times 10^7 x - 1.18 \times 10^6$	0.943	78.9-126.3	36.2
Erlotinib	C	Positive	1	128	$5.09 \times 10^7 x + 8.37 \times 10^7$	0.911	111.7-124.5	13.0
Idarubicin	C	Positive	0.008	1	$2.08 \times 10^6 x - 1.55 \times 10^4$	0.980	79.0-94.5	19.7
Sunitinib	C	Positive	0.063	8	$1.15 \times 10^8 x + 3.15 \times 10^4$	0.999	63.4-98.8	21.1
Dasatinib	D	Positive	0.25	32	$2.08 \times 10^7 x + 9.45 \times 10^5$	0.974	72.8-88.8	9.1
Mebendazole	D	Positive	0.5	64	$1.99 \times 10^7 x + 1.43 \times 10^7$	0.953	78.5-108.4	13.9
Fluorouracil	D	Negative	4	256	$2.89 \times 10^6 x + 1.15 \times 10^7$	0.947	66.6-137.7	22.3

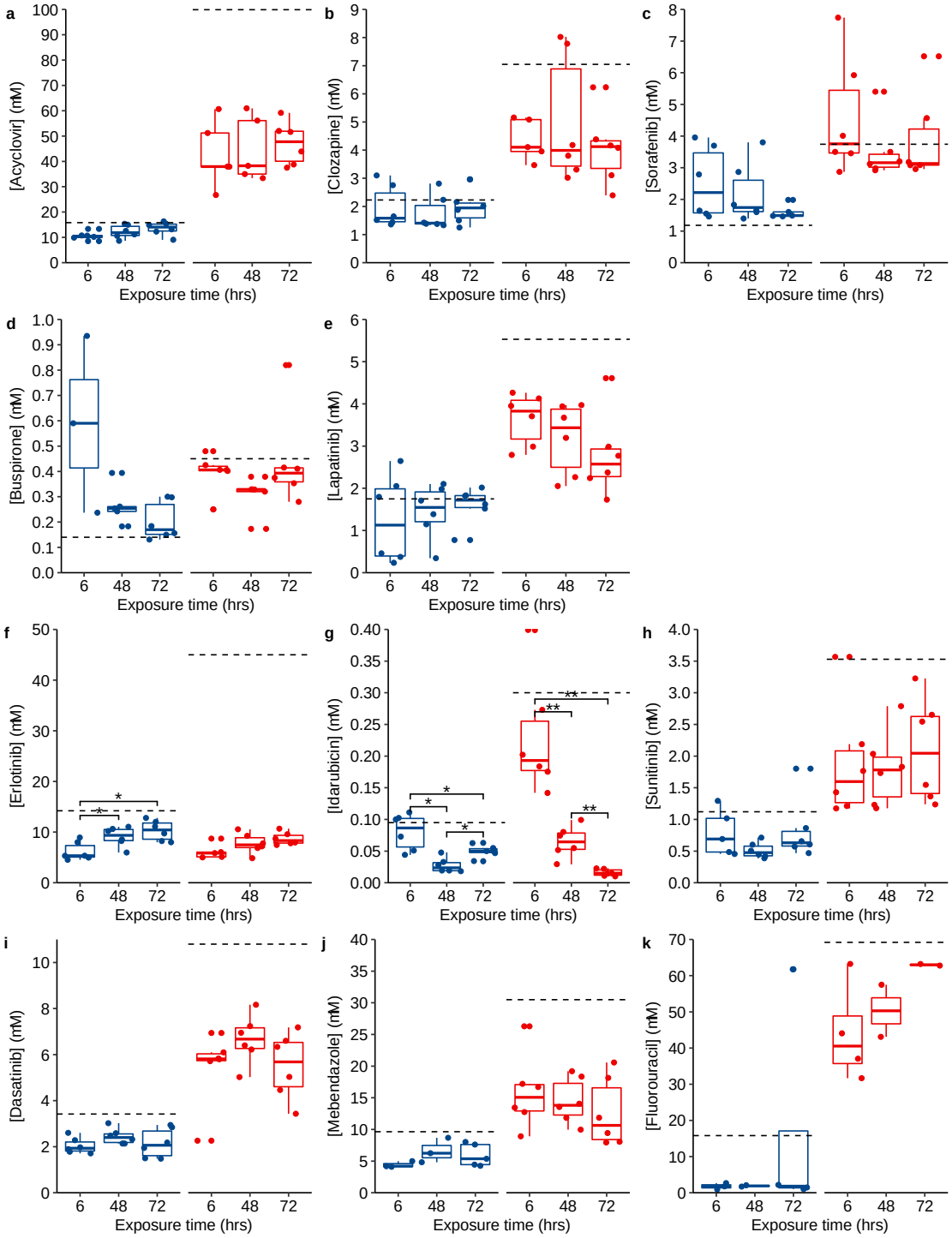


Figure 5.4 Quantitation of eleven parent xenobiotics in spent culture medium of cardiac microtissues.

Boxplots displaying the concentrations of xenobiotics in samples of pooled spent culture medium from 28 cardiac microtissues, incubated for 6-, 48- and 72-hours (hrs) following addition of the xenobiotics at the nominal concentrations. Concentrations were calculated by external calibration. Blue and red represent calculated concentrations in samples spiked with nominal low and high concentration, respectively. The dashed lines represent the nominal concentrations. Individual points show data from N=6 replicates. * and ** represent $p<0.05$ and $p<0.01$ significant difference between measured concentrations at each time point (two-sided *t*-test with Holm's multiple test correction).

External calibration enabled absolute quantitation of eleven of the twelve xenobiotics in samples of spent culture medium. Concentrations of doxorubicin could not be reliably quantified since either the corresponding chromatographic peak was not detected, relative intensities were below the threshold for quantitation, or calculated concentrations were less than the lower limit of quantitation (LLOQ). The results revealed the free concentrations of xenobiotic in the culture media to which microtissues were exposed during the experiments to be significantly lower than nominal concentrations for 16 of the 22 quantifiable exposure conditions when combining measurements from all exposure durations (Table 5.5). Explanations for this include lower than nominal concentrations as a consequence of non-specific binding to culture medium constituents such as serum, or sorption to the culture vessel and other plasticware (251, 256). It is also possible some xenobiotics may have dropped out of solution during preparation (257). Since measured free concentrations of the xenobiotics in stability control samples (nominal high concentration of each xenobiotic spiked in culture medium and incubated for 6-, 48- or 72-hours in the absence of microtissues) are also lower than the nominal concentrations (Table 5.5), it is unlikely these observations are a consequence of measurable uptake into the microtissues or partitioning into cell membranes (251).

Table 5.5 Difference between nominal and measured concentrations of eleven quantifiable xenobiotics.
The mean calculated concentration of each xenobiotic in spent culture medium of exposed microtissues is reported as a percentage of the nominal concentration. The significance of differences (*p*-value) was calculated by two-tailed *t*-test. N = 6 for nominal low and high concentrations, N = 3 for stability controls.

Xenobiotic	Low concentration		High concentration		Stability controls	
	Mean % nominal	*p*-value	Mean % nominal	*p*-value	Mean % nominal	*p*-value
Acyclovir	76.3	<0.001	45.1	<0.001	48.0	<0.001
Clozapine	85.1	0.038	63.6	<0.001	79.8	0.077
Sorafenib	180.8	0.001	107.0	0.455	107.5	0.605
Buspirone	220.2	0.012	85.7	0.065	87.5	0.376
Lapatinib	81.9	0.078	57.9	<0.001	68.0	0.001
Erlotinib	60.1	<0.001	16.9	<0.001	15.6	<0.001
Idarubicin	55.3	<0.001	34.4	<0.001	44.0	0.001
Sunitinib	62.9	<0.001	54.6	<0.001	50.2	<0.001
Dasatinib	64.7	<0.001	54.4	<0.001	61.3	<0.001
Mebendazole	59.2	<0.001	30.5	<0.001	40.8	<0.001
Fluorouracil	53.1	0.299	72.7	0.004	78.7	<0.001

The free concentrations of nine of the xenobiotics did not significantly change between the three measured exposure durations, indicating stability under experimental conditions for up to 72-hours (Figure 5.4, Figure D.5). The lack of change over time in the presence of cardiac microtissues also suggests concentrations are in excess of any uptake and biotransformation mechanisms of the test system. Conversely, the concentration of idarubicin, at both low and high nominal concentrations, reduced over time (Figure 5.4). This may be explained by instability of idarubicin under experimental conditions, which is substantiated by the consistent observation of significantly reduced concentration of idarubicin in stability control samples (Figure D.5).

The observed differences in measured compared with nominal exposure concentrations highlights the importance of quantifying sample-specific concentrations. In the absence of free concentration measurements, the use of nominal exposure concentrations can lead to inaccurate descriptions of concentration-response behaviour, limiting inter-study comparisons and IVIVE.

Quantifying the concentration of free xenobiotic as part of pharmaco- or toxico-dynamic *in vitro* assays, as presented here, enables a better estimation of the biologically effective dose, i.e., the dose at the target site in cells that causes an effect, facilitating more accurate prediction of *in vivo* efficacy or toxicity, respectively (251).

5.3.1.2 Xenobiotic biotransformation competency of cardiac microtissues

Biotransformation products of exposure xenobiotics formed by test systems in metabolomics studies may be discovered by application of an untargeted ADME/TK workflow to the acquired data, as demonstrated previously (Chapter 2). To this end, the biotransformation capacity of cardiac microtissues, the test system in this study, was evaluated using the intracellular (DIMS) and extracellular (UHPLC-MS) metabolomics datasets acquired here. The three intensity-based filters of the workflow were applied to twelve peak matrices, one per xenobiotic, separately, per analytical assay (six in total – four DIMS, two UHPLC-MS assays). Features retained by the three filters were annotated against SyGMa biotransformation predictions for each of the twelve parent xenobiotics using BEAMSpy (MS^1 data) and MetFrag (MS/MS data).

Implementation of the workflow to the DIMS intracellular data discovered 139, 159, 152 and 74 putatively annotated xenobiotic-related features across eleven of the twelve parent xenobiotics. No doxorubicin-related features were discovered, consistent with the inability to quantify the parent. The putative annotations of the discovered features indicate detection of up to 57 biotransformation products, including 9, 5, 16, 2, 8, 4, 4, and 9 biotransformation products of clozapine, dasatinib, erlotinib, idarubicin, lapatinib, mebendazole, sorafenib, and sunitinib, respectively (Figure 5.5, Table eD.1).

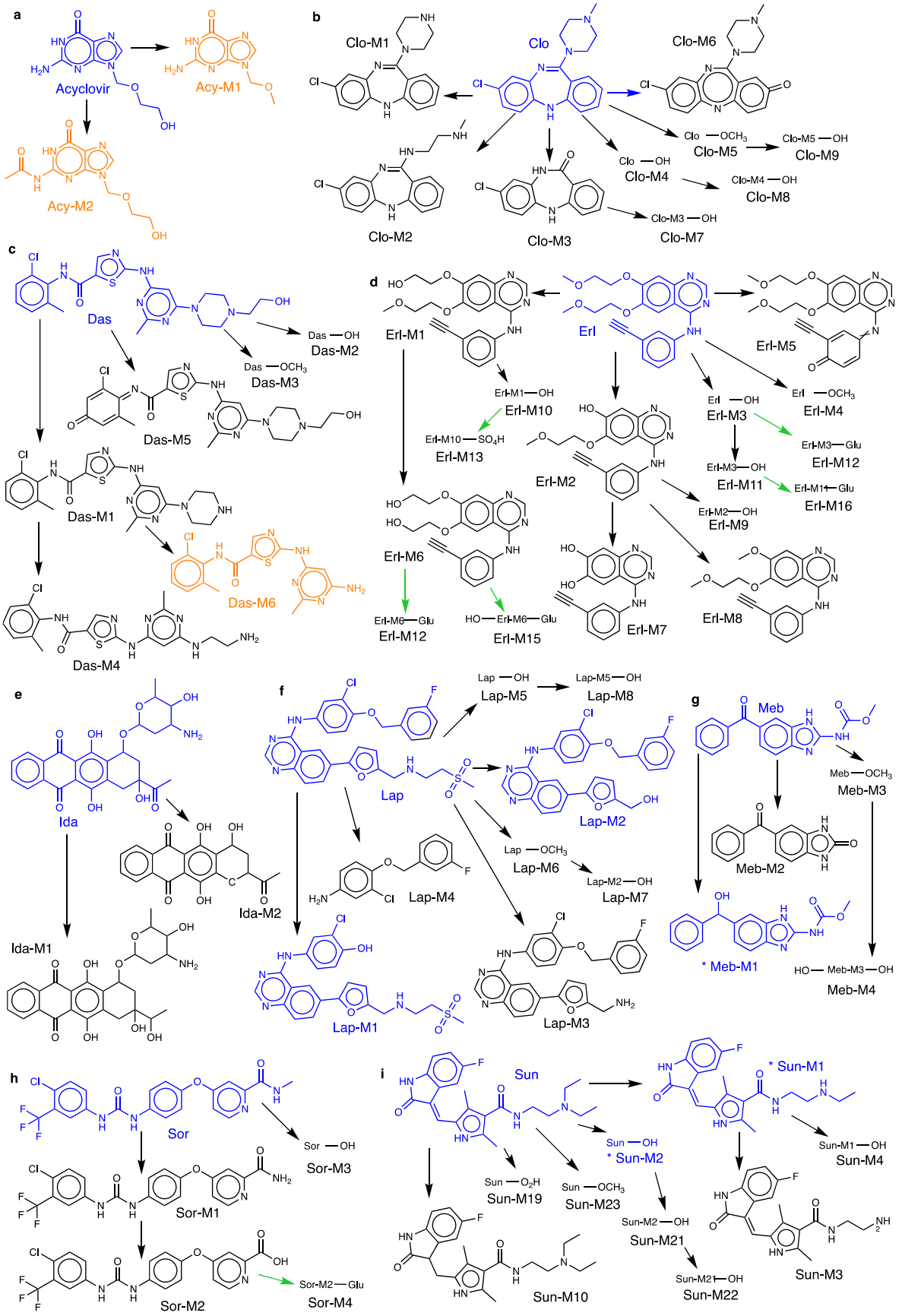


Figure 5.5 Parent xenobiotics and products of their biotransformation discovered in intracellular extracts and spent culture medium of exposed cardiac microtissues.

Shown, are the molecular structures of nine parent xenobiotics for which biotransformation products were discovered: **a** acyclovir, **b** clozapine, **c** dasatinib, **d** erlotinib, **e** idarubicin, **f** lapatinib, **g** mebendazole, **h** sorafenib and, **i** sunitinib. Arrows from the parent structures indicate routes of biotransformation, with the molecular structures of resulting biotransformation products shown. Biotransformation products in black were discovered in only the intracellular extracts, those drawn in orange were discovered only in the spent culture medium, and those drawn in blue were discovered in both intracellular extracts and the spent culture medium. The structural annotations of the biotransformation products presented are putative with most based on MS^1 *m/z* measurement only (MSI level 3-4, Schymanski level 3-4). Structures annotated with * are supported by MS/MS fragmentation data (MSI level 2-3, Schymanski level 2b-3). The colour of the arrow indicates the type of metabolic reaction required to form the discovered biotransformation product from the parent xenobiotic (black – phase I metabolic reactions, green – phase II conjugative metabolic reactions. *Glu - glucuronide

While putative annotations suggest these features are biotransformation products, it is also possible that features may arise from in-source modification, including adduct formation, heterodimerisation and fragmentation (95, 258). The absence of RT in DIMS data makes it unfeasible to distinguish between products of analytical and biological transformation, hence care must be taken in the interpretation of results from untargeted ADME/TK analysis of DIMS data.

Interrogation of the workflow outputs when applied to the UHPLC-MS data revealed eight biotransformation products across five parent xenobiotics within the spent culture media (Figure 5.5, Table 5.6). Here, the availability of chromatographic RT data provided greater confidence in the annotation of putative xenobiotic-related features since products of biological transformation have distinct RT to parent xenobiotics. Five of the biotransformation products were also discovered within the intracellular extracts. Assuming correct annotations, the larger number of biotransformation products discovered in the intracellular DIMS data compared with extracellular UHPLC-MS data are likely the combined result of biotransformation products being in greater concentration intracellularly and the greater analytical sensitivity of DIMS.

Table 5.6 Biotransformation products of test xenobiotics discovered in the spent culture media of exposed cardiac microtissues.
Biotransformation products discovered by application of the untargeted TK/ADME workflow to datasets acquired by HILIC positive and HILIC negative UHPLC-MS/MS analysis of the spent culture media from exposed cardiac microtissue cultures are listed. Details reported include the parent xenobiotic, an identifier for each biotransformation product, and its molecular formula. Also reported is the ion form by which the biotransformation product was detected, and its measured *m/z* and chromatographic retention time (RT). The confidence in annotation of each biotransformation product according to MSI and Schymanski confidence levels are reported, and where MS/MS data were available, the *m/z* and putative molecular formula of MS/MS fragments annotated by MetFrag are listed.

Parent xenobiotic	ID	Molecular Formula	Ion form	*m/z*	Rt (min)	MS| Confidence Level	Schymanski Confidence Level	Annotated MS/MS fragment ions
Acyclovir	Acy-M1	$C_7H_9N_5O_2$	$[M+H]^+$	196.0829	1.70	3	4	-
Acyclovir	Acy-M2	$C_{10}H_{13}N_5O_4$	$[M+H]^+$	268.1040	1.22	3	4	-
Dasatinib	Das-M6	$C_{16}H_{15}ClN_6OS$	$[M+H]^+$	375.0791	0.57	3	4	-
Lapatinib	Lap-M1	$C_{22}H_{21}ClN_4O_4S$	$[M+H]^+$	473.1046	1.15	3	4	-
Lapatinib	Lap-M2	$C_{26}H_{19}ClFN_3O_3$	$[M+H]^+$	476.1175	0.50	3	4	-
Mebendazole	Meb-M1	$C_{16}H_{15}N_3O_3$	$[M+H]^+$	298.1186	0.52	2	3	95.0491 ($[C_6H_6O]^+H^+$) 105.0446 ($[C_6H_4N_2]^+H^+$) 266.0925 ($[C_{15}H_{12}N_3O_2]^+$)
Sunitinib	Sun-M1	$C_{20}H_{23}FN_4O_2$	$[M+H]^+$	371.1879	4.20	2	2b	283.0878 ($[C_{16}H_{13}FN_2O_2\text{-}H]^+$) 326.1301 ($[C_{18}H_{17}FN_3O_2]^+$)
Sunitinib	Sun-M1	$C_{20}H_{23}FN_4O_2$	$[M-H]^-$	369.1730	3.85	2	2b	255.0941 ($[C_{15}H_{12}FN_2O]^-$)
Sunitinib	Sun-M2	$C_{22}H_{27}FN_4O_3$	$[M+H]^+$	415.2140	4.17	2	3	326.1300 ($[C_{18}H_{17}FN_3O_2]^+$)

Considering the metabolism required to form the biotransformation products discovered intracellularly and extracellularly from the parent xenobiotics, the results presented here demonstrate cardiac microtissues possess both phase I and phase II metabolic capabilities (Figure 5.5). Phase I metabolism was responsible for the formation of 89.5% of the biotransformation products discovered, while biotransformation products formed by phase II reactions (glucuronide or sulfate conjugation) were discovered for only two parent xenobiotics, erlotinib and sorafenib. Findings presented here in terms of the metabolic capability of microtissues are consistent with previously reported findings on the metabolic capability of hiPSC-CMs (Section 2.3.6), the most abundant of the three cell types in cardiac

microtissues (36). Comparison with the earlier study revealed six of nine, and two of five sunitinib biotransformation products discovered intracellularly and in the spent culture medium of hiPSC-CMs, respectively, were also discovered in this current study. All the biotransformation products of sunitinib discovered in both test systems were formed by phase I oxidative and/or hydrolytic reactions.

Taken together, results presented here demonstrate cardiac microtissues possess some xenobiotic biotransformation competency, including for phase I and phase II-type reactions. This is the first reported direct evidence demonstrating xenobiotic biotransformation by cardiac microtissues. The demonstrated ability to biotransform xenobiotics may promote the use of cardiac microtissues for predicting *in vivo* toxicity given the greater translational relevance of *in vitro* models which more closely replicate the *in vivo* exposure environment, where cells are typically exposed to both parent xenobiotics and their biotransformation products (200). Considering the toxicity of xenobiotics, it is possible that the products of a xenobiotic's biotransformation may be more toxic than the parent, thus highlighting the pertinence of an *in vitro* model with capacity for biotransformation for *in vivo* toxicity prediction (259). Future efforts to compare the biotransformation of xenobiotics in cardiac microtissues with xenobiotic biotransformation products distributed to cardiac tissue *in vivo* would further assist the evaluation of cardiac microtissues as an *in vitro* model with high translational relevance for cardiac safety assessment .

5.3.2 Exploring the metabolic responses of cardiac microtissues to xenobiotic exposure

The final peak-intensity matrices were first analysed by univariate statistics, to compare and contrast the magnitude of perturbation induced in the cardiac microtissues by each of the 72 exposure conditions (12 xenobiotics, 2

concentrations, 3 exposure durations). Results of Welch's *t*-tests evaluating the number of *m/z* features with significantly different relative abundance in exposed samples relative to batch- and exposure duration-matched controls reveal exposure to the low concentration of fluorouracil (15.8 μM) for 72-hours induces the greatest perturbation of the intracellular polar metabolome compared with all other exposure conditions (Figure 5.6a-b). Similarly, exposure to the high concentration of fluorouracil (69.2 μM) for 72-hours induced the greatest perturbation in the intracellular lipidome according to negative ionisation data (Figure 5.6d), but exposure to the high concentration of erlotinib for 72-hours induced the greatest perturbation to the intracellular lipidome according to the positive ionisation data (Figure 5.6c). This discrepancy may be explained by the difference in selectivity of the positive and negative ionisation assays, *e.g.,* the lipids positive assay has better coverage of triacylglycerols, while the lipids negative assay has better coverage of ceramides, thus indicates differences in the classes of lipids perturbed by fluorouracil compared with erlotinib. The smallest intracellular perturbation, consistently observed in three of four datasets, was induced by exposure to the high concentration of buspirone for 6-hours (Figure 5.6a-d).

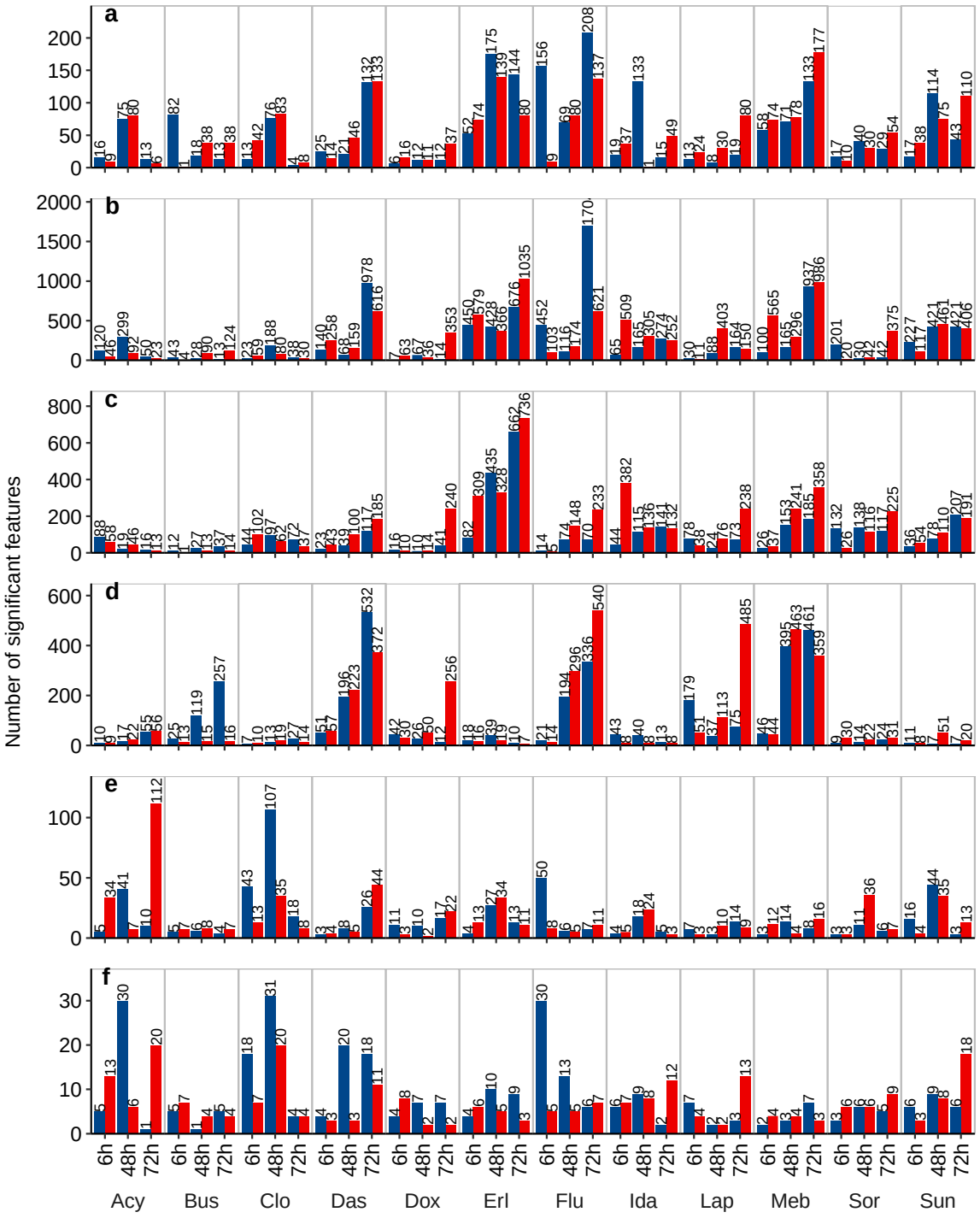


Figure 5.6 Magnitude of perturbation in cardiac microtissues induced by 72 exposure conditions.

Bar charts display the number of *m/z* features measured in intracellular **a-b** polar metabolite, and **c-d** lipid extracts of cardiac microtissues exposed to one of the twelve xenobiotics at either a low (blue bars) or high (red bars) concentration for 6-, 48- or 72-hours, with significantly different intensity relative to batch- and time-matched controls. Also shown, **e-f,** are the number of *m/z*-RT features measured in spent culture media of exposed cardiac microtissues with significantly different intensity relative to controls. Data were measured by **a** DIMS polar positive, **b** DIMS polar negative, **c** DIMS lipids positive, **d** DIMS lipids negative, **e** HILIC positive UHPLC-MS and **f** HILIC negative UHPLC-MS analytical assays. Significance was defined as p <0.01, as determined by two-tailed Welch's t-test.

The largest perturbation to the intracellular metabolome and lipidome was most frequently observed (57.3% of cases) after a 72-hour exposure to a xenobiotic, followed by 48-hours (28.1%). Consistent with expectations, these results evidence a trend of greater perturbation with longer exposure. The magnitude of response as a factor of exposure concentration was also explored. Results demonstrate exposure to a higher concentration of xenobiotic is more likely to induce a stronger perturbation to the intracellular metabolome and lipidome, with this occurring in 54.9% of cases. This incidence may be considered lower than expected. The quantitation of free xenobiotic concentrations in the culture media to which microtissues were exposed reveals why: the difference in free concentrations between high and low exposures were often smaller than between each pair of nominal concentrations (Figure 5.4). These smaller than anticipated differences in free concentrations subsequently gave rise to relatively comparable magnitudes of perturbations induced by exposure to the low and high nominal concentrations of a given xenobiotic in comparison to the effect of other factors, e.g., exposure duration.

Considering the responses measured by analysis of the spent culture media, perturbation of the microtissue metabolic footprint was of relatively low magnitude, with an average of just 16 and 8 *m/z*-RT positive and negative ion features, respectively, found to be significant in response to the 72 exposure conditions (Figure 5.6e-f). This may be explained by the relatively small ratio of cells to media such that any changes in the uptake or release of metabolites into or out of the microtissue are negligible with respect to the total abundances of the metabolites already within the media. Furthermore, considering the very low biomass, the abundance of any metabolites released by the microtissue that are not already

present within the media are likely to be below the limit of detection of the analytical assays.

Putative annotation of the significant features was used to explore the perturbations induced by the twelve xenobiotics at the metabolite and lipid level (Table eD.2, Table eD.3). Notable perturbations include the significant change to intracellular levels of galactitol induced by all twelve xenobiotics after 6-, 48- or 72-hour exposure, although the direction of change varied. Galactitol is the product of galactose reduction, thus galactitol levels are likely tightly associated with galactose levels. In turn, galactose is a primary carbon source in hiPSC-based cultures (260, 261), thus an interpretation of this finding is that all twelve xenobiotics effect cardiac microtissue energetics. Perturbations to Cer 40:2;O_2, Cer 42:2;O_2, glutamic acid/N-methyl-D-aspartic acid (isobaric), isoleucylproline/leucylproline (isobaric), L-threonine/L-homoserine (isobaric), maltitol, pantothenic acid, PC 32:0, PC 34:0, and taurine, after 6-, 48- or 72-hours exposures were also highly conserved across the test xenobiotics (significant for ≥10 of the twelve), although the direction and magnitude of change varied. In addition to these consistent perturbations, results revealed some metabolic changes specific to select xenobiotics, e.g., the erlotinib-specific perturbation of 5-hydroxy-L-tryptophan, choline, lactic acid and xanthine (Table eD.2).

Changes specific to and conserved amongst structurally cardiotoxic xenobiotics were less evident. Of the changes observed only in response to structurally cardiotoxic xenobiotics, a significant reduction in the intracellular levels of *sn*-glycero-3-phosphoethanolamine was the most conserved. The perturbation occurred in response to either 48- or 72-hour exposure to clozapine, dasatinib, fluorouracil, idarubicin, sorafenib and sunitinib (Figure 5.7a-b). Glycero-3-phosphoethanolamine

is the breakdown product of phosphatidylethanolamine, with changes in its intracellular levels conceivably a marker of disrupted glycerophospholipid metabolism. Perturbation of both Cer 33:1;O_2 and Cer 43:2;O_2 were also specific to structurally cardiotoxic xenobiotics, with significant reduction in their intracellular levels induced by 72-hour exposures to dasatinib, fluorouracil, lapatinib, and sunitinib (Figure 5.7c-d). This suggests these four xenobiotics may share a similar MoA involving these ceramides in the onset of structural cardiotoxicity.

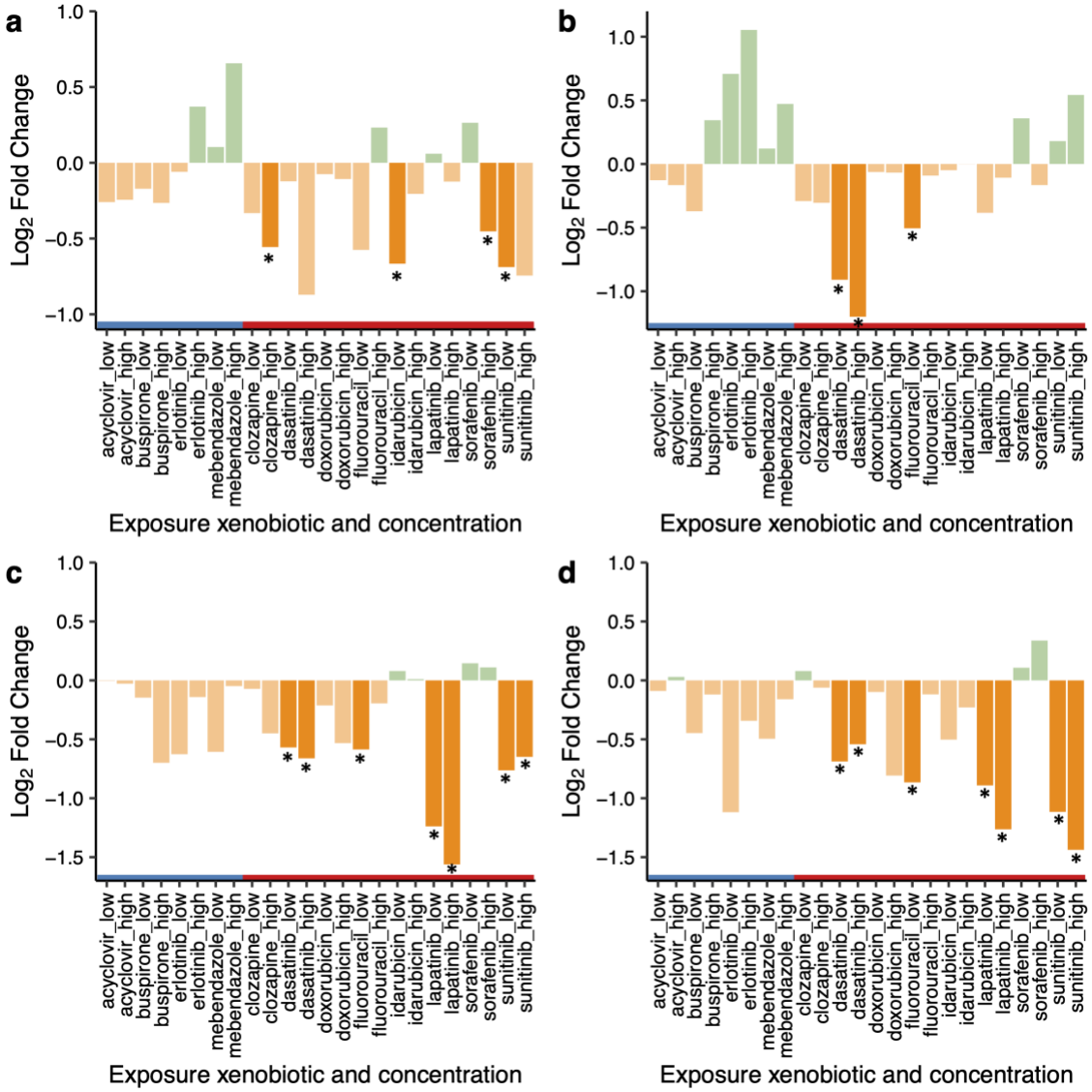


Figure 5.7 Structural cardiotoxin-specific significant intracellular metabolic perturbations in cardiac microtissues.
Plots show the average log_2 fold change of features putatively annotated as **a-b** glycerol-3-phosphoethanolamine, **c** Cer 33:1;O_2 and **d** Cer 43:2;O_2 in response to twelve xenobiotics, each at

two concentrations. Responses were measured after a 48-hour, and b-d 72-hour exposures. The colours on the *x*-axes indicate the structural cardiotoxicity label of each xenobiotic, blue: not structurally cardiotoxic, red: structurally cardiotoxic. The colour of the bars indicates the direction of change in the relative abundance of features following xenobiotic exposure relative to batch- and time-matched controls, green: increase, orange: decrease. Darker shading and * highlight changes that were found significant according to Welch's *t*-test (p <0.05, at least one representative feature).

Taken together, the application of univariate analysis of untargeted metabolomics data provided some insights into the magnitude of responses induced by several exposure conditions, revealing xenobiotic-, concentration-, and temporal-based trends. Furthermore, putative annotation of significantly perturbed *m/z* features demonstrated both conserved and xenobiotic-specific perturbations at the metabolite and lipid level. However, the discovery by this approach of perturbations which are specific to and conserved across structural cardiotoxins were limited.

Unsupervised clustering-based multivariate analysis, e.g., HCA, may be used to reveal which exposure conditions resulted in similar metabolic responses. HCA was applied to a matrix combining intracellular data acquired by all four DIMS assays and separately, a matrix of extracellular data acquired by two UHCPLC-MS assays (Figure 5.8).

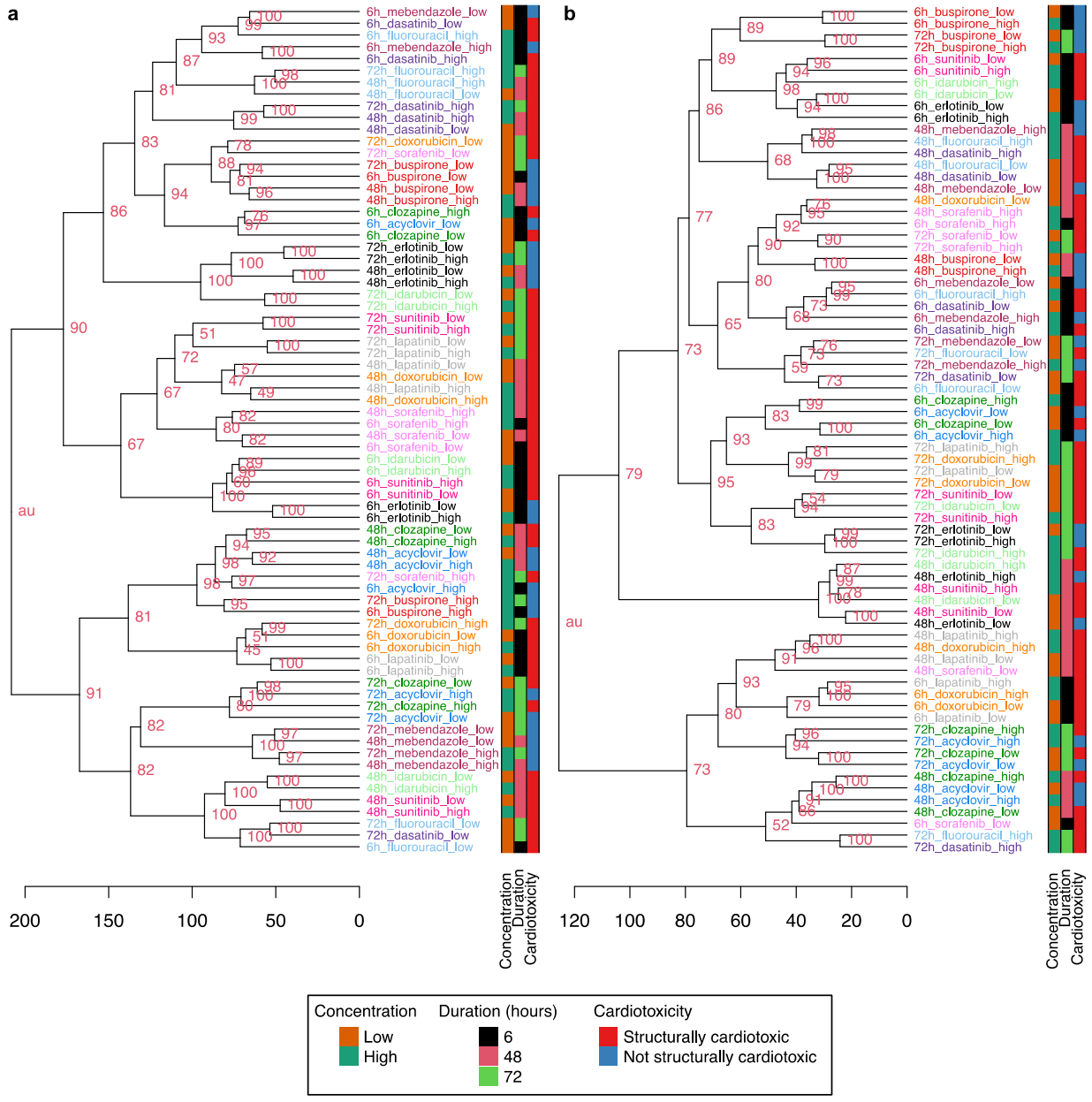


Figure 5.8 Unsupervised clustering of metabolic responses induced by each exposure condition.

Dendrograms show the results of hierarchical clustering analysis of **a** intracellular and **b** extracellular changes of cardiac microtissues to each exposure condition measured by four DIMS and two UHPLC-MS assays, respectively. Clustering analysis was performed on hard block variance scaled matrices of *t*-statistics calculated by Welch's *t*-test comparing exposed relative to batch and time matched controls. Each exposure condition is defined by the combination of duration, xenobiotic, and concentration. Exposure condition labels are coloured according to the exposure xenobiotics. The colour bars to the right of the dendrogram display additional metadata for each branch, mainly the exposure concentration, exposure duration and cardiotoxicity label. See the bottom of the figure for the colour keys. Approximately Unbiased *p*-values (au) displayed on the dendrogram in red were calculated by multiscale bootstrap resampling and indicate the reliability of each cluster. Clusters with au >95% may be considered strongly supported by the data.

Inspection of the dendrogram of intracellular responses (Figure 5.8a) reveals clustering is primarily driven by the exposure xenobiotic, with the most similar responses corresponding to responses induced by low and high concentrations of a given xenobiotic. Secondly, there is a trend towards clustering based on exposure duration, with responses induced by the same length exposure to different xenobiotics tending to cluster. The third most observed cluster pair corresponds to similar responses induced by the same xenobiotic and concentration after 48- and 72-hour exposures. The dendrogram of extracellular data (Figure 5.8b) reveals comparable trends except the most similar responses often correspond to exposure duration, with the same length of exposure to different xenobiotics clustering. Results reveal a few consistent trends when considering the similarity of responses induced by different xenobiotics, for example, high similarity of responses induced by acyclovir and clozapine at each of the three exposure durations according to both the intracellular and extracellular data. Also, clustering of lapatinib and doxorubicin after 6-, 48- and 72-hour exposures using extracellular data, in addition to similarity of responses induced by the same two xenobiotics after 6- and 48-hour exposure according to the intracellular data.

Taken together, unsupervised multivariate-based clustering has revealed trends in the data corresponding to exposure conditions, e.g., similarities in the responses induced by the same xenobiotic at two concentrations. However, the discovered similarities lack a strong association with the cardiotoxicity potential of xenobiotics (Figure 5.8). This is likely due to responses specific to the onset of structural cardiotoxicity representing a minor proportion of all responses induced by exposure to the xenobiotics, i.e., structural cardiotoxic-specific effects are responsible for only

a small proportion of the total metabolic variation, which is not well explored by unsupervised statistical approaches.

5.3.3 Measuring the intracellular and extracellular effects of xenobiotic exposure: analytical sensitivity, reproducibility and mass accuracy

This study was designed to investigate the response of cardiac microtissues following exposure to eight structurally cardiotoxic and four non-structurally cardiotoxic xenobiotics. The responses after 6-, 48- and 72-hours exposure to two phenotypically anchored concentrations of each xenobiotic (Table 5.1) were measured by DIMS-based untargeted metabolomics of microtissue polar metabolite and lipid intracellular extracts, and HILIC UHPLC-MS-based untargeted metabolomics of the microtissue spent culture medium. In total, 504 polar metabolite intracellular extracts, 504 lipid intracellular extracts and 504 preparations of spent culture medium were analysed in both positive and negative ionisation mode.

Samples were generated, prepared, and analysed in four batches, with each batch composed of 21 exposure conditions: exposure to two structurally cardiotoxic xenobiotics, and one non-structurally cardiotoxic xenobiotic, each at two concentrations, and exposure to 0.1% DMSO (controls), for 6-, 48- and 72-hours. Data from all four batches were processed simultaneously to produce a single peak-intensity matrix per analytical assay, to ensure alignment of *m/z* or *m/z*-RT features across batches, enabling later inter-batch comparisons. Subsequent assessment of the processed data revealed inter-batch variation, as evidenced by total ion intensity measurements and PCA (Figure 5.9a). Further interrogation of the data suggests the inter-batch variation was of a biological origin, with batch correction algorithms using intra-study QCs failing to correct the effect (Figure 5.9b). To overcome this challenge, all peak matrix filtering, normalisation, and other processing were

performed per batch. Meanwhile, later statistical analysis employed the availability of batch-specific control samples to negate inter-batch biological variation as a confounding factor in the comparison of responses to xenobiotics between batches.

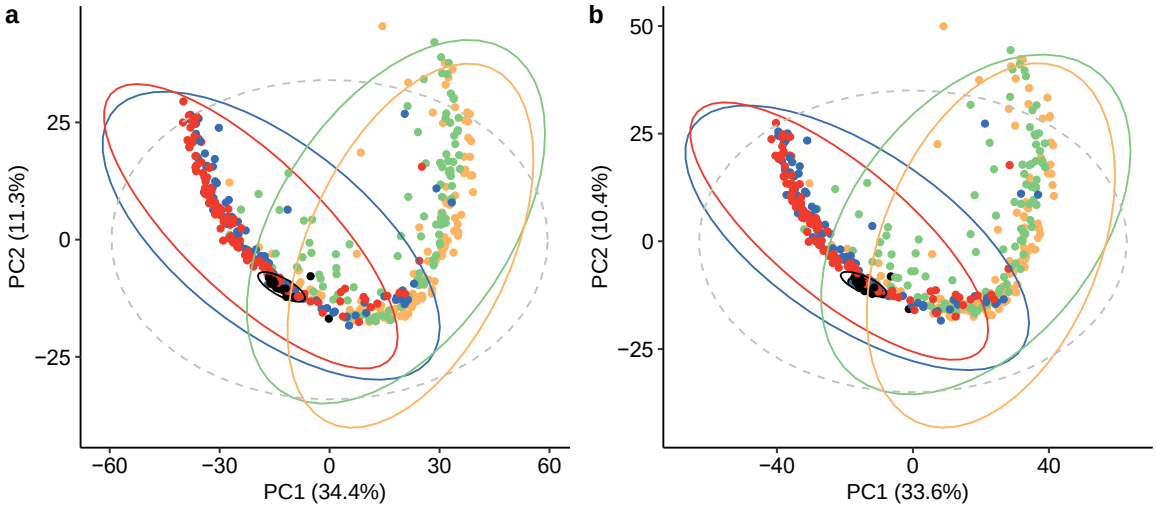


Figure 5.9 Inter-batch variation in processed metabolomics data.
PCA scores plots demonstrating variation between the four exposure batches: A (●), B (●), C (●), and D (●), in processed metabolomics data acquired by analysis of cardiac microtissue intracellular extracts using the polar negative DIMS assay. The separation of samples per exposure batch is observed both **a** before, and **b** after, batch correction by robust-spline correction using intra-study QCs (●) as reference (118), indicating inter-batch variation is not of analytical origin. Solid lines show the 95% confidence intervals for each sample group. The dashed line shows the 95% confidence interval around all samples. Data shown is representative of data from all four DIMS assays.

Prior to statistical analysis, filtered and normalised assay- and batch-specific peak matrices were assessed with respect to sensitivity and reproducibility. Average biological feature counts were 1692, 4503, 3291, and 4487 for DIMS polar positive, polar negative, lipids positive and lipids negative assays, respectively (Table 5.7). These counts are consistent with or exceed those observed previously for DIMS-based analysis of cardiac microtissue intracellular extracts (Section 3.3.3), evidencing sufficient analytical sensitivity in this study. Average biological feature counts for datasets obtained from UHPLC-MS analysis of spent culture media were 1337 and 3843 for HILIC positive and HILIC negative assays, respectively. Similarly,

these counts exceeded those of previous comparable datasets (Section 3.3.3), indicating good analytical sensitivity.

Table 5.7 Quality assessment of batch- and assay-specific metabolomics data.
Metrics used to evaluate the sensitivity and reproducibility of each DIMS and UHPLC-MS assay performed to analyse the intracellular extracts or spent culture media of cardiac microtissues, respectively, are reported. Specifically, the feature count, used to evaluate analytical sensitivity, in each processed peak intensity matrix (one per exposure batch, per assay) is reported. The mRSD of normalised feature intensities measured in intra-study QCs is reported as a measure of technical reproducibility. The range of mRSDs calculated from the normalised feature intensities measured in biological samples belonging to a given exposure condition (total: 21 per batch) are also reported, as an indication of the total metabolic variation between biological replicates.

Analytical platform	Assay	Batch	Feature Count	Intra-study QC mRSD (%)	Sample group mRSDs (%)
DIMS	Polar positive	A	1773	20.6	23.3 – 42.6
		B	2003	18.6	23.5 – 32.6
		C	1703	20.5	15.8 – 40.5
		D	1287	20.5	21.9 – 37.4
	Polar negative	A	4891	12.2	23.8 – 42.0
		B	4577	12.1	17.1 – 34.8
		C	4150	14.5	17.1 – 35.0
		D	4392	11.5	16.2 – 36.5
	Lipids positive	A	4235	11.8	23.2 – 39.5
		B	2892	13.9	21.9 – 33.6
		C	3414	14.2	18.5 – 29.5
		D	2621	14.3	21.8 – 28.2
	Lipids negative	A	4633	16.4	33.4 – 44.7
		B	4702	12.1	20.8 – 41.2
		C	3524	15.4	24.4 – 43.2
		D	5090	11.9	20.8 – 33.7
UHPLC-MS	HILIC positive	A	1393	17.7	14.3 – 19.5
		B	1519	18.1	13.3 – 22.0
		C	1135	17.1	13.1 – 25.1
		D	1301	15.4	16.2 – 22.7
	HILIC negative	A	2052	14.2	18.5 – 30.1
		B	1857	17.5	20.4 – 34.0
		C	1825	18.8	26.9 – 54.8
		D	1951	17.0	21.4 – 34.4

Technical variation was assessed according to the mRSD of intra-study QCs. Consistent with previous studies (Section 3.3.3), mRSDs ≤ 20.6% were calculated for data measured by all four DIMS assays, indicating good technical reproducibility (Table 5.7). Technical reproducibility across the two UHPLC-MS assays (intra-study QC mRSDs ≤18.8%, Table 5.7), after correction for the observed instrument drift in intensity measurements per batch, was also deemed sufficient for robust biological-based data analysis and interpretation. The mRSDs of feature intensities across

samples of the same exposure condition (considering xenobiotic, dose, and time) were used to evaluate the intra-group total metabolic variation in this study (Table 5.7). Values range from 15.8 to 44.7%, with no clear trend with respect to assay, batch, or exposure condition, except values were notably lower for data acquired by HILIC positive UHPLC-MS.

Taken together, all processed datasets passed quality control measures in place to ensure high data quality, the robustness of downstream analyses and interpretation, and the potential for biomarker discovery. The polar negative assay achieved the greatest sensitivity and reproducibility in the analysis of intracellular extracts compared with the three other DIMS assays implemented in this study. Similarly, the HILIC negative assay achieved greater sensitivity and technical reproducibility compared with the HILIC positive assay in the analysis of spent culture media.

Mass accuracy was assessed according to the error of internal standard *m/z* measurements across all samples in each assay. Measurements were within ±1 ppm of theoretical *m/z* throughout analysis, with the exception of a few outliers (0.7%, 1.4%, 8.2%, 2.3%, 0.0%, and 0.1% and of samples measured by DIMS polar positive, DIMS polar negative, DIMS lipids positive, DIMS lipids negative, UHPLC-MS HILIC positive, and UHPLC-MS HILIC negative, respectively, Figure 5.10). This is deemed excellent mass accuracy, enhancing the potential to gain biological insights by enabling the use of a smaller mass tolerance for metabolite annotation, reducing the proportion of false positives.

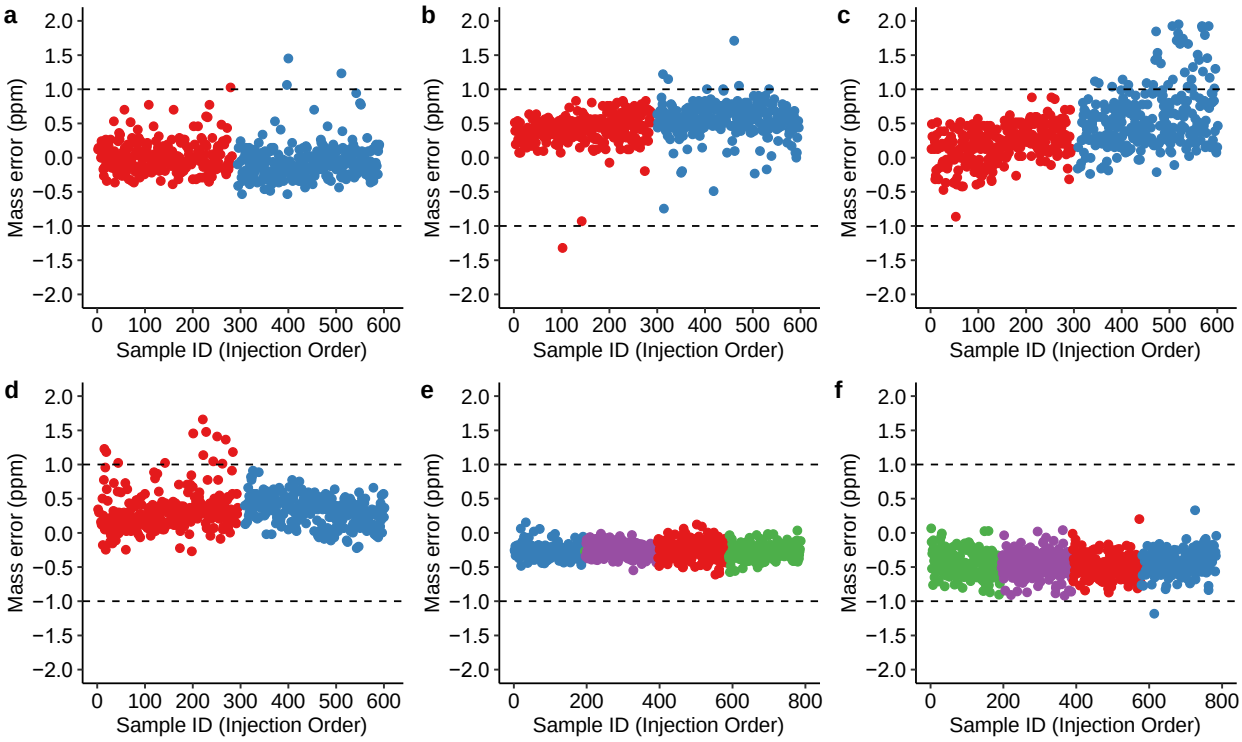


Figure 5.10 Mass error of internal standard measurements across analytical sequences. The error, in parts per million (ppm), of the measured *m/z* compared to the theoretical *m/z* of the, **a** and **e** $[M+H]^+$, and, **b** and **f** $[M-H]^-$, ion forms of L-tryptophan-d5-indole, and, **c** $[M+H]^+$, and, **d** $[M+acetate]^-$, ion forms of dodecylphosphorylcholine-d38. Measurements were made by **a** DIMS polar positive, **b** DIMS polar negative, **c** DIMS lipids positive, **d** DIMS lipids negative, **e** HILIC positive UHPLC-MS and **f** HILIC negative UHPLC-MS analytical assays. Colour of points in each panel indicate analytical batch: **a-d** an analytical batch is composed of two exposure batches (red: analytical batch 1, blue: analytical batch 2), **e-f** analytical batches are equivalent to exposure batches (blue: B, purple: D, green: C, red: A)

5.3.4 Discovering a predictive signature of drug-induced structural cardiotoxicity

Supervised multivariate analysis, e.g., (O)PLS-DA, is a powerful approach to mine datasets for measured variables associated with defined class labels, thereby to discover signatures predictive of phenotype (262). As such, OPLS-DA was applied to mine the untargeted metabolomics datasets acquired as part of this study for metabolic and lipid features which discriminate between responses of cardiac microtissues induced by structurally cardiotoxic and non-structurally cardiotoxic xenobiotics. Analysis was conducted separately for each combination of analytical assay and exposure duration. Initial models, separating samples exposed to structurally cardiotoxic xenobiotics from samples exposed to non-structurally

cardiotoxic xenobiotics, were built with an optimum number of latent variables selected according to the balanced error rate (BER). These initial models were used to create subsets of the data consisting of only the most predictive features (VIP ≥1), which, in turn, were used to build refined models (Figure 5.11, Figure D.6). The predictive performance of the refined models was assessed by cross-validation and permutation tests (Figure 5.11, Table 5.8).

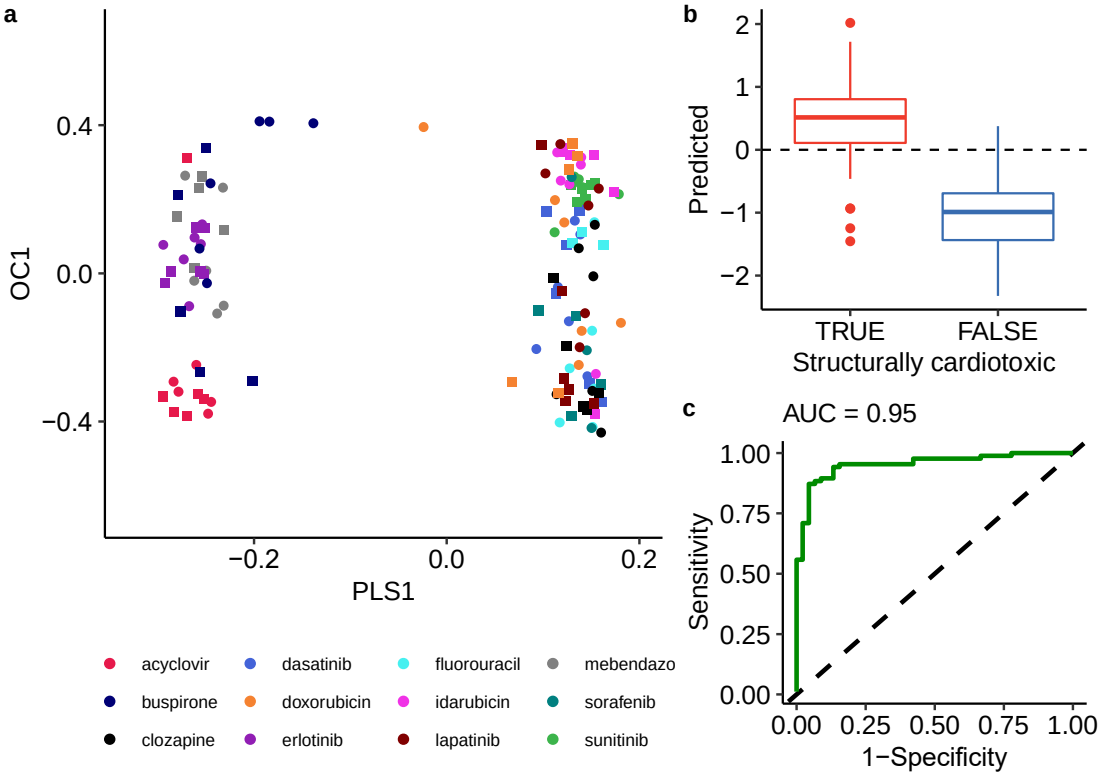


Figure 5.11 OPLS-DA model predictive of structural cardiotoxicity.
a OPLS-DA scores plot showing the predictive (PLS1) and first orthogonal (OC1) components of a model which discriminates between the responses of cardiac microtissues induced by 48-hour exposure to structurally cardiotoxic xenobiotics compared with non-structurally cardiotoxic xenobiotics. Shaded regions represent the 95% confidence regions for structurally cardiotoxic (red) and non-structurally cardiotoxic (blue) xenobiotics. Responses to both low (■) and high (●) concentrations of the twelve test xenobiotics were used for model training. **b** Boxplot of predicted values compared with true values as determined by *k*-fold cross validation, where a value of 1 corresponds to a sample exhibiting structural cardiotoxicity, demonstrating good predictive accuracy. **c** Receiver operator curve (ROC) demonstrating good specificity and sensitivity of the model in the prediction of structural cardiotoxicity label, as determined by *k*-fold cross validation. The model shown was built from a subset of predictive features, determined according to VIP scores (VIP ≥1) in a preliminary model, measured by polar negative DIMS of cardiac microtissue intracellular extracts. Intensity measurements were corrected for batch and baseline temporal effects by normalisation against the median intensities in batch and time matched controls prior to analysis.

Table 5.8 Performance of OPLS-DA models.
The table reports performance metrics for the refined OPLS-DA models, built for each analytical assay and exposure duration combination (18 total) using data matrices of the most predictive features, determined by VIP score (VIP ≥1) calculated in preliminary models. The number of features in the input data and the number of orthogonal components used in each model are shown. Performance metrics reported include model sensitivity, specificity, area under the curve (AUC) and balanced error rate (BER), each calculated by *k*-fold cross-validation (*k* = 5), and *p*-values assessing the significance of the BER as calculated by permutation tests with *k*-fold cross validation.

Platform	Assay	Exposure duration (hours)	Number of features	Number of orthogonal components	Specificity	Sensitivity	AUC	BER	BER *p*-value
DIMS	Polar positive	6	412	12	0.83	0.72	0.86	0.215	0.01
		48	351	3	0.85	0.86	0.93	0.140	0.01
		72	307	8	0.89	0.88	0.95	0.135	0.01
	Polar negative	6	833	10	0.74	0.87	0.89	0.165	0.01
		48	1171	13	0.80	0.96	0.95	0.103	0.01
		72	1154	13	0.85	0.98	0.98	0.098	0.01
	Lipids positive	6	744	10	0.67	0.87	0.85	0.284	0.01
		48	705	9	0.86	0.94	0.97	0.096	0.01
		72	644	11	0.84	1.00	0.99	0.091	0.01
	Lipids negative	6	1172	7	0.60	0.66	0.63	0.408	0.06
		48	1074	8	0.69	0.85	0.83	0.278	0.01
		72	1112	8	0.67	0.58	0.68	0.353	0.01
UHPLC-MS	HILIC positive	6	240	3	0.68	0.79	0.83	0.291	0.01
		48	220	4	0.74	0.67	0.81	0.277	0.01
		72	232	9	0.68	0.79	0.83	0.291	0.01
	HILIC negative	6	378	4	0.62	0.72	0.79	0.300	0.01
		48	419	8	0.68	0.70	0.75	0.346	0.01
		72	361	4	0.67	0.83	0.84	0.230	0.01

Taken together, valid models, i.e., demonstrating significantly better predictivity relative to models built after randomly permuting the input data, were built from responses measured after 6-, 48- and 72-hour exposures in the intracellular metabolome and lipidome by polar positive, polar negative, and lipids positive DIMS assay. As for responses measured by the lipids negative assay, valid models could only be built from the 48- and 72-hour data. Valid OPLS-DA models significantly predictive of structural cardiotoxicity were also built from responses measured in the spent culture media by HILIC positive and negative UHPLC-MS analysis after 6-, 48- and 72-hour exposure. However, according to performance metrics (specificity, sensitivity, AUC and BER) of the OPLS-DA models, the responses measured by

UHPLC-MS analysis of the spent culture media are typically less predictive than those measured by DIMS analysis of intracellular extracts. This is consistent with the lesser perturbation of the metabolic footprint (culture medium) compared with the metabolic fingerprint (intracellular) observed via univariate analysis (Figure 5.6). Furthermore, greater predictive capacity of intracellular measurements may be explained by the metabolic fingerprinting being more comprehensive in its coverage of metabolic pathways and demonstrates the greater potential for discovery when measurements are not limited to the metabolic footprint in investigative studies using *in vitro* test systems. However, predictive biomarkers that are measurable in the culture medium are more amenable to high-throughput screening which could be implemented in the future to predict structural cardiotoxicity potential during drug discovery, given the relative ease of sampling compared with the intracellular metabolome. As such, OPLS-DA models of both the metabolic fingerprint and footprint were interrogated further.

Further comparative evaluation of the models based on performance metrics reveals responses measured after only 6-hours of exposure are the least predictive of structural cardiotoxicity compared with 48- and 72-hour. This is consistent with the results of univariate analysis, demonstrating lesser perturbation after 6-hours compared with later timepoints (Figure 5.6). Considering this result from a MoA or AOP framework perspective; theoretically, it is perturbations either causative or reactive of shared KEs, or points at which structurally cardiotoxic xenobiotic-specific MoAs converge, that are most likely to be predictive of structural cardiotoxicity. Such shared KEs or convergence points, are more likely to occur later after first exposure. Despite this, early-response predictive biomarkers are desirable since they are more amenable to early-stage drug discovery, e.g., high-throughput screening and the

DMTA cycle, and are a key advantage of molecular biomarkers over apical endpoint assays, which typically rely on later stage perturbations.

Comparison of the features used to build the refined predictive models revealed a conservation of a relatively large proportion (ranging 16.2 to 35%) of features predictive of structural cardiotoxicity between 48- and 72-hours (Figure 5.12). The lower end of this range is explained by less conservation of predictive features between 48- and 72-hours in the metabolic footprint compared to intracellular data. Commonalities in predictive features demonstrates some stability of responses associated with structural cardiotoxicity induced by the xenobiotics between 48- and 72-hours of exposure. From a mechanistic perspective, these may be associated with compensatory mechanism(s) of cardiac microtissues to adapt to perturbations induced by structurally cardiotoxic xenobiotics.

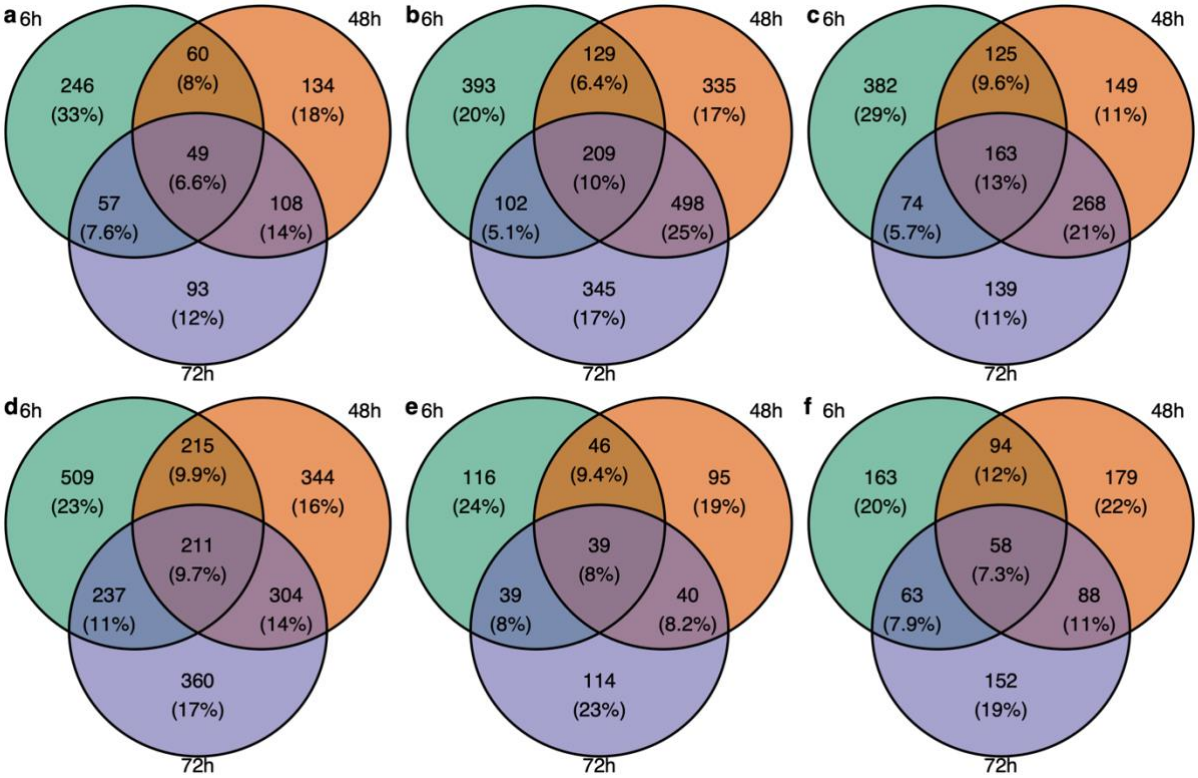


Figure 5.12 Conservation of predictive features over time.
Venn diagrams comparing the *m/z* or *m/z*-RT features found to be predictive of structural cardiotoxicity (VIP >1) in preliminary models built using the entire dataset and used to build the refined OPLS-DA models, across three exposure durations. Data were acquired by **a** polar positive, **b**

polar negative, **c** lipids positive, **d** lipids negative nESI-DIMS analysis of intracellular extracts, and **e** HILIC positive and **f** HILIC negative UHPLC-MS analysis of spent culture media of cardiac microtissues.

Annotation of the discovered predictive features was performed to reveal putative biomarkers at the metabolite and lipid level (Table eD.4, Table eD.5). The annotation of features enables anchoring of the discovered predictive metabolic and lipid signatures to established MoA, providing confidence in the putative biomarker panel. Furthermore, and arguably more importantly, considering the current relative lack of mechanistic understanding of structural cardiotoxicity, annotation enables the generation of new hypotheses on shared MoA of structurally cardiotoxic xenobiotics. Of note, interrogation of the putatively annotated features revealed a total of 29 intracellular ceramides (43.3% of all ceramides previously discovered in untreated cardiac microtissue extracts, Table eC.2) whose responses are predictive of structural cardiotoxicity according to OPLS-DA. Concomitantly, intracellular levels of 27 of these putatively annotated ceramides were also significantly perturbed by structurally cardiotoxic xenobiotics according to univariate statistical analysis (Figure 5.13, Table eD.2). Ceramides are integral cell membrane components which act as second messengers in cell signalling processes. As such, changes to the combined abundance and ratio of ceramides of different chain lengths will influence the biophysical properties of the cell membrane, eliciting subsequent signalling processes dependently (263). Ceramides have been linked to multiple cardiac pathologies and are proposed clinical biomarkers of myocardial infarction and risk of death in patients with stable coronary heart disease (CERT2 risk score) (264). Furthermore, ceramides have been associated with mitochondrial dysfunction and oxidative stress, established key events of drug-induced structural cardiotoxicity (265-268). Despite the evidenced association of ceramides to pathological

mechanisms associated with structural cardiotoxicity, the underlying MoA and the relationship between chain length and effect is yet to be established.

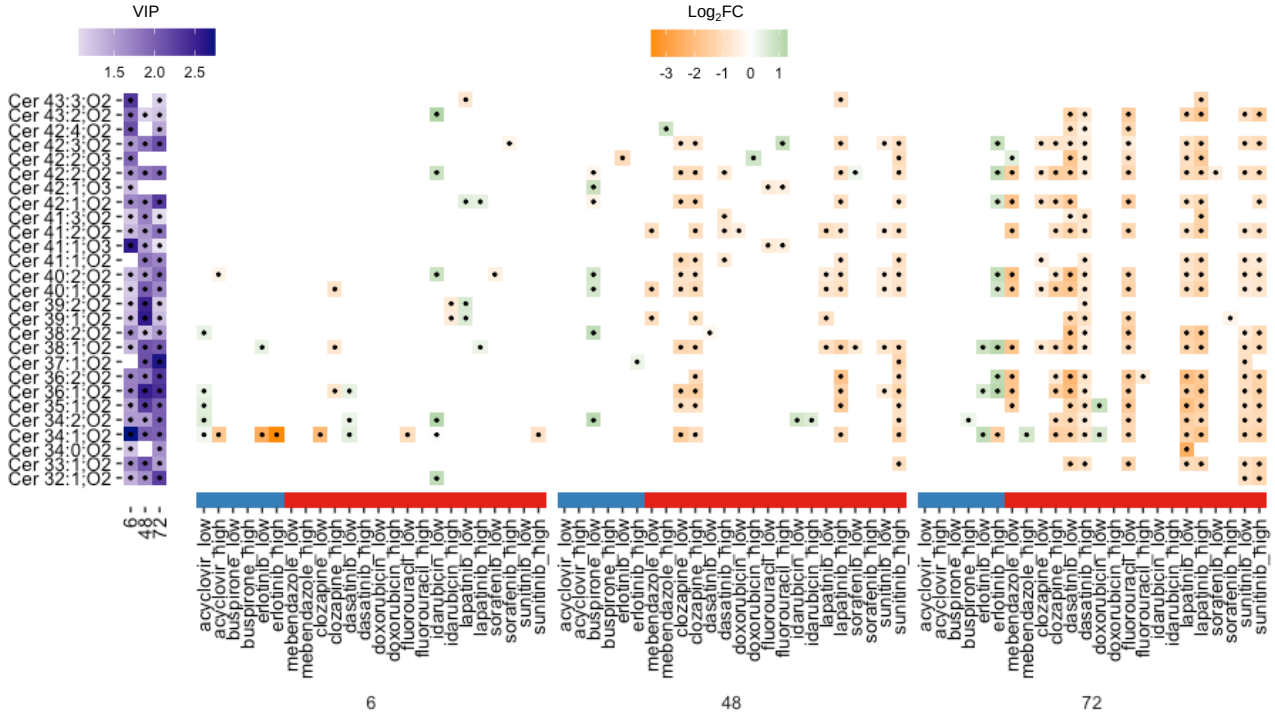


Figure 5.13 The responses of intracellular ceramides in cardiac microtissues are predictive of the structural cardiotoxicity potential of exposure xenobiotics.
Shown, far left, are the average VIP scores per exposure duration of 27 ceramides included in the refined OPLS-DA models, and thus deemed predictive of the structural cardiotoxicity label of the exposure xenobiotics. The average VIP score for each ceramide is the mean VIP score of *m/z* features within the refined OPLSD-DA models that were putatively annotated as the given ceramide. Also shown are $\log_2$ fold changes representing the responses of the 27 ceramides induced by each of the exposure xenobiotics, at two concentrations (low, high) and three exposure durations (6-, 48-, and 72-hours). Values shown for each ceramide are the mean $\log_2$ fold change of significantly perturbed *m/z* features putatively annotated as the given ceramide, per exposure condition. Univariate analyses were calculated for each exposure condition relative to batch- and time-matched controls. Significance was defined as $p < 0.05$ (Welch's *t*-test). The coloured bar on the *x*-axis indicates the structural cardiotoxicity label of the exposure xenobiotics (blue: not structurally cardiotoxic, red: structurally cardiotoxic).

Also noteworthy, intracellular levels of ATP, adenosine diphosphate (ADP) and adenosine monophosphate (AMP) were found to be associated with structural cardiotoxicity based on putative annotation of features important for OPLS-DA models from three of four assays (Table eD.2). This is consistent with the reports of a central role for cellular energetics in the onset and development of structural cardiotoxicity (265, 269). Related, creatine levels were found to be associated with

structural cardiotoxicity at 48- and 72-hours by OPLS-DA while univariate analysis revealed five of eight structurally cardiotoxic xenobiotics significantly reduced creatine levels after a 72-hour exposure (Table eD.2). The creatine kinase system (Equation 5.1) has a critical role in cardiac energy metabolism, functioning as a primary energy store, restoring ATP concentration at times of increased energy demand and shuttling energy between the ATP synthesising mitochondria and ATP-consuming sites within the cytosol (231, 270).

Equation 5.1 The creatine kinase system.
Reversible synthesis of phosphocreatine and ADP from creatine and ATP catalysed by creatine kinase.

$$\text{Creatine} + \text{ATP} \leftrightarrows \text{Phosphocreatine} + \text{ADP} + H^+$$

Perturbed creatine levels are likely causative or reactive of a disrupted creatine kinase system and consequential myocardial energy depletion, consistent with previously reported findings on anthracycline-induced cardiotoxicity (231). Furthermore, intracellular levels of several constituents of the purine metabolism pathway (deoxyadenosine, inosine, cyclic AMP, cyclic guanosine monophosphate (GMP), GMP, adenosine/deoxyguanosine, xanthine and glutamine, in addition to AMP, ADP and ATP) were also discovered to be the predictive of structural cardiotoxicity by OPLS-DA (Figure 5.14, Table eD.2). The perturbation of these purine metabolism intermediates may also be linked to disrupted energy metabolism and the onset of structural cardiotoxicity since a key role of purine metabolism is restoration of the adenine nucleotide pool (271). Taken together, results shown here evidence an association between perturbed cardiac energetics and drug-induced structural cardiotoxicity and demonstrate metabolic biomarkers of cardiac energy status are suitable for predicting drug-induced structural cardiotoxicity.

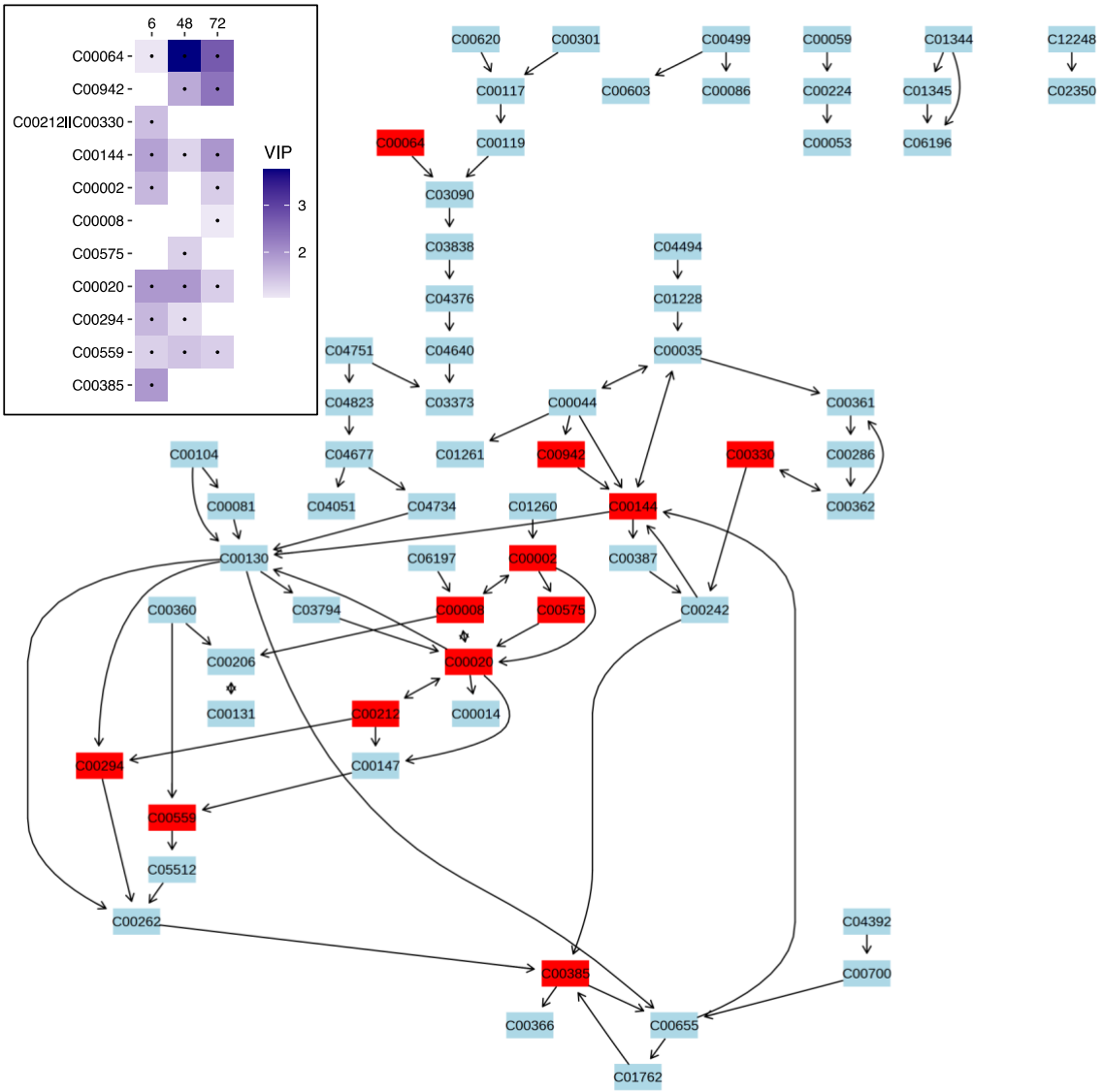


Figure 5.14 Intracellular levels of purine metabolism intermediates in cardiac microtissues are predictive of the structural cardiotoxicity potential of exposure xenobiotics.
The KEGG purine metabolism pathway (PATHWAY: map00230, (211)). Intermediates of the pathway found to be predictive of structural cardiotoxicity by OPLS-DA of intracellular metabolomics data from xenobiotic exposed cardiac microtissues are highlighted in red. The inset heatmap (top left) displays the average VIP scores for the metabolites (purine metabolism intermediates) included in the refined OPLS-DA models. The average VIP score shown for each metabolite per exposure duration is the mean VIP score of *m/z* features within the refined OPLSD-DA models that were putatively annotated as the given metabolite. Metabolites are referred to by their KEGG identifiers (C00064: L-glutamine; C00942: cyclic-GMP; C00330: deoxyguanosine; C00144: guanosine monophosphate; C00002: adenosine triphosphate; C00008: adenosine diphosphate; C00575: cyclic-AMP; C00020: adenosine monophosphate; C00212: adenosine; C00294: inosine; C00559: deoxyadenosine; C00385: xanthine).

The intracellular levels of pantothenic acid were also found to be associated with structural cardiotoxicity by OPLS-DA. This is supported by univariate analyses where

five structurally cardiotoxic xenobiotics were shown to have significantly increased pantothenic acid levels and two non-structurally cardiotoxic xenobiotics significantly reduced pantothenic acid levels in cardiac microtissues after 72-hour exposures. Consistent with this discovery, levels of pantothenic acid in H9C2 cells have previously been reported as potential biomarkers of doxorubicin-induced cardiotoxicity (272, 273). A MoA explaining this association is yet to be established but it may be related to the conversion of pantothenic acid to Coenzyme A (CoA) (274). CoA is critical to ATP synthesis by fatty acyl β-oxidation through activation of fatty acyls, forming acyl-CoA. Thus, pantothenic acid may be a biomarker of perturbed fatty acyl β-oxidation and disrupted cardiac energetics.

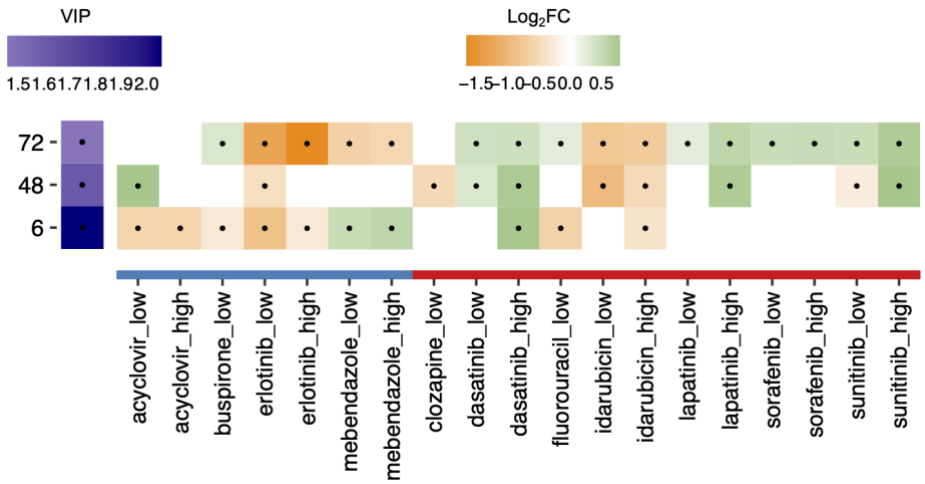


Figure 5.15 Intracellular levels of pantothenic acid in cardiac microtissues are predictive of the structural cardiotoxicity potential of exposure xenobiotics.
Shown, far left, are the average VIP scores of pantothenic acid per exposure duration, evidencing the responses of the metabolite are predictive of the structural cardiotoxicity label of the exposure xenobiotics. The average VIP score of pantothenic acid for each exposure duration (6-, 48- and 72-hours) is the mean VIP score of *m/z* features within the refined OPLSD-DA models that were putatively annotated as pantothenic acid. Also shown are $\log_2$ fold changes representing the responses of pantothenic acid induced by each of the exposure xenobiotics, at two concentrations (low, high) and three exposure durations (6-, 48-, and 72-hours). Values shown are the mean $\log_2$ fold change of significantly perturbed *m/z* features putatively annotated as pantothenic acid. Univariate analyses were calculated for each exposure condition relative to batch- and time-matched controls. Significance was defined as $p < 0.05$ (Welch's *t*-test). The coloured bar on the *x*-axis indicates the structural cardiotoxicity label of the exposure xenobiotics (blue: not structurally cardiotoxic, red: structurally cardiotoxic).

Other predictive putatively annotated features discovered by OPLS-DA include reduced and oxidised glutathione. The evidenced predictive capacity of intracellular glutathione levels is consistent with the established association of oxidative stress with structural cardiotoxicity (275, 276).

Considering features measured within the metabolic footprint of cardiac microtissues, three of four metabolites previously selected for a targeted metabolomics screening assay to predict structural and functional cardiotoxicity from measurements of spent culture media of hiPSC-CMs (61) were also discovered predictive of structural cardiotoxicity here by OPLS-DA: lactic acid (6- and 48-hours), thymidine (48- and 72-hours) and deoxycytidine (6-, 48- and 72-hours) (Table eD.5). Furthermore, additional metabolites, L-alanine (72-hours) and N-acetylaspartic acid (6-, 48- and 72-hours), found to be predictive of cardiotoxicity but not included in the final assay panel by Palmer *et al*., were similarly discovered predictive in this study. These findings demonstrate reliability in Palmer *et al*.'s proposed assay, given the consistency observed despite experimental differences such as the *in vitro* test system (hiPSC-CMs vs. cardiac microtissues), exposure concentrations, and analytical assay(s) used. The approach taken in this study discovered an extracellular predictive signature containing many additional metabolites, e.g., inosine and cytosine which had high VIP scores at 6-, 48- and 72-hours (Table eD.5). Future evaluation of the metabolite signature discovered here using a wider set of xenobiotics would enable more robust assessment of specificity and sensitivity and could be used to determine if the inclusion of the additional metabolites enhances predictivity compared to Palmer *et al.*'s four-metabolite-based assay.

Overall, OPLS-DA analysis of untargeted metabolomics data measuring responses of cardiac microtissues induced by eight structurally cardiotoxic and four non-

structurally cardiotoxic xenobiotics, at two concentrations, after 6-, 48-, and 72-hours has discovered *m/z* and *m/z*-RT features with capacity to predict structural cardiotoxicity. Represented amongst the panel of predictive features are putatively annotated metabolites associated with myocardial energy status, including ATP, ADP, AMP, creatine, and purine metabolism pathway constituents. The predictive metabolic signature also includes putatively annotated markers of mitochondrial oxidative stress, mainly reduced and oxidised glutathione. These findings are consistent with established mechanisms of structural cardiotoxicity. The inclusion of many ceramides in the predictive signature evidences a role for these lipids in the onset of structural cardiotoxicity. A mechanism explaining this association is less established, as with the association of pantothenic acid with structural cardiotoxicity. Taken together, the evidence provided by putative annotation of the discovered metabolite and lipid signatures suggests prediction of structural cardiotoxicity may be achieved through a laboratory deployed biomarker panel which combines markers against multiple known, and some currently undefined, mechanisms of structural cardiotoxicity. By combining metabolic biomarkers of several MoA into a single panel, the specificity and sensitivity is likely improved. To this end, a list of 47 polar metabolites and lipids has been recommended for inclusion in a metabolic biomarker panel for prediction of the structurally cardiotoxic potential of xenobiotics, based on findings presented within this thesis chapter which are supported by other sources, e.g., published literature (Table 5.9).

Table 5.9 Proposed structural cardiotoxicity metabolic biomarker panel.
Listed are 47 polar metabolites and lipids recommended for inclusion in a metabolic biomarker panel for prediction of the structurally cardiotoxic potential of xenobiotics. The responses of the listed metabolites/lipids, i.e., change in abundance in exposed cardiac microtissues relative to control, as measured by untargeted metabolomics, were discovered to be predictive of the cardiotoxicity potential of twelve test xenobiotics by OPLS-DA. Moreover, the association of all the listed polar metabolites and lipids recommended for inclusion in the metabolic biomarker panel is supported by other findings, either reported within this thesis or in the literature, providing confidence in their predictive capacity (Justification).

Location	Metabolite / Lipid name	Justification
Intracellular	Cer 32:1; O_2	Based on findings of OPLS-DA and univariate statistical analysis of new data presented in this chapter; consistent with previous findings of significant perturbation of ceramides in rat heart and plasma following treatment with sunitinib or KU60648 (Chapter 2).
	Cer 33:1; O_2	
	Cer 34:0; O_2	
	Cer 34:1; O_2	
	Cer 34:2; O_2	
	Cer 35:1; O_2	
	Cer 36:1; O_2	
	Cer 36:2; O_2	
	Cer 37:1; O_2	
	Cer 38:1; O_2	
	Cer 38:2; O_2	
	Cer 39:1; O_2	
	Cer 40:1; O_2	
	Cer 40:2; O_2	
	Cer 41:1; O_2	
	Cer 41:1; O_3	
	Cer 41:2; O_2	
	Cer 41:3; O_2	
	Cer 42:1; O_2	
	Cer 42:1; O_3	
	Cer 42:2; O_2	
	Cer 42:2; O_3	
	Cer 42:3; O_2	
	Cer 42:4; O_2	
	Cer 43:2; O_2	
	Cer 43:3; O_2	
	Creatine	Based on findings of OPLS-DA of new data presented in this chapter; consistent with reports of an association between anthracycline-induced cardiotoxicity and disrupted creatine kinase system (231)
	Pantothenic acid	Based on findings of OPLS-DA and univariate statistical analysis of new data presented in this chapter; consistent with previous reports as biomarker of doxorubicin-induced cardiotoxicity (272, 273)
	L-glutamine	Based on findings of OPLS-DA of new data presented in this chapter; consistent with the previous association of structural cardiotoxicity with perturbed purine metabolism (Chapter 3, (277))
	Deoxyadenosine	
	Inosine	
	Cyclic AMP	
	Cyclic GMP	
	GMP	
	Adenosine	
	Deoxyguanosine	
	ATP	
	ADP	
	AMP	
	Reduced/Oxidised glutathione	Based on findings of OPLS-DA of new data presented in this chapter; established marker of mitochondrial oxidative stress, a phenotype of structural cardiotoxicity (275, 276)
Culture medium	Lactic acid	Based on OPLS-DA findings of new data presented in this chapter; consistent with Palmer *et al.* (61)
	Thymidine	
	Deoxycytidine	
	L-alanine	
	N-acetylaspartic acid	

5.4 CONCLUSIONS

In summary, extensive untargeted metabolomics data measuring the fate of eight structurally cardiotoxic and four non-structurally cardiotoxic xenobiotics and the effects they induced on the intracellular metabolome, intracellular lipidome and metabolic footprint of cardiac microtissues after 6-, 48-, and 72-hours exposure to two concentrations were acquired. Quantitation of the xenobiotics in the spent culture medium revealed free concentrations to which the microtissues were exposed were typically less than nominal concentrations. This demonstrated the importance of these measurements in *in vitro* assays where data may be extrapolated to predict clinical toxicity or efficacy, with the use of measured free concentrations expected to improve prediction accuracy compared to nominal concentrations. Meanwhile, discovery of xenobiotic biotransformation products both intracellularly and within the spent culture medium provided the first reported direct evidence of phase I and phase II biotransformation competency of cardiac microtissues. Characterisation of the biotransformation competency of test systems is an important consideration for IVIVE. Meanwhile, the demonstrated ability to biotransform signifies the high translational relevance of cardiac microtissues.

Investigation into the effects of xenobiotic exposure revealed concentration-dependent and temporal trends in the magnitude of perturbation induced by each xenobiotic. Annotation of features found to be significantly perturbed revealed commonalities in the responses induced across multiple xenobiotics independent of cardiotoxicity label, in addition to xenobiotic-specific perturbations. Unsupervised multivariate analysis did not primarily cluster the measured responses according to cardiotoxicity label of the exposure xenobiotic, suggesting perturbations specific to structural cardiotoxicity represent a minor proportion of the complete response to

xenobiotic exposure, as would be expected. Consequently, supervised multivariate analysis was employed to mine the data for features predictive of structural cardiotoxicity. Multiple significantly predictive OPLS-DA models were built (per assay/exposure duration combination), discovering signatures within the metabolic and lipid fingerprints and metabolic footprint capable of predicting the cardiotoxicity label of the test xenobiotics. Annotation of these signatures revealed consistencies with previous findings, anchoring them to established MoAs, and provided evidence to hypothesise novel MoAs.

Taken together, a list of 47 polar metabolites and lipids, each discovered to be predictive of the structurally cardiotoxic potential of xenobiotics, has been recommended for use as a structural cardiotoxicity metabolic biomarker panel. Future efforts to refine and validate the panel are now required to strive toward the ultimate aim of accurate prediction of structural cardiotoxicity during the early stages of drug discovery. The availability of free xenobiotic exposure concentrations and understanding of the extent of xenobiotic biotransformation in cardiac microtissues will support these future efforts, mainly in the translation of findings across test systems.

CHAPTER 6: CONCLUSIONS AND FUTURE WORK

The overarching aim of this thesis was to develop and apply untargeted metabolomics workflows to characterise the fate and effects of xenobiotics in model systems, ultimately, to discover a molecular signature predictive of drug-induced structural cardiotoxicity. This aim was set out to address a significant challenge faced by the pharmaceutical industry; high attrition rates resulting from a limited ability to accurately predict the structurally cardiotoxic potential of NCEs (2, 18).

Effective safety assessment strategies in drug discovery and development rely on mechanistic understanding, i.e., established MoAs and AOPs, and an availability of predictive biomarkers (5, 10). Meanwhile, 'omics approaches, including untargeted metabolomics, are well-suited to elucidating toxicological MoAs and discovering biomarkers, driven by their ability to comprehensively map xenobiotic-induced perturbations at a given molecular level, e.g., the metabolome (52, 55, 64). However, the full capabilities of untargeted metabolomics, i.e., to reveal information on both the fate and effects of xenobiotics, has so far been underexploited, with limited use of freely available xenobiotic-related data to inform on ADME/TK. Furthermore, several challenges are faced when trying to apply untargeted metabolomics to study more physiologically relevant *in vitro* test systems such as cardiac microtissues. These matters were addressed in Chapters 2, 3 and 4 of this thesis, before implementation of the developed workflows in an extensive untargeted metabolomics study designed to discover a predictive metabolic signature of drug-induced structural cardiotoxicity (Chapter 5).

6.1 SIMULTANEOUSLY DISCOVERING THE FATE AND BIOCHEMICAL EFFECTS OF XENOBIOTICS THROUGH UNTARGETED METABOLOMICS

In Chapter 2, the unfulfilled potential of untargeted metabolomics to inform on xenobiotic ADME/TK properties in test systems was addressed. This was achieved by first developing a computational open-source workflow which could semi-automatically discover and visualise measurements of xenobiotics and their biotransformation products within untargeted metabolomics datasets. Implementation of the workflow on two routine UHPLC-MS untargeted metabolomics datasets from studies designed to explore the effects of sunitinib and KU60648 treatment on rats demonstrated the capability to discover information on xenobiotic disposition. Analysis of the xenobiotic-related measurements revealed by the workflow enabled characterisation of the biotransformation, tissue distribution and temporal changes in relative systemic exposure of the xenobiotics in the exposed rats. In summary, this work demonstrated enriched value of untargeted metabolomics, with the ability to explore the ADME/TK fate of xenobiotics, in addition to their effects, pertinent to toxicological investigations. It is envisioned that more tailored experimental design could extend the types of xenobiotic ADME/TK properties that might be characterised from untargeted metabolomics data, e.g., calculation of uptake and clearance rates.

The capabilities of the untargeted ADME/TK workflow were further demonstrated by application to an untargeted metabolomics experiment with hiPSC-CMs, revealing the ability to discover metabolic competencies of *in vitro* model systems. This capability was further demonstrated and exploited in Chapter 5, to reveal the metabolic competency of cardiac microtissues. Aside from hepatic model systems, metabolic competencies of *in vitro* systems used in toxicity testing are often uncharacterised, despite the potential for biotransformation to significantly influence

the toxicity potential of xenobiotics. The demonstrated ability to characterise xenobiotic biotransformation, in a given test system, as part of an untargeted metabolomics experiment into the effects of the xenobiotic offers a solution to this issue without the need for additional sample generation and analysis. Furthermore, the availability of measurements on xenobiotic disposition has the potential to improve IVIVE and give rise to more accurate prediction of xenobiotic safety.

It was also demonstrated that internal dose measurements made by untargeted metabolomics can be used to reveal endogenous biochemical responses that are directly associated with internal xenobiotic exposure, expanding the toolbox of approaches for discovering toxicity MoA and biomarkers. This approach could be particularly beneficial to untargeted metabolomics-based toxicological studies performed with dose resolution; the use of measured concentrations in place of nominal offers the potential for more accurate dose (concentration)-response modelling and would enable discovery of endogenous effects sensitive to relative internal dose.

While demonstrated for pharmaceutical drugs, it's envisioned that the developed workflow could have far broader impact. For example, the ability to measure fate and effects of xenobiotics within a single metabolomics-based experiment has the potential to transform toxicity testing for industrial chemical and biocides risk assessment, reducing the number of experiments necessary to meet regulatory requirements, while providing more extensive insights into MoA. Moreover, beyond its application to characterise the fate of known exposure xenobiotics in toxicological investigations, the untargeted ADME/TK workflow may be implemented for exposomics, i.e., discovery of exposure to suspect xenobiotics and their biotransformation products. This was demonstrated through implementation of the

workflow to discover exposure to suspect pharmaceuticals and subsequently map their biotransformation pathways in human plasma. Taken together, the established untargeted ADME/TK workflow has potentially far-reaching applications.

In later chapters of this thesis (Chapter 3 and 5), approaches to discover the fate of xenobiotics in test systems via untargeted metabolomics measurements were extended to include absolute quantitation of known parent xenobiotics. This enabled measurement of free concentrations of exposure xenobiotics, facilitating analyses such as comparison to nominal concentrations, and assessment of xenobiotic stability over experiment durations, which could prove beneficial to IVIVE of measured xenobiotic effects. Similar integration of parent xenobiotic quantitation, as part of an *in vivo* metabolomics study, would take the capabilities of untargeted ADME/TK a step closer to regulatory requirements for toxicokinetic reporting in drug development, enabling greater impact of the approach. Moreover, future work focusing on quantitation of biotransformation products could further advance the capabilities of untargeted metabolomics in terms of xenobiotic ADME/TK profiling. Ideally, quantitation of biotransformation products would be performed without the need for reference standards, thus enabling discovery and quantitation within a single analytical experiment and overcoming the lack of availability of reference standards for these compounds. This could be achieved through “pseudo-calibration" using, e.g., reference standard of the known parent xenobiotic, coupled with ionisation efficiency predictions to correct for differences in sensitivity of measurement between the related compounds. Through quantitation of both parent xenobiotic and biotransformation products, mass balance inferences could be achieved without the need for radiolabelling, as required for the established mass balance approaches.

6.2 An extensive metabolomics workflow to discover cardiotoxin-induced molecular perturbations in microtissues

In Chapter 3, a fit-for-purpose workflow enabling the measurement of xenobiotic exposure effects on the intracellular metabolome and lipidome, and extracellular metabolic footprint of cardiac microtissues was established. First, the challenge of sampling cardiac microtissues, in particular their isolation from spent culture media in a rapid and reproducible manner, was addressed. A filtration-based approach employing cell strainers was demonstrated to be quicker and more reproducible than the alternative centrifugation-based approach. To further maximise the isolation of microtissues from their culture media, the number and volume of saline washes performed as part of the sampling workflow was optimised, with 3x 1 mL washes found sufficient to remove residual media from microtissue-containing cell strainers. While foremost enabling suitable sample generation for cardiac microtissue-based untargeted metabolomics experiments presented in this thesis, the established workflow could have broader impact as an ideal approach for sampling other small-scale suspended cell-based test systems, i.e., other types of organoids, for metabolomics analysis.

Spectral-stitching nESI-DIMS enables high throughput, high sensitivity sample analysis, making it appropriate for the analysis of very low biomass samples. However, thus far, the ‘high’ sensitivity has been proven for samples with biomass only as low as 50,000 cells/sample (87), while the cardiac microtissues used here are composed of just 500 cells. As such, the sensitivity of spectral-stitching nESI-DIMS-based untargeted metabolomics with respect to coverage of the microtissue metabolome and lipidome after pooling of either 7, 14, 21 or 28 microtissues was evaluated. Through reproducible detection of biological *m/z* features from samples with as few as 7-pooled microtissues (ca. 3,500 cells/sample, >10-fold less sample

biomass than previously reported minimum), the sensitivity of the spectral-stitching nESI-DIMS method was demonstrated to be far greater in this thesis than previously established. Meanwhile, samples with 28-pooled microtissues were recommended for future toxicology studies based on achieving sufficiently high and consistent data quality. Despite the demonstrated excellent sensitivity of spectral stitching nESI-DIMS-based metabolomics, the approach is limited by the lack of orthogonal chromatographic separation which could otherwise be used to substantially aid annotation of *m/*z features. Thus, while nESI-DIMS was the appropriate approach for untargeted metabolomics of microtissue intracellular extracts in this thesis, particularly considering its place as an established approach within the research group, future efforts to develop more sensitive hyphenated MS approaches, e.g., nano-LC-MS (278), could augment the potential of high sensitivity (high throughput) metabolomics.

Having established a workflow for microtissue-based untargeted metabolomics, the ability to detect perturbations induced by a model cardiotoxin was demonstrated. In summary, analysis of the intracellular metabolome of microtissues exposed to either a ‘low’ or ‘high’ concentration of sunitinib for 2-, 6-, 48- or 72-hours revealed time- and concentration-dependent responses, relative to biological control samples. Putative annotation of statistically significant perturbations (as determined by ANOVA) and features discovered by supervised multivariate analysis (PLS-DA) provided evidence to support MoA hypotheses (disruption of purine metabolism and role for polyunsaturated fatty acids). Despite this success, there were many features with multiple annotation hits, i.e., there was a high rate of false positive annotation, thus confidence in the biological interpretations was limited. Complementary UHPLC-MS analysis of the microtissue spent culture media helped counteract the

challenge of DIMS data annotation to some extent: more confident annotation of detected significant perturbations to the metabolic footprint, using *m/*z, RT, and MS/MS measurements, provided supporting evidence for the biological interpretations. UHPLC-MS analysis of the spent culture media also facilitated quantitation of free exposure concentrations, as discussed earlier in this chapter.

Taken together, the untargeted toxico-metabolomics study into the effects of sunitinib exposure on cardiac microtissues demonstrated the established workflow was fit-for-purpose. Considering wider impact, the workflow may be emulated to explore other organ toxicities using advanced *in vitro* models, i.e., organoids. Despite the successes of the study, two key limitations of the experimental design were realised: (1) the approaches implemented were not capable of detecting any sunitinib-induced perturbation after just 2-hours exposure, and (2), challenges in annotation of DIMS intracellular data limited confidence in biological interpretation. The former limitation was considered in future study designs (e.g., the study presented in Chapter 5 did not include 2-hour timepoints); the latter was addressed in Chapter 4 (curation of a test system-specific metabolite and lipid library that can be used to limit false positive annotations) and Chapter 5 (inclusion of DIMS-MS^n measurements, providing an additional metric for more confident annotation).

6.3 Characterising the cardiac microtissue metabolome and lipidome

In Chapter 4, the challenge of accurate and reliable annotation of MS-based untargeted metabolomics data was addressed through the curation of a metabolite and lipid library specific to cardiac microtissues. This was achieved by implementing four UHPLC-MS^n assays, intelligent MS^n data acquisition, three data processing workflows and several metabolite and lipid annotation databases. The curated library

is composed of 315 polar metabolites and 2450 lipids. It includes compounds both previously associated with toxicity and of high relevance to cardiac biology.

The use of this library to annotate nESI-DIMS untargeted metabolomics datasets, e.g., as in Chapter 5, is expected to greatly reduce the proportion of false positive annotations otherwise attained when feature annotation is performed using much larger non-specific databases such as HMDB and LMSD. In turn, this will provide greater confidence in annotations, and subsequent biological interpretations and MoA-related hypotheses. Beyond cardiac microtissues, the approach taken here could be applied to many other test systems for relatively fast initial characterisation of their metabolomes. Such efforts would serve the same purpose of achieving more confident annotation in untargeted metabolomics studies employing these test systems.

While the work presented in Chapter 4 is a constructive step toward higher confidence annotation of MS-based untargeted metabolomics datasets, the curated library is by no means exhaustive of the cardiac microtissue metabolome and lipidome. Thus, future efforts should focus on expanding the library through implementation of a more comprehensive workflow, e.g., combining solid phase extraction, UHPLC-MS(/MS), GC-MS, NMR and DIMS-MS^n as implemented for DMA of *D. magna* (220) . Use of a more comprehensive test system-specific library would lead to greater annotation coverage of untargeted metabolomics datasets, increasing the opportunity for biological interpretation.

Further to a more comprehensive library, a complementary database of spectral data derived from analysis of authentic reference standards would be a valuable addition. Construction of a spectral database by the same analytical method, i.e., same

instrument, same fragmentation mode, same collision energies, etc., as the method used to acquire MS^n data as part of metabolomics studies would enable MSI level 1 identification, i.e., annotation at the highest level of confidence. Moreover, deployment of the developed cardiac microtissue-specific metabolite and lipid library as a hybrid metabolomics assay, in combination with a spectral database, would facilitate the highest confidence measurement of the metabolites and lipids within the library, ultimately enhancing the biological interpretability of the acquired data.

6.4 Discovering a predictive metabolic signature of drug-induced structural cardiotoxicity in cardiac microtissues

In Chapter 5, work from Chapters 2, 3 and 4 culminated in the implementation of an extensive untargeted metabolomics-based experiment measuring the fate and effects of twelve small molecule xenobiotics (eight structurally cardiotoxic, four non-structurally cardiotoxic) at two concentrations in cardiac microtissues, after 6-, 48- and 72-hour exposure. Spectral stitching nESI-DIMS and UHPLC-MS were implemented to measure the intracellular metabolome and lipidome, and extracellular metabolic footprint, respectively, of exposed and biological control cardiac microtissues.

Regarding xenobiotic fate: measurements were used to reveal both Phase I and Phase II biotransformation by cardiac microtissues, and quantify extracellular free concentrations, the advantages of which, and opportunities for future improvements, have been discussed above.

Regarding xenobiotic effects: univariate-based statistical analysis of processed data revealed the magnitude of perturbations induced by each exposure condition, including xenobiotic-, concentration- and temporal-based trends. Further exploration of the discovered significant changes revealed some consistencies in responses

induced across the twelve xenobiotics but was not an effective approach toward revealing putative biomarkers of structural cardiotoxicity. Meanwhile, exploratory multivariate analysis (HCA) of response vectors per exposure condition provided evidence that molecular perturbations associated with development of structural cardiotoxicity are minor with respect to total changes induced by xenobiotic exposure. As such, a more powerful supervised multivariate analysis was required to mine the data for features belonging to the intracellular metabolome intracellular lipidome, and metabolic footprint, predictive of structural cardiotoxicity. To this end, OPLS-DA successfully discovered predictive metabolic signature(s) from data acquired across all exposure durations assessed and analytical assays implemented. Annotation of features within these signatures enabled anchoring of the proposed biomarker panel to established structural cardiotoxicity MoAs, e.g., perturbed creatine kinase system and disrupted purine metabolism, providing confidence in the findings. Results also provided sufficient evidence to support novel MoA hypotheses, e.g., role of ceramides in onset of structural cardiotoxicity.

Despite its successes here, supervised multivariate analyses, e.g., OPLS-DA, for biomarker discovery has recognised limitations. This includes the potential for overfitting which, while considered and addressed to some extent through internal cross-validation, is pertinent here due to the absence of a distinct test dataset to validate the models. Future implementation of machine learning approaches, e.g., random forests, support vector machines or neural networks, to the same data could address this limitation through provision of complementary findings: there would be more confidence in the predictive capacity of *m/z* features discovered by multiple, distinct approaches, than by a single approach only (279-281).

With consideration beyond the remit of this thesis, it is envisioned that the study design implemented in Chapter 5 could be a proficient template for discovery of predictive metabolic signatures of other drug-induced target organ toxicities, e.g., hepatotoxicity, neurotoxicity, using relevant organoids as the test system.

6.5 FUTURE DIRECTIONS

Ultimately, a metabolic biomarker panel for the prediction of structurally cardiotoxic potential of xenobiotics was proposed based on the research presented in this thesis (Table 5.9). However, substantial further work is required to translate the findings into drug discovery pipeline-ready screening of NCEs. To this end, I propose future efforts are directed at:

1. (short-term) Refining, validating and comprehensive MoA anchoring of the proposed structural cardiotoxicity metabolic biomarker panel.

   Refinement and validation could be achieved by extending the metabolomics measurements to a wider panel of structurally cardiotoxic and non-structurally cardiotoxic xenobiotics. Implementation of a hybrid metabolomics-based approach would be pertinent for this purpose, enabling targeted measurement and validation of the putatively predictive *m/z* features discovered in Chapter 5, while also acquiring (untargeted) data which could be used for further discovery-based analyses in the event that the previously discovered predictive signature doesn't generalise.

   MoA anchoring (and elucidation) foremost requires confident identification of metabolites and lipids represented by the predictive *m/z* or *m/z*-RT features discovered in Chapter 5. This requires greater coverage and confidence in annotation than already achieved to enable association with known metabolic

pathways and networks, and subsequent mechanistic inference (126). The previously proposed work to expand the microtissue metabolite and lipid library, coupled with acquisition of MS^n and RT data for features of interest, would aid these efforts.

Attempts at MoA anchoring would further benefit from integrative multi-omics analysis through which causative associations, e.g., change in metabolite X driven by activation of protein Y and/or increased transcription of gene Z, could be derived (282). A parallel transcriptomics dataset was acquired alongside the metabolomics data presented in Chapter 5, opening the door for such analysis. Additionally, MoA anchoring attempts would benefit from implementation of spatial omics-based approaches including mass spectrometry-based imaging, e.g., by desorption electrospray ionisation (283) or matrix-assisted laser desorption/ionisation (284), and spatial transcriptomics (285). These approaches would enable xenobiotic-induced perturbations to be distinguished by cardiac cell type, providing deeper mechanistic understanding, e.g., cell type(s) driving toxicity. Furthermore, coupling with imaging-based xenobiotic distribution measurements could enable direct association of spatial xenobiotic effects with its distribution. Taken together, the proposed experiments could contribute substantially toward the construction of an AOP for drug-induced structural cardiotoxicity, to which discovered (and validated) metabolic biomarkers could be anchored.

2. (mid-term) Development of a targeted, quantitative metabolomics-based high-throughput screening assay.

Following refinement and validation efforts, it would be pertinent to transform the structural cardiotoxicity metabolic biomarker panel into a high-throughput targeted metabolomics-based screening assay that would be suitable for early-stage drug discovery. Maximising throughput would be a key objective and could be achieved, first, by automated sample preparation using liquid handling stations, and second, by use of suitable analytical technology, e.g., acoustic mist ionisation-based mass spectrometry, a relatively recently developed platform capable of analysis of small molecules in biological matrices in as little as 3-seconds-per-sample (286). The development of the assay would require establishment of appropriate thresholds for decision making, i.e., “toxic” / “not toxic”, based on results for a panel of known structurally cardiotoxic and control xenobiotics. Taken further, acquisition of concentration-response profiles by a high-throughput analytical method could be translated, e.g., via benchmark dose (concentration) modelling (287) and/or IVIVE (288), for clinical safety margin prediction.

3. (long-term) *In silico* prediction and establishment of SAR.

   In the long term, implementation of a developed screening assay across many xenobiotics could contribute towards building of an extensive database of concentration-response behaviour with respect to the biomarker panel. With the availability of such a database, the development of *in silico* prediction models would be enabled and SARs associated with cardiac safety liabilities could be elucidated. *In silico* prediction models have the potential to significantly reduce the time and cost of safety screening NCEs, thereby increasing the efficiency of drug development. Meanwhile, with an awareness of the relevant SARs, the number of NCEs with potential to induce

> cardiotoxicity could be confined at the very earliest stages of drug discovery and lead to substantial reduction in project attrition caused by otherwise later detection of cardiac safety liabilities (289).

Notwithstanding these proposed future research directions, results delivered in this thesis will enable the scientific community to take a substantial step closer to better predicting the structurally cardiotoxic potential of NCEs. Moreover, the workflows developed and demonstrated as part of this thesis may have wide-reaching impact in application areas seeking comprehensive characterisation of the fate and effects of xenobiotics using untargeted metabolomics and advanced *in vitro* test systems.

APPENDIX A

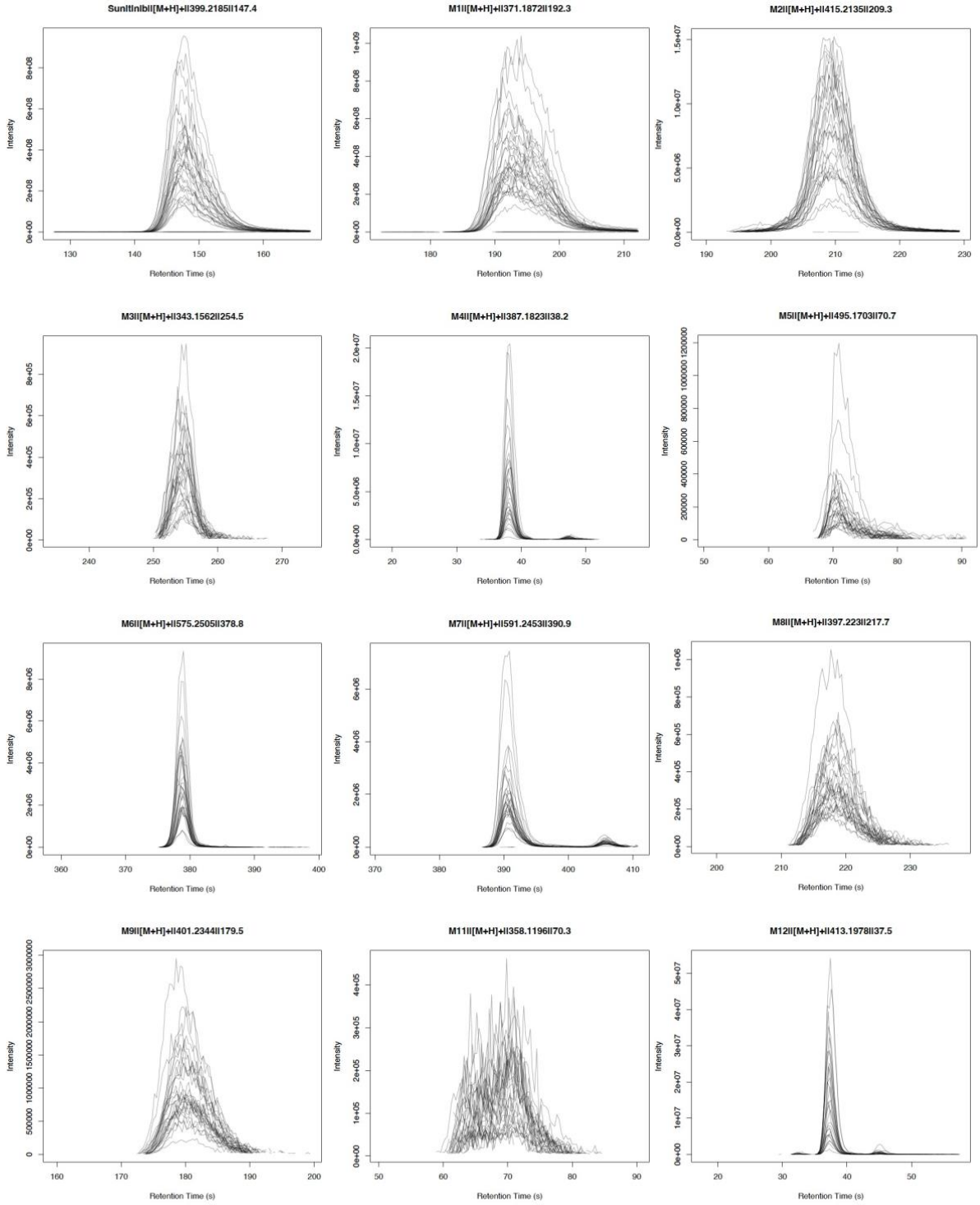
Table A.1 A summary of the datasets analysed.
For each dataset analysed, the experimental model and matrix, exposure (parent) substance, dose(s), measured time points, and the reason for analysis are reported.

Dataset	Biological system and sample type	Exposure substance	Dose(s)	Sampling time points	Reason for analysis
Sunitinib Rat Plasma	Rat – Plasma	Sunitinib	25 mg/kg/day for 14 consecutive days	4-hours post-dose on days 1, 2, 4 and 8; 28-hours post-dose on day 14.	Biotransformation map; temporal tracking of parent and biotransformation product levels; endogenous metabolic and lipid signature
Sunitinib Rat Cardiac Tissue	Rat – Cardiac Tissue			28-hours post day 14 dose (i.e., day 15)	Biotransformation map; endogenous metabolic and lipid signature
KU60648 Rat Plasma	Rat - Plasma	KU60648	150 mg/kg/day on days 1 and 2; 225 mg/kg on day 3	4-hours post-dose on days 1 and 2; 24-hours post-dose on day 3.	Biotransformation map; temporal tracking of parent and biotransformation product levels; endogenous metabolic and lipid signature
KU60648 Rat Cardiac Tissue	Rat – Cardiac Tissue			24-hours post day 3 dose (i.e., day 4)	Biotransformation map; endogenous metabolic and lipid signature
Sunitinib – cardiomyocytes	Cardiomyocyte intracellular extracts	Sunitinib	5 µM	1-, 6- and 24-hours	Biotransformation map; evaluation of metabolite *in vitro* competency
	Spent culture media of cardiomyocytes				
Fate of pharmaceuticals in humans	Human - Plasma	Unknown	Unknown	Unknown	Discovering exposure; biotransformation maps

Table A.2 Summary of the two pharmaceuticals investigated in rats.
The number of biotransformation products (BTPs) of sunitinib and KU60648 that have been reported in published literature are noted, in addition to how many of those are available to purchase as analytical standards, based on information found within the "Chemical Vendors" section of PubChem records. Also presented are the number of biotransformation products which were predicted by either SyGMa[40] or the "Generate Expected Compounds" tool of Compound Discoverer (Thermo Scientific) and the number of biotransformations discovered in the plasma of exposed rats through application of the untargeted ADME/TK workflow on UHPLC-MS-based metabolomics datasets.

Parent	Number of BTPs previously reported in literature	Number of BTPs available as analytical standards	Number of *in silico* predicted BTPs	Number of BTPs discovered by untargeted ADME/TK workflow
Sunitinib	11[†]	4	1492	19
KU60648	0	0	1108	22

[†]Speed *et al.,* 2012


SunItInIbII[M+H]+II399.2185II147.4
M1II[M+H]+II371.1872II192.3
M2II[M+H]+II415.2135II209.3
M3II[M+H]+II343.1562II254.5
M4II[M+H]+II387.1823II38.2
M5II[M+H]+II495.1703II70.7
M6II[M+H]+II575.2505II378.8
M7II[M+H]+II591.2453II390.9
M8II[M+H]+II397.223II217.7
M9II[M+H]+II401.2344II179.5
M11II[M+H]+II358.1196II70.3
M12II[M+H]+II413.1978II37.5
Intensity
Retention Time (s)

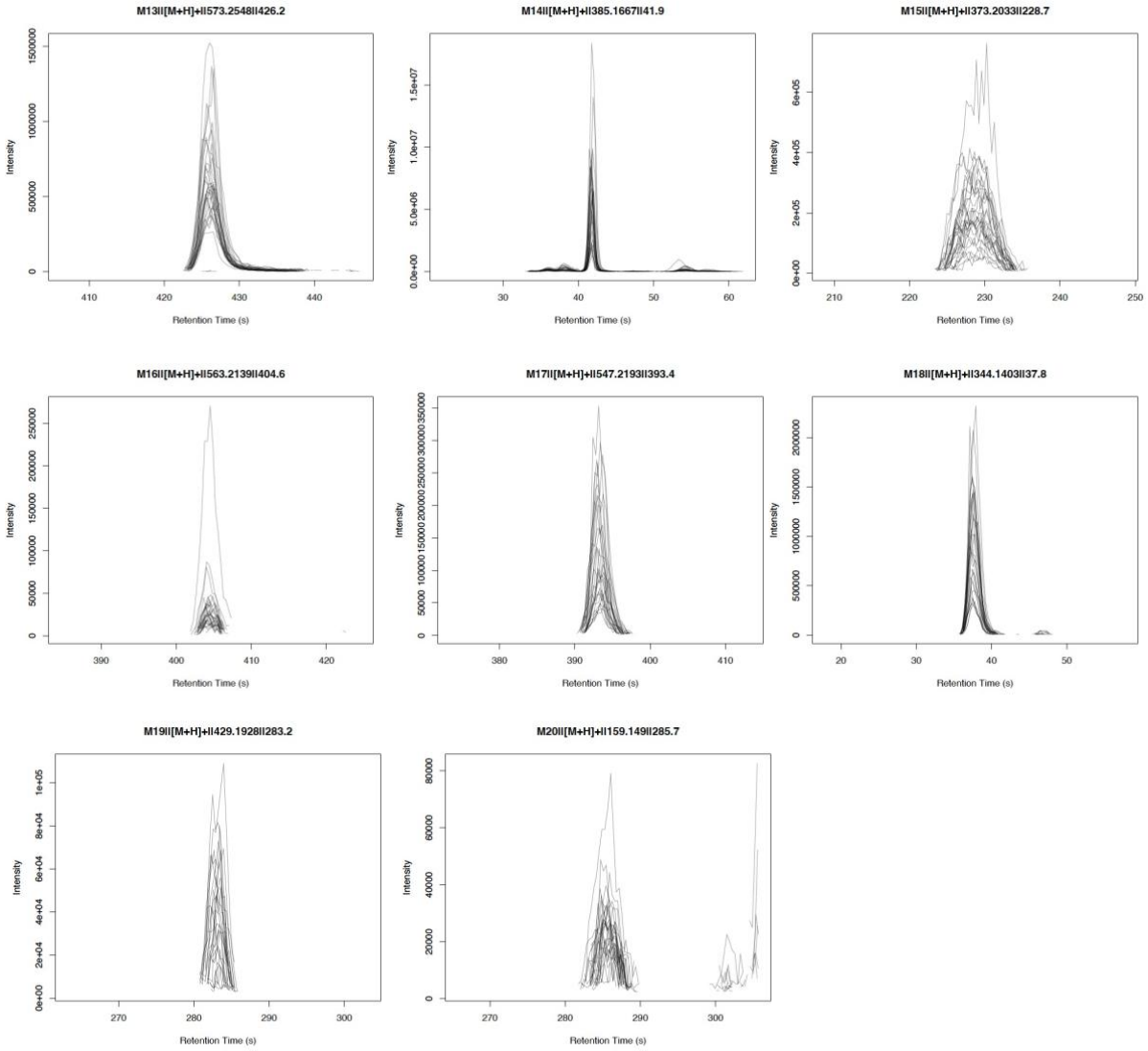


Figure A.1 Chromatographic peaks of sunitinib and related compounds measured in rat plasma.

Extracted ion chromatograms (EICs) of sunitinib and its biotransformation products measured in the plasma of rats treated with sunitinib by HILIC positive UHPLC-MS untargeted metabolomics.

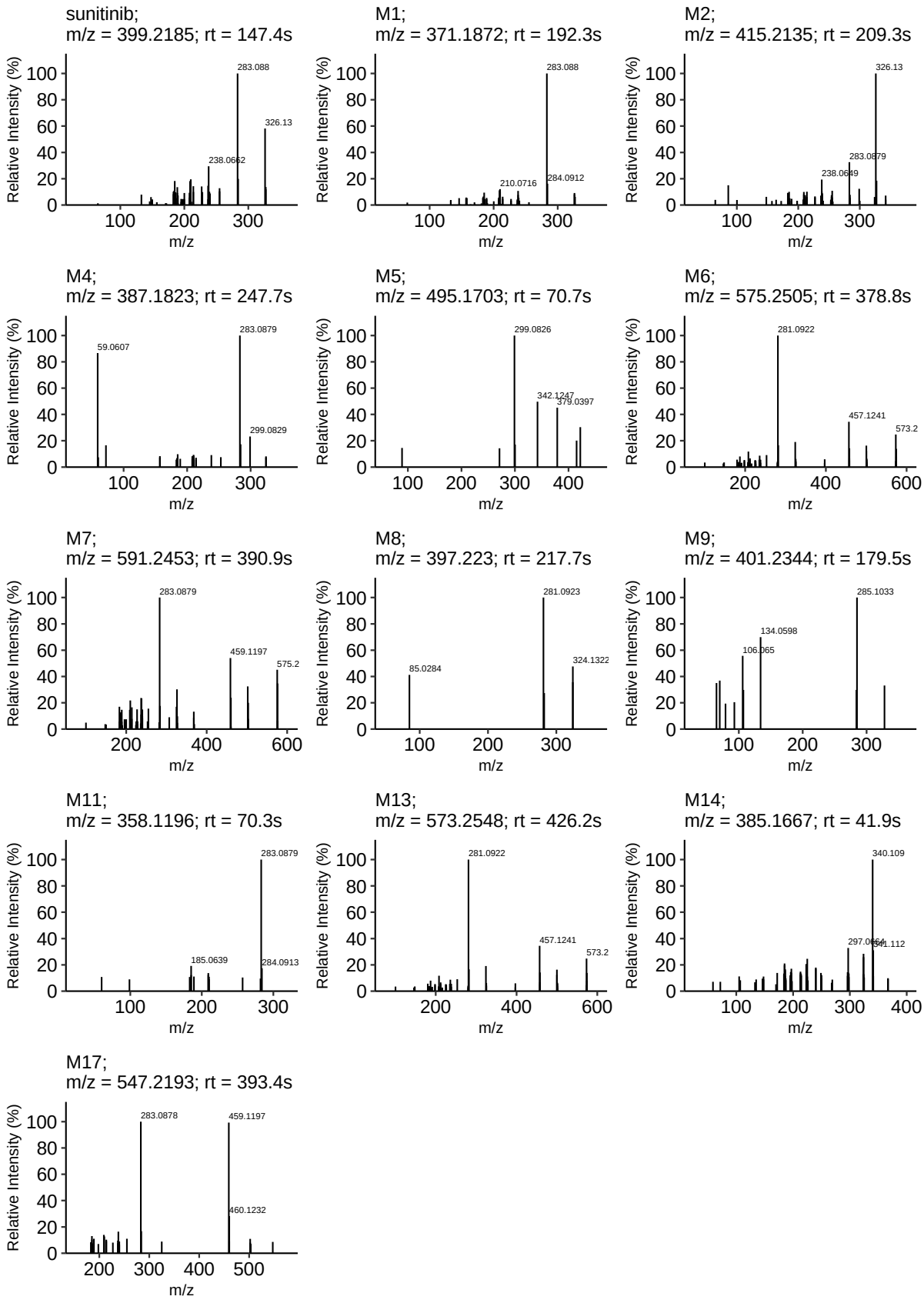
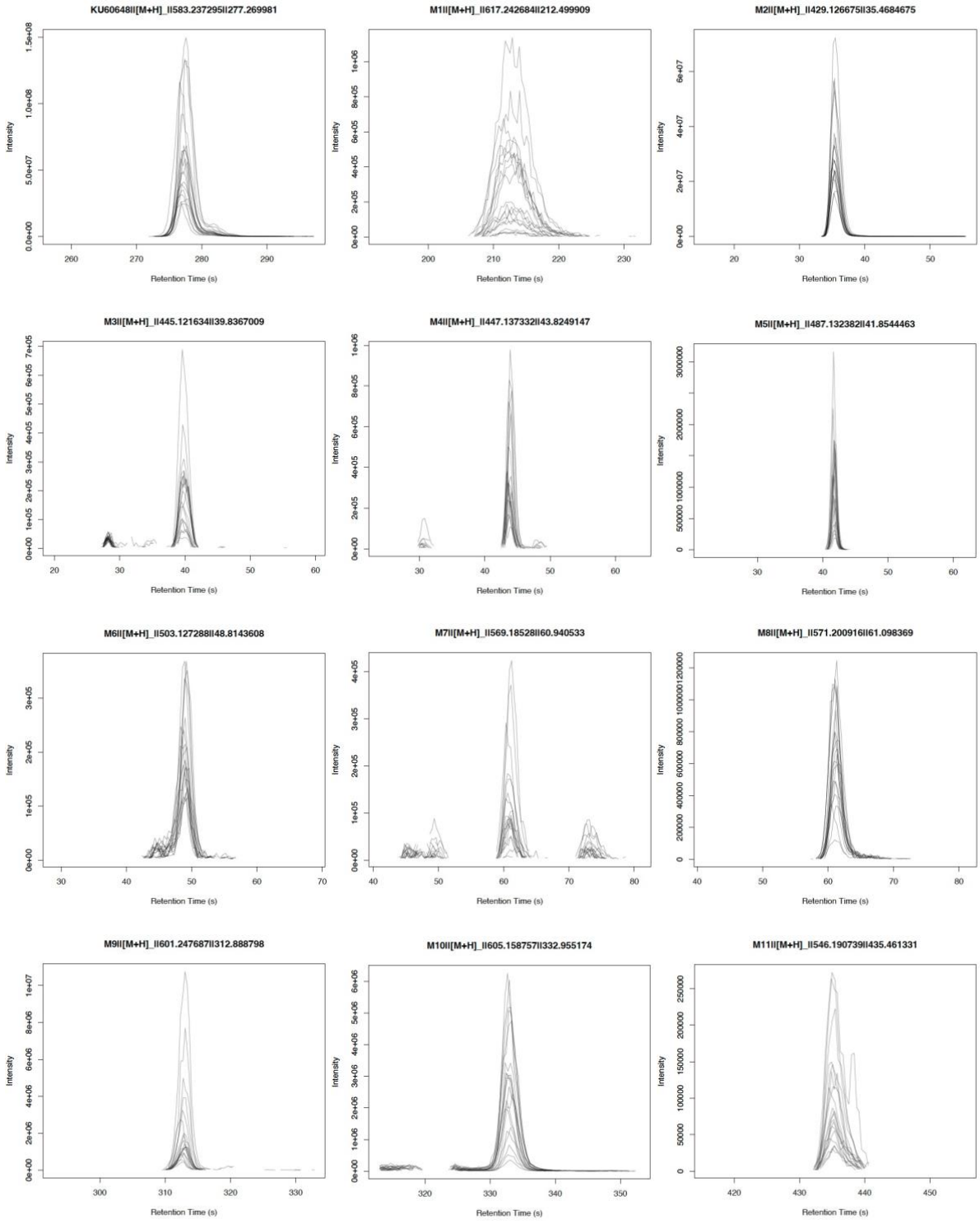


Figure A.2 Mass spectra of sunitinib biotransformation products measured in rat plasma. MS/MS fragmentation spectra of biotransformation products of sunitinib measured in the plasma of rats treated with sunitinib by HILIC positive UHPLC-MS untargeted metabolomics.


KU60648II[M+H]_II583.237295II277.269981
M1II[M+H]_II617.242684II212.499909
M2II[M+H]_II429.126675II35.4684675
M3II[M+H]_II445.121634II39.8367009
M4II[M+H]_II447.137332II43.8249147
M5II[M+H]_II487.132382II41.8544463
M6II[M+H]_II503.127288II48.8143608
M7II[M+H]_II569.18528II60.940533
M8II[M+H]_II571.200916II61.098369
M9II[M+H]_II601.247687II312.888798
M10II[M+H]_II605.158757II332.955174
M11II[M+H]_II546.190739II435.461331
Intensity
Retention Time (s)

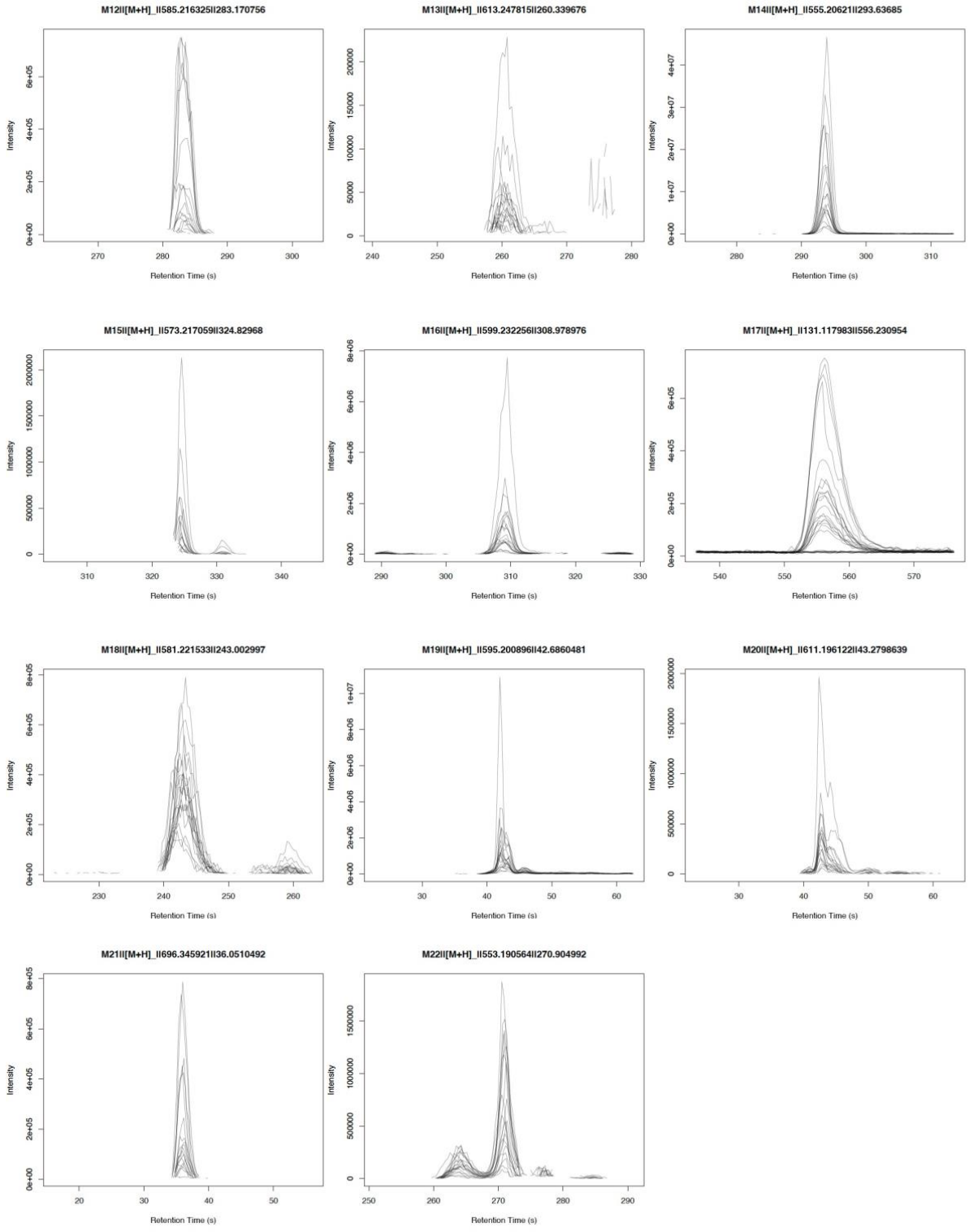


Figure A.3 Chromatographic peaks of KU6068 and related compounds measured in rat plasma. Extracted ion chromatograms (EICs) of KU60648 and its biotransformation products measured in the plasma of rats treated with KU60648 by HILIC positive UHPLC-MS untargeted metabolomics.

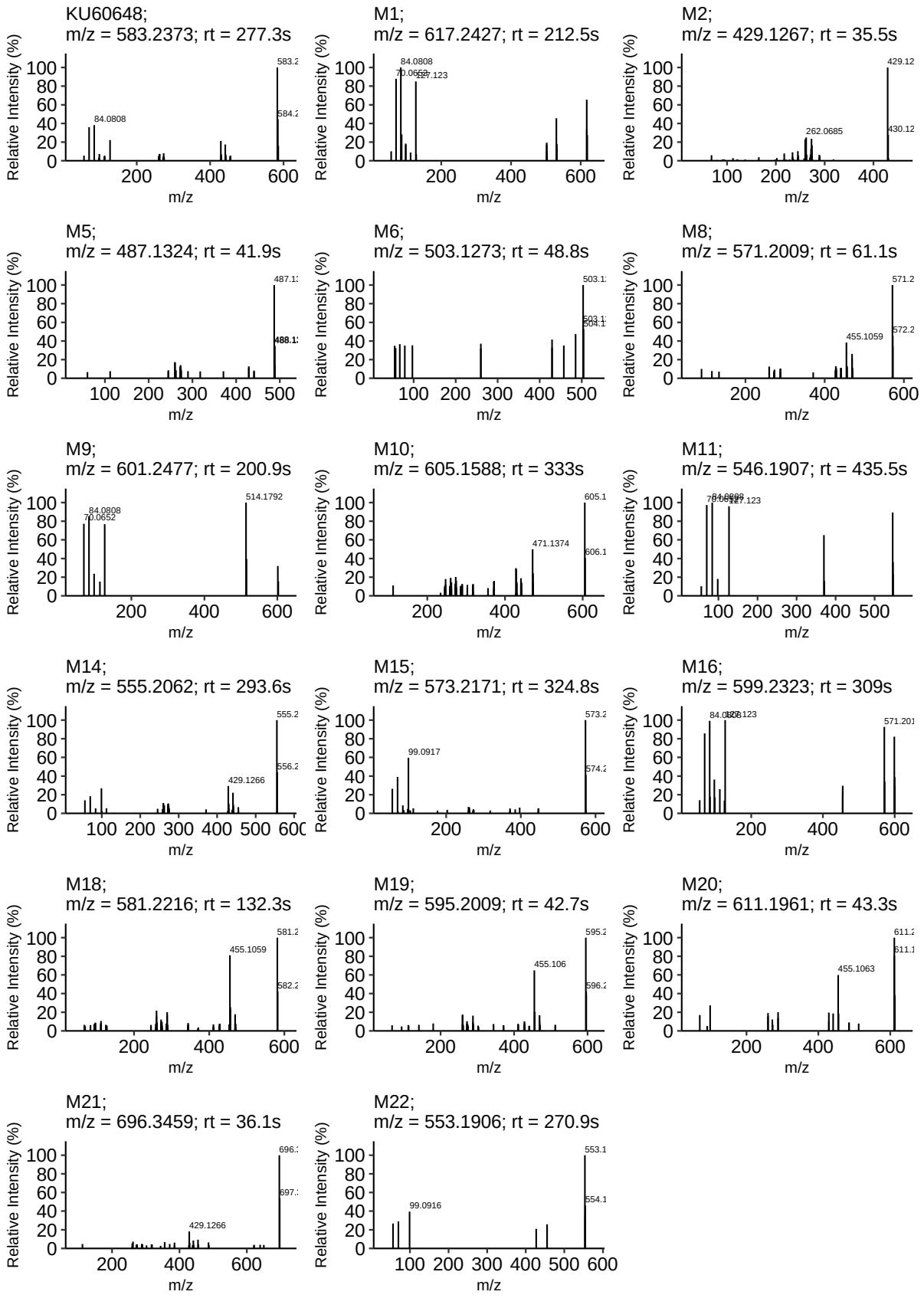


Figure A.4 Mass spectra of KU60648 biotransformation products measured in rat plasma. MS/MS fragmentation spectra of the biotransformation products of KU60648 measured in the plasma of rats treated with KU60648 by HILIC positive UHPLC-MS untargeted metabolomics.

Table A.3 UK National Health Service Top20 most prescribed drugs between 2014 and 2020 and their detection.
The top 20 most prescribed pharmaceuticals, according to UK National Health Service reports from 2014, 2017 and 2020 are presented, alongside their molecular formula and NORMAN database identifier. Details of their measurement in human plasma samples by UHPLC-MS untargeted metabolomics, including the *m/z*, retention time (RT), ion form, and confidence of annotation (MSI annotation level) are also reported.

Overall Rank	Pharmaceutical	2014 Rank	2017 Rank	2020 Rank	Molecular Formula	NORMAN	CECscreen	*m/z*	RT (secs)	Ion Form	MSI Annotation Level	Schymanski Annotation Level
1	Paracetamol	1	1	1	C8H9NO2	NS00000231	Y	152.0707	31.8	$[M+H]^+$	1	1
2	Metformin hydrochloride	3	2	2	C4H11N5	NS00000333	Y	300.1595	24.5	$[M+H]^+$	MS^1 only	4
3	Codeine phosphate	4	3	3	C18H21NO3	NS00000391	Y	Not detected				
4	Lactulose	2	4	6	C12H22O11	Not in database	Y	365.1056	446.5	$[M+Na]^+$	MS^1 only	4
5	Methadone hydrochloride	5	6	5	C21H27NO	NS00000411	Y	332.1988	353.9	$[M+Na]^+$	MS^1 only	4
6	Omeprazole	8	8	7	C17H19N3O3S	NS00003072	Y	346.1221	33.9	$[M+H]^+$	2	2a
7	Atorvastatin	15	7	4	C33H35FN2O5	NS00009054	Y	559.2601	34.0	$[M+H]^+$	2	2a
8	Levothyroxine sodium	7	9	8	C15H11I4NO4	Not in database	Y	Not detected				
9	Cholecalciferol	9	10	9	C27H44O	NS00077941	Y	385.3468	25.4	$[M+H]^+$	MS^1 only	4
10	Ramipril	11	11	11	C23H32N2O5	NS00004700	Y	417.2386	39.8	$[M+H]^+$	1	1
11	Amlodipine	12	12	10	C20H25ClN2O5	NS00000043	Y	Not detected				
12	Simvastatin	6	13	18	C25H38O5	NS00008782	Y	419.2794	27.6	$[M+H]^+$	MS^1 only	4
13	Lansoprazole	16	14	12	C16H14F3N3O2S	NS00000543	Y	370.0834	30.5	$[M+H]^+$	1	1
14	Aspirin	10	16	17	C9H8O4	NS00015094	Y	Not detected				
15	Morphine sulfate	18	18	14	C17H19NO3	NS00093493	Y	286.1439	27.0	$[M+H]^+$	2	2a
16	Bisoprolol fumarate	21	15	13	C18H31NO4	NS00009929	Y	326.2327	95.0	$[M+H]^+$	2	2a
17	Gabapentin	24	17	15	C9H17NO2	NS00000149	Y	172.1334	844.0	$[M+H]^+$	MS^1 only	4
18	Tramadol hydrochloride	13	19	21	C16H25NO2	NS00000338	Y	Not detected				
19	Amitriptyline hydrochloride	20	20	16	C20H23N	NS00000032	Y	278.1904	67.0	$[M+H]^+$	1	1
20	Ibuprofen	17	21	22	C13H18O2	NS00035725	Y	207.1380	27.5	$[M+H]^+$	MS^1 only	4

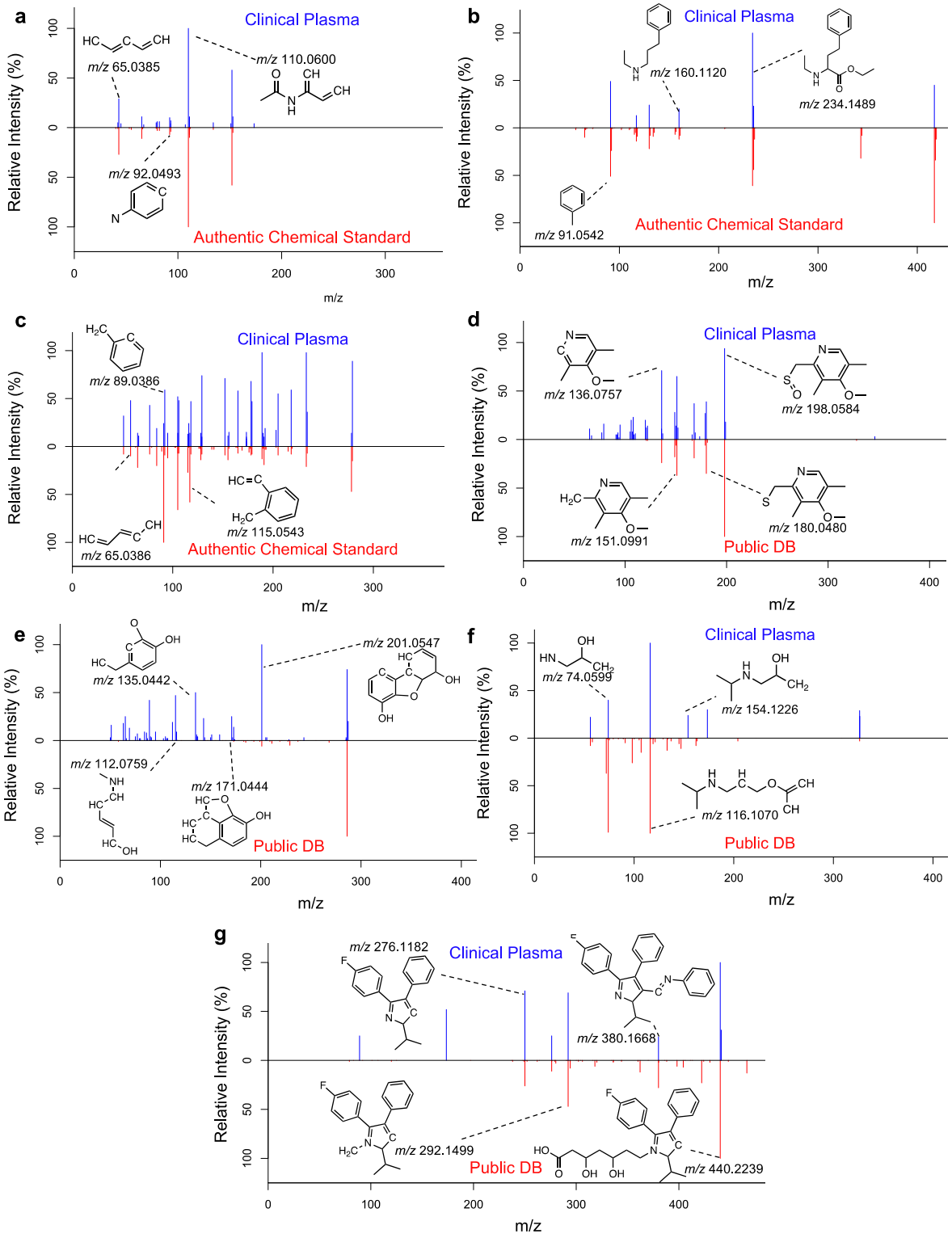
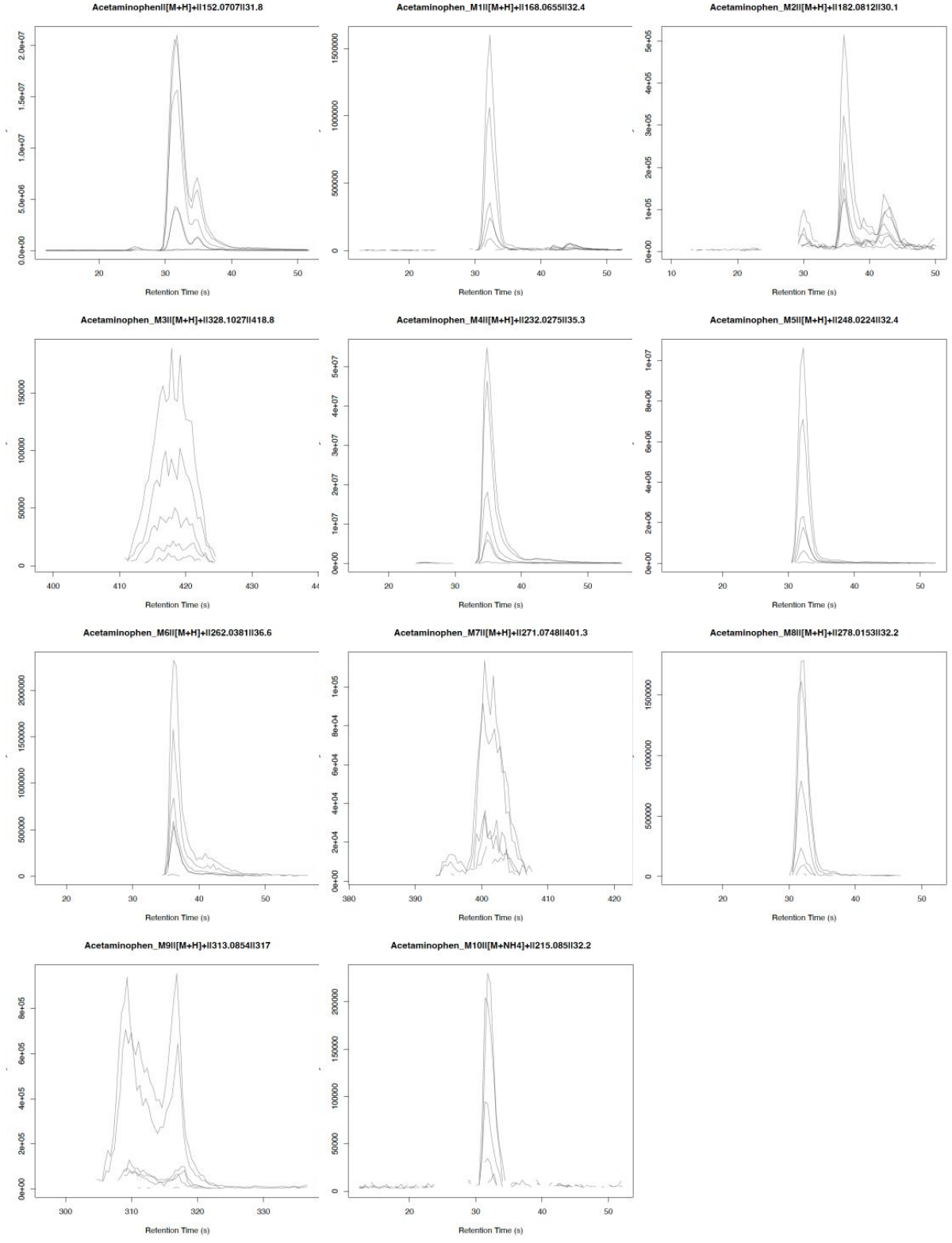
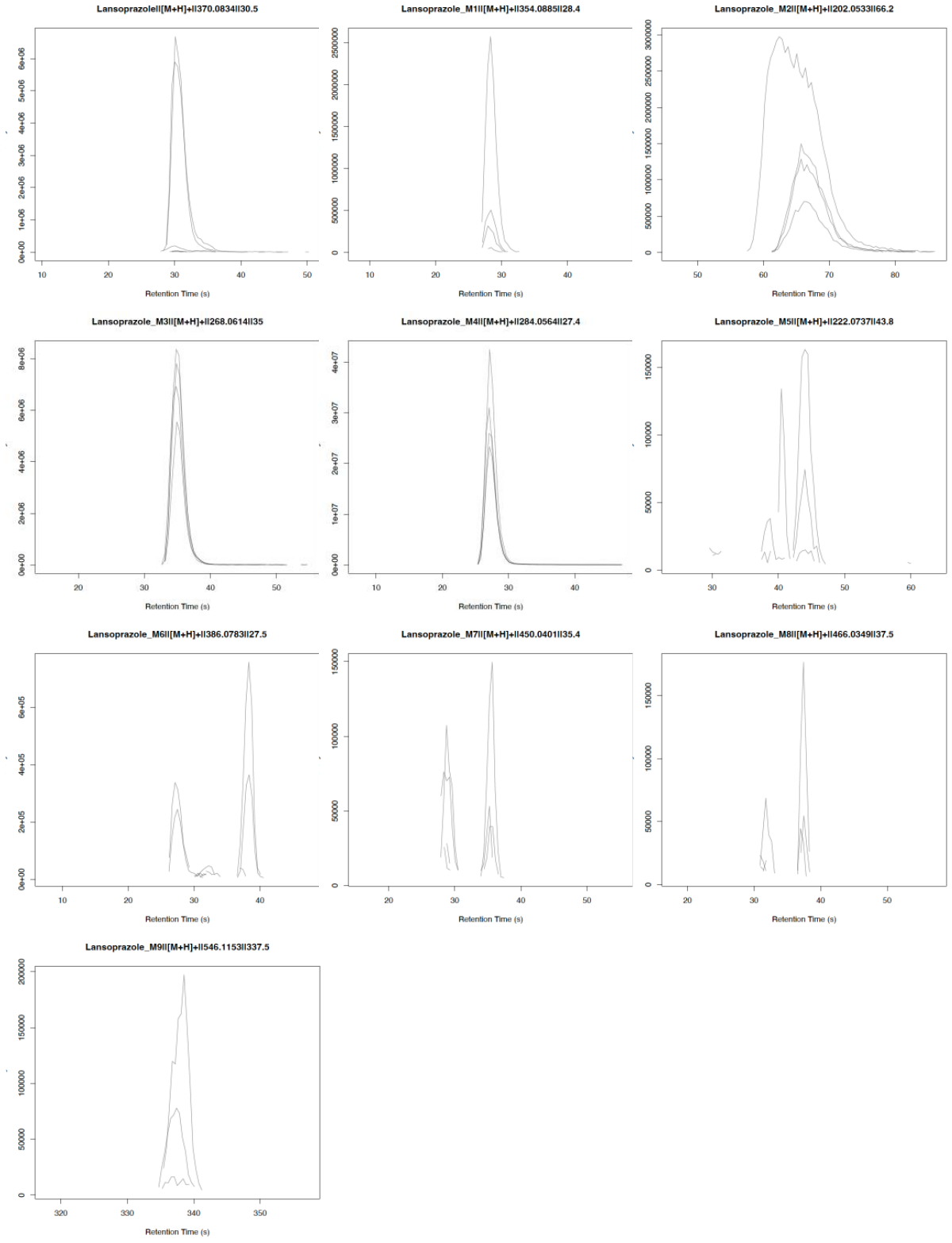
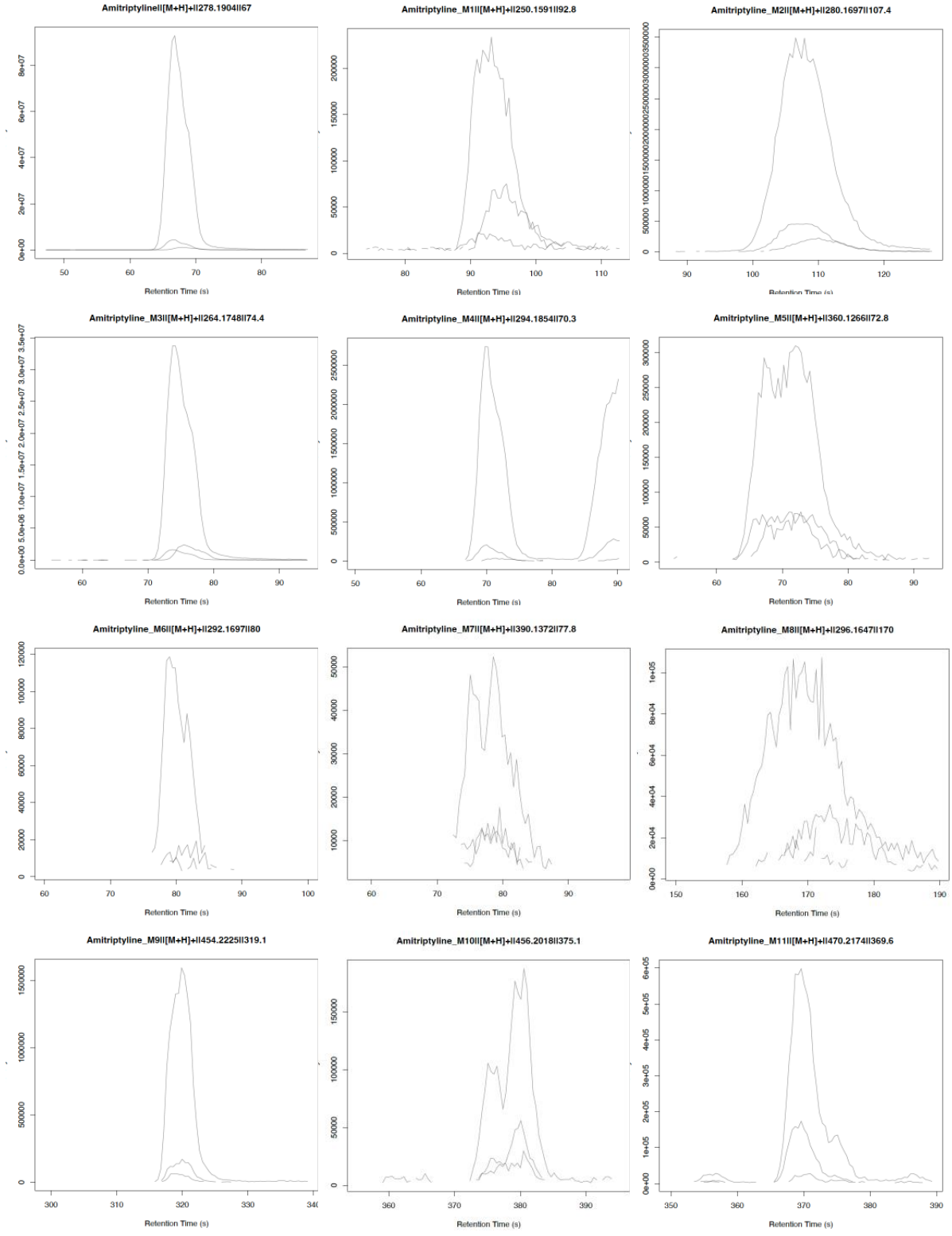
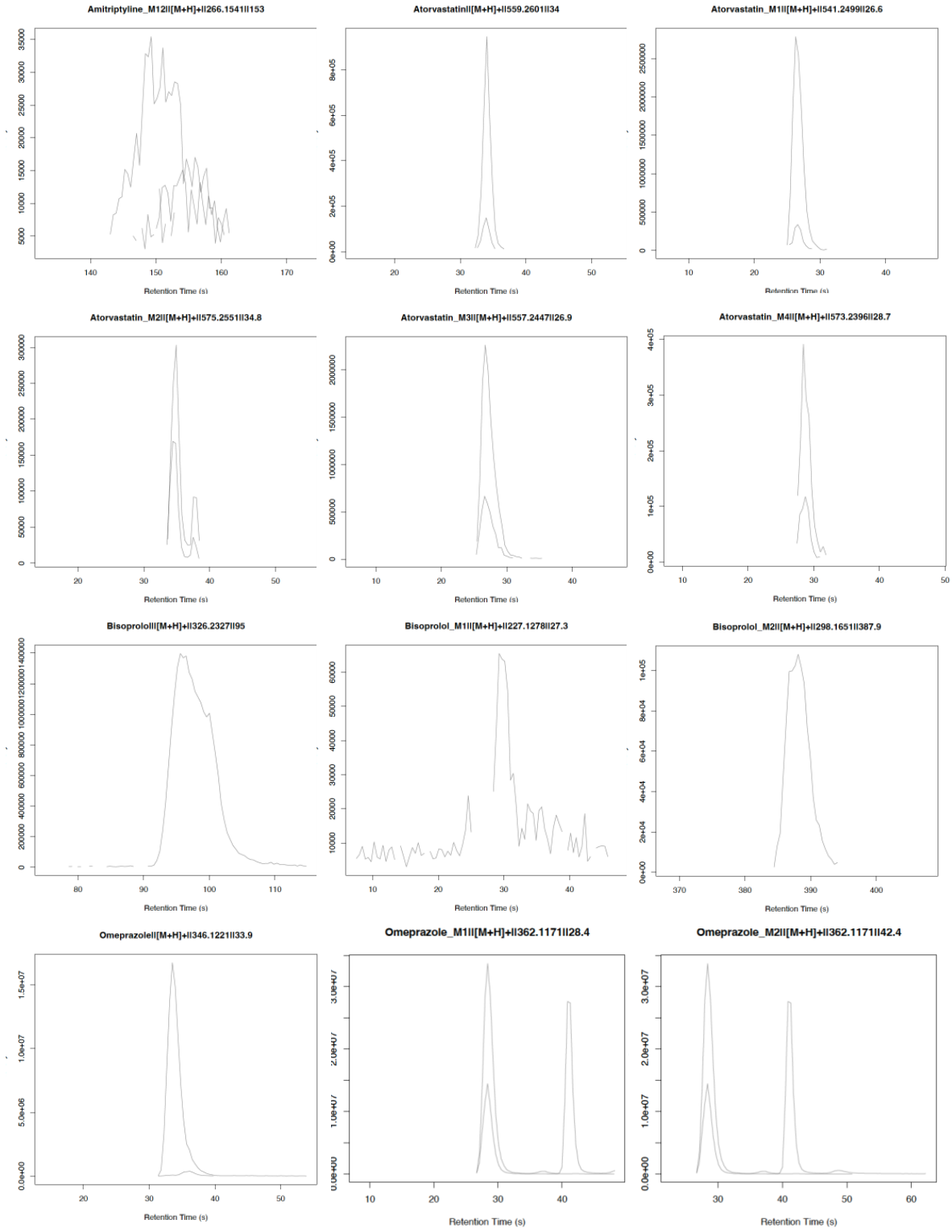


Figure A.5 Confident annotation of pharmaceuticals detected in human plasma. Comparison of measured MS/MS fragmentation spectra for **a** Paracetamol (acetaminophen), **b** ramipril, and **c** amitriptyline in human plasma (top) vs authentic chemical standards (bottom) and the corresponding MetFrag-annotated structures of major peaks. Comparison of MS/MS fragmentation spectra for **d** omeprazole, **e** morphine, **f** bisoprolol and **g** atorvastatin in human plasma (top) vs spectrum from a public database (MassBank of North America; accession codes: MoNA037611, LU138502, EA274410 and EQ301303 for omeprazole, atorvastatin, morphine and bisoprolol, respectively) (bottom) and the corresponding MetFrag-annotated structures of major peaks.


Acetaminophenll[M+H]+ll152.0707ll31.8
Acetaminophen_M1ll[M+H]+ll168.0655ll32.4
Acetaminophen_M2ll[M+H]+ll182.0812ll30.1
Acetaminophen_M3ll[M+H]+ll328.1027ll418.8
Acetaminophen_M4ll[M+H]+ll232.0275ll35.3
Acetaminophen_M5ll[M+H]+ll248.0224ll32.4
Acetaminophen_M6ll[M+H]+ll262.0381ll36.6
Acetaminophen_M7ll[M+H]+ll271.0748ll401.3
Acetaminophen_M8ll[M+H]+ll278.0153ll32.2
Acetaminophen_M9ll[M+H]+ll313.0854ll317
Acetaminophen_M10ll[M+NH4]+ll215.085ll32.2
Retention Time (s)


Lansoprazole||[M+H]+||370.0834||30.5
Lansoprazole_M1||[M+H]+||354.0885||28.4
Lansoprazole_M2||[M+H]+||202.0533||66.2
Lansoprazole_M3||[M+H]+||268.0614||35
Lansoprazole_M4||[M+H]+||284.0564||27.4
Lansoprazole_M5||[M+H]+||222.0737||43.8
Lansoprazole_M6||[M+H]+||386.0783||27.5
Lansoprazole_M7||[M+H]+||450.0401||35.4
Lansoprazole_M8||[M+H]+||466.0349||37.5
Lansoprazole_M9||[M+H]+||546.1153||337.5
Retention Time (s)


Amitriptylinell[M+H]+ll278.1904ll67
Amitriptyline_M1ll[M+H]+ll250.1591ll92.8
Amitriptyline_M2ll[M+H]+ll280.1697ll107.4
Amitriptyline_M3ll[M+H]+ll264.1748ll74.4
Amitriptyline_M4ll[M+H]+ll294.1854ll70.3
Amitriptyline_M5ll[M+H]+ll360.1266ll72.8
Amitriptyline_M6ll[M+H]+ll292.1697ll80
Amitriptyline_M7ll[M+H]+ll390.1372ll77.8
Amitriptyline_M8ll[M+H]+ll296.1647ll170
Amitriptyline_M9ll[M+H]+ll454.2225ll319.1
Amitriptyline_M10ll[M+H]+ll456.2018ll375.1
Amitriptyline_M11ll[M+H]+ll470.2174ll369.6
Retention Time (s)


Amitriptyline_M12II[M+H]+II266.1541II153
AtorvastatinII[M+H]+II559.2601II34
Atorvastatin_M1II[M+H]+II541.2499II26.6
Atorvastatin_M2II[M+H]+II575.2551II34.8
Atorvastatin_M3II[M+H]+II557.2447II26.9
Atorvastatin_M4II[M+H]+II573.2396II28.7
BisoprololII[M+H]+II326.2327II95
Bisoprolol_M1II[M+H]+II227.1278II27.3
Bisoprolol_M2II[M+H]+II298.1651II387.9
OmeprazoleII[M+H]+II346.1221II33.9
Omeprazole_M1II[M+H]+II362.1171II28.4
Omeprazole_M2II[M+H]+II362.1171II42.4
Retention Time (s)

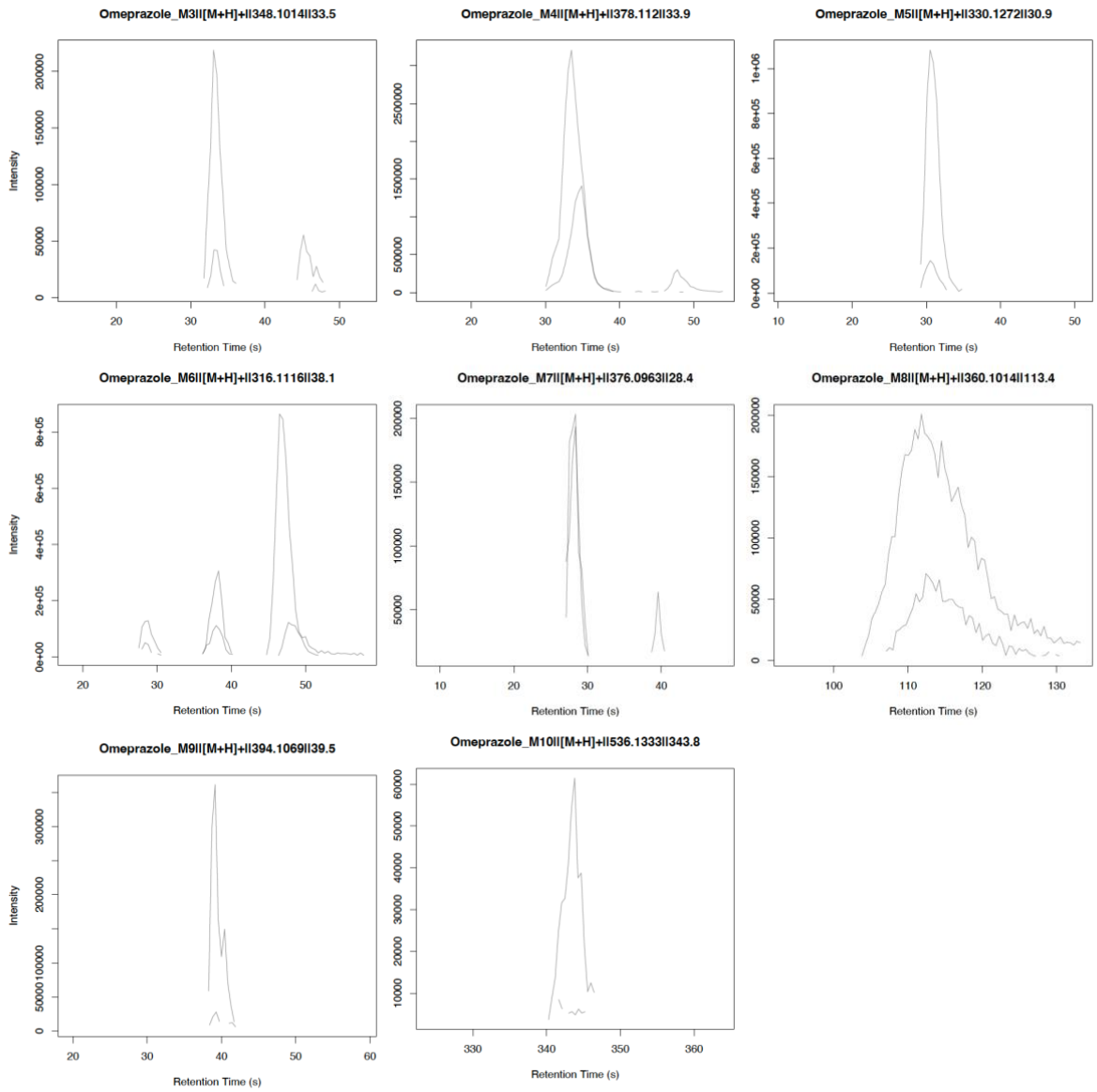
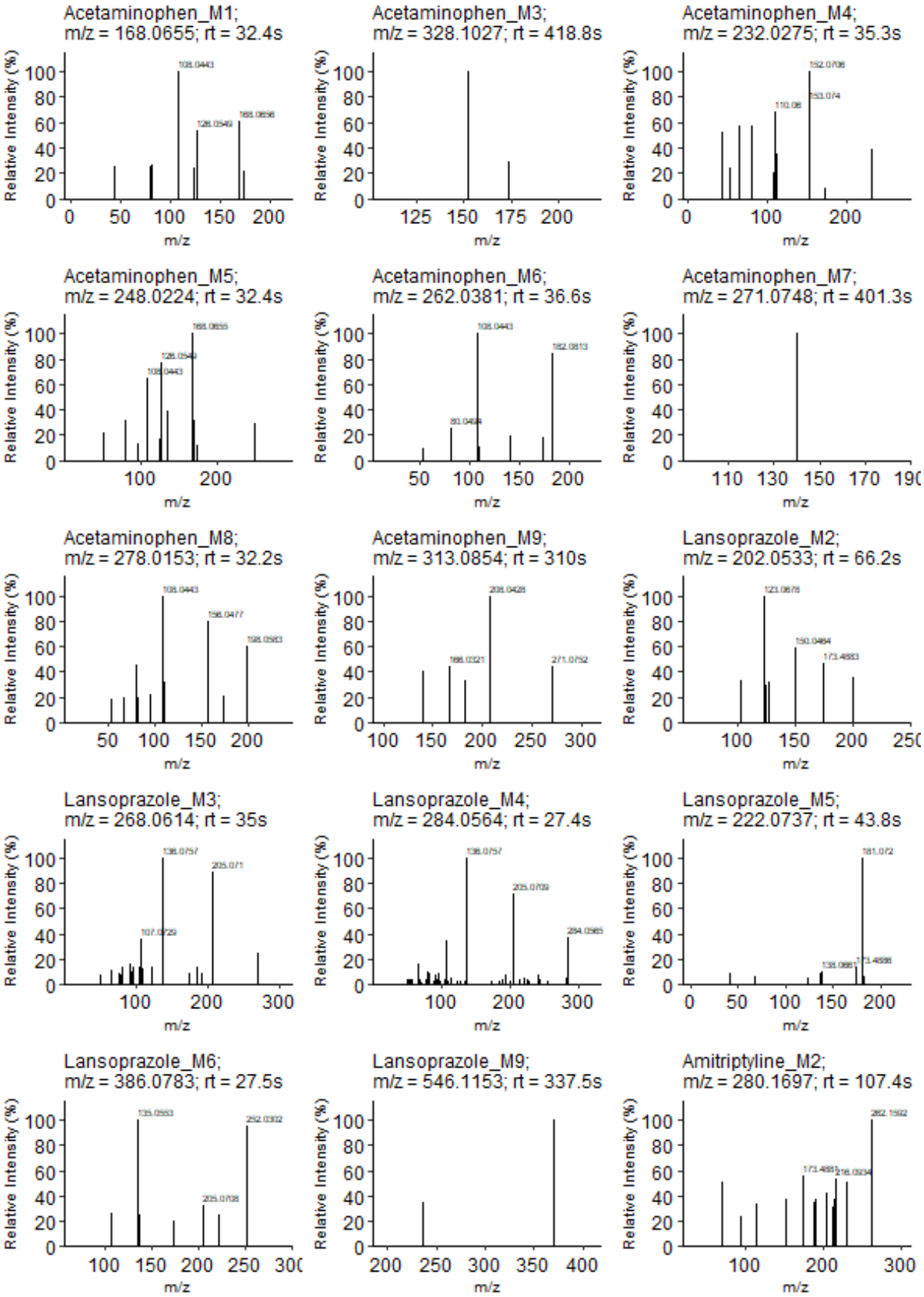


Figure A.6 Chromatographic peaks of pharmaceuticals and their biotransformation products measured in human plasma.
Extracted ion chromatograms (EICs) of Paracetamol (acetaminophen), lansoprazole, amitriptyline, atorvastatin, bisoprolol and omeprazole, and their biotransformation products measured in the human plasma samples by HILIC positive UHPLC-MS untargeted metabolomics.


Acetaminophen_M1;
m/z = 168.0655; rt = 32.4s
Acetaminophen_M3;
m/z = 328.1027; rt = 418.8s
Acetaminophen_M4;
m/z = 232.0275; rt = 35.3s
Acetaminophen_M5;
m/z = 248.0224; rt = 32.4s
Acetaminophen_M6;
m/z = 262.0381; rt = 36.6s
Acetaminophen_M7;
m/z = 271.0748; rt = 401.3s
Acetaminophen_M8;
m/z = 278.0153; rt = 32.2s
Acetaminophen_M9;
m/z = 313.0854; rt = 310s
Lansoprazole_M2;
m/z = 202.0533; rt = 66.2s
Lansoprazole_M3;
m/z = 268.0614; rt = 35s
Lansoprazole_M4;
m/z = 284.0564; rt = 27.4s
Lansoprazole_M5;
m/z = 222.0737; rt = 43.8s
Lansoprazole_M6;
m/z = 386.0783; rt = 27.5s
Lansoprazole_M9;
m/z = 546.1153; rt = 337.5s
Amitriptyline_M2;
m/z = 280.1697; rt = 107.4s
Relative Intensity (%)
m/z

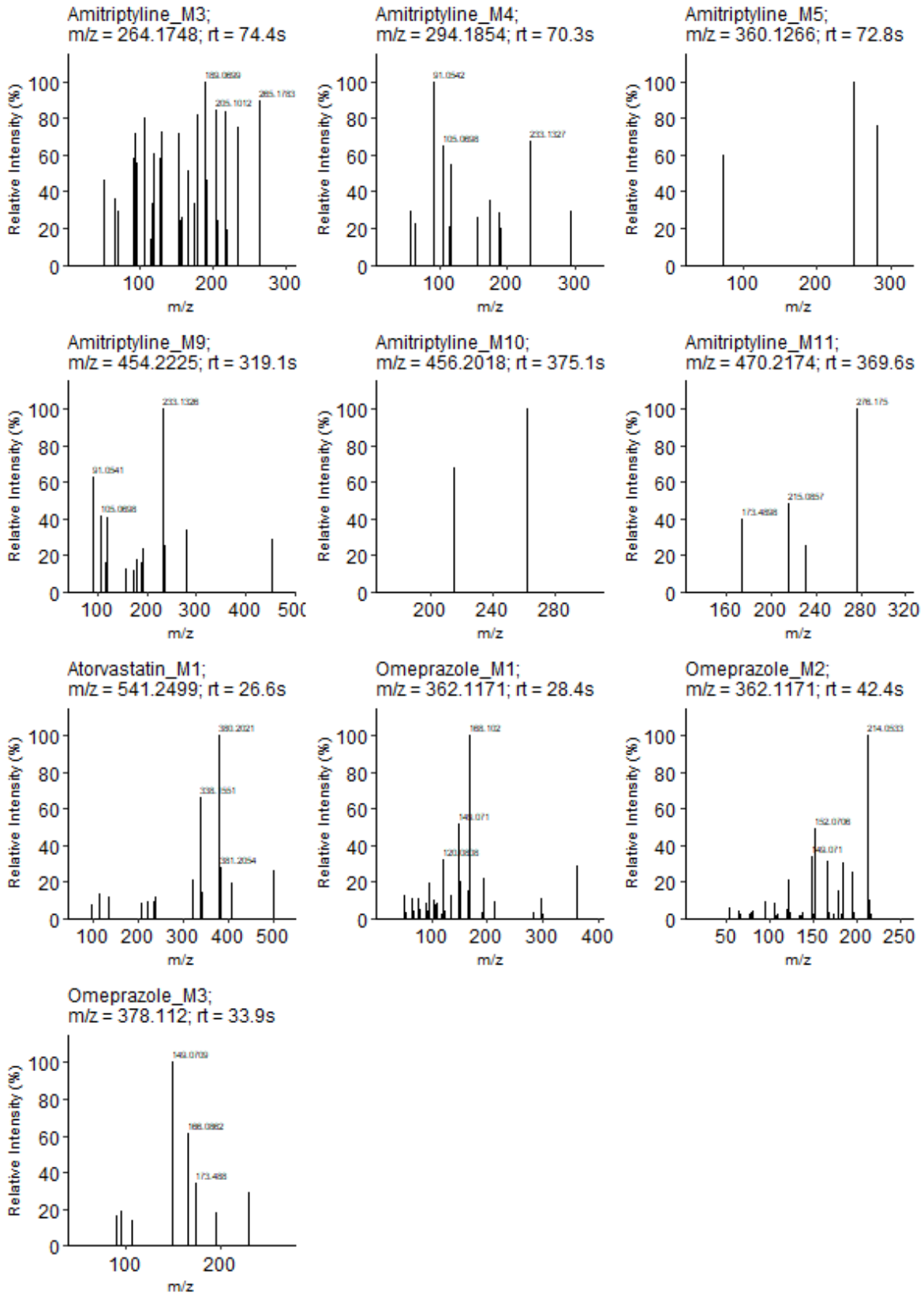


Figure A.7 Mass spectra of pharmaceuticals and their biotransformation products detected in human plasma.

MS/MS fragmentation spectra of the biotransformation products of Paracetamol (acetaminophen), amitriptyline, omeprazole, atorvastatin and bisoprolol measured in human plasma samples by HILIC positive UHPLC-MS untargeted metabolomics.

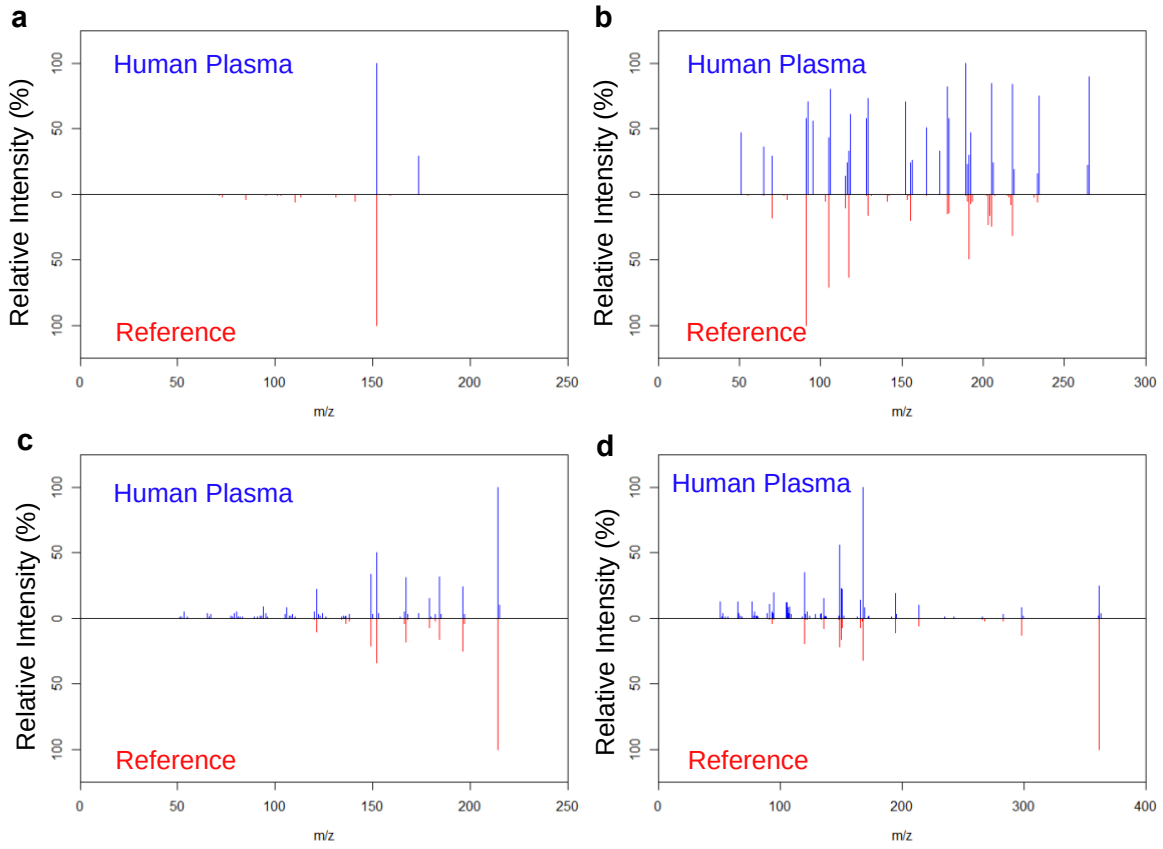


Figure A.8 Confident annotation of four biotransformation products detected in human plasma.
Comparison of measured MS/MS fragmentation spectra for **a** acetaminophen glucuronide (acetaminophen M3), **b** nortriptyline (amitriptyline M3), and **c** 5-hydroxyomeprazole (omeprazole M2) and **d** omeprazole sulfone (omeprazole M1) in human plasma (top) vs reference spectra (bottom) from a public database (**a**, **b**: MassBank of North America, accession codes: FiehnHILIC000149 and EQ369204, respectively; **c**, **d**: mzCloud, accession codes: Reference1851 and Reference2488, respectively).

APPENDIX B

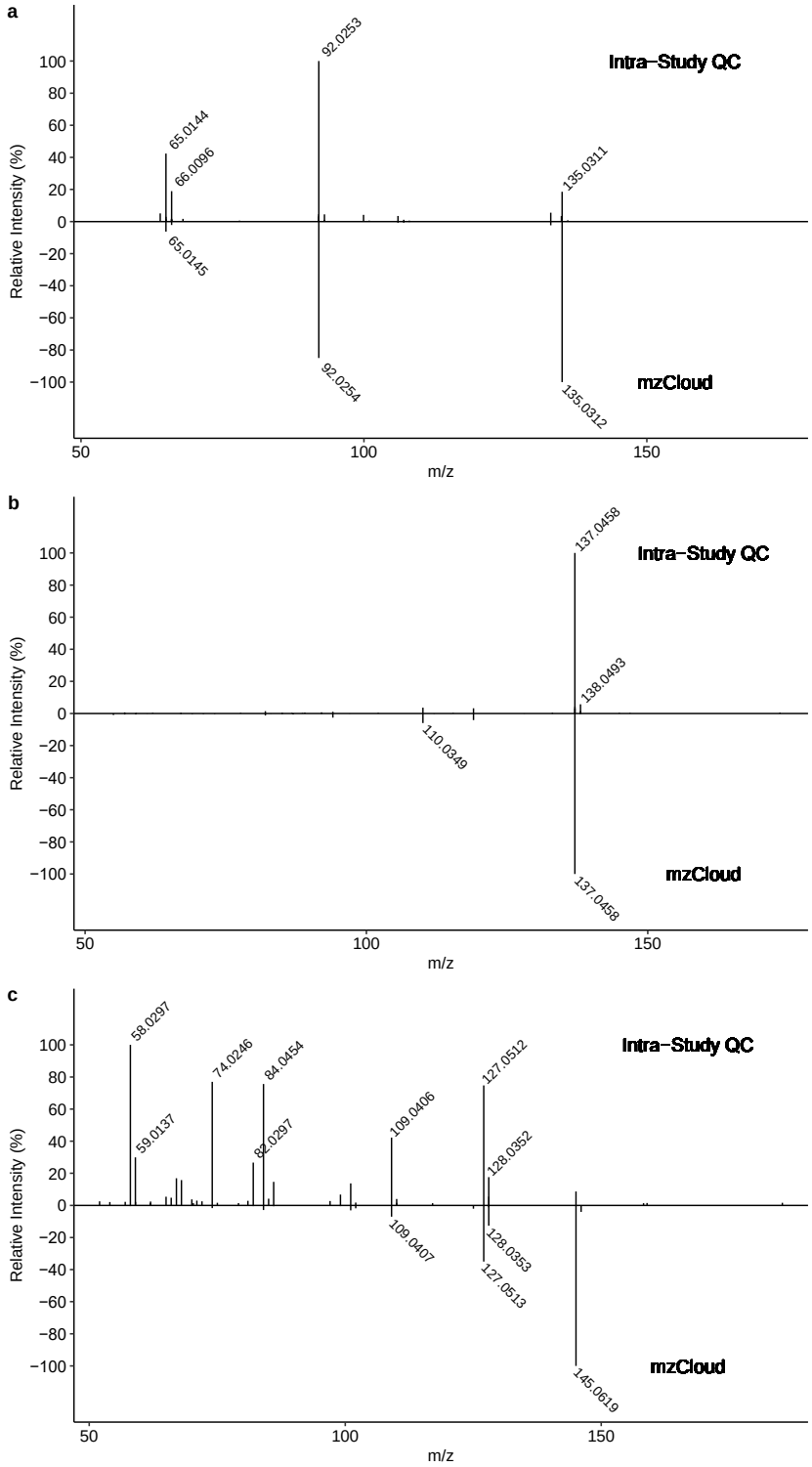


Figure B.1 Comparison of measured MS/MS fragmentation spectra for each annotated feature (top) and reference spectra for the corresponding metabolite from the mzCloud library (www.mzcloud.org; bottom).

Spectral match scores of 86.1%, 86.4% and 78.8%, were calculated for **a** hypoxanthine, **b** inosine and **c** L-glutamine, respectively, using the HighChem HighRes algorithm in Compound Discoverer (Thermo Scientific).

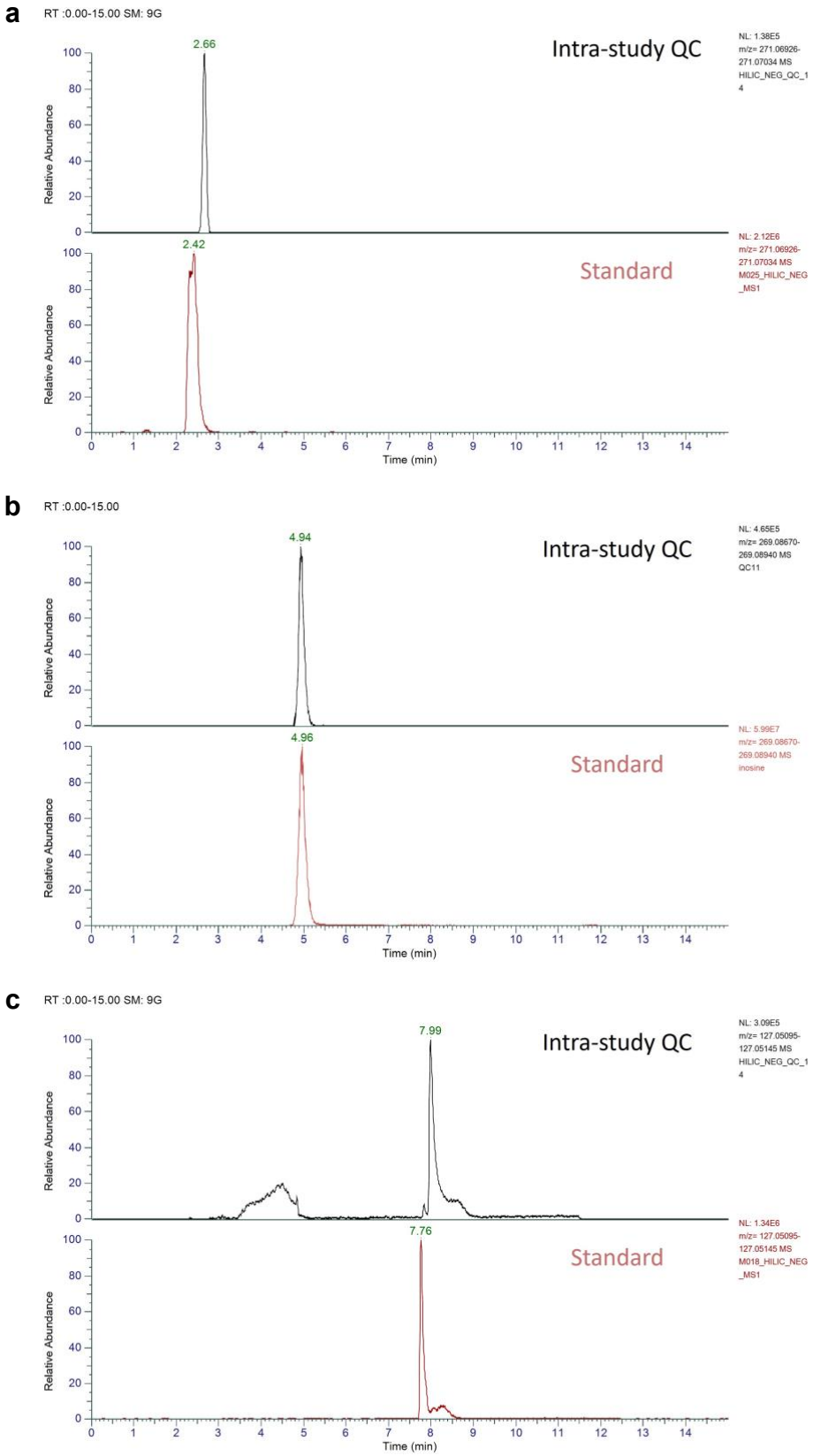


Figure B.2 Extracted ion chromatograms (EICs) showing matching retention times (±30-second tolerance) between each annotated feature, as measured in an intra-study QC sample (top EIC, labelled "intra-study QC"), and the corresponding reference standard (bottom EIC, labelled "standard").

a hypoxanthine (2M-H)$^-$, *m/z* 271.0697), **b** inosine ([M+H]$^+$, *m/z* 269.0880) and **c** L-glutamine ([M-H-H_2O]$^-$, *m/z* 127.0513).

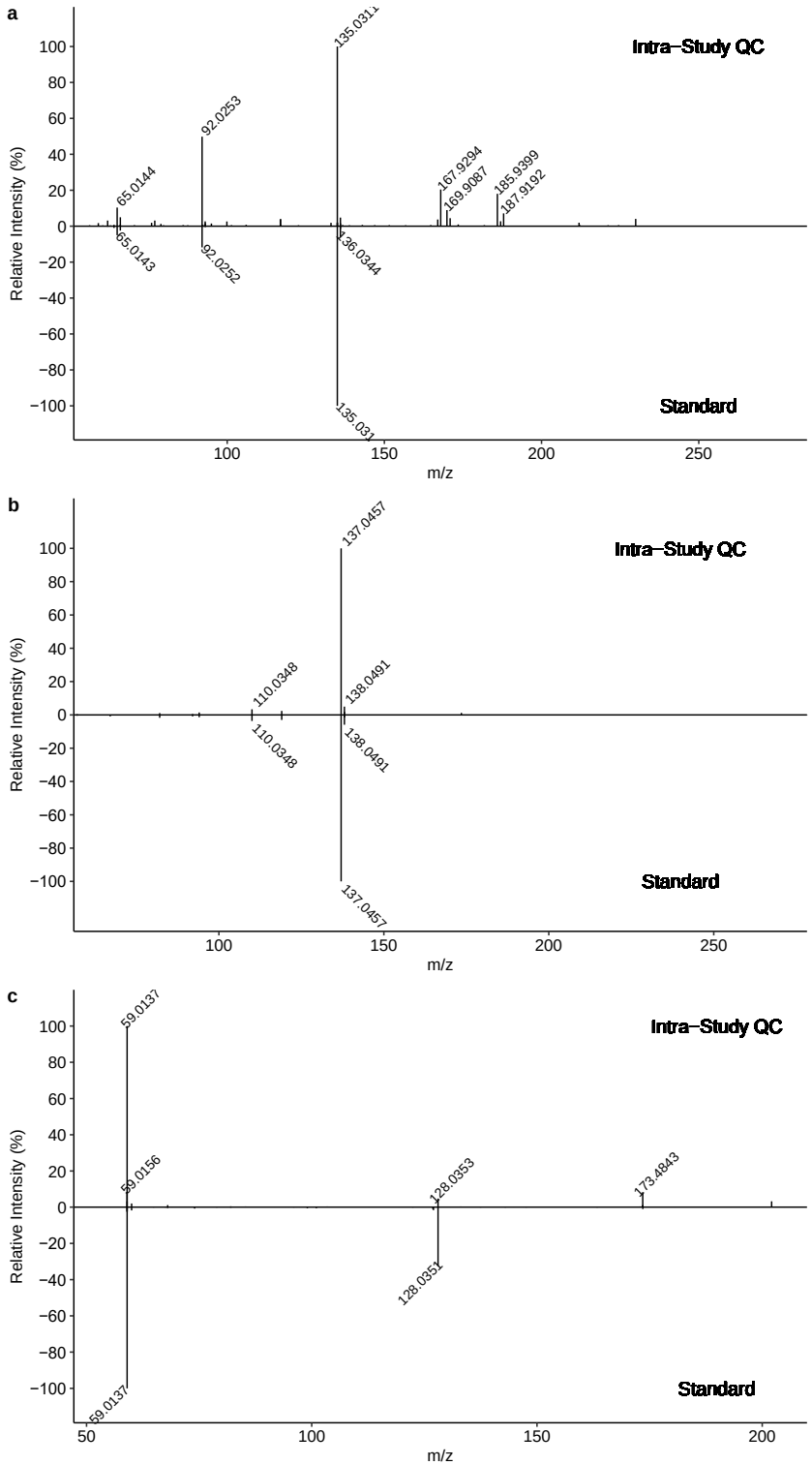


Figure B.3 Comparison of measured MS/MS fragmentation spectra for each annotated feature (top) and reference spectra for the corresponding metabolite from analysis of a reference standard.

Average (across scans) raw MS/MS spectra of **a** hypoxanthine (precursor ion: *m/z* 271.0697, retention time: 2.3 - 2.8 min), **b** inosine (precursor ion: *m/z* 269.0880, retention time: 4.7 - 5.5 min) and **c** L-glutamine (precursor ion: *m/z* 127.0513, retention time: 7.7 - 8.9 min), measured in an intra-study QC sample (top plot, labelled “intra-study QC”), and the corresponding reference standard (bottom plot, labelled “standard”). The spectral similarity (cosine dot product) scores are 0.91, 1.00 and 0.95 for hypoxanthine, inosine, and L-glutamine, respectively.

APPENDIX C

Table C.1 Number of features reported by XCMS processing of UHPLC-MS datasets acquired by analysis of cardiomyocytes and rat cardiac tissue, before and after peak matrix filtering. The number of features reported by XCMS processing of HILIC positive and negative and RP-C_{18} positive and negative-based analysis of intracellular polar metabolite and lipid extracts of human-induced pluripotent stem cell-derived cardiomyocytes, respectively, are presented (data discussed in Section 2.3.6). Also shown are the number of features following XCMS processing of datasets acquired from cardiac tissue extracts, by the same analytical methods (data discussed in Section 2.3.5). The number of features both before and after filtering of the peak matrix (filtering included blank subtraction and filtering according to incidence by sample, incidence by feature, and reproducibility in quality control samples, as described in Section 2.2.11 are presented.

Dataset	Cardiomyocytes				Cardiac tissue			
	HILIC positive	HILIC negative	RP-C_{18} positive	RP-C_{18} negative	HILIC positive	HILIC negative	RP-C_{18} positive	RP-C_{18} negative
Number of features reported by XCMS	11795	5912	7923	3665	8202	7585	11832	6273
Number of features after peak matrix filtering	816	266	3736	2204	1369	2058	6922	4320

APPENDIX D

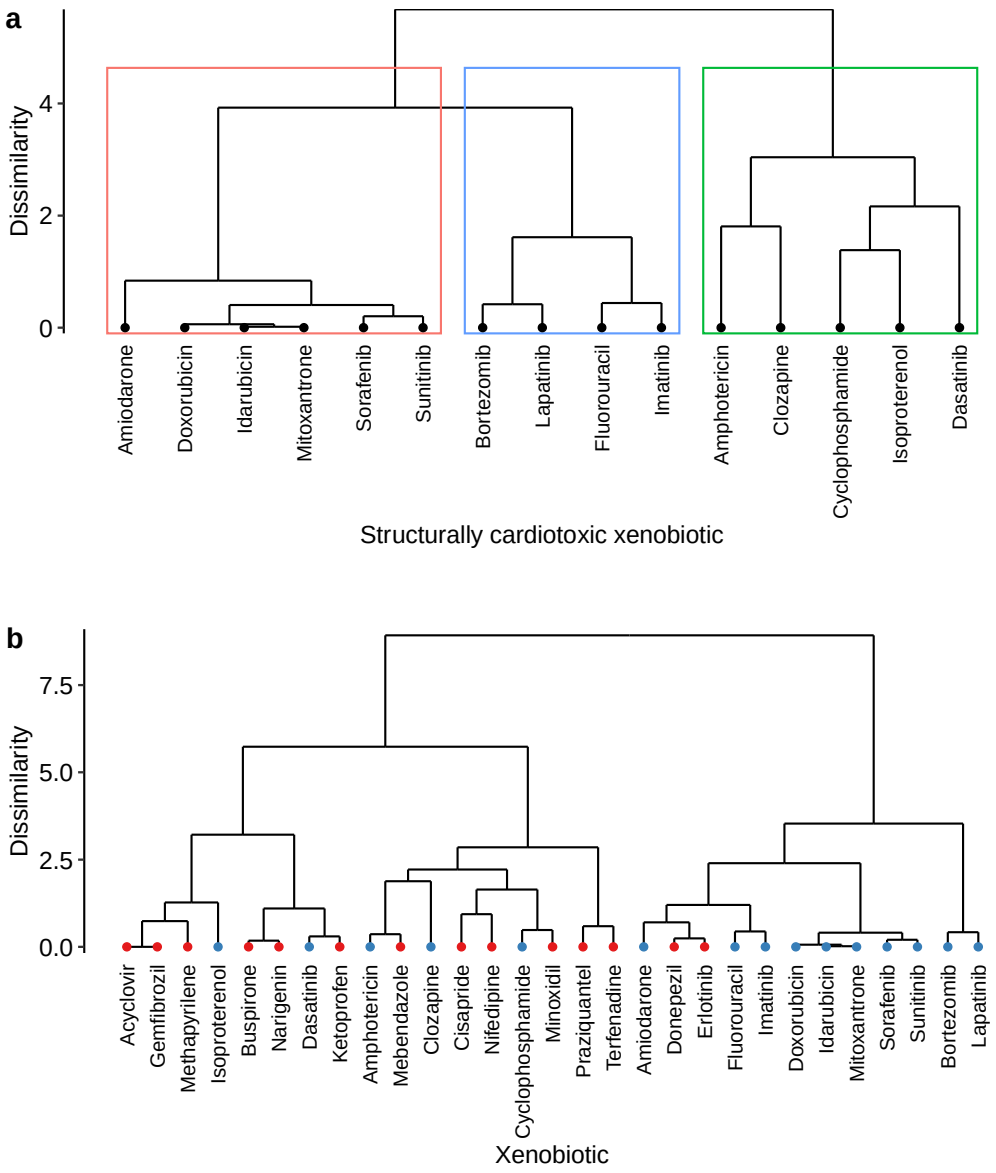


Figure D.1 (Dis)similarity of the cardiac microtissue response to xenobiotics.
The dendrograms show the dissimilarity of the cardiac microtissues response following exposure to **a** 15 structurally cardiotoxic xenobiotics and **b** 29 xenobiotics, 15 structurally cardiotoxic (blue) and 14 non-structurally cardiotoxic (red), for 72-hours. Responses were defined by three parameters: % ATP depletion, % mitochondrial membrane permeability (Δψm) and % endoplasmic reticulum (ER) stress, measured by high content biology. The dissimilarity matrices were calculated using the Euclidean distance metric and clustering performed using Ward's method. Coloured boxes in **a** indicate three separate clusters of xenobiotics which induce highly similar responses in cardiac microtissues: the red box highlights xenobiotics which present relatively high potency against all three indicators, the blue box highlights xenobiotics which present relatively high potency against Δψm and ATP indicators, but relatively low potency according to % ER stress, and the green box highlights xenobiotics which present relatively low potency against all three indicators.

Table D.1 SIM window definitions for nESI-DIMS-based untargeted metabolomics.
The *m/z* ranges and widths of SIM windows employed in the nESI-DIMS-based untargeted metabolomics assays performed using an Orbitrap ID-X Tribrid mass spectrometer.

Assay	SIM window ID	Start *m/z*	End *m/z*	SIM window width (Da)
Polar positive	PP-SIM-1	50	125	75
Polar positive	PP-SIM-2	115	150	35
Polar positive	PP-SIM-3	140	165	25
Polar positive	PP-SIM-4	155	190	35
Polar positive	PP-SIM-5	180	210	30
Polar positive	PP-SIM-6	200	235	35
Polar positive	PP-SIM-7	225	255	30
Polar positive	PP-SIM-8	245	285	40
Polar positive	PP-SIM-9	275	315	40
Polar positive	PP-SIM-10	305	340	35
Polar positive	PP-SIM-11	330	365	35
Polar positive	PP-SIM-12	355	380	25
Polar positive	PP-SIM-13	370	395	25
Polar positive	PP-SIM-14	385	415	30
Polar positive	PP-SIM-15	405	435	30
Polar positive	PP-SIM-16	425	460	35
Polar positive	PP-SIM-17	450	490	40
Polar positive	PP-SIM-18	480	555	75
Polar positive	PP-SIM-19	545	620	75
Polar negative	PN-SIM-1	50	120	70
Polar negative	PN-SIM-2	110	145	35
Polar negative	PN-SIM-3	135	160	25
Polar negative	PN-SIM-4	150	195	45
Polar negative	PN-SIM-5	185	220	35
Polar negative	PN-SIM-6	210	255	45
Polar negative	PN-SIM-7	245	270	25
Polar negative	PN-SIM-8	260	285	25
Polar negative	PN-SIM-9	275	300	25
Polar negative	PN-SIM-10	290	320	30
Polar negative	PN-SIM-11	310	340	30
Polar negative	PN-SIM-12	330	370	40
Polar negative	PN-SIM-13	360	390	30
Polar negative	PN-SIM-14	380	405	25
Polar negative	PN-SIM-15	395	425	30
Polar negative	PN-SIM-16	415	465	50
Polar negative	PN-SIM-17	455	500	45
Polar negative	PN-SIM-18	490	555	65
Polar negative	PN-SIM-19	545	620	75
Lipids positive	LP-SIM-2	190	225	35
Lipids positive	LP-SIM-2	215	245	30
Lipids positive	LP-SIM-3	235	260	25
Lipids positive	LP-SIM-4	250	280	30
Lipids positive	LP-SIM-5	270	305	35
Lipids positive	LP-SIM-6	295	320	25
Lipids positive	LP-SIM-7	310	345	35
Lipids positive	LP-SIM-8	335	360	25
Lipids positive	LP-SIM-9	350	375	25
Lipids positive	LP-SIM-10	365	405	40
Lipids positive	LP-SIM-11	395	420	25
Lipids positive	LP-SIM-12	410	440	30
Lipids positive	LP-SIM-13	430	460	30
Lipids positive	LP-SIM-14	450	480	30
Lipids positive	LP-SIM-15	470	495	25
Lipids positive	LP-SIM-16	485	520	35
Lipids positive	LP-SIM-17	510	545	35
Lipids positive	LP-SIM-18	535	575	40
Lipids positive	LP-SIM-19	565	600	35
Lipids positive	LP-SIM-20	590	625	35

Lipids positive	LP-SIM-21	615	655	40
Lipids positive	LP-SIM-22	645	680	35
Lipids positive	LP-SIM-23	670	710	40
Lipids positive	LP-SIM-24	700	730	30
Lipids positive	LP-SIM-25	720	745	25
Lipids positive	LP-SIM-26	735	760	25
Lipids positive	LP-SIM-27	750	780	30
Lipids positive	LP-SIM-28	770	795	25
Lipids positive	LP-SIM-29	785	815	30
Lipids positive	LP-SIM-30	805	840	35
Lipids positive	LP-SIM-31	830	960	130
Lipids positive	LP-SIM-32	950	1080	130
Lipids positive	LP-SIM-33	1070	1200	130
Lipids negative	LN-SIM-1	190	215	25
Lipids negative	LN-SIM-2	205	230	25
Lipids negative	LN-SIM-3	220	245	25
Lipids negative	LN-SIM-4	235	260	25
Lipids negative	LN-SIM-5	250	275	25
Lipids negative	LN-SIM-6	265	290	25
Lipids negative	LN-SIM-7	280	305	25
Lipids negative	LN-SIM-8	295	320	25
Lipids negative	LN-SIM-9	310	335	25
Lipids negative	LN-SIM-10	325	355	30
Lipids negative	LN-SIM-11	345	380	35
Lipids negative	LN-SIM-12	370	400	30
Lipids negative	LN-SIM-13	390	425	35
Lipids negative	LN-SIM-14	415	450	35
Lipids negative	LN-SIM-15	440	485	45
Lipids negative	LN-SIM-16	475	505	30
Lipids negative	LN-SIM-17	495	530	35
Lipids negative	LN-SIM-18	520	545	25
Lipids negative	LN-SIM-19	535	570	35
Lipids negative	LN-SIM-20	560	585	25
Lipids negative	LN-SIM-21	575	600	25
Lipids negative	LN-SIM-22	590	615	25
Lipids negative	LN-SIM-23	605	630	25
Lipids negative	LN-SIM-24	620	645	25
Lipids negative	LN-SIM-25	635	660	25
Lipids negative	LN-SIM-26	650	695	45
Lipids negative	LN-SIM-27	685	725	40
Lipids negative	LN-SIM-28	715	755	40
Lipids negative	LN-SIM-29	745	800	55
Lipids negative	LN-SIM-30	790	850	60
Lipids negative	LN-SIM-31	840	960	120
Lipids negative	LN-SIM-32	950	1080	130
Lipids negative	LN-SIM-33	1070	1200	130

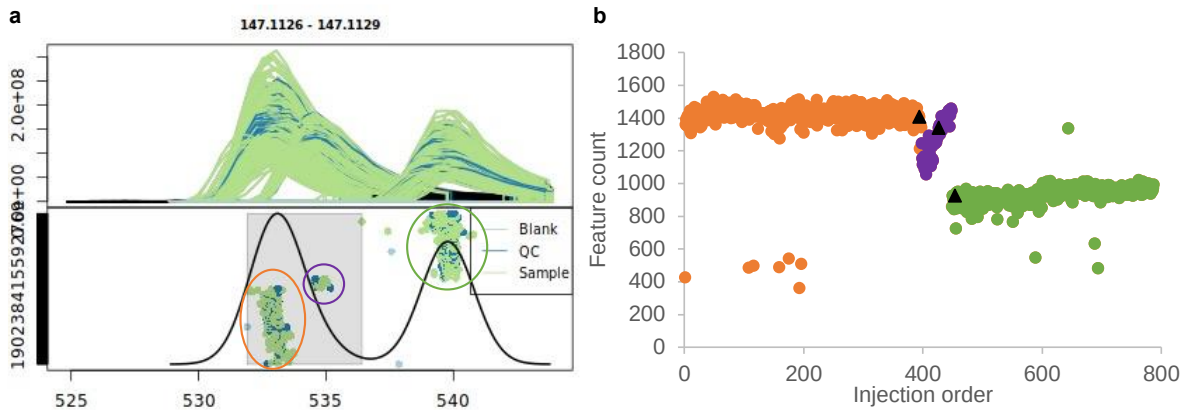


Figure D.2 Retention time shifts observed in HILIC positive dataset.
a Top, extracted ion chromatograms from each sample and, bottom, scatter plot of injection order against retention time, demonstrating the shifts in retention time for one representative *m/z*-RT feature. Ellipses highlight the three clusters of samples separated based on retention time: group 1 (orange), group 2 (purple) and group 3 (green). **b** Scatter plot showing relationship between number of features per sample after preliminary XCMS peak picking and correspondence and the injection order, evidencing three sample 'groups': group 1 (orange), group 2 (purple) and group 3 (green). The intra-study QCs used as reference samples in the calculation of functions to align retention times between the groups are displayed as black triangles (▲).

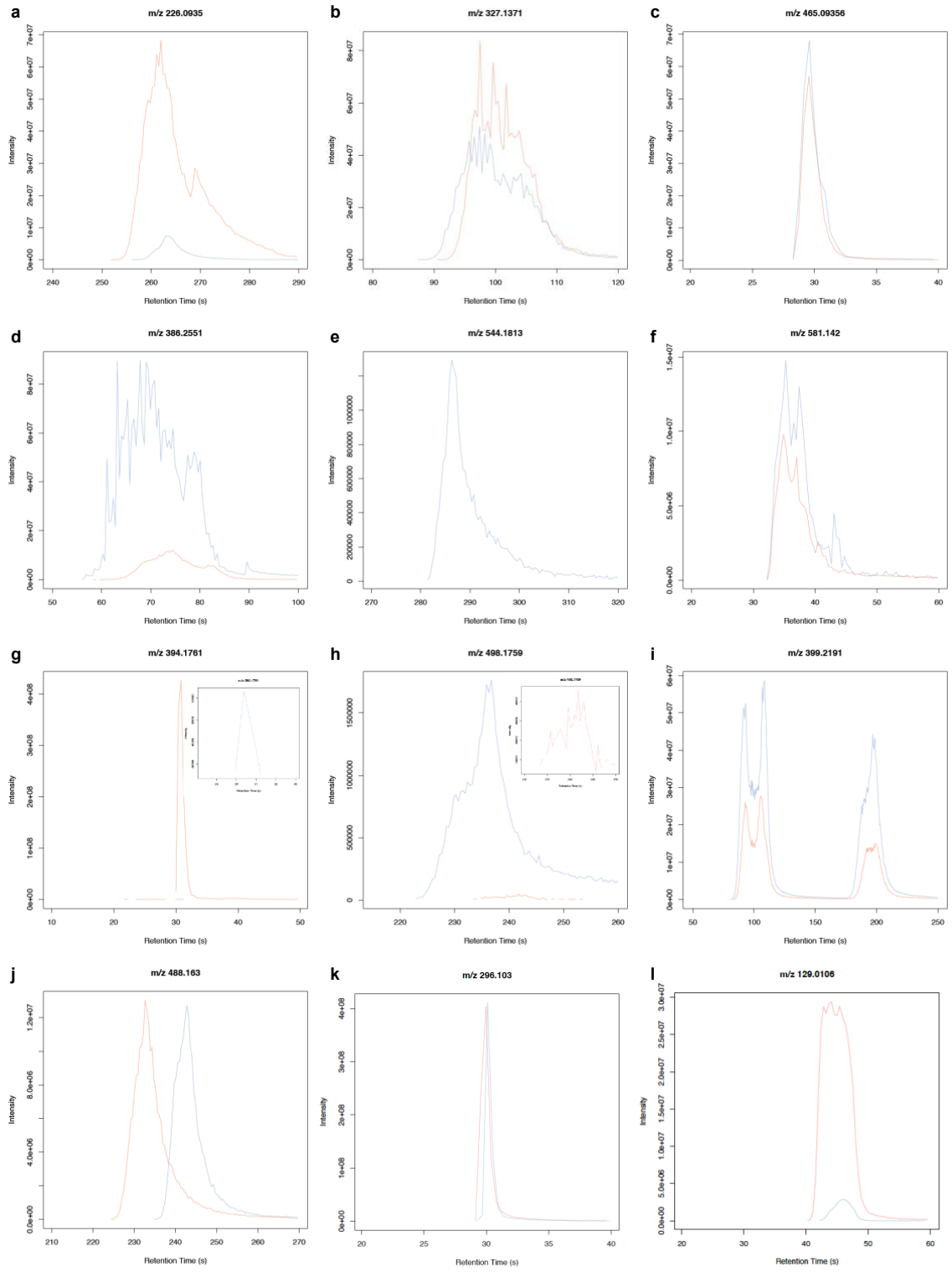


Figure D.3 Extracted ion chromatograms of parent xenobiotic peaks.
Extracted ion chromatograms of the $[M+H]^+$ ion form of **a** acyclovir, **b** clozapine, **c** sorafenib, **d** buspirone, **e** doxorubicin, **f** lapatinib, **g** erlotinib, **h** idarubicin, **i** sunitinib, **j** dasatinib, and **k** mebendazole, as measured by HILIC positive UHPLC-MS, and the $[M-H]^-$ ion form of **l** fluorouracil, as measured by HILIC negative UHPLC-MS, of representative biological sample (red) and preparation of authentic chemical standards (blue). Inset plots (**g** and **h**), show plot zoomed in on shaded regions.

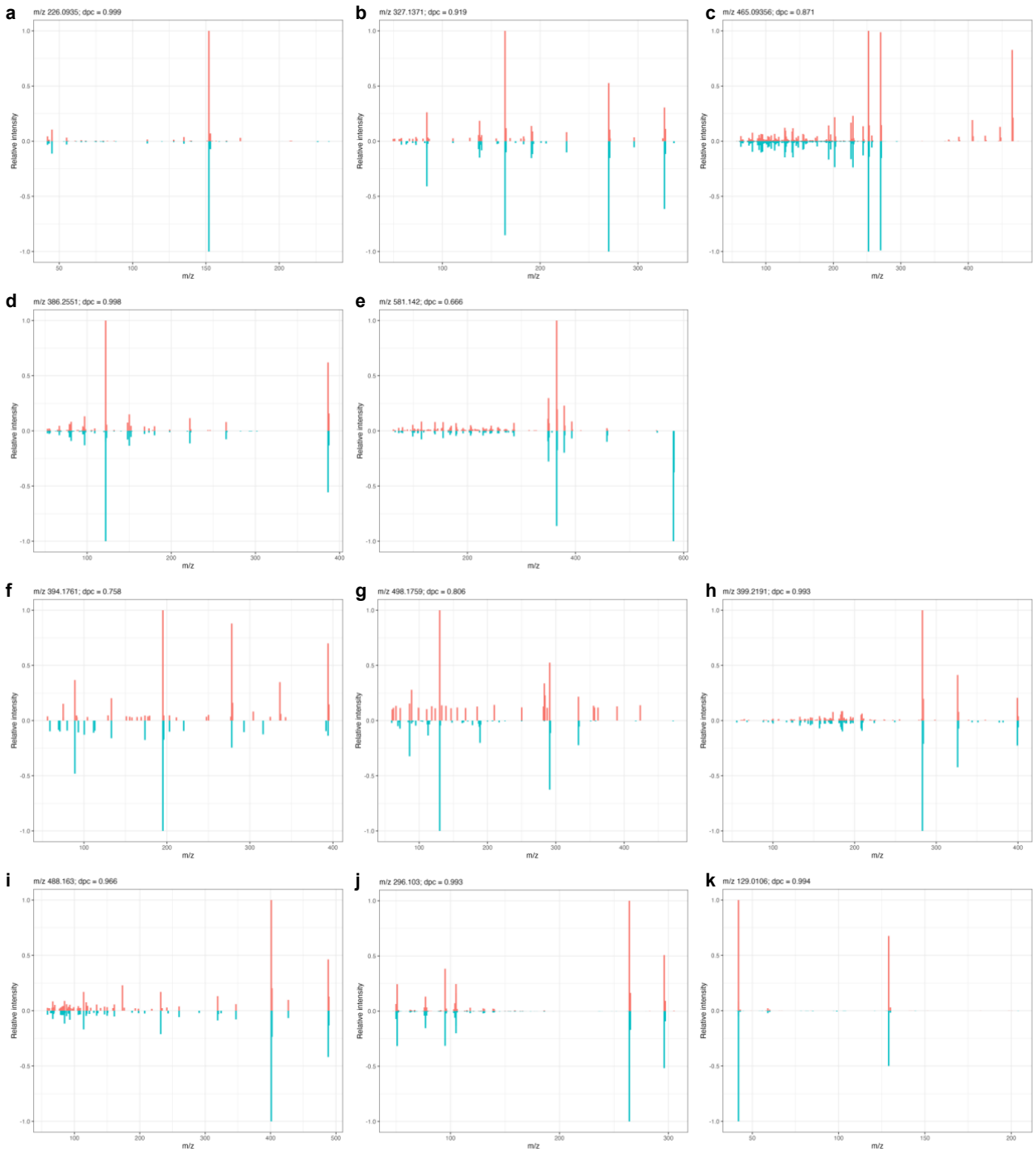


Figure D.4 MS/MS spectra of parent xenobiotics.
MS/MS spectra measured by higher-collision energy dissociation-based fragmentation of the $[M+H]^+$ ion form (HILIC positive UHPLC-MS/MS) of **a** acyclovir, **b** clozapine, **c** sorafenib, **d** buspirone, **e** lapatinib, **f** erlotinib, **g** idarubicin, **h** sunitinib, **i** dasatinib and **j** mebendazole, and of the $[M-H]^-$ ion form (HILIC negative UHPLC-MS/MS) of **k** fluorouracil. Mirror plots show spectra measured by analysis of representative biological samples (top, red) and authentic chemical standards (bottom, blue). Dot product cosine (dpc) scores, reported in the title of each plot, were >0.6 in all cases, indicating a good match between spectra.

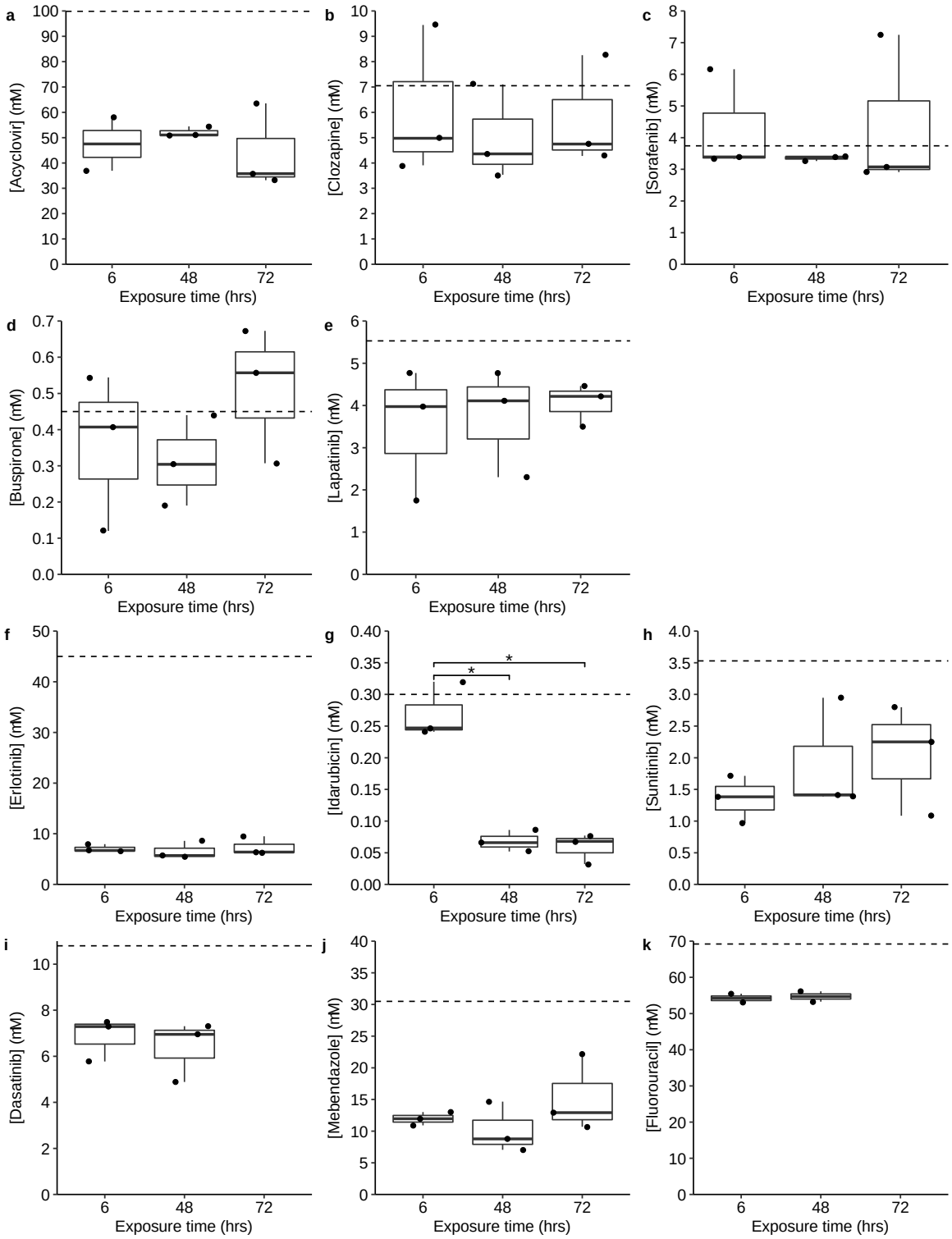


Figure D.5 Quantitation of eleven parent xenobiotics in stability control samples. Boxplots displaying the concentrations of the **a** acyclovir, **b** clozapine, **c** sorafenib, **d** buspirone, **e** lapatinib, **f** erlotinib, **g** idarubicin, **h** sunitinib, **i** dasatinib, **j** mebendazole, and **k** fluorouracil in samples composed of culture medium, absent of cardiac microtissues, incubated for 6-, 48- and 72-hours following addition of the xenobiotics at the nominal high concentrations. Concentrations were calculated by external calibration. The dashed lines represent the nominal concentrations. Individual points show data from N = 3 replicates. * p <0.05 significant difference between measured concentrations at each time point (two-sided t-test with Holm multiple test correction).

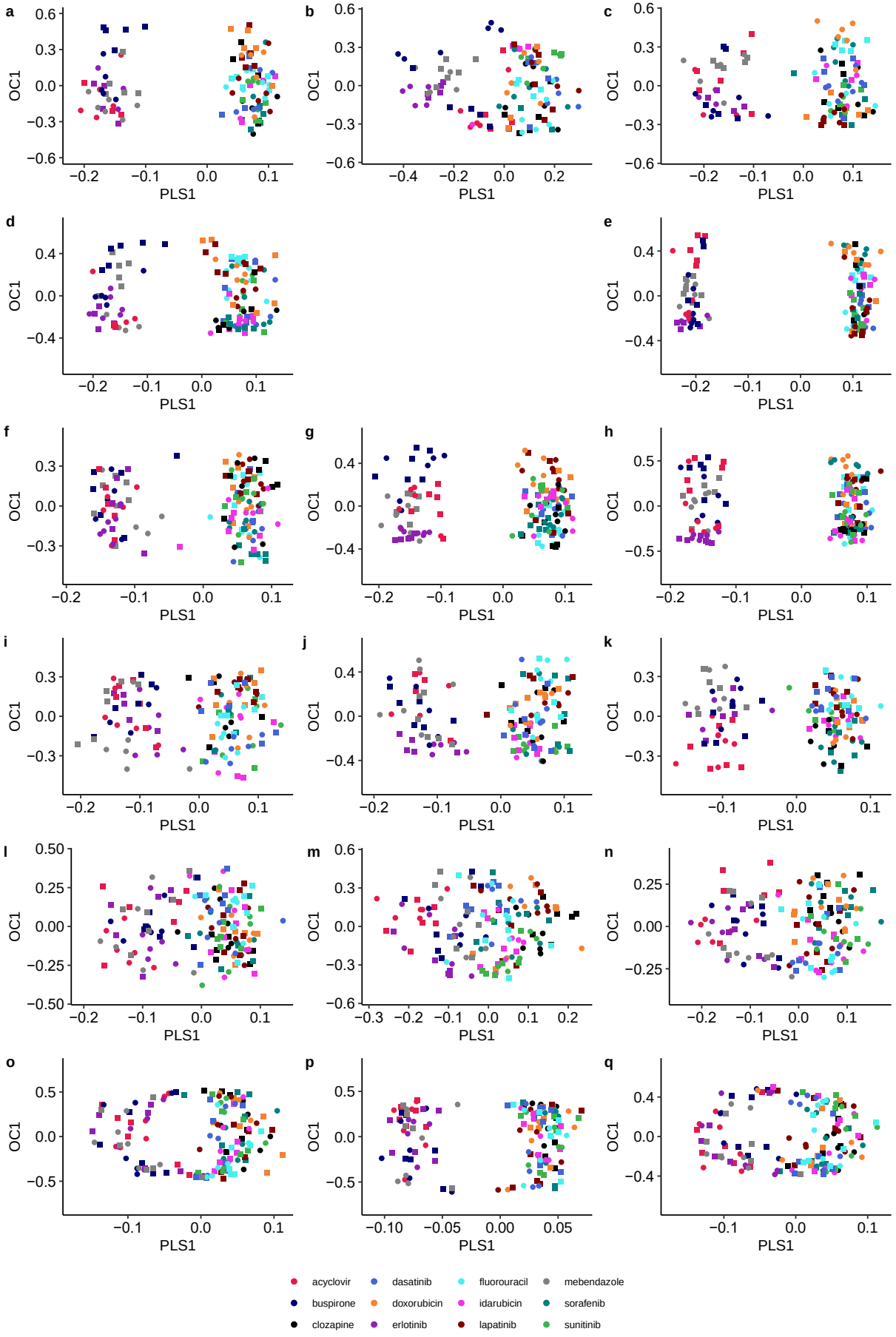


Figure D.6 OPLS-DA models predictive of structural cardiotoxicity.

OPLS-DA scores plots showing the predictive and first orthogonal latent variables of a model which discriminates between the responses of cardiac microtissues induced by **a**, **d**, **f,** **i**, **l**, **o** 6- , **b**, **g**, **j**, **m**, **p** 48-, and **c**, **e**, **h**, **k**, **n**, **q** 72-hour exposure to structurally cardiotoxic xenobiotics compared with non-structurally cardiotoxic xenobiotics. Models were built from subsets of predictive features, determined according to VIP score (VIP ≥ 1) calculated in preliminary models, measured by **a-c** polar positive, **d-e** polar negative, **f-h** lipids positive, and **i-k** lipids negative DIMS-based analysis of intracellular extracts, and **l-n** HILIC positive and **o-q** HILIC negative UHPLC-MS analysis of spent culture media of cardiac microtissues. Shaded regions represent the 95% confidence intervals for structurally cardiotoxic (red) and non-structurally cardiotoxic (blue) xenobiotics. Responses to both low (■) and high (●) concentrations of the twelve xenobiotics were used for model training. Intensity measurements were corrected for batch and baseline temporal effects by normalisation against the median intensities in batch and time matched DMSO controls prior to analysis.

REFERENCES

1. PhRMA. Biopharmaceutical R&D: The Process Behind New Medicines. 2015 20/08/2015.
2. Cook D, Brown D, Alexander R, March R, Morgan P, Satterthwaite G, et al. Lessons learned from the fate of AstraZeneca's drug pipeline: a five-dimensional framework. Nature reviews Drug discovery. 2014;13(6):419-31.
3. EUPATI. Making a Medicine https://toolbox.eupati.eu/resources [
4. Weaver RJ, Valentin J-P. Today's Challenges to De-Risk and Predict Drug Safety in Human "Mind-the-Gap". Toxicological Sciences. 2019;167(2):307-21.
5. Bowes J, Brown AJ, Hamon J, Jarolimek W, Sridhar A, Waldron G, et al. Reducing safety-related drug attrition: the use of in vitro pharmacological profiling. Nature reviews Drug discovery. 2012;11(12):909-22.
6. Paul SM, Mytelka DS, Dunwiddie CT, Persinger CC, Munos BH, Lindborg SR, et al. How to improve R&D productivity: the pharmaceutical industry's grand challenge. Nature reviews Drug discovery. 2010;9(3):203-14.
7. Waring MJ, Arrowsmith J, Leach AR, Leeson PD, Mandrell S, Owen RM, et al. An analysis of the attrition of drug candidates from four major pharmaceutical companies. Nature reviews Drug discovery. 2015;14(7):475-86.
8. U.S. Food and Drug Administration. S7A Safety Pharmacology Studies for Human Pharmaceuticals. 2001.
9. Olson H, Betton G, Robinson D, Thomas K, Monro A, Kolaja G, et al. Concordance of the toxicity of pharmaceuticals in humans and in animals. Regul Toxicol Pharmacol. 2000;32(1):56-67.
10. Beilmann M, Boonen H, Czich A, Dear G, Hewitt P, Mow T, et al. Optimizing drug discovery by Investigative Toxicology: Current and future trends. Altex. 2019;36(2):289-313.
11. Sewell F, Edwards J, Prior H, Robinson S. Opportunities to Apply the 3Rs in Safety Assessment Programs. ILAR Journal. 2016;57(2):234-45.
12. Morgan P, Brown DG, Lennard S, Anderton MJ, Barrett JC, Eriksson U, et al. Impact of a five-dimensional framework on R&D productivity at AstraZeneca. Nature reviews Drug discovery. 2018;17(3):167-81.
13. Pollard CE, Abi Gerges N, Bridgland-Taylor MH, Easter A, Hammond TG, Valentin JP. An introduction to QT interval prolongation and non-clinical approaches to assessing and reducing risk. British journal of pharmacology. 2010;159(1):12-21.
14. Li X, Zhang R, Zhao B, Lossin C, Cao Z. Cardiotoxicity screening: a review of rapid-throughput in vitro approaches. Arch Toxicol. 2016;90(8):1803-16.
15. Wallis R, Benson C, Darpo B, Gintant G, Kanda Y, Prasad K, et al. CiPA challenges and opportunities from a non-clinical, clinical and regulatory perspectives. An overview of the safety pharmacology scientific discussion. Journal of Pharmacological and Toxicological Methods. 2018;93:15-25.
16. Gintant G, Sager PT, Stockbridge N. Evolution of strategies to improve preclinical cardiac safety testing. Nature reviews Drug discovery. 2016;15(7):457-71.
17. Wadman M. FDA no longer has to require animal testing for new drugs. Science. 2023;379(6628):127-8.
18. Laverty H, Benson C, Cartwright E, Cross M, Garland C, Hammond T, et al. How can we improve our understanding of cardiovascular safety liabilities to develop safer medicines? British journal of pharmacology. 2011;163(4):675-93.
19. Onakpoya IJ, Heneghan CJ, Aronson JK. Post-marketing withdrawal of 462 medicinal products because of adverse drug reactions: a systematic review of the world literature. BMC Med. 2016;14(1):10.

20. Pointon A, Harmer AR, Dale IL, Abi-Gerges N, Bowes J, Pollard C, et al. Assessment of cardiomyocyte contraction in human-induced pluripotent stem cell-derived cardiomyocytes. Toxicol Sci. 2015;144(2):227-37.
21. Pointon A, Pilling J, Dorval T, Wang Y, Archer C, Pollard C. From the Cover: High-Throughput Imaging of Cardiac Microtissues for the Assessment of Cardiac Contraction during Drug Discovery. Toxicol Sci. 2017;155(2):444-57.
22. Harmer AR, Abi-Gerges N, Morton MJ, Pullen GF, Valentin JP, Pollard CE. Validation of an in vitro contractility assay using canine ventricular myocytes. Toxicol Appl Pharmacol. 2012;260(2):162-72.
23. Morton MJ, Armstrong D, Abi Gerges N, Bridgland-Taylor M, Pollard CE, Bowes J, et al. Predicting changes in cardiac myocyte contractility during early drug discovery with in vitro assays. Toxicology and Applied Pharmacology. 2014;279(2):87-94.
24. Cross MJ, Berridge BR, Clements PJ, Cove-Smith L, Force TL, Hoffmann P, et al. Physiological, pharmacological and toxicological considerations of drug-induced structural cardiac injury. British journal of pharmacology. 2015;172(4):957-74.
25. Force T, Kolaja KL. Cardiotoxicity of kinase inhibitors: the prediction and translation of preclinical models to clinical outcomes. Nature reviews Drug discovery. 2011;10(2):111-26.
26. Ravenscroft S, Bauch C, Hinton L, Walker PJDDW. Microtissues for in vitro toxicity assessment: cost effective and in vivo relevant toxicology tools. Drug Discov World. 2016.
27. Ravenscroft SM, Pointon A, Williams AW, Cross MJ, Sidaway JE. Cardiac Non-myocyte Cells Show Enhanced Pharmacological Function Suggestive of Contractile Maturity in Stem Cell Derived Cardiomyocyte Microtissues. Toxicol Sci. 2016;152(1):99-112.
28. Gunter J, Wolint P, Bopp A, Steiger J, Cambria E, Hoerstrup SP, et al. Microtissues in Cardiovascular Medicine: Regenerative Potential Based on a 3D Microenvironment. Stem Cells Int. 2016;2016:9098523.
29. Ishida S. Research and Development of Microphysiological Systems in Japan Supported by the AMED-MPS Project. Frontiers in Toxicology. 2021;3.
30. Doherty KR, Talbert DR, Trusk PB, Moran DM, Shell SA, Bacus S. Structural and functional screening in human induced-pluripotent stem cell-derived cardiomyocytes accurately identifies cardiotoxicity of multiple drug types. Toxicol Appl Pharmacol. 2015;285(1):51-60.
31. Doherty KR, Wappel RL, Talbert DR, Trusk PB, Moran DM, Kramer JW, et al. Multi-parameter in vitro toxicity testing of crizotinib, sunitinib, erlotinib, and nilotinib in human cardiomyocytes. Toxicol Appl Pharmacol. 2013;272(1):245-55.
32. Pointon A, Abi-Gerges N, Cross MJ, Sidaway JE. Phenotypic profiling of structural cardiotoxins in vitro reveals dependency on multiple mechanisms of toxicity. Toxicol Sci. 2013;132(2):317-26.
33. Truitt R, Mu A, Corbin EA, Vite A, Brandimarto J, Ky B, et al. Increased Afterload Augments Sunitinib-Induced Cardiotoxicity in an Engineered Cardiac Microtissue Model. JACC Basic Transl Sci. 2018;3(2):265-76.
34. Gintant G, Burridge P, Gepstein L, Harding S, Herron T, Hong C, et al. Use of Human Induced Pluripotent Stem Cell-Derived Cardiomyocytes in Preclinical Cancer Drug Cardiotoxicity Testing: A Scientific Statement From the American Heart Association. Circ Res. 2019;125(10):e75-e92.
35. Giacomelli E, Bellin M, Sala L, van Meer BJ, Tertoolen LG, Orlova VV, et al. Three-dimensional cardiac microtissues composed of cardiomyocytes and endothelial cells co-differentiated from human pluripotent stem cells. Development. 2017;144(6):1008-17.
36. Archer CR, Sargeant R, Basak J, Pilling J, Barnes JR, Pointon A. Characterization and Validation of a Human 3D Cardiac Microtissue for the Assessment of Changes in Cardiac Pathology. Sci Rep. 2018;8(1):10160.
37. Brutsaert DL. Cardiac Endothelial-Myocardial Signaling: Its Role in Cardiac Growth, Contractile Performance, and Rhythmicity. Physiological Reviews. 2003;83(1):59-115.

38. Grosberg A, Alford PW, Mccain ML, Parker KK. Ensembles of engineered cardiac tissues for physiological and pharmacological study: Heart on a chip. Lab on a Chip. 2011;11(24):4165.
39. Michaud V, Frappier M, Dumas MC, Turgeon J. Metabolic activity and mRNA levels of human cardiac CYP450s involved in drug metabolism. PLoS One. 2010;5(12):e15666.
40. Evangelista EA, Kaspera R, Mokadam NA, Jones JP, 3rd, Totah RA. Activity, inhibition, and induction of cytochrome P450 2J2 in adult human primary cardiomyocytes. Drug Metab Dispos. 2013;41(12):2087-94.
41. Oleaga C, Riu A, Rothemund S, Lavado A, Mcaleer CW, Long CJ, et al. Investigation of the effect of hepatic metabolism on off-target cardiotoxicity in a multi-organ human-on-a-chip system. Biomaterials. 2018;182:176-90.
42. Dame K, Ribeiro AJ. Microengineered systems with iPSC-derived cardiac and hepatic cells to evaluate drug adverse effects. Experimental Biology and Medicine. 2021;246(3):317-31.
43. Picollet-D'Hahan N, Zuchowska A, Lemeunier I, Le Gac S. Multiorgan-on-a-Chip: A Systemic Approach To Model and Decipher Inter-Organ Communication. Trends in Biotechnology. 2021;39(8):788-810.
44. O'Brien PJ. Cardiac troponin is the most effective translational safety biomarker for myocardial injury in cardiotoxicity. Toxicology. 2008;245(3):206-18.
45. Reagan WJ. Troponin as a Biomarker of Cardiac Toxicity:Past, Present, and Future. Toxicologic Pathology. 2010;38(7):1134-7.
46. Adamcová M, Šimůnek T, Kaiserová H, Popelová O, Štěrba M, Potáčová A, et al. In vitro and in vivo examination of cardiac troponins as biochemical markers of drug-induced cardiotoxicity. Toxicology. 2007;237(1):218-28.
47. Mamoshina P, Rodriguez B, Bueno-Orovio A. Toward a broader view of mechanisms of drug cardiotoxicity. Cell Reports Medicine. 2021;2(3):100216.
48. Ankley GT, Bennett RS, Erickson RJ, Hoff DJ, Hornung MW, Johnson RD, et al. Adverse outcome pathways: A conceptual framework to support ecotoxicology research and risk assessment. Environmental toxicology and chemistry. 2010;29(3):730-41.
49. Vinken M, Knapen D, Vergauwen L, Hengstler JG, Angrish M, Whelan M. Adverse outcome pathways: a concise introduction for toxicologists. Arch Toxicol. 2017;91(11):3697-707.
50. Sewell F, Gellatly N, Beaumont M, Burden N, Currie R, de Haan L, et al. The future trajectory of adverse outcome pathways: a commentary. Arch Toxicol. 2018;92(4):1657-61.
51. Burden N, Sewell F, Andersen ME, Boobis A, Chipman JK, Cronin MT, et al. Adverse Outcome Pathways can drive non-animal approaches for safety assessment. J Appl Toxicol. 2015;35(9):971-5.
52. Bouhifd M, Hartung T, Hogberg HT, Kleensang A, Zhao L. Review: toxicometabolomics. J Appl Toxicol. 2013;33(12):1365-83.
53. Ramirez T, Daneshian M, Kamp H, Bois FY, Clench MR, Coen M, et al. Metabolomics in toxicology and preclinical research. Altex. 2013;30(2):209-25.
54. Alexander-Dann B, Pruteanu LL, Oerton E, Sharma N, Berindan-Neagoe I, Módos D, et al. Developments in toxicogenomics: understanding and predicting compound-induced toxicity from gene expression data. Molecular Omics. 2018;14(4):218-36.
55. Campos B, Colbourne JK. How omics technologies can enhance chemical safety regulation: perspectives from academia, government, and industry: The Perspectives column is a regular series designed to discuss and evaluate potentially competing viewpoints and research findings on current environmental issues. Environmental toxicology and chemistry. 2018;37(5):1252-9.
56. Davis JM, Ekman DR, Skelton DM, Lalone CA, Ankley GT, Cavallin JE, et al. Metabolomics for informing adverse outcome pathways: Androgen receptor activation and the pharmaceutical spironolactone. 2017;184:103-15.

57. Brockmeier EK, Hodges G, Hutchinson TH, Butler E, Hecker M, Tollefsen KE, et al. The Role of Omics in the Application of Adverse Outcome Pathways for Chemical Risk Assessment. Toxicol Sci. 2017;158(2):252-62.
58. Nguyen N, Jennen D, Kleinjans J. Omics technologies to understand drug toxicity mechanisms. Drug Discovery Today. 2022;27(11):103348.
59. García- Cañaveras JC, Castell JV, Donato MT, Lahoz A. A metabolomics cell-based approach for anticipating and investigating drug-induced liver injury. Scientific Reports. 2016;6(1):27239.
60. Selevsek N, Caiment F, Nudischer R, Gmuender H, Agarkova I, Atkinson FL, et al. Network integration and modelling of dynamic drug responses at multi-omics levels. Communications Biology. 2020;3(1).
61. Palmer JA, Smith AM, Gryshkova V, Donley ELR, Valentin J-P, Burrier RE. A Targeted Metabolomics-Based Assay Using Human Induced Pluripotent Stem Cell-Derived Cardiomyocytes Identifies Structural and Functional Cardiotoxicity Potential. Toxicological Sciences. 2020;174(2):218-40.
62. Van Hasselt JGC, Rahman R, Hansen J, Stern A, Shim JV, Xiong Y, et al. Transcriptomic profiling of human cardiac cells predicts protein kinase inhibitor-associated cardiotoxicity. Nature Communications. 2020;11(1).
63. Verheijen M, Schrooders Y, Gmuender H, Nudischer R, Clayton O, Hynes J, et al. Bringing in vitro analysis closer to in vivo: Studying doxorubicin toxicity and associated mechanisms in 3D human microtissues with PBPK-based dose modelling. Toxicol Lett. 2018;294:184-92.
64. Araújo AM, Carvalho F, Guedes De Pinho P, Carvalho M. Toxicometabolomics: Small Molecules to Answer Big Toxicological Questions. Metabolites. 2021;11(10):692.
65. Dettmer K, Aronov PA, Hammock BD. Mass spectrometry-based metabolomics. Mass Spectrometry Reviews. 2007;26(1):51-78.
66. Roux A, Lison D, Junot C, Heilier JF. Applications of liquid chromatography coupled to mass spectrometry-based metabolomics in clinical chemistry and toxicology: A review. Clinical biochemistry. 2011;44(1):119-35.
67. Dunn WB, Broadhurst D, Begley P, Zelena E, Francis-McIntyre S, Anderson N, et al. Procedures for large-scale metabolic profiling of serum and plasma using gas chromatography and liquid chromatography coupled to mass spectrometry. Nature Protocols. 2011;6(7):1060-83.
68. Alonso A, Marsal S, Julia A. Analytical methods in untargeted metabolomics: state of the art in 2015. Frontiers in bioengineering and biotechnology. 2015;3:23.
69. Viant MR, Ebbels TMD, Beger RD, Ekman DR, Epps DJT, Kamp H, et al. Use cases, best practice and reporting standards for metabolomics in regulatory toxicology. Nat Commun. 2019;10(1):3041.
70. Wang P, Shehu AI, Ma X. The Opportunities of Metabolomics in Drug Safety Evaluation. Current Pharmacology Reports. 2017;3(1):10-5.
71. Alarcon-Barrera JC, Kostidis S, Ondo-Mendez A, Giera M. Recent advances in metabolomics analysis for early drug development. Drug Discovery Today. 2022;27(6):1763-73.
72. Hartung T, Daston G. Are in vitro tests suitable for regulatory use? Toxicol Sci. 2009;111(2):233-7.
73. Li AP. Accurate prediction of human drug toxicity: a major challenge in drug development. Chem Biol Interact. 2004;150(1):3-7.
74. Ramirez T, Strigun A, Verlohner A, Huener HA, Peter E, Herold M, et al. Prediction of liver toxicity and mode of action using metabolomics in vitro in HepG2 cells. Arch Toxicol. 2018;92(2):893-906.
75. Cuykx M, Rodrigues RM, Laukens K, Vanhaecke T, Covaci A. In vitro assessment of hepatotoxicity by metabolomics: a review. Archives of Toxicology. 2018;92(10):3007-29.

76. Southam AD, Haglington LD, Najdekr L, Jankevics A, Weber RJM, Dunn WB. Assessment of human plasma and urine sample preparation for reproducible and high-throughput UHPLC-MS clinical metabolic phenotyping. The Analyst. 2020.
77. Southam AD, Pursell H, Frigerio G, Jankevics A, Weber RJM, Dunn WB. Characterization of Monophasic Solvent-Based Tissue Extractions for the Detection of Polar Metabolites and Lipids Applying Ultrahigh-Performance Liquid Chromatography–Mass Spectrometry Clinical Metabolic Phenotyping Assays. Journal of Proteome Research. 2020.
78. Smith L, Villaret-Cazadamont J, Claus SP, Canlet C, Guillou H, Cabaton NJ, et al. Important Considerations for Sample Collection in Metabolomics Studies with a Special Focus on Applications to Liver Functions. Metabolites. 2020;10(3):104.
79. Bordag N, Janakiraman V, Nachtigall J, Gonzalez Maldonado S, Bethan B, Laine JP, et al. Fast Filtration of Bacterial or Mammalian Suspension Cell Cultures for Optimal Metabolomics Results. PLoS One. 2016;11(7):e0159389.
80. Dettmer K, Nurnberger N, Kaspar H, Gruber MA, Almstetter MF, Oefner PJ. Metabolite extraction from adherently growing mammalian cells for metabolomics studies: optimization of harvesting and extraction protocols. Anal Bioanal Chem. 2011;399(3):1127-39.
81. Sellick CA, Hansen R, Stephens GM, Goodacre R, Dickson AJ. Metabolite extraction from suspension-cultured mammalian cells for global metabolite profiling. Nat Protoc. 2011;6(8):1241-9.
82. Kvitvang HFN, Bruheim P. Fast filtration sampling protocol for mammalian suspension cells tailored for phosphometabolome profiling by capillary ion chromatography – tandem mass spectrometry. Journal of Chromatography B. 2015;998-999:45-9.
83. Goracci L, Valeri A, Sciabola S, Aleo MD, Moritz W, Lichtenberg J, et al. A Novel Lipidomics-Based Approach to Evaluating the Risk of Clinical Hepatotoxicity Potential of Drugs in 3D Human Microtissues. Chemical Research in Toxicology. 2020;33(1):258-70.
84. Volmer M, Northoff S, Scholz S, Thüte T, Büntemeyer H, Noll T. Fast filtration for metabolome sampling of suspended animal cells. Biotechnology Letters. 2011;33(3):495-502.
85. Hernandez Bort JA, Shanmukam V, Pabst M, Windwarder M, Neumann L, Alchalabi A, et al. Reduced quenching and extraction time for mammalian cells using filtration and syringe extraction. J Biotechnol. 2014;182-183:97-103.
86. Wu H, Southam AD, Hines A, Viant MR. High-throughput tissue extraction protocol for NMR- and MS-based metabolomics. Anal Biochem. 2008;372(2):204-12.
87. Malinowska JM, Palosaari T, Sund J, Carpi D, Bouhifd M, Weber RJM, et al. Integrating in vitro metabolomics with a 96-well high-throughput screening platform. Metabolomics. 2022;18(1).
88. Ren J-L, Zhang A-H, Kong L, Wang X-J. Advances in mass spectrometry-based metabolomics for investigation of metabolites. RSC Advances. 2018;8(40):22335-50.
89. Tugizimana F, Steenkamp PA, Piater LA, Dubery IA. Mass spectrometry in untargeted liquid chromatography/mass spectrometry metabolomics: Electrospray ionisation parameters and global coverage of the metabolome. Rapid Communications in Mass Spectrometry. 2018;32(2):121-32.
90. Milne SB, Mathews TP, Myers DS, Ivanova PT, Brown HA. Sum of the Parts: Mass Spectrometry-Based Metabolomics. Biochemistry. 2013;52(22):3829-40.
91. Banerjee S, Mazumdar S. Electrospray Ionization Mass Spectrometry: A Technique to Access the Information beyond the Molecular Weight of the Analyte. International Journal of Analytical Chemistry. 2012;2012:282574.
92. Konermann L, Ahadi E, Rodriguez AD, Vahidi S. Unraveling the Mechanism of Electrospray Ionization. Analytical Chemistry. 2013;85(1):2-9.
93. Karas M, Bahr U, Dülcks T. Nano-electrospray ionization mass spectrometry: addressing analytical problems beyond routine. Fresenius' Journal of Analytical Chemistry. 2000;366(6):669-76.

94. Hop CECA, Chen Y, Yu LJ. Uniformity of ionization response of structurally diverse analytes using a chip-based nanoelectrospray ionization source. Rapid Communications in Mass Spectrometry. 2005;19(21):3139-42.
95. Nash WJ, Dunn WB. From mass to metabolite in human untargeted metabolomics: Recent advances in annotation of metabolites applying liquid chromatography-mass spectrometry data. TrAC Trends in Analytical Chemistry. 2019;120.
96. Brown M, Dunn WB, Dobson P, Patel Y, Winder CL, Francis-Mcintyre S, et al. Mass spectrometry tools and metabolite-specific databases for molecular identification in metabolomics. The Analyst. 2009;134(7):1322.
97. Makarov A. Electrostatic Axially Harmonic Orbital Trapping: A High-Performance Technique of Mass Analysis. Analytical Chemistry. 2000;72(6):1156-62.
98. Eliuk S, Makarov A. Evolution of Orbitrap Mass Spectrometry Instrumentation. Annual Review of Analytical Chemistry. 2015;8(1):61-80.
99. Zubarev RA, Makarov A. Orbitrap Mass Spectrometry. Analytical Chemistry. 2013;85(11):5288-96.
100. Makarov A, Denisov E, Lange O, Horning S. Dynamic range of mass accuracy in LTQ orbitrap hybrid mass spectrometer. Journal of the American Society for Mass Spectrometry. 2006;17(7):977-82.
101. Hecht ES, Scigelova M, Eliuk S, Makarov A. Fundamentals and Advances of Orbitrap Mass Spectrometry. Encyclopedia of Analytical Chemistry. 2019:1-40.
102. Kelstrup CD, Jersie-Christensen RR, Batth TS, Arrey TN, Kuehn A, Kellmann M, et al. Rapid and Deep Proteomes by Faster Sequencing on a Benchtop Quadrupole Ultra-High-Field Orbitrap Mass Spectrometer. Journal of Proteome Research. 2014;13(12):6187-95.
103. Chawla G, Ranjan C. Principle, Instrumentation, and Applications of UPLC: A Novel Technique of Liquid Chromatography. Open Chemistry Journal. 2016;3(1):1-16.
104. Verheijen M, Sarkans U, Wolski W, Jennen D, Caiment F, Kleinjans J, et al. Multi-omics HeCaToS dataset of repeated dose toxicity for cardiotoxic & hepatotoxic compounds. Scientific Data. 2022;9(1).
105. Jankevics A, Jenkins A, Dunn WB, Najdekr L. An improved strategy for analysis of lipid molecules utilising a reversed phase C30 UHPLC column and scheduled MS/MS acquisition. Talanta. 2021;229:122262.
106. Schultz GA, Corso TN, Prosser SJ, Zhang S. A Fully Integrated Monolithic Microchip Electrospray Device for Mass Spectrometry. Analytical Chemistry. 2000;72(17):4058-63.
107. Southam AD, Payne TG, Cooper HJ, Arvanitis TN, Viant MR. Dynamic Range and Mass Accuracy of Wide-Scan Direct Infusion Nanoelectrospray Fourier Transform Ion Cyclotron Resonance Mass Spectrometry-Based Metabolomics Increased by the Spectral Stitching Method. Analytical Chemistry. 2007;79(12):4595-602.
108. Southam AD, Weber RJ, Engel J, Jones MR, Viant MR. A complete workflow for high-resolution spectral-stitching nanoelectrospray direct-infusion mass-spectrometry-based metabolomics and lipidomics. Nat Protoc. 2016;12(2):310-28.
109. Southam AD, Lange A, Al-Salhi R, Hill EM, Tyler CR, Viant MR. Distinguishing between the metabolome and xenobiotic exposome in environmental field samples analysed by direct-infusion mass spectrometry based metabolomics and lipidomics. Metabolomics. 2014;10(6):1050-8.
110. Schade S, Butler E, Gutsell S, Hodges G, Colbourne JK, Viant MR. Improved Algal Toxicity Test System for Robust Omics-Driven Mode-of-Action Discovery in Chlamydomonas reinhardtii. Metabolites. 2019;9(5):94.
111. Taylor NS, Weber RJM, Southam AD, Payne TG, Hrydziuszko O, Arvanitis TN, et al. A new approach to toxicity testing in Daphnia magna: application of high throughput FT-ICR mass spectrometry metabolomics. Metabolomics. 2009;5(1):44-58.
112. Sarvin B, Lagziel S, Sarvin N, Mukha D, Kumar P, Aizenshtein E, et al. Fast and sensitive flow-injection mass spectrometry metabolomics by analyzing sample-specific ion distributions. Nature Communications. 2020;11(1).

113. Kang W-Y, Thompson PT, El-Amouri SS, Fan TWM, Lane AN, Higashi RM. Improved segmented-scan spectral stitching for stable isotope resolved metabolomics (SIRM) by ultra-high-resolution Fourier transform mass spectrometry. Analytica Chimica Acta. 2019;1080:104-15.
114. Sumner LW, Urbanczyk-Wochniak E, Broeckling CD. Metabolomics data analysis, visualization, and integration. Methods Mol Biol. 2007;406:409-36.
115. Smith CA, Want EJ, O'Maille G, Abagyan R, Siuzdak G. XCMS: processing mass spectrometry data for metabolite profiling using nonlinear peak alignment, matching, and identification. Anal Chem. 2006;78(3):779-87.
116. Weber RJMZ, J. DIMSpy: Python package for processing direct-infusion mass spectrometry-based metabolomics and lipidomics data. 2020.
117. Prince JT, Marcotte EM. Chromatographic Alignment of ESI-LC-MS Proteomics Data Sets by Ordered Bijective Interpolated Warping. Analytical Chemistry. 2006;78(17):6140-52.
118. Kirwan JA, Broadhurst DI, Davidson RL, Viant MR. Characterising and correcting batch variation in an automated direct infusion mass spectrometry (DIMS) metabolomics workflow. Analytical and Bioanalytical Chemistry. 2013;405(15):5147-57.
119. Benjamini Y, Hochberg Y. Controlling the False Discovery Rate: A Practical and Powerful Approach to Multiple Testing. Journal of the Royal Statistical Society: Series B (Methodological). 1995;57(1):289-300.
120. Sumner LW, Amberg A, Barrett D, Beale MH, Beger R, Daykin CA, et al. Proposed minimum reporting standards for chemical analysis. Metabolomics. 2007;3(3):211-21.
121. Di Guida R, Engel J, Allwood JW, Weber RJ, Jones MR, Sommer U, et al. Non-targeted UHPLC-MS metabolomic data processing methods: a comparative investigation of normalisation, missing value imputation, transformation and scaling. Metabolomics. 2016;12(5):93.
122. Worley B, Powers R. Multivariate Analysis in Metabolomics. Current Metabolomics. 2012;1(1):92-107.
123. Bylesjö M, Rantalainen M, Cloarec O, Nicholson JK, Holmes E, Trygg J. OPLS discriminant analysis: combining the strengths of PLS-DA and SIMCA classification. Journal of Chemometrics. 2006;20(8-10):341-51.
124. Kanehisa M, Furumichi M, Sato Y, Kawashima M, Ishiguro-Watanabe M. KEGG for taxonomy-based analysis of pathways and genomes. Nucleic Acids Research. 2023;51(D1):D587-D92.
125. Wieder C, Frainay C, Poupin N, Rodríguez-Mier P, Vinson F, Cooke J, et al. Pathway analysis in metabolomics: Recommendations for the use of over-representation analysis. PLOS Computational Biology. 2021;17(9):e1009105.
126. Malinowska JM, Viant MR. Confidence in metabolite identification dictates the applicability of metabolomics to regulatory toxicology. Current Opinion in Toxicology. 2019;16:32-8.
127. Mahieu NG, Patti GJ. Systems-Level Annotation of a Metabolomics Data Set Reduces 25 000 Features to Fewer than 1000 Unique Metabolites. Analytical Chemistry. 2017;89(19):10397-406.
128. Wishart DS, Guo A, Oler E, Wang F, Anjum A, Peters H, et al. HMDB 5.0: the Human Metabolome Database for 2022. Nucleic Acids Research. 2021;50(D1):D622-D31.
129. Sud M, Fahy E, Cotter D, Brown A, Dennis EA, Glass CK, et al. LMSD: LIPID MAPS structure database. Nucleic Acids Research. 2007;35(Database):D527-D32.
130. Dunn WB, Erban A, Weber RJM, Creek DJ, Brown M, Breitling R, et al. Mass appeal: metabolite identification in mass spectrometry-focused untargeted metabolomics. Metabolomics. 2012;9(S1):44-66.
131. Schymanski EL, Jeon J, Gulde R, Fenner K, Ruff M, Singer HP, et al. Identifying Small Molecules via High Resolution Mass Spectrometry: Communicating Confidence. Environmental Science & Technology. 2014;48(4):2097-8.

132. Brown M, Wedge DC, Goodacre R, Kell DB, Baker PN, Kenny LC, et al. Automated workflows for accurate mass-based putative metabolite identification in LC/MS-derived metabolomic datasets. Bioinformatics. 2011;27(8):1108-12.
133. Kachman M, Habra H, Duren W, Wigginton J, Sajjakulnukit P, Michailidis G, et al. Deep annotation of untargeted LC-MS metabolomics data with Binner. Bioinformatics. 2020;36(6):1801-6.
134. Senan O, Aguilar-Mogas A, Navarro M, Capellades J, Noon L, Burks D, et al. CliqueMS: a computational tool for annotating in-source metabolite ions from LC-MS untargeted metabolomics data based on a coelution similarity network. Bioinformatics. 2019;35(20):4089-97.
135. Kuhl C, Tautenhahn R, Böttcher C, Larson TR, Neumann S. CAMERA: An Integrated Strategy for Compound Spectra Extraction and Annotation of Liquid Chromatography/Mass Spectrometry Data Sets. Analytical Chemistry. 2012;84(1):283-9.
136. Domingo-Almenara X, Montenegro-Burke JR, Benton HP, Siuzdak G. Annotation: A Computational Solution for Streamlining Metabolomics Analysis. Analytical Chemistry. 2018;90(1):480-9.
137. MassBank of North America [Available from: http://mona.fiehnlab.ucdavis.edu/.
138. Guo J, Huan T. Comparison of Full-Scan, Data-Dependent, and Data-Independent Acquisition Modes in Liquid Chromatography-Mass Spectrometry Based Untargeted Metabolomics. Analytical Chemistry. 2020.
139. Wolf S, Schmidt S, Muller-Hannemann M, Neumann S. In silico fragmentation for computer assisted identification of metabolite mass spectra. BMC Bioinformatics. 2010;11(1):148.
140. Ruttkies C, Schymanski EL, Wolf S, Hollender J, Neumann S. MetFrag relaunched: incorporating strategies beyond in silico fragmentation. J Cheminform. 2016;8(1):3.
141. Lawson TN, Weber RJ, Jones MR, Chetwynd AJ, Rodri Guez-Blanco G, Di Guida R, et al. msPurity: Automated Evaluation of Precursor Ion Purity for Mass Spectrometry-Based Fragmentation in Metabolomics. Anal Chem. 2017;89(4):2432-9.
142. Wang Y, Feng R, Wang R, Yang F, Li P, Wan J-B. Enhanced MS/MS coverage for metabolite identification in LC-MS-based untargeted metabolomics by target-directed data dependent acquisition with time-staggered precursor ion list. Analytica Chimica Acta. 2017;992:67-75.
143. Mullard G, Allwood JW, Weber R, Brown M, Begley P, Hollywood KA, et al. A new strategy for MS/MS data acquisition applying multiple data dependent experiments on Orbitrap mass spectrometers in non-targeted metabolomic applications. Metabolomics. 2015;11(5):1068-80.
144. Viant MR, Kurland IJ, Jones MR, Dunn WB. How close are we to complete annotation of metabolomes? Current Opinion in Chemical Biology. 2017;36:64-9.
145. ICH. S3A: Toxicokinetics: A Guidance for Assessing Systemic Exposure in Toxicology Studies. 1995.
146. Dixit R, Riviere J, Krishnan K, Andersen ME. Toxicokinetics and physiologically based toxicokinetics in toxicology and risk assessment. J Toxicol Environ Health B Crit Rev. 2003;6(1):1-40.
147. Coecke S, Pelkonen O, Leite SB, Bernauer U, Bessems JG, Bois FY, et al. Toxicokinetics as a key to the integrated toxicity risk assessment based primarily on non-animal approaches. Toxicology in Vitro. 2013;27(5):1570-7.
148. Blaauboer BJ. Biokinetic Modeling andin Vitro–in VivoExtrapolations. Journal of Toxicology and Environmental Health, Part B. 2010;13(2-4):242-52.
149. Schadt S, Bister B, Chowdhury SK, Funk C, Hop C, Humphreys WG, et al. A Decade in the MIST: Learnings from Investigations of Drug Metabolites in Drug Development under the "Metabolites in Safety Testing" Regulatory Guidance. Drug Metab Dispos. 2018;46(6):865-78.

150. Wen B, Zhu M. Applications of mass spectrometry in drug metabolism: 50 years of progress. Drug Metab Rev. 2015;47(1):71-87.
151. Li F, Pang X, Krausz KW, Jiang C, Chen C, Cook JA, et al. Stable Isotope- and Mass Spectrometry-based Metabolomics as Tools in Drug Metabolism: A Study Expanding Tempol Pharmacology. Journal of Proteome Research. 2013;12(3):1369-76.
152. Takahashi M, Izumi Y, Iwahashi F, Nakayama Y, Iwakoshi M, Nakao M, et al. Highly Accurate Detection and Identification Methodology of Xenobiotic Metabolites Using Stable Isotope Labeling, Data Mining Techniques, and Time-Dependent Profiling Based on LC/HRMS/MS. Analytical Chemistry. 2018;90(15):9068-76.
153. Speed B, Bu HZ, Pool WF, Peng GW, Wu EY, Patyna S, et al. Pharmacokinetics, distribution, and metabolism of [14C]sunitinib in rats, monkeys, and humans. Drug Metab Dispos. 2012;40(3):539-55.
154. Loiodice S, Nogueira da Costa A, Atienzar F. Current trends in in silico, in vitro toxicology, and safety biomarkers in early drug development. Drug and Chemical Toxicology. 2019;42(2):113-21.
155. Kumar B, Prakash A, Ruhela RK, Medhi B. Potential of metabolomics in preclinical and clinical drug development. Pharmacol Rep. 2014;66(6):956-63.
156. Bedia C. Metabolomics in environmental toxicology: Applications and challenges. Trends in Environmental Analytical Chemistry. 2022;34:e00161.
157. Johnson CH, Ivanisevic J, Siuzdak G. Metabolomics: beyond biomarkers and towards mechanisms. Nat Rev Mol Cell Biol. 2016;17(7):451-9.
158. van Ravenzwaay B, Herold M, Kamp H, Kapp MD, Fabian E, Looser R, et al. Metabolomics: a tool for early detection of toxicological effects and an opportunity for biology based grouping of chemicals-from QSAR to QBAR. Mutat Res. 2012;746(2):144-50.
159. Vermeulen R, Schymanski Emma L, Barabási A-L, Miller Gary W. The exposome and health: Where chemistry meets biology. Science. 2020;367(6476):392-6.
160. Roggeman M, Belova L, Fernández SF, Kim D-H, Jeong Y, Poma G, et al. Comprehensive suspect screening for the identification of contaminants of emerging concern in urine of Flemish adolescents by liquid chromatography high-resolution mass spectrometry. Environmental Research. 2022;214:114105.
161. Barton HA, Pastoor TP, Baetcke K, Chambers JE, Diliberto J, Doerrer NG, et al. The acquisition and application of absorption, distribution, metabolism, and excretion (ADME) data in agricultural chemical safety assessments. Crit Rev Toxicol. 2006;36(1):9-35.
162. European Chemicals Agency. Guidance on information requirements and chemical safety assessment. Chaper R.7c: endpoint specific guidance. 2017.
163. EFSA PPP Panel (Panel on Plant Protection Products and their Residues). Guidance on the establishment of the residue definition for dietary risk assessment. EFSA Journal. 2016;14(12):e04549.
164. Nyman A-M, Schirmer K, Ashauer R. Importance of Toxicokinetics for Interspecies Variation in Sensitivity to Chemicals. 2014;48(10):5946-54.
165. OECD. Test No. 417: Toxicokinetics2010.
166. U.S. Food and Drug Administration. Guidance for industry: Safety Testing of Drug Metabolites. 2020.
167. Baduel C, Lai FY, van Nuijs ALN, Covaci A. Suspect and Nontargeted Strategies to Investigate in Vitro Human Biotransformation Products of Emerging Environmental Contaminants: The Benzotriazoles. Environmental Science & Technology. 2019;53(17):10462-9.
168. Zhou ZM, Wang YK, Yan DM, Fang JH, Xiao XR, Zhang T, et al. Metabolic pro fi ling of tyrosine kinase inhibitor nintedanib using metabolomics. J Pharm Biomed Anal. 2020;180:113045.
169. Flasch M, Bueschl C, Del Favero G, Adam G, Schuhmacher R, Marko D, et al. Elucidation of xenoestrogen metabolism by non-targeted, stable isotope-assisted mass spectrometry in breast cancer cells. Environ Int. 2022;158:106940.

170. Ribbenstedt A, Posselt M, Benskin JP. Toxicometabolomics and Biotransformation Product Elucidation in Single Zebrafish Embryos Exposed to Carbamazepine from Environmentally-Relevant to Morphologically Altering Doses. Chemical Research in Toxicology. 2022;35(3):431-9.
171. Hemmer S, Wagmann L, Pulver B, Westphal F, Meyer MR. In Vitro and In Vivo Toxicometabolomics of the Synthetic Cathinone PCYP Studied by Means of LC-HRMS/MS. Metabolites. 2022;12(12):1209.
172. Magny R, Mégarbane B, Guillaud P, Chevillard L, Auzeil N, Thiebot P, et al. Life-Threatening Cardiogenic Shock Related to Venlafaxine Poisoning—A Case Report with Metabolomic Approach. Metabolites. 2023;13(3):353.
173. Thevis M, Piper T, Thomas A. Recent advances in identifying and utilizing metabolites of selected doping agents in human sports drug testing. Journal of Pharmaceutical and Biomedical Analysis. 2021;205:114312.
174. Caldwell J, Gardner I, Swales N. An Introduction to Drug Disposition: The Basic Principles of Absorption, Distribution, Metabolism, and Excretion. Toxicologic Pathology. 1995;23(2):102-14.
175. European Chemicals Agency. Read-Across Assessment Framework (RAAF). 2017.
176. Adeyemi O, Parker N, Pointon A, Rolf M. A pharmacological characterization of electrocardiogram PR and QRS intervals in conscious telemetered rats. Journal of Pharmacological and Toxicological Methods. 2020;102:106679.
177. Chambers MC, Maclean B, Burke R, Amodei D, Ruderman DL, Neumann S, et al. A cross-platform toolkit for mass spectrometry and proteomics. Nat Biotechnol. 2012;30(10):918-20.
178. Lloyd GR, Jankevics A, Weber RJM. struct: an R/Bioconductor-based framework for standardized metabolomics data analysis and beyond. Bioinformatics. 2021;36(22-23):5551-2.
179. Shannon P, Markiel A, Ozier O, Baliga NS, Wang JT, Ramage D, et al. Cytoscape: a software environment for integrated models of biomolecular interaction networks. Genome Res. 2003;13(11):2498-504.
180. Ridder L, Wagener M. SyGMa: combining expert knowledge and empirical scoring in the prediction of metabolites. ChemMedChem. 2008;3(5):821-32.
181. Do KT, Wahl S, Raffler J, Molnos S, Laimighofer M, Adamski J, et al. Characterization of missing values in untargeted MS-based metabolomics data and evaluation of missing data handling strategies. Metabolomics. 2018;14(10).
182. Martínez-Sena T, Luongo G, Sanjuan-Herráez D, Castell JV, Vento M, Quintás G, et al. Monitoring of system conditioning after blank injections in untargeted UPLC-MS metabolomic analysis. Scientific Reports. 2019;9(1).
183. Camacho D, de la Fuente A, Mendes P. The origin of correlations in metabolomics data. Metabolomics. 2005;1(1):53-63.
184. Wang Z, Walker GW, Muir DCG, Nagatani-Yoshida K. Toward a Global Understanding of Chemical Pollution: A First Comprehensive Analysis of National and Regional Chemical Inventories. Environmental Science & Technology. 2020;54(5):2575-84.
185. Law V, Knox C, Djoumbou Y, Jewison T, Guo AC, Liu Y, et al. DrugBank 4.0: shedding new light on drug metabolism. Nucleic Acids Research. 2014;42(D1):D1091-D7.
186. Tozuka Z, Kaneko H, Shiraga T, Mitani Y, Beppu M, Terashita S, et al. Strategy for structural elucidation of drugs and drug metabolites using (MS)n fragmentation in an electrospray ion trap. 2003;38(8):793-808.
187. Jeon J, Kurth D, Hollender J. Biotransformation Pathways of Biocides and Pharmaceuticals in Freshwater Crustaceans Based on Structure Elucidation of Metabolites Using High Resolution Mass Spectrometry. 2013;26(3):313-24.
188. Torok S, Vegvari A, Rezeli M, Fehniger TE, Tovari J, Paku S, et al. Localization of sunitinib, its metabolites and its target receptors in tumour-bearing mice: a MALDI-MS imaging study. British journal of pharmacology. 2015;172(4):1148-63.

189. Park TS, Yamashita H, Blaner WS, Goldberg IJ. Lipids in the heart: a source of fuel and a source of toxins. Curr Opin Lipidol. 2007;18(3):277-82.
190. Goldberg IJ, Trent CM, Schulze PC. Lipid metabolism and toxicity in the heart. Cell Metab. 2012;15(6):805-12.
191. Andrieu-Abadie N, Jaffrezou JP, Hatem S, Laurent G, Levade T, Mercadier JJ. L-carnitine prevents doxorubicin-induced apoptosis of cardiac myocytes: role of inhibition of ceramide generation. FASEB J. 1999;13(12):1501-10.
192. D'Souza K, Nzirorera C, Kienesberger PC. Lipid metabolism and signaling in cardiac lipotoxicity. Biochim Biophys Acta. 2016;1861(10):1513-24.
193. Park JY, Lee S-H, Shin M-J, Hwang G-S. Alteration in Metabolic Signature and Lipid Metabolism in Patients with Angina Pectoris and Myocardial Infarction. PLOS ONE. 2015;10(8):e0135228.
194. Burrello J, Biemmi V, Dei Cas M, Amongero M, Bolis S, Lazzarini E, et al. Sphingolipid composition of circulating extracellular vesicles after myocardial ischemia. Scientific Reports. 2020;10(1):16182.
195. Bhattacharyya S, Pence L, Beger R, Chaudhuri S, McCullough S, Yan K, et al. Acylcarnitine profiles in acetaminophen toxicity in the mouse: comparison to toxicity, metabolism and hepatocyte regeneration. Metabolites. 2013;3(3):606-22.
196. McCann MR, George De La Rosa MV, Rosania GR, Stringer KA. L-Carnitine and Acylcarnitines: Mitochondrial Biomarkers for Precision Medicine. Metabolites. 2021;11(1):51.
197. Varga ZV, Ferdinandy P, Liaudet L, Pacher P. Drug-induced mitochondrial dysfunction and cardiotoxicity. Am J Physiol Heart Circ Physiol. 2015;309(9):H1453-67.
198. Hunter WG, Kelly JP, McGarrah RW, Khouri MG, Craig D, Haynes C, et al. Metabolomic Profiling Identifies Novel Circulating Biomarkers of Mitochondrial Dysfunction Differentially Elevated in Heart Failure With Preserved Versus Reduced Ejection Fraction: Evidence for Shared Metabolic Impairments in Clinical Heart Failure. Journal of the American Heart Association.5(8):e003190.
199. Makrecka-Kuka M, Sevostjanovs E, Vilks K, Volska K, Antone U, Kuka J, et al. Plasma acylcarnitine concentrations reflect the acylcarnitine profile in cardiac tissues. Scientific Reports. 2017;7(1):17528.
200. Coecke S, Ahr H, Blaauboer BJ, Bremer S, Casati S, Castell J, et al. Metabolism: a bottleneck in in vitro toxicological test development. The report and recommendations of ECVAM workshop 54. Altern Lab Anim. 2006;34(1):49-84.
201. Gomez-Lechon MJ, Tolosa L, Conde I, Donato MT. Competency of different cell models to predict human hepatotoxic drugs. Expert Opin Drug Metab Toxicol. 2014;10(11):1553-68.
202. Mohammed Taha H, Aalizadeh R, Alygizakis N, Antignac J-P, Arp HPH, Bade R, et al. The NORMAN Suspect List Exchange (NORMAN-SLE): facilitating European and worldwide collaboration on suspect screening in high resolution mass spectrometry. Environmental Sciences Europe. 2022;34(1).
203. Meijer J, Lamoree M, Hamers T, Antignac J-P, Hutinet S, Debrauwer L, et al. An annotation database for chemicals of emerging concern in exposome research. Environment International. 2021;152:106511.
204. Escher BI, Hackermüller J, Polte T, Scholz S, Aigner A, Altenburger R, et al. From the exposome to mechanistic understanding of chemical-induced adverse effects. Environment International. 2017;99:97-106.
205. Soares CP, Midlej V, Oliveira MEWD, Benchimol M, Costa ML, Mermelstein C. 2D and 3D-Organized Cardiac Cells Shows Differences in Cellular Morphology, Adhesion Junctions, Presence of Myofibrils and Protein Expression. PLoS ONE. 2012;7(5):e38147.
206. Russell S, Wojtkowiak J, Neilson A, Gillies RJ. Metabolic Profiling of healthy and cancerous tissues in 2D and 3D. Scientific Reports. 2017;7(1).
207. Hinson JT, Chopra A, Lowe A, Sheng CC, Gupta RM, Kuppusamy R, et al. Integrative Analysis of PRKAG2 Cardiomyopathy iPS and Microtissue Models Identifies

AMPK as a Regulator of Metabolism, Survival, and Fibrosis. Cell Reports. 2016;17(12):3292-304.
208. Li Y, Ju L, Hou Z, Deng H, Zhang Z, Wang L, et al. Screening, verification, and optimization of biomarkers for early prediction of cardiotoxicity based on metabolomics. J Proteome Res. 2015;14(6):2437-45.
209. Wang J, Reijmers T, Chen L, Van Der Heijden R, Wang M, Peng S, et al. Systems toxicology study of doxorubicin on rats using ultra performance liquid chromatography coupled with mass spectrometry based metabolomics. Metabolomics. 2009;5(4):407-18.
210. Wishart DS, Feunang YD, Marcu A, Guo AC, Liang K, Vázquez-Fresno R, et al. HMDB 4.0: the human metabolome database for 2018. Nucleic Acids Research. 2018;46(D1):D608-D17.
211. Kanehisa M. KEGG: Kyoto Encyclopedia of Genes and Genomes. Nucleic Acids Research. 2000;28(1):27-30.
212. Dodder N. OrgMassSpecR: Organic Mass Spectrometry. 2017.
213. Pang Z, Chong J, Li S, Xia J. MetaboAnalystR 3.0: Toward an Optimized Workflow for Global Metabolomics. Metabolites. 2020;10(5):186.
214. Parsons HM, Ekman DR, Collette TW, Viant MR. Spectral relative standard deviation: a practical benchmark in metabolomics. The Analyst. 2009;134(3):478-85.
215. Deng J, Zhang G, Neubert TA. Metabolomic Analysis of Glioma Cells Using Nanoflow Liquid Chromatography–Tandem Mass Spectrometry. In: Placantonakis DG, editor. Glioblastoma: Methods and Protocols. New York, NY: Springer New York; 2018. p. 125-34.
216. Chaudhari U, Nemade H, Wagh V, Gaspar JA, Ellis JK, Srinivasan SP, et al. Identification of genomic biomarkers for anthracycline-induced cardiotoxicity in human iPSC-derived cardiomyocytes: an in vitro repeated exposure toxicity approach for safety assessment. Arch Toxicol. 2016;90(11):2763-77.
217. Hsu H-C, Chen C-Y, Chen M-F. N-3 polyunsaturated fatty acids decrease levels of doxorubicin-induced reactive oxygen species in cardiomyocytes -- involvement of uncoupling protein UCP2. Journal of Biomedical Science. 2014;21(1).
218. Wang ZQ, Chen MT, Zhang R, Zhang Y, Li W, Li YG. Docosahexaenoic Acid Attenuates Doxorubicin-induced Cytotoxicity and Inflammation by Suppressing NF-kappaB/iNOS/NO Signaling Pathway Activation in H9C2 Cardiac Cells. J Cardiovasc Pharmacol. 2016;67(4):283-9.
219. Bonini P, Kind T, Tsugawa H, Barupal DK, Fiehn O. Retip: Retention Time Prediction for Compound Annotation in Untargeted Metabolomics. Analytical Chemistry. 2020;92(11):7515-22.
220. Jones MRL, T.N.; Weber, R.J.M.; Dunn, W.B.; Viant, M.R. Deep Metabolome Annotation of the model organism *Daphnia magna*. Unpublished work. 2018.
221. Edison A, Hall R, Junot C, Karp P, Kurland I, Mistrik R, et al. The Time Is Right to Focus on Model Organism Metabolomes. Metabolites. 2016;6(1):8.
222. Roux A, Xu Y, Heilier J-F, Olivier M-F, Ezan E, Tabet J-C, et al. Annotation of the Human Adult Urinary Metabolome and Metabolite Identification Using Ultra High Performance Liquid Chromatography Coupled to a Linear Quadrupole Ion Trap-Orbitrap Mass Spectrometer. Analytical Chemistry. 2012;84(15):6429-37.
223. Xu M, Legradi J, Leonards P. Cross platform solutions to improve the zebrafish polar metabolome coverage using LC-QTOF MS: Optimization of separation mechanisms, solvent additives, and resuspension solvents. Talanta. 2021;234:122688.
224. Hackbusch S, Peake DA, Kiyonami R. Improved lipid annotation depth using automatically generated inclusion and exclusion lists on an Orbitrap-based mass spectrometer. Poster at 67th ASMS Conference on Mass Spectrometry and Allied Topics2019.
225. Sostare E, Lawson TN, Saunders LR, Colbourne JK, Weber RJM, Sobanski T, et al. Knowledge-driven approaches to create the MTox700+ metabolite panel for predicting toxicity. Toxicological Sciences. 2022.

226. Kind T, Liu K-H, Lee DY, Defelice B, Meissen JK, Fiehn O. LipidBlast in silico tandem mass spectrometry database for lipid identification. Nature Methods. 2013;10(8):755-8.
227. mzCloud [Available from: https://www.mzcloud.org/.
228. Nabben M, Glatz JFC. Chapter 2 - Basics in Metabolically Relevant Biochemistry. In: Schwarzer M, Doenst T, editors. The Scientist's Guide to Cardiac Metabolism. Boston: Academic Press; 2016. p. 7-18.
229. Xiong Y, Jiang L, Li T. Aberrant branched-chain amino acid catabolism in cardiovascular diseases. Frontiers in Cardiovascular Medicine. 2022;9.
230. Karwi QG, Lopaschuk GD. Branched-Chain Amino Acid Metabolism in the Failing Heart. Cardiovascular Drugs and Therapy. 2022.
231. Balestrino M. Role of Creatine in the Heart: Health and Disease. Nutrients. 2021;13(4):1215.
232. Li F, Song J, Zhang Y, Wang S, Wang J, Lin L, et al. LINT-Web: A Web-Based Lipidomic Data Mining Tool Using Intra-Omic Integrative Correlation Strategy. Small Methods. 2021;5(9):2100206.
233. Rubio Gomez MA, Ibba M. Aminoacyl-tRNA synthetases. Rna. 2020;26(8):910-36.
234. Vander Heiden MG, Cantley LC, Thompson CB. Understanding the Warburg Effect: The Metabolic Requirements of Cell Proliferation. Science. 2009;324(5930):1029-33.
235. Asnani A, Shi X, Farrell L, Lall R, Sebag IA, Plana JC, et al. Changes in Citric Acid Cycle and Nucleoside Metabolism Are Associated with Anthracycline Cardiotoxicity in Patients with Breast Cancer. Journal of Cardiovascular Translational Research. 2020;13(3):349-56.
236. Damiani RM, Moura DJ, Viau CM, Caceres RA, Henriques JAP, Saffi J. Pathways of cardiac toxicity: comparison between chemotherapeutic drugs doxorubicin and mitoxantrone. Archives of Toxicology. 2016;90(9):2063-76.
237. Liebisch G, Vizcaíno JA, Köfeler H, Trötzmüller M, Griffiths WJ, Schmitz G, et al. Shorthand notation for lipid structures derived from mass spectrometry. Journal of Lipid Research. 2013;54(6):1523-30.
238. Koelmel JP, Li X, Stow SM, Sartain MJ, Murali A, Kemperman R, et al. Lipid Annotator: Towards Accurate Annotation in Non-Targeted Liquid Chromatography High-Resolution Tandem Mass Spectrometry (LC-HRMS/MS) Lipidomics Using a Rapid and User-Friendly Software. Metabolites. 2020;10(3):101.
239. Han RH, Wang M, Fang X, Han X. Simulation of triacylglycerol ion profiles: bioinformatics for interpretation of triacylglycerol biosynthesis. Journal of Lipid Research. 2013;54(4):1023-32.
240. Vaňková Z, Peterka O, Chocholoušková M, Wolrab D, Jirásko R, Holčapek M. Retention dependences support highly confident identification of lipid species in human plasma by reversed-phase UHPLC/MS. Analytical and Bioanalytical Chemistry. 2022;414(1):319-31.
241. van der Veen JN, Kennelly JP, Wan S, Vance JE, Vance DE, Jacobs RL. The critical role of phosphatidylcholine and phosphatidylethanolamine metabolism in health and disease. Biochimica et Biophysica Acta (BBA) - Biomembranes. 2017;1859(9, Part B):1558-72.
242. Evans RD, Hauton D. The role of triacylglycerol in cardiac energy provision. Biochimica et Biophysica Acta (BBA) - Molecular and Cell Biology of Lipids. 2016;1861(10):1481-91.
243. Wu R, Wang HL, Yu HL, Cui XH, Xu MT, Xu X, et al. Doxorubicin toxicity changes myocardial energy metabolism in rats. Chem Biol Interact. 2016;244:149-58.
244. Sun Z, Schriewer J, Tang M, Marlin J, Taylor F, Shohet RV, et al. The TGF-β pathway mediates doxorubicin effects on cardiac endothelial cells. Journal of Molecular and Cellular Cardiology. 2016;90:129-38.
245. Ngere JB, Ebrahimi KH, Williams R, Pires E, Walsby-Tickle J, McCullagh JSO. Ion-Exchange Chromatography Coupled to Mass Spectrometry in Life Science, Environmental, and Medical Research. Analytical Chemistry. 2023;95(1):152-66.

246. Schnackenberg LK, Pence L, Vijay V, Moland CL, George N, Cao Z, et al. Early metabolomics changes in heart and plasma during chronic doxorubicin treatment in B6C3F1 mice. J Appl Toxicol. 2016;36(11):1486-95.
247. Chaudhari U, Ellis JK, Wagh V, Nemade H, Hescheler J, Keun HC, et al. Metabolite signatures of doxorubicin induced toxicity in human induced pluripotent stem cell-derived cardiomyocytes. Amino Acids. 2017;49(12):1955-63.
248. Yin J, Xie J, Guo X, Ju L, Li Y, Zhang Y. Plasma metabolic profiling analysis of cyclophosphamide-induced cardiotoxicity using metabolomics coupled with UPLC/Q-TOF-MS and ROC curve. J Chromatogr B Analyt Technol Biomed Life Sci. 2016;1033-1034:428-35.
249. Jensen B, Parry T, Huang W, Ilaiwy A, Bain J, Muehlbauer M, et al. Non-Targeted Metabolomics Analysis of the Effects of Tyrosine Kinase Inhibitors Sunitinib and Erlotinib on Heart, Muscle, Liver and Serum Metabolism In Vivo. Metabolites. 2017;7(3):31.
250. Jensen BC, Parry TL, Huang W, Beak JY, Ilaiwy A, Bain JR, et al. Effects of the kinase inhibitor sorafenib on heart, muscle, liver and plasma metabolism in vivo

using non-targeted metabolomics analysis. British journal of pharmacology. 2017;174(24):4797-811.
251. Groothuis FA, Heringa MB, Nicol B, Hermens JLM, Blaauboer BJ, Kramer NI. Dose metric considerations in in vitro assays to improve quantitative in vitro–in vivo dose extrapolations. Toxicology. 2015;332:30-40.
252. Malinowska JM, Palosaari T, Sund J, Carpi D, Lloyd GR, Weber RJM, et al. Automated Sample Preparation and Data Collection Workflow for High-Throughput In Vitro Metabolomics. Metabolites. 2022;12(1):52.
253. Campos MP, Reis MS. Data preprocessing for multiblock modelling – A systematization with new methods. Chemometrics and Intelligent Laboratory Systems. 2020;199:103959.
254. Suzuki R, Terada, Y., Shimodaira, H. pvclust: Hierarchical Clustering with P-Values via Multiscale Bootstrap Resampling R package version 2.2.0. https://CRANR-projectorg/package=pvclust. 2019.
255. U.S. Food and Drug Administration. Bioanalytical Method Validation Guidance for Industry. 2018.
256. Kramer NI, Krismartina M, Rico-Rico Á, Blaauboer BJ, Hermens JLM. Quantifying Processes Determining the Free Concentration of Phenanthrene in Basal Cytotoxicity Assays. Chemical Research in Toxicology. 2012;25(2):436-45.
257. Tanneberger K, Rico-Rico A, Kramer NI, Busser FJM, Hermens JLM, Schirmer K. Effects of Solvents and Dosing Procedure on Chemical Toxicity in Cell-Based in Vitro Assays. Environmental Science & Technology. 2010;44(12):4775-81.
258. Mahieu NG, Spalding JL, Gelman SJ, Patti GJ. Defining and Detecting Complex Peak Relationships in Mass Spectral Data: The Mz.unity Algorithm. Analytical Chemistry. 2016;88(18):9037-46.
259. Garcia-Canton C, Minet E, Anadon A, Meredith C. Metabolic characterization of cell systems used in in vitro toxicology testing: Lung cell system BEAS-2B as a working example. Toxicology in Vitro. 2013;27(6):1719-27.
260. Rana P, Anson B, Engle S, Will Y. Characterization of Human-Induced Pluripotent Stem Cell–Derived Cardiomyocytes: Bioenergetics and Utilization in Safety Screening. Toxicological Sciences. 2012;130(1):117-31.
261. Correia C, Koshkin A, Duarte P, Hu D, Teixeira A, Domian I, et al. Distinct carbon sources affect structural and functional maturation of cardiomyocytes derived from human pluripotent stem cells. Sci Rep. 2017;7(1):8590.
262. Quintás G, Martínez-Sena T, Conde I, Pareja Ibars E, Kleinjans J, Castell JV. Metabolomic analysis to discriminate drug-induced liver injury (DILI) phenotypes. Archives of Toxicology. 2021;95(9):3049-62.

263. Castro BM, Prieto M, Silva LC. Ceramide: A simple sphingolipid with unique biophysical properties. Progress in Lipid Research. 2014;54:53-67.
264. Shu H, Peng Y, Hang W, Li N, Zhou N, Wang DW. Emerging Roles of Ceramide in Cardiovascular Diseases. Aging and disease. 2022;13(1):232.
265. Rocca C, De Francesco EM, Pasqua T, Granieri MC, De Bartolo A, Gallo Cantafio ME, et al. Mitochondrial Determinants of Anti-Cancer Drug-Induced Cardiotoxicity. Biomedicines. 2022;10(3):520.
266. Bekhite M, González-Delgado A, Hübner S, Haxhikadrija P, Kretzschmar T, Müller T, et al. The role of ceramide accumulation in human induced pluripotent stem cell-derived cardiomyocytes on mitochondrial oxidative stress and mitophagy. Free Radic Biol Med. 2021;167:66-80.
267. Law BA, Liao X, Moore KS, Southard A, Roddy P, Ji R, et al. Lipotoxic very-long-chain ceramides cause mitochondrial dysfunction, oxidative stress, and cell death in cardiomyocytes. The FASEB Journal. 2018;32(3):1403-16.
268. Kretzschmar T, Bekhite MM, Wu JMF, Haase D, Förster M, Müller T, et al. Long-Chain and Very Long-Chain Ceramides Mediate Doxorubicin-Induced Toxicity and Fibrosis. International Journal of Molecular Sciences. 2021;22(21):11852.
269. Russo M, Della Sala A, Tocchetti CG, Porporato PE, Ghigo A. Metabolic Aspects of Anthracycline Cardiotoxicity. Current Treatment Options in Oncology. 2021;22(2).
270. Del Franco A, Ambrosio G, Baroncelli L, Pizzorusso T, Barison A, Olivotto I, et al. Creatine deficiency and heart failure. Heart Failure Reviews. 2022;27(5):1605-16.
271. Zieliński J, Slominska EM, Król-Zielińska M, Krasiński Z, Kusy K. Purine metabolism in sprint- vs endurance-trained athletes aged 20–90 years. Scientific Reports. 2019;9(1).
272. Wen J, Zhang L, Wang J, Wang J, Wang L, Wang R, et al. Therapeutic effects of higenamine combined with [6]-gingerol on chronic heart failure induced by doxorubicin via ameliorating mitochondrial function. J Cell Mol Med. 2020;24(7):4036-50.
273. Yi X, Zhu J, Zhang J, Gao Y, Chen Z, Lu S, et al. Investigation of the reverse effect of Danhong injection on doxorubicin-induced cardiotoxicity in H9c2 cells: Insight by LC-MS based non-targeted metabolomic analysis. J Pharm Biomed Anal. 2018;152:264-70.
274. Leonardi R, Jackowski S. Biosynthesis of Pantothenic Acid and Coenzyme A. EcoSal Plus. 2007;2(2).
275. Bouitbir J, Alshaikhali A, Panajatovic MV, Abegg VF, Paech F, Krahenbuhl S. Mitochondrial oxidative stress plays a critical role in the cardiotoxicity of sunitinib: Running title: Sunitinib and oxidative stress in hearts. Toxicology. 2019;426:152281.
276. Songbo M, Lang H, Xinyong C, Bin X, Ping Z, Liang S. Oxidative stress injury in doxorubicin-induced cardiotoxicity. Toxicology Letters. 2019;307:41-8.
277. Bowen TJ, Hall AR, Lloyd GR, Weber RJM, Wilson A, Pointon A, et al. An Extensive Metabolomics Workflow to Discover Cardiotoxin-Induced Molecular Perturbations in Microtissues. Metabolites. 2021;11(9):644.
278. Chetwynd AJ, David A. A review of nanoscale LC-ESI for metabolomics and its potential to enhance the metabolome coverage. Talanta. 2018;182:380-90.
279. Gromski PS, Muhamadali H, Ellis DI, Xu Y, Correa E, Turner ML, et al. A tutorial review: Metabolomics and partial least squares-discriminant analysis – a marriage of convenience or a shotgun wedding. Analytica Chimica Acta. 2015;879:10-23.
280. Lin X, Wang Q, Yin P, Tang L, Tan Y, Li H, et al. A method for handling metabonomics data from liquid chromatography/mass spectrometry: combinational use of support vector machine recursive feature elimination, genetic algorithm and random forest for feature selection. Metabolomics. 2011;7(4):549-58.
281. Lisitsyna A, Moritz F, Liu Y, Al Sadat L, Hauner H, Claussnitzer M, et al. Feature Selection Pipelines with Classification for Non-targeted Metabolomics Combining the Neural Network and Genetic Algorithm. Analytical Chemistry. 2022;94(14):5474-82.

282. Canzler S, Schor J, Busch W, Schubert K, Rolle-Kampczyk UE, Seitz H, et al. Prospects and challenges of multi-omics data integration in toxicology. Archives of Toxicology. 2020;94(2):371-88.
283. Smith MJ, Weber RJM, Viant MR. Spatially Mapping the Baseline and Bisphenol-A Exposed Daphnia magna Lipidome Using Desorption Electrospray Ionization—Mass Spectrometry. Metabolites. 2022;12(1):33.
284. Neumann EK, Migas LG, Allen JL, Caprioli RM, Van De Plas R, Spraggins JM. Spatial Metabolomics of the Human Kidney using MALDI Trapped Ion Mobility Imaging Mass Spectrometry. Analytical Chemistry. 2020;92(19):13084-91.
285. Rao A, Barkley D, França GS, Yanai I. Exploring tissue architecture using spatial transcriptomics. Nature. 2021;596(7871):211-20.
286. Smith MJ, Ivanov DP, Weber RJM, Wingfield J, Viant MR. Acoustic Mist Ionization Mass Spectrometry for Ultrahigh-Throughput Metabolomics Screening. Analytical Chemistry. 2021;93(26):9258-66.
287. Malinowska JM, Palosaari T, Sund J, Carpi D, Weber RJM, Lloyd GR, et al. Derivation of metabolic point of departure using high-throughput in vitro metabolomics: investigating the importance of sampling time points on benchmark concentration values in the HepaRG cell line. Archives of Toxicology. 2023;97(3):721-35.
288. Chang X, Tan Y-M, Allen DG, Bell S, Brown PC, Browning L, et al. IVIVE: Facilitating the Use of In Vitro Toxicity Data in Risk Assessment and Decision Making. Toxics. 2022;10(5):232.
289. Hemmerich J, Ecker GF. In silico toxicology: From structure–activity relationships towards deep learning and adverse outcome pathways. WIREs Computational Molecular Science. 2020;10(4):e1475.